

Exploring Possible Coupling between Phonons and Internal Nuclear States

by

Siyuan Lu

B.E., Zhejiang University (2011)
M.S., Columbia University (2013)

Submitted to the Department of Electrical Engineering and Computer Science
in Partial Fulfillment of the Requirements for the Degree of

Doctor of Philosophy

at the

MASSACHUSETTS INSTITUTE OF TECHNOLOGY
September 2018

© 2018 Massachusetts Institute of Technology. All rights reserved

Signature redacted

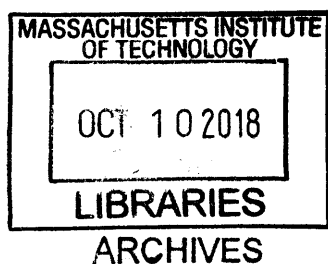
Signature of Author: _____
Department of Electrical Engineering and Computer Science
August 10, 2018

Signature redacted

Certified by: _____
Peter L. Hagelstein
Associate Professor of Electrical Engineering and Computer Science
Thesis Supervisor

Signature redacted

Accepted by: _____
Leslie A. Kolodziejski
Professor of Electrical Engineering and Computer Science
Chair, Department Committee on Graduate Students



Exploring Possible Coupling between Phonons and Internal Nuclear States

by

Siyuan Lu

Submitted to the Department of Electrical Engineering and Computer Science
on August 10, 2018 in Partial Fulfillment of the Requirements for the Degree of
Doctor of Philosophy in Electrical Engineering and Computer Science

ABSTRACT

During the past three decades, there were approximately 25 different anomalies in the field of condensed matter nuclear science reported by researchers. One example involves collimated X-rays coming from metal samples with vibrations without a clear explanation or understanding of the underlying physics involved. Another example involves unexpected non-exponential decay of radioactive sources.

These anomalies have motivated a research effort by my Ph.D. advisor at MIT, Professor Peter Hagelstein, to investigate the physical phenomena involved. Hagelstein came up with a theory predicting coupling between phonons and internal nuclear states, leading to excitation transfer between nuclei. The aim of this Ph.D. thesis is to experimentally test Hagelstein's theory.

In this research, we used Co-57 as the sample to investigate the nuclear excited states. Unexpected non-exponential decay was seen in the first attempt to look for excitation transfer effect. Heat pulse can trigger X-ray signal increments. We performed angular anisotropy experiments which appears to support the conjecture that slow resonant excitation transfer occurs for the 136 keV excited state of Co-57. We also performed delocalization experiments which appears to support the conjecture that fast excitation transfer occurs for the 14.4 keV excited state of Co-57. Our conclusion is that the experimental data are not inconsistent with Hagelstein's theory.

Thesis Supervisor: Peter L. Hagelstein

Title: Associate Professor of Electrical Engineering and Computer Science

Acknowledgement

It is challenging to do a Ph.D. at MIT. It has been a long and difficult journey for me to reach this point. I feel so fortunate that during the past five years I got lots of help from many people. Without them, I would not be able to make it. I do not take this for granted. I would like to express my sincere thanks to all of them.

I first met my research supervisor Professor Peter Hagelstein when I took his Quantum Physics class during the Fall 2013 semester. That class was tough, but Professor Hagelstein made the class very interesting. He cared about his class and his students. Though he had taught this class several times, he still spent several hours re-writing his notes for every single lecture and recitation. He even joined the office hours every week to answer students' questions about homework. Students loved him, and many students said that he was the best teacher they had ever seen.

It was fortunate for me that later I could have the chance to work with him for my thesis. As he cared about his students in his class, he cared about me. He gave everything he could to make me succeed. He spent several months teaching his theory to me as if he was teaching an official MIT class with only one student. He was always patient with all my questions no matter how stupid those questions might be. He spent days working in the lab together with me when the experiments got stuck. He was able to make me motivated every single time when I felt sad and depressed. Without him, I would not be able to make this far. I would still choose him as my supervisor if I could repeat my graduate school at MIT.

I would like to thank my thesis committee members, Professor Cardinal Warde and Professor Jeffrey Lang. They have been helpful and supportive for a long time. We had a total of nine committee meetings from March 2017 to May 2018. They were very interested in my research, and they always offered great suggestions. Many significant results in this thesis would not exist without the committee's willingness to see strong positive results. Both Professor Warde and Professor Lang offered lots of valuable comments and suggestions for my final thesis writing.

My colleague Florian Metzler is a very good experimentalist. He helped a lot with the experiments in this thesis. There were many days that we worked together late until midnight. He also contributed a lot in fundraising for the group. Without his generous help, I would not get as many good results as reviewed in this thesis.

Clarice Aiello was the teaching assistant for Professor Hagelstein's Quantum Physics class. She joined Hagelstein's group as a postdoc after finishing her Ph.D. at MIT. Later she kindly invited me to join the group and recommend me to Professor Hagelstein. Without her, I would not be able to join Hagelstein's group.

Industrial Heat is the sponsor for our research. Dewey Weaver helped a lot supporting our group. Dewey is very interested in our research. I am very grateful that he flew to MIT from another state to join my thesis defense.

My good friend Yang Yang, who is also a Ph.D. student at MIT EECS, helped me a lot in my study during the past years. We took several classes together during my first two years. Later he offered many great ideas and suggestions for my research.

Another friend Xin Qiu, who graduated from MIT in 2016, was always helpful talking with me when I got stressed under pressure. He is very busy with his job but he is willing to talk to me whenever I need. Talking with him can always make me feel relaxed.

The family of Lei Hou and Na Sun offered great support to my family during the last year of my Ph.D. at MIT. Not only we are close friends, my son and their daughter used to be classmates in the same daycare. Several times when I talked with them after school in front of the daycare gate, I could tell how fortunate both my son and I got such a valuable friendship.

My parents Zhiyong Lu and Yanli Li have been supportive for the past 30 years of my life. They always tried to give me the best they could offer. Without them I would not be able to study in the US, I would not have a chance to do a Ph.D. at MIT. They have always been the best parents.

Last but not the least, I would like to thank my wife, Pengqi. There is not a word that I could express how fortunate I have her in my life. There is not a word that I could express how important she is in my life. If I have to choose one single person as the most important person in my Ph.D. life at MIT, it must be my wife, Pengqi. Without her, I would not be able to make it for sure.

It was a rainy day in December 2012 that my wife Pengqi and I stepped into the MIT campus for the first time. On that day I knew that she would help me a lot during the coming years by offering me emotional support and taking care of the family. I did not expect any help from her for my research as she was not from an engineering or science background. However, this was not the case. Pengqi is super super smart. She could understand our theory very well. She knew the meaning of phonon nuclear coupling. She even helped solve the indirect coupling terms for the complicated excitation transfer problems. Moreover, she offered many great suggestions for my experiments. There was one time that my experiment got stuck for several weeks with the X-ray air attenuation problem. It was finally her suggestion that helped me solve the problem and move forward. Every day when I came home from the lab, I enjoyed talking with her about my experiment progress as her response was always helpful. If Pengqi were the person doing this Ph.D. instead of me, she probably would not need five years.

It is easy for a Ph.D. student to get sad or even depressed. In my first two years, I struggled taking classes. In the following three years experiment failures happen in my daily life. It is Pengqi who always stands at my side and helps make me motivated. She always believes that I can make it, even when sometimes I do not believe in myself. We had our first son Panda soon after I started at MIT. Later we had our second son Nono in my third Ph.D. year. Graduate school at MIT is not easy, having two children in the meantime is very tough. It was Pengqi who took great care of the whole family day by day during the past five years allowing me enough time to do research in the lab. I would also like to say thank you to my sons Panda and Nono. Though taking care of them is not easy, both of them brought us great happiness. It turns out that parents' memories are selective. Now I can only remember the happy moments the two boys have brought to us.

Doing research with Professor Hagelstein and living at MIT with my family is the best time of my life. At this point, I feel a little disappointed that I need to say goodbye to this journey. I hope that I could return some day in the future.

Outline

1	Introduction	9
2	Claims for Collimated X-ray and Gamma Emission	27
2.1	The Karabut Experiment	27
2.2	The Kornilova Experiment	30
2.3	The Ivlev Experiment	35
3	Phonon-Nuclear Coupling Mechanism	39
4	Resonant Phonon-Nuclear Excitation Transfer Mechanism	43
4.1	Example 1 (No phonon exchange or loss)	43
4.2	Example 2 (Adding phonon exchange but no loss)	45
5	Observation of Unexpected Non-Exponential Decay from Co-57	50
6	Heat Pulse Experiment	56
7	Theory: Angular Anisotropy	59
8	Experiment: Angular Anisotropy	61
9	Theory: Delocalization	70
10	Experiment: Pinhole/Film	72
11	Experiment: Pinhole/SDD	78
12	Interpretations	88
13	Summaries, Conclusions, and Future Work	94

Appendix

A	Sample Model for Excitation Transfer with Loss	101
B	Conjecture to Explain the Karabut and Kornilova Experiment	104
C	Up-conversion and down-conversion	107
D	Water Jet Experiment at MIT	113
E	Amplitude Modulation Studies	119
F	Mercury Co-Deposition	149
G	Film Calibration	162
H	Pinhole/Film Experiment with 0.2 mm Pinhole	164
I	Pinhole/Film Experimental Results for Sample 2	168
J	More Angular Anisotropy Experimental Data	170
K	Bent Crystal Spectrometer	175

1. Introduction

There have always been various experiments, theoretical ideas, and even entire fields which exist outside of the scientific mainstream, and which are pursued by those who are interested and sufficiently brave. From time to time the borders of science are expanded to include research results from outside of science: for example, the revolutionary notion of Semmelweis¹ that a reduction of the mortality rate associated with birth might be accomplished by doctors washing their hands; another example is the radical idea put forth by Wegener² that continents can move over time. Similarly, mainstream notions can be thrown out as well: for example, the notion of the aether³ was dispensed with following the Michelson and Morley experiment;⁴ and alchemy⁵ was set aside finally with the advent of modern nuclear physics.

The notion of an anomaly has had a particularly interesting history in science. In earlier times the notion of an anomaly (such as the observed precession of mercury,⁶ which disagreed with predictions from Newton's laws) was accepted, in part since science generally was immature and emerging. A survey of the use of the word anomaly in current mainstream journals indicates an effect that generally would be considered to be unusual, but which lies within the realm of science and is understood. Examples of this include the Kohn anomaly,⁷ the dielectric anomaly,⁸ the chiral anomaly,^{9,10} the quantum anomaly,^{11,12} the gravitational anomaly,¹³ and the hyperfine anomaly¹⁴ (none of which at present involves a lack of theoretical or experimental understanding). One of the few modern anomalies in mainstream science which remains truly anomalous is the Pioneer anomaly,¹⁵ which is an unaccounted for acceleration of the Pioneer spacecraft in the outer reaches of the solar system.

There have been reported a large number of anomalies in the (new) field of Condensed Matter Nuclear Science (a research area considered at this time to lie outside of the well demarcated boundary of mainstream science) that have been the focus of a committed group of researchers for nearly three decades. One of the anomalies involves the production of excess heat

in a heavy water electrochemical experiment with a palladium cathode, which was first reported by Fleischmann and Pons in 1989.¹⁶ Much attention was focused on the announcement, and much controversy followed, resulting ultimately in a rejection of the claim and the determination that this experiment lies outside of mainstream science.¹⁷ However, the focus at the time on a misunderstanding of the experiment and its significance has detracted from the much more substantial set of anomalies seen in hundreds of experiments, some of which are much earlier, some of which were reported around the time of the controversy, and many of which have been observed subsequently.

At this point we recognize the anomalies to include excess heat generation in PdD and in NiH electrochemical experiments, and also in electrochemical experiments with other metal hydrides and deuterides.¹⁸⁻²¹ Claims for thermal effects have been made also for glow discharge experiments;²² simpler experiments in which hydrogen or deuterium is desorbed from a loaded metal,²³ or even flowed through a metal foil;²⁴ experiments where nano materials loaded with hydrogen or deuterium are simply heated;²⁵ and where a current is passed through a loaded nano material.²⁶

There have been numerous reports of ^4He generated in connection with the energy in PdD experiments, in amounts that may be consistent with the mass difference between D_2 and ^4He .²⁷⁻²⁹ The relative absence of energetic radiation from the experiments when thermal effects are seen allow for an interpretation that the ^4He nucleus is born very nearly stationary,³⁰ and that the energy produced is communicated to the surroundings via unconventional channels. There have also been many observations of tritium generation in PdD experiments,³¹ with a similar absence of associated energetic radiation, which allows for an interpretation that the tritium is also born essentially stationary.³²

There are more than 100 reports of observations of low-level nuclear radiation from metal deuterides in a variety of experiments (electrochemical, glow discharge, low energy ion

implantation, and desorption), which include d+d fusion reaction products ($p+t$, $n+3\text{He}$), and also unconventional products including energetic alphas and neutrons with energies above 10 MeV.³³⁻
⁴³ Neutron and alpha emission have been reported from fracture experiments with granite,⁴⁴⁻⁴⁶ and from steel samples following intensive mechanical stimulation.⁴⁷⁻⁴⁹

Many claims have been made for observations of new elements at this point in electrochemical, gas loading, and deuterium flow experiments. In some cases, there have been reported macroscopic amounts of lower mass elements,^{50,51} suggestive of unconventional fission (but without energetic products). Much harder to understand are reported observations where higher mass products are claimed.^{52,53}

The response of the mainstream scientific community has largely been one of a blanket rejection of all such claims. From the experience of 1989 some understanding is possible of why this might be. In earlier times the observation of an anomaly could be accepted since it was understood that science was immature, and that an anomaly might hold the promise of new science. However, in the 20th century the large strides in experimental and theoretical physics has resulted in a new maturity of the hard sciences. With the advent of quantum electrodynamics by about 1950, quantum chromodynamics around 1965, and electro-weak field theory in the early 1970s, the basic laws of physics that apply to electrons, light, and nuclei have become understood in a fundamental way. In the clear light of understanding that has emerged from these advances, modern physics understands how the world works under conventional laboratory conditions (the clear light of understanding has not yet extended to the fundamentals of gravity combined with quantum mechanics), and there is no longer any room in physics for anomalies which seem not to work in well understood ways. This point of view came through clearly in the controversy in 1989, with the rejection of the Fleischmann-Pons experiment based much more on the absence of a theoretical understanding of how the effect might work, than on any compelling identification of a problem with the experiment in the case of the excess heat claim.⁵⁴

The only possible resolution of this situation (which has gone on now for nearly three decades since the 1989 controversy, and much longer if one adopts a more generalized view) is to sort things out theoretically, and to provide a fundamental understanding of how the anomalies work.

On the face of it the associated theoretical problem is much bigger, and also much harder, than the experimental one. For example, it is possible to do new experiments which are something like previous experiments, and from experience we know now that some of these new experiments work. However, the development of a new theory in the seeming absence of relevant earlier work is a different story. This was the task faced by the theorists back in 1989.

Quite a few theorists put forth proposals of one sort or another following the initial announcement of Fleischmann and Pons in 1989. In retrospect the majority of these were naive, and focused on specific issues that seemed to be important in the early PdD experiments. The biggest problem was that there was insufficient information available from the early experiments to have much chance of developing an appropriate theoretical response. Few theorists have managed a sustained effort as the field has evolved.

One theoretical approach which seems promising is based on phonon-nuclear coupling, following the ideas of Hagelstein,⁵⁵ and Hagelstein and Chaudhary.⁵⁶⁻⁶⁰ The foundation of this approach is quite general, and started decades ago from the presumption that there exists a coupling between the internal nuclear degrees of freedom and vibrations in the local condensed matter system. Although the research focused initially on accounting for excess heat effect in the Fleischmann-Pons experiment, the approach is sufficiently general that it has benefitted from the inclusion of a consideration of the larger set of anomalies.

According to this model, phonon-nuclear coupling in its most basic form allows for the exchange of a single vibrational quantum coupled to a single nuclear transition. In Chapter 3 we will review a derivation of this coupling directly from a relativistic model for nucleons in a nucleus that was found initially around 2011. The interaction is similar to photon-nuclear coupling, which

in its most basic form allows for the exchange of a single photon coupled to a single nuclear transition. This photon-nuclear coupling makes possible the radiative decay of excited nuclear states by single photon emission. An analogous channel for the decay of a nuclear excited state by single phonon emission is not available due to a mismatch between the nuclear excitation energy (keV or higher) and the available phonon mode energies (typically less than 100 meV). Consequently, interactions between the internal nuclear states and the vibrational modes work differently, and we cannot make use of our intuition based on photon-nuclear coupling. Since first-order processes do not contribute, we need to focus on second-order and higher-order processes.

At second-order there are a variety of two-phonon interactions that might be considered. We might consider two-phonon decay, but once again there is the problem of a mismatch between the nuclear transition energy and the phonon energies. A more subtle second-order effect is excitation transfer, in which the nuclear excitation at one site is transferred to another site, with the exchange of at least one phonon from a common vibrational mode at each site. This relatively simple nuclear excitation transfer effect is the lowest-order process within the theory generally, and as such becomes important primarily in providing a mechanism that can be tested to see whether the predicted phonon-nuclear effect is real.

The most astonishing feature associated with the excess heat effect in the Fleischmann-Pons experiment is the absence of commensurate energetic nuclear radiation. In a conventional incoherent nuclear reaction, the simultaneous conservation of energy and momentum dictates that in the case of an energy-producing nuclear reaction, the mass energy converted must be carried away by energetic particles in the exit channel of the final state. Since there are no commensurate energetic particles observed in the Fleischmann-Pons experiment, since there is quite a bit of energy observed, and a commensurate amount of ^4He observed, it can be concluded that a conventional incoherent reaction is not involved. Within the framework of the phonon

theory, the nuclear energy ends up ultimately as a large number of phonons within a quantum mechanical picture involving coherent processes.

The thought initially was to try down-converting the nuclear energy to vibrations all at once in a high-order coherent process. However, models for this ran immediately into difficulty for a variety of reasons. In the most recent coherent reaction scheme, the excitation of the D_2 viewed as an excited state of the mass 4 system is transferred and subdivided to produce many excited nuclei in long-lived states which subsequently de-excite through the coherent sequential emission of many phonons. This kind of scheme leads to the weakest requirements on the various components of the model. There are reports of gamma emission from long-lived excited nuclear states from Fleischmann-Pons cells,²⁸ consistent with the coherent reaction picture.

Incoherent excitation transfer from the $D_2/{}^4\text{He}$ system to the host lattice nuclei can account for low-level emission of alpha particles and other unconventional nuclear products.

There are many more specific connections between the phonon theory and experiment; however, our purpose here is not to convince, but instead to draw attention to the existence of a rich theoretical foundation, formalism, and set of reaction schemes that have the potential to account for a majority of the claimed anomalies systematically. What has not been established in earlier work is any direct verification that the predicted relativistic phonon-nuclear interaction exists, and that the lowest-order excitation transfer process actually occurs.

An effort to address this was initiated in 2013 when vibrating plate experiments were subcontracted to SRI. The basic idea at the time was as follows. The same models that predicted down-conversion in the Fleischmann-Pons experiment also predict up-conversion. A number of experiments had been reported by other groups which could be interpreted as being due to an up-conversion of vibrational energy to nuclear energy, so the plan was to attempt a controlled experiment in which vibrations were applied to a plate, and evidence for up-conversion was looked for. In the experiments at SRI in 2013, signals were observed that seemed to be consistent

with up-conversion to x-rays, and with charge emission from the plate. Analysis of the x-ray data indicated a problem, and eventually it was concluded that the x-ray signals at SRI were an artifact.

An effort was initiated at MIT in 2014 by Clarice Aiello to seek confirmation of the charge emission effect. A vibrating plate experiment was developed, and detection similar to what was used at SRI was carried out. In some experiments a similar charge emission effect was observed, which when studied further was found to be an artifact. SRI carried out similar tests with their version of the experiment and confirmed that the charge emission was an artifact at SRI.

Subsequently, new tests were carried out. In one set of experiments the author carried out a set of waterjet experiments (discussed in the Appendix D), looking for collimated x-ray emission as had been claimed by Kornilova and coworkers (discussed further below), which could be interpreted as being due to the up-conversion of phonons to produce nuclear excitation. Although film exposures were found, in most cases these could be attributed to artifacts.

In another set of experiments, steel plates were vibrated with a transducer, and detectors were fielded looking for x-ray emission and also charge emission. Although counts were registered in some of the experiments, these counts were found to be due to artifacts. The lowest energy accessible nuclear transition from the ground state among the stable nuclei is the 1565 eV transition in ^{201}Hg , which was a primary candidate nuclear transition for an up-conversion experiment. We were interested in developing an experiment in which a plate with mercury on the surface was subject to vibrational stimulation and x-ray emission monitored. The author was involved in a research project aimed at developing suitable samples for testing, where mercury was deposited on copper plates (discussed further in the Appendix F). A steel plate with a copper coating was developed, on which mercury can be deposited.

An effort was made to connect with up-conversion in the Karabut experiment, which was a glow discharge experiment (discussed below in Chapter 2) in which collimated x-ray emission near 1.5 keV was claimed. The idea was that the steel resonator was involved in the up-conversion, so

for this we worked with a smaller steel resonator, and made use of an ultrasonic transducer to vibrate it. The idea was to field a sample with mercury on the surface connected to the resonator, and drive it strongly with a transducer. Some of this work is discussed in the Appendix E. Before this experiment was completed, Metzler had some success with a different kind of experiment, which changed the focus and direction of subsequent research in our group.

Our goal of this early research was the development of a controlled experiment which showed up-conversion; however, as is often the case the development of a new experiment where an anomaly is involved is problematic. The many failures in this early part of the experimental effort serves as a testimony to the difficulties involved. A decision was made in early 2017 to develop a new kind of experiment which based on theory was "easier" in the sense of requiring less phonon exchange. For an up-conversion experiment to succeed, a great many phonon exchange events are needed; however, in an excitation transfer experiment one only needs a few phonon exchange events to occur. The idea was to place a radioactive source on a plate in order to produce a daughter in an excited state, then see whether excitation transfer could be observed upon stimulation with vibrations.

In May 2017 one of the new excitation transfer experiments was run, and gave a positive result (this is discussed below in Chapter 5), although not in response to the strong MHz vibrations used. In this experiment a high power MHz transducer was used to drive the plate, and x-ray detectors were positioned around the plate to monitor for excitation transfer. We had hoped to see a prompt response with a decrease in signal from the detector in front of the radioactive sample, and an increase in the other detectors. When the experiment was done no prompt response was seen. However, there was an obvious decay of the signal two orders of magnitude faster than would have been expected given the half-life of the Co-57 used. In this experiment, we saw our first anomaly. Instead of being stimulated by MHz vibrations, this effect was probably induced by much higher frequency vibrations, perhaps in the THz regime.

Subsequent experimentation in our lab largely became focused on following up on this important observation. A weak version of the effect was seen in subsequent experiments during the following months, with little understanding of what made the effect big or small. In an experiment in July a response was noticed when transducers were run at high power for a long time, but it was suspected that the response was due to the temperature increase and not as a result of MHz vibrations. In August an experiment was done that showed a strong response to thermal pulses (discussed below in Chapter 6). This opened the door for a more controlled set of experiments.

Following the May 2017 experiment, I was involved initially in some up-conversion experiments, where we sought to make use of what was learned from the excitation transfer experiment and apply it to the up-conversion experiments.

In late 2017 the thesis committee required new experimentation, and in response it was decided to pursue the development of a bent crystal spectrometer. This was a long range experiment, with the ultimate goal of detecting net energy exchange between the nuclei and vibrations through measurements of the 14.4 keV line shape during stimulation. From an initial review of the experiment, it became clear that the measurement would be difficult, and we thought that much could be learned by first focusing on the Fe K-alpha at 6.4 keV. A crystal was ordered, and a bent crystal experiment was developed. It was decided to work with a 1 meter focal length in order to get good resolution; however, air absorption for a 2 meter path length is problematic. I needed to make use of a helium path in order to get the signal up to the point of taking measurements. Line shape measurements were made on the Fe K-alpha showing the bent crystal instrument worked, and a measurement on a live sample was planned. However, the committee provided encouragement to take on new experiments that would have a better chance of showing a positive result, so this live measurement was deferred (and not completed). Some exploratory work was done with the bent crystal looking at emission on the 14.4 keV line, which was plagued by signal to noise problems. In the end, it is likely that we got a weak version of the

14.4 keV signal, and from the experience we are in a much better position to specify an experiment capable of looking at the 14.4 keV line shape under live conditions. A brief summary of this work appears in the Appendix K.

In January 2018 Hagelstein proposed a scenario in which excitation transfer of the excited nuclei occurred on the surface of the plate was responsible for the unexpected dynamical effects seen in the various 2017 experiments. This scenario could be tested, and in the first set of experiments intended to clarify the situation I developed a pinhole imaging experiment on film (described in Chapter 10). This was used to image the low energy (6-14 keV) emission in the vicinity of the Co-57, and then to check whether a change in the spatial distribution of the emission could be seen comparing a cold plate to a hot one. While there were subtle differences seen in the images, subtlety was not going to clarify the situation unambiguously.

We next moved to new pinhole/SDD experiments (discussed below in Chapter 11) in which the time history from a localized region of the radioactive sample could be obtained. The idea is that if there was an excitation transfer effect that could move excitation from one place to another on the surface of the sample, then we should be able to see the emission change in a localized region. If the excitation left to go elsewhere, then the local emission should decrease; if the excitation was coming from other regions then the local emission should increase. There are lots of reasons that this experiment might not have been able to work, including signal to noise issues, absence of any such effect, thermal problems and alignment issues. In the end, we saw changes in the emission in response to thermal pulses, an effect which is consistent with a large excitation transfer effect.

In the Spring 2018 Hagelstein proposed that I work on an angular anisotropy experiment, in addition to the other experiments already under way. The motivation for this was that the thesis committee was insistent that there be some strong positive experimental results to report, and it was thought that an angular anisotropy experiment would have low associated risk. The idea in

this case is that weak excitation transfer should be dominated by resonant excitation transfer, which could produce phase coherence among the excited nuclei. Evidence for this effect appeared in the time histories of the harder gammas in previous experiments with the first sample, so there was confidence that the effect could be seen. The only question was whether the second sample that was made could show the effect (this new sample had not been showing convincing signs of life in earlier experiments).

In what follows, we first consider some of the up-conversion experiments reported by other groups which motivated the early experimental research of our group. Next we review basic theoretical issues associated with phonon-nuclear exchange and with excitation transfer. The important excitation transfer experiments discussed above are reviewed. Following this we give a brief discussion of angular anisotropy, followed by results from experiments I did that focused on this effect. Next appears a discussion of delocalization, followed by chapters on the pinhole/film and pinhole/SDD experiments. The following chapter considers possible interpretations consistent with the experimental results so far. We conclude with a discussion of what was learned, and avenues for further research.

Much input to this chapter was provided by Hagelstein.

References

- 1 Ignaz Semmelweis. (2018, July 23). In *Wikipedia*. Retrieved July 24, 2018, from https://en.wikipedia.org/wiki/Ignaz_Semmelweis
- 2 Alfred Wegener. (2018, July 23). In *Wikipedia*. Retrieved July 24, 2018, from https://en.wikipedia.org/wiki/Alfred_Wegener
- 3 Luminiferous aether. (2018, January 28). In *Wikipedia*. Retrieved July 24, 2018, from https://simple.wikipedia.org/wiki/Luminiferous_aether
- 4 Michelson-Morley experiment. (2018, July 21). In *Wikipedia*. Retrieved July 24, 2018, from https://simple.wikipedia.org/wiki/Michelson-Morley_experiment
- 5 Alchemy. (2018, July 23). In *Wikipedia*. Retrieved July 24, 2018, from <https://en.wikipedia.org/wiki/Alchemy>
- 6 Tests of general relativity. (2018, July 17). In *Wikipedia*. Retrieved July 24, 2018, from https://en.wikipedia.org/wiki/Tests_of_general_relativity
- 7 Kohn, W. (1959). Image of the Fermi Surface in the Vibration Spectrum of a Metal. *Physical Review Letters*, 2(9), 393-394. doi:10.1103/physrevlett.2.393
- 8 Bancroft, D. (1938). The Effect of Hydrostatic Pressure on the Susceptibility of Rochelle Salt. *Physical Review*, 53(7), 587-590. doi:10.1103/physrev.53.587
- 9 Friedman, M. H., Sokoloff, J. B., Widom, A., & Srivastava, Y. N. (1984). Chiral Anomaly and the Rational Quantization of the Hall Conductance. *Physical Review Letters*, 52(18), 1587-1589. doi:10.1103/physrevlett.52.1587
- 10 Behrends, J., Grushin, A. G., Ojanen, T., & Bardarson, J. H. (2016). Visualizing the chiral anomaly in Dirac and Weyl semimetals with photoemission spectroscopy. *Physical Review B*, 93(7). doi:10.1103/physrevb.93.075114

- 11 Gelder, A. V. (1966). Quantum anomaly of the extreme anomalous skin effect. *Physics Letters*, 21(1), 18-20. doi:10.1016/0031-9163(66)91321-7
- 12 Mosekilde, E., Carlson, D. G., & Segmuller, A. (1974). Quantum anomaly in acoustic parametric interaction. *Journal of Physics C: Solid State Physics*, 7(23), 4281-4292. doi:10.1088/0022-3719/7/23/015
- 13 Bardeen, W. A., & Zumino, B. (1984). Consistent and covariant anomalies in gauge and gravitational theories. *Nuclear Physics B*, 244(2), 421-453. doi:10.1016/0550-3213(84)90322-5
- 14 Goldhaber, M. (1956). Possible Method of Measuring Magnetic Moments of V Particles. *Physical Review*, 101(6), 1828-1828. doi:10.1103/physrev.101.1828
- 15 Turyshchev, S. G., Toth, V. T., Kinsella, G., Lee, S., Lok, S. M., & Ellis, J. (2012). Support for the Thermal Origin of the Pioneer Anomaly. *Physical Review Letters*, 108(24). doi:10.1103/physrevlett.108.241101
- 16 Fleischmann, M., Pons, S., Anderson, M. W., Li, L. J., & Hawkins, M. (1990). Calorimetry of the palladium-deuterium-heavy water system. *Journal of Electroanalytical Chemistry and Interfacial Electrochemistry*, 287(2), 293-348. doi:10.1016/0022-0728(90)80009-u
- 17 Pownall, G. (2009). *Demarcating Science: The case of Cold Fusion* (Unpublished master's thesis). Dublin City University. Retrieved July 25, 2018, from <http://newenergytimes.com/v2/library/2009/2009PownallGrant-ThesisDemarcatingScienceColdFusion.pdf>
- 18 Mckubre, M., Crouch-Baker, S., Rocha-Filho, R., Smedley, S., Tanzella, F., Passell, T., & Santucci, J. (1994). Isothermal flow calorimetric investigations of the D/Pd and H/Pd systems. *Journal of Electroanalytical Chemistry*, 368(1-2), 55-66. doi:10.1016/0022-0728(93)03070-6
- 19 Ohmori, T., & Enyo, M. (1993). Excess Heat Evolution during Electrolysis of H₂O with Nickel, Gold, Silver, and Tin Cathodes. *Fusion Technology*, 24(3), 293-295. doi:10.13182/fst93-a30204
- 20 Kopecek, R., & Dash, J. (1996) Excess Heat and Unexpected Elements from Electrolysis of Heavy Water with Titanium Cathodes. *Journal of New Energy*, 1(3), 46-46.

- 21 Mizuno, T., & Toriyabe, Y. (2006). Anomalous Energy Generation During Conventional Electrolysis. *Condensed Matter Nuclear Science*. doi:10.1142/9789812772985_0006
- 22 Dardik, I., Branover, H., El-Boher, A., Gazit, D., Golbreich, E., Greenspan, E., . . . Zilov, T. (2005). Intensification Of Low Energy Nuclear Reactions Using Superwave Excitation. *Condensed Matter Nuclear Science*. doi:10.1142/9789812701510_0007
- 23 Tanzella, F., Bao, J., McKubre, M., & Hagelstein, P. (2012). Stimulation of Metal Deuteride Wires at Cryogenic Temperatures. *Condensed Matter Nuclear Science*, 8, 176-186.
- 24 Li, X. Z., Liu, B., Tian, J., Wei, Q. M., Zhou, R., & Yu, Z. W. (2003). Correlation between abnormal deuterium flux and heat flow in a D/Pd system. *Journal of Physics D: Applied Physics*, 36(23), 3095-3097. doi:10.1088/0022-3727/36/23/035
- 25 Kitamura, A., Takahashi, A., Seto, R., Fujita, Y., Taniike, A., & Furuyama, Y. (2015). Brief summary of latest experimental results with a mass-flow calorimetry system for anomalous heat effect of nano-composite metals under D (H)-gas charging. *Current Science*, 108(4), 589-593.
- 26 Swartz, M., Verner, G., Tolleson, J., & Hagelstein, P. (2015). Dry, preloaded NANOR®-type CF/LANR components. *Current Science*, 108(4), 595-600.
- 27 McKubre, M., Tanzella, F., Tripodi, P., & Hagelstein, P. (2000). The Emergence of a Coherent Explanation for Anomalies Observed in D/Pd and H/Pd System: Evidence for ^4He and ^3He Production. In *8th International Conference on Cold Fusion*. Lerici (La Spezia), Italy: Italian Physical Society, Bologna, Italy.
- 28 Gozzi, D., Cellucci, F., Cignini, P., Gigli, G., Tomellini, M., Cisbani, E., . . . Urciuoli, G. (1998). X-ray, heat excess and ^4He in the D/Pd system. *Journal of Electroanalytical Chemistry*, 452, 251-271.
- 29 Hagelstein, P. L., McKubre, M. C., Nagel, D. J., Chubb, T. A., & Hekman, R. J. (2006). New Physical Effects In Metal Deuterides. *Condensed Matter Nuclear Science*, 23-59. doi:10.1142/9789812774354_0003

- 30 Hagelstein, P. L. (2010). Constraints on energetic particles in the Fleischmann–Pons experiment. *Naturwissenschaften*, 97(4), 345-352. doi:10.1007/s00114-009-0644-4
- 31 Hagelstein, P. (1990). Status of coherent fusion theory. In *The First Annual Conference on Cold Fusion* (Vol. 99, pp. 99-118). Salt Lake City, Utah: National Cold Fusion Institute, University of Utah Research Park.
- 32 Taylor, S., Claytor, T., Tuggle, D., & Jones, S. (1993). Search for neutrons from deuterated palladium subject to high electrical currents. In *The Fourth International Conference on Cold Fusion*
- 33 Jones, S., Keeney, F., Johnson, A., Buehler, D., Cecil, F., Hubler, G., . . . Scott, M. (2003). Charged-particle Emissions from Metal Deuterides. In *Tenth International Conference on Cold Fusion*. Cambridge, MA: LENR-CANR.org.
- 34 Boss, P., Forsley, L., Roussetski, A., Lipson, A., Tanzella, F., Saunin, E., . . . Zhou, D. (2015). Use of CR-39 detectors to determine the branching ratio in Pd/D co-deposition. *Current Science*, 108, 585-588.
- 35 Cecil, F. E., Ferg, D., Furtak, T. E., Mader, C., Mcneil, J. A., & Williamson, D. L. (1990). Study of energetic charged particles emitted from thin deuterated palladium foils subject to high current densities. *Journal of Fusion Energy*, 9(2), 195-197. doi:10.1007/bf02627584
- 36 Cecil, F. E., Liu, H., Beddingfield, D., & Galovich, C. S. (1991). Observation of charged particle bursts from deuterium loaded thin titanium foils. *AIP Conference Proceedings*. doi:10.1063/1.40706
- 37 Derjaguin, B., Lipson, A., Kluev, V., Sakov, D., & Toporov, Y. (1989). Titanium fracture yields neutrons? *Nature*, 341, 492-492.
- 38 Li, X. Z., Tian, J., Mei, M. Y., & Li, C. X. (2000). Sub-barrier fusion and selective resonant tunneling. *Physical Review C*, 61(2). doi:10.1103/physrevc.61.024610
- 39 Lipson, A., Chernov, I., Roussetski, A., Cherdantsev, Y., Tsivadze, A., Lyakhov, B., . . . Melich, M. (2009). Hot Deuteron Generation and Charged Particle Emissions on Excitation of Deuterium Subsystem in Metal

Deuterides. *ACS Symposium Series Low-Energy Nuclear Reactions and New Energy Technologies*

Sourcebook Volume 2, 95-117. doi:10.1021/bk-2009-1029.ch006

40 Montgomery, J. R., Jeffery, R., Amiri, F., & Adams, J. (1991). Correlated nuclear and thermal measurements in D/Pd and H/Pd systems. *AIP Conference Proceedings*. doi:10.1063/1.40702

41 Mosier-Boss, P. A., Szpak, S., Gordon, F. E., & Forsley, L. P. (2009). Characterization of tracks in CR-39 detectors obtained as a result of Pd/D Co-deposition. *The European Physical Journal Applied Physics*, 46(3), 30901. doi:10.1051/epjap/2009067

42 Mosier-Boss, P., Gordon, F., Forsley, L., & Zhou, D. (2017). Detection of high energy particles using CR-39 detectors part 1: Results of microscopic examination, scanning, and LET analysis. *International Journal of Hydrogen Energy*, 42(1), 416-428. doi:10.1016/j.ijhydene.2016.09.223

43 Storms, E., & Scanlan, B. (2008). Detection of Radiation Emitted from LENR. In *14th International Conference on Condensed Matter Nuclear Science*. Washington, DC.

44 Carpinteri, A., Lacidogna, G., Manuello, A., & Borla, O. (2011). Energy emissions from brittle fracture: Neutron measurements and geological evidences of piezonuclear reactions. *Strength, Fracture and Complexity*, 7, 13-31. doi:10.3233/SFC-2011-0120

45 Carpinteri, A., Lacidogna, G., Manuello, A., & Borla, O. (2012). Piezonuclear Fission Reactions in Rocks: Evidences from Microchemical Analysis, Neutron Emission, and Geological Transformation. *Rock Mechanics and Rock Engineering*, 45(4), 445-459. doi:10.1007/s00603-011-0217

46 Carpinteri, A., Lacidogna, G., Manuello, A., & Borla, O. (2013). Piezonuclear Fission Reactions from Earthquakes and Brittle Rocks Failure: Evidence of Neutron Emission and Non-Radioactive Product Elements. *Experimental Mechanics*, 53, 345-365. doi:10.1007/s11340-012-9629-x

47 Albertini, G., Calbucci, V., Cardone, F., Fattorini, G., Mignani, R., Petrucci, A., . . . Rotili, A. (2013). Evidence Of Alpha Emission From Compressed Steel Bars. *International Journal of Modern Physics B*, 27(23), 1350124. doi:10.1142/s0217979213501245

- 48 Albertini, G., Calbucci, V., Cardone, F., & Petrucci, A. (2013). Piezonuclear reactions and DST-reactions. *Materials and Processes for Energy: Communicating Current Research and Technological Developments*, 769-780.
- 49 Cardone, F., Cherubini, G., Lammardo, M., Mignani, R., Petrucci, A., Rosada, A., . . . Santoro, E. (2015). Violation of local Lorentz invariance for deformed space-time neutron emission. *The European Physical Journal Plus*, 130(3). doi:10.1140/epjp/i2015-15055-y
- 50 Campari, E., Focardi, S., Gabbani, V., Montalbano, V., Piantelli, F., Veronesi, S., & Veronesi, S. (2006). Surface Analysis Of Hydrogen-Loaded Nickel Alloys. *Condensed Matter Nuclear Science*. doi:10.1142/9789812774354_0034
- 51 Nassisi, V., Caretto, G., Lorusso, A., Manno, D., Famà, L., Buccolieri, G., . . . Mastromatteo, U. (2011). Modification of Pd–H₂ and Pd–D₂ Thin Films Processed by He–Ne Laser. *Journal of Condensed Matter Nuclear Science*, 5, 1-6.
- 52 Iwamura, Y., Itoh, T., Sakano, M., Sakai, S., & Kuribayashi, S. (2003). Low Energy Nuclear Transmutation In Condensed Matter Induced By D₂ Gas Permeation Through Pd Complexes: Correlation Between Deuterium Flux And Nuclear Products. In *Tenth International Conference on Cold Fusion*. Cambridge, MA: LENR-CANR.org.
- 53 Iwamura, Y., Itoh, T., Yamazaki, N., Kasagi, J., Terada, Y., Ishikawa, T., . . . Fukutani, K. (2011). Observation of Low Energy Nuclear Transmutation Reactions Induced by Deuterium Permeation through Multilayer Pd and CaO thin Film. *Journal of Condensed Matter Nuclear Science*, 4, 132-144.
- 54 Goodstein, D. (2000). Whatever happened to cold fusion? *Accountability in Research*, 8(1-2), 59-75. doi:10.1080/08989620008573966
- 55 Hagelstein, P. (2016). Quantum Composites: A Review, and New Results for Models for Condensed Matter Nuclear Science. *Journal of Condensed Matter Nuclear Science*, 20, 139-225.

- 56 Hagelstein, P., & Chaudhary, I. (2011). Energy Exchange In The Lossy Spin-Boson Model. *Journal of Condensed Matter Nuclear Science*, 5, 52-71.
- 57 Hagelstein, P., & Chaudhary, I. (2011). Dynamics in the case of coupled degenerate states. *Journal of Condensed Matter Nuclear Science*, 5, 72-86.
- 58 Hagelstein, P., & Chaudhary, I. (2011). Second-order formulation and scaling in the lossy spin-boson model. *Journal of Condensed Matter Nuclear Science*, 5, 87-101.
- 59 Hagelstein, P., & Chaudhary, I. (2011). Local approximation for the lossy spin-boson model. *Journal of Condensed Matter Nuclear Science*, 5, 102-115.
- 60 Hagelstein, P., & Chaudhary, I. (2011). Coherent energy exchange in the strong coupling limit of the lossy spin-boson model. *Journal of Condensed Matter Nuclear Science*, 5, 116-139.

2. Claims for Collimated X-ray and Gamma Emission

Anomalies are so called because they are not expected. The observed anomalies do not follow our expectations but clearly the anomalies are manifestations of the laws of physics. Working with anomalies is difficult. When doing research with anomalies, we can not work with established equations or theories. If we could, they are not anomalies. If we could find explanations for anomalies, we would switch them from anomalies to examples following new physical laws or new understandings of existing physical laws.

There are a variety of anomalies that might be considered in the first place; however, our attention will be focused on one which we consider to be fundamental. In this section we focus on examples of anomalies involving collimated X-ray emission. In 1966, it was reported in the Gorazdovskii experiment that when applying strong shear force to a solid sample, radiation signals were detected on a nearby photographic film¹. The Gorazdovskii experiment might be considered as one of the earliest example of the kind of anomaly discussed in this chapter.

2.1 The Karabut Experiment

Collimated X-ray emission of energy around 1.5 keV was reported in a high-current density glow discharge experiment by Karabut in 2002;^{2,3} subsequently, he studied the effect with different cathode materials, gasses, and diagnostics over the following decade.⁴ Figure 2.1 shows the scheme of the Karabut experiment. The experiment was conducted inside a vacuum chamber made of steel. A high current density glow discharge was generated inside the chamber with cathode, anode, and gas. Karabut detected collimated X-rays using in different experiments a scintillator, a thermal luminescent detector, an X-ray film with a pinhole camera, and a bent mica crystal spectrometer.

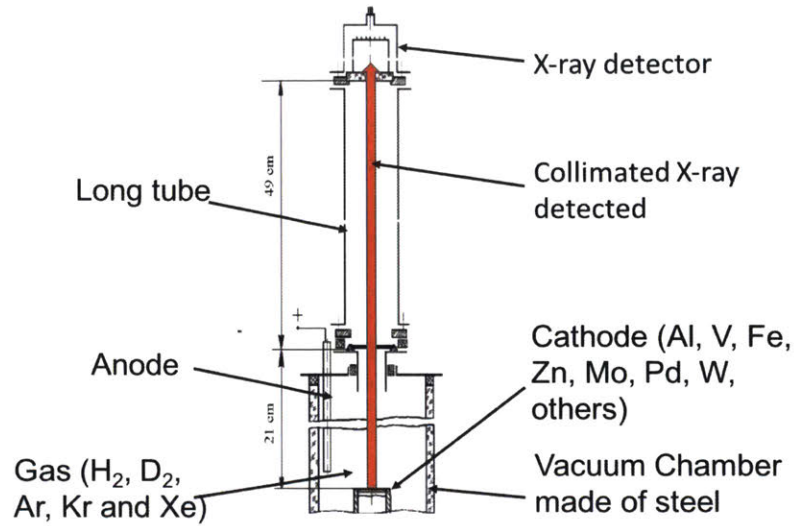


Figure 2.1: Scheme of a version of the Karabut experiment⁴

Figure 2.2 shows the pinhole camera image of cathode in his experiment. Very bright collimated X-rays originate from the cathode surface.

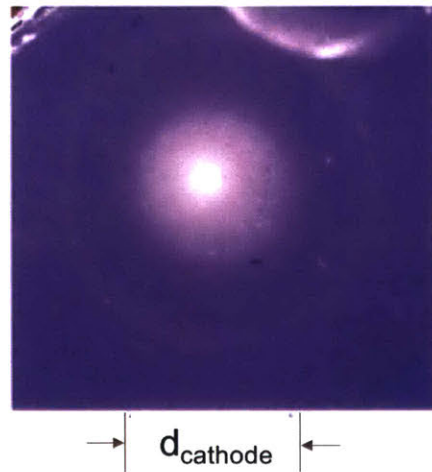


Figure 2.2: Pinhole camera image of the cathode⁴

With the discharge running in steady state mode, collimated X-ray emission was detected with a diffused spectrum around 1.5 keV from the bent mica spectrometer. Figure 2.3 shows the scheme of the bent mica spectrometer. Karabut repeated the same experiment with many different cathode metals (Al, V, Fe, Zn, Mo, Pd, W, others) and different gases (H_2 , D_2 , He, Ar, Kr,

and Xe). The collimated X-ray emission effect is reproducible with different cathode and gas combinations. Figure 2.4 shows X-ray spectra taken with a tungsten cathode in He gas, and Figure 2.5 shows a densitometer scan of the spectrum from an experiment with Pd cathode in D₂ gas.

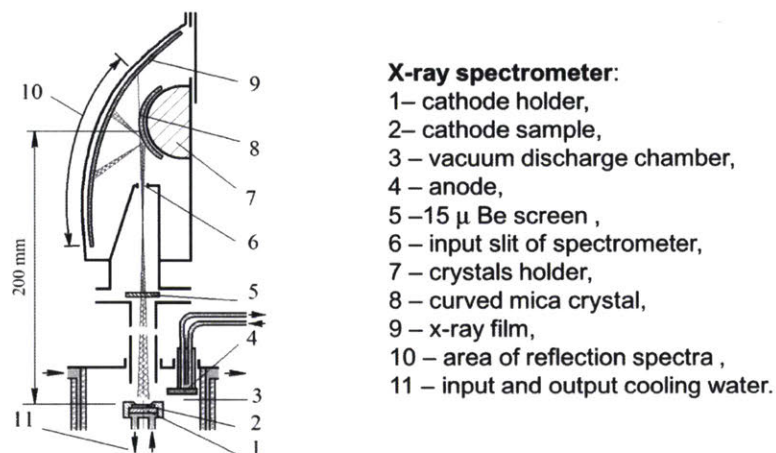


Figure 2.3: Scheme of the bent mica spectrometer⁴

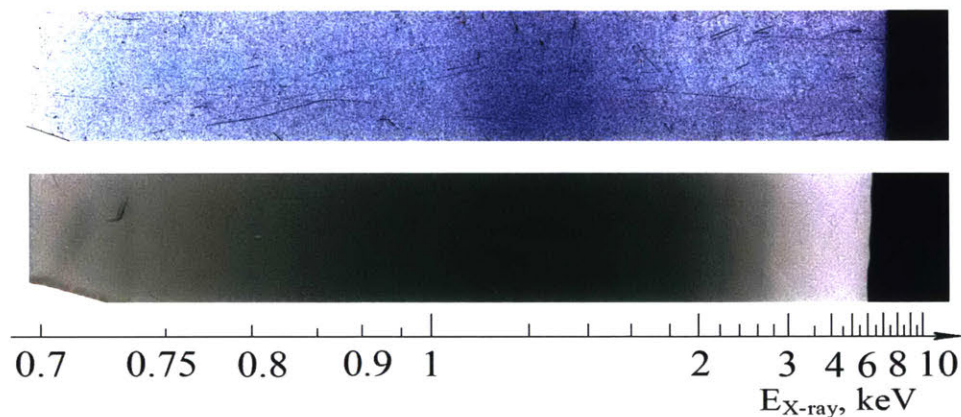


Figure 2.4: Diffuse emission near 1.5 keV for a W cathode in He gas; top spectrum taken with a discharge voltage of 1850 V; bottom spectrum also for a W cathode in He gas at 4000 V.⁴

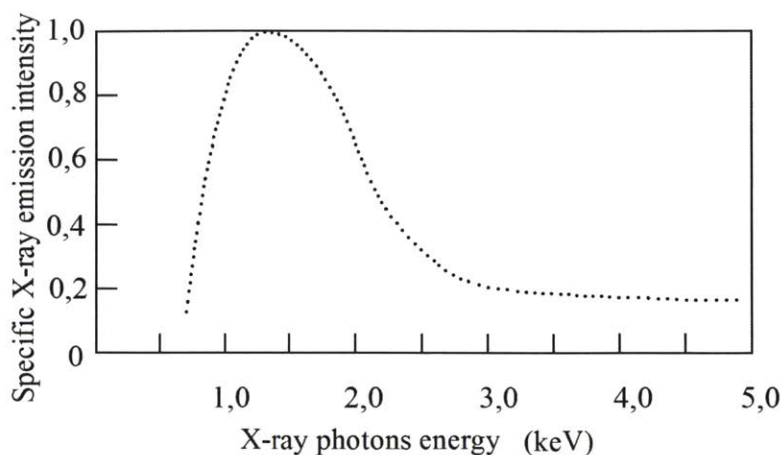


Figure 2.5: Densitometer scan of a spectrum with a Pd cathode and D₂ gas⁴

2.2 The Kornilova Experiment

Collimated X-ray emission was also reported in the Kornilova experiment.⁵ Collimated x-ray emission in the Karabut experiment is a stronger experimental result, but the Kornilova experiment appears to give a similar effect and is more accessible. One version of the experiment is shown in Figure 2.6. High-pressure water flow is generated from the water jet through the narrow nozzle made of steel. An X-ray detector placed near the water jet nozzle detected X-rays with an energy spectrum that peaks near 1.7 keV. Figure 2.7 shows the X-ray spectrum in their publication.⁵

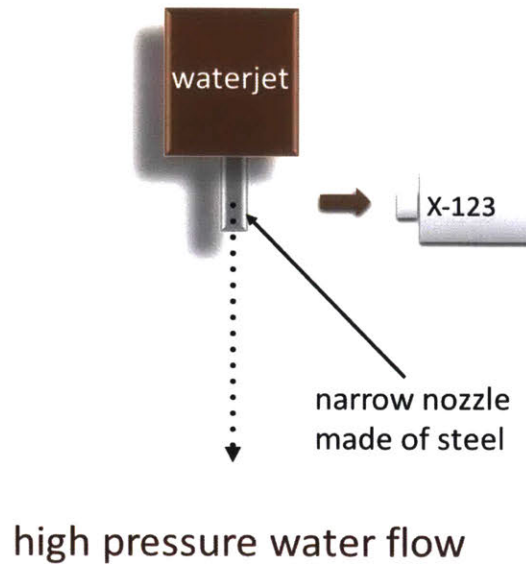


Figure 2.6: Scheme of the version of Kornilova experiment with an X-ray detector⁵

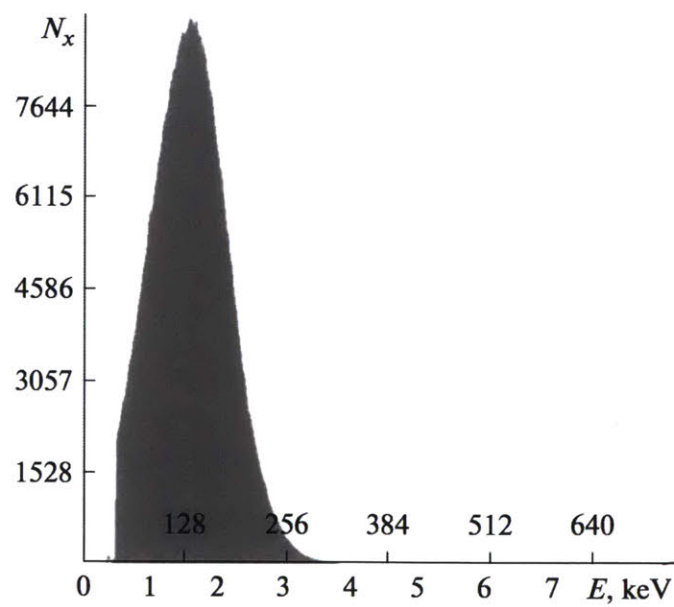


Figure 2.7: X-ray spectrum near nozzle surface in Kornilova experiment⁵

X-ray films were also used to detect X-rays in this version of the experiment. Figure 2.8 shows the scheme of the 1st version of Kornilova experiment with X-ray film. Two pieces of X-ray film in a light protective envelope were rolled in the form of a cylindrical surface and were fitted over the entire length of the steel nozzle. Figure 2.9 shows the X-ray film results in their experiment

after 15 minutes of exposure at 600 atm pressure. The left darker film was closer to the water jet nozzle compared to the right film. It was claimed that the energy of X-ray signals on the films corresponded to about 2 keV based on film absorption.

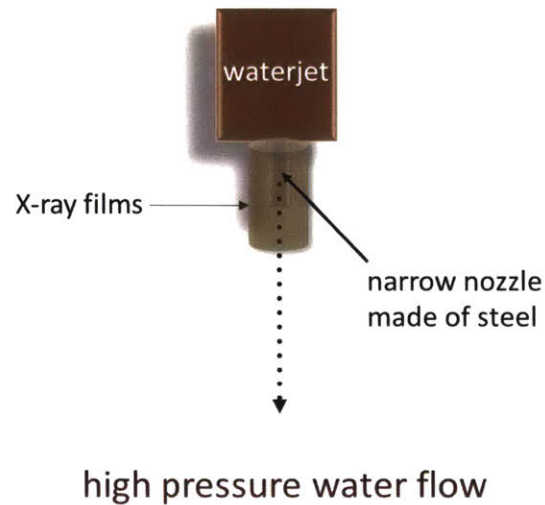


Figure 2.8: Scheme of the 1st version of Kornilova experiment with X-ray films⁵

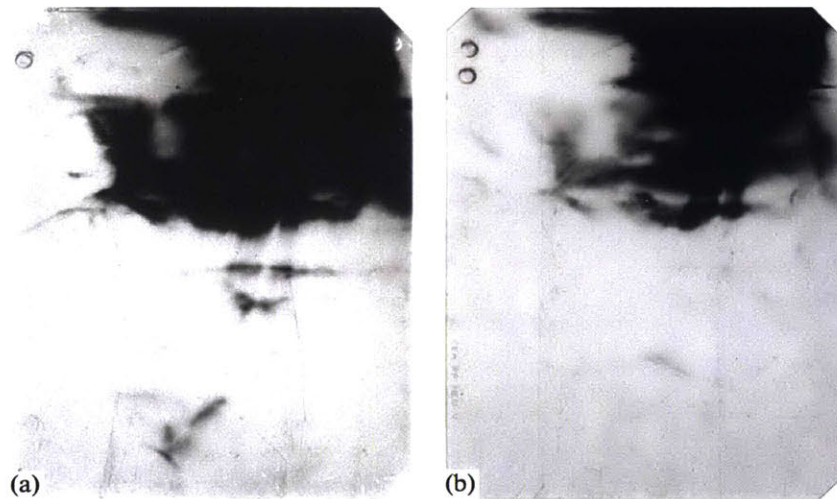


Figure 2.9: Images of X-ray films in the 1st version of Kornilova experiment with X-ray films⁵

Figure 2.10 shows a 2nd version of the Kornilova experiment with X-ray films. A steel plate was placed near the water jet away from the nozzle. The distance between the plate and water jet was 3 cm. A pack of two X-ray films was put 1 cm behind the steel plate. On the other side of

the water flow, another pack of two films was placed without a steel plate in front of it. The distance between this pack of films and the plate was 6 cm.

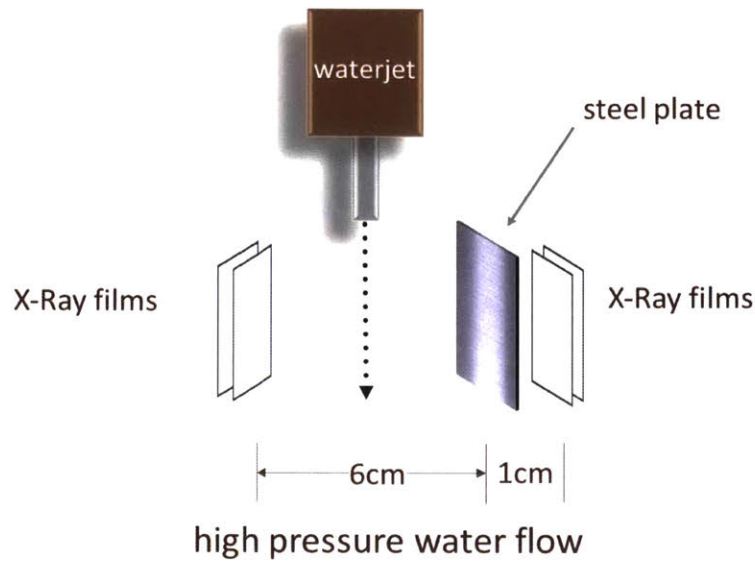


Figure 2.10: Scheme of the 2nd version of Kornilova experiment⁵

Figure 2.11 shows the X-ray films results in their experiment after 30 minutes of exposure at 600 atm pressure. Signals were detected on the two X-ray films 1 cm behind the steel plate. Nothing showed up on the two films 6 cm from the steel plate. The film (a) with much darker spots was placed closer to the plate than film (b) was. The position and size of those spots on both films were almost identical.

According to their publication, there was a thin layer of paint on the back side of the steel plate. However, due to unforeseen reasons, a few places on the back side of the steel plate were free of paint. Those places free of paint correlated to the positions of dark spots on the X-ray films. Also, there was no paint at all on the bottom part of the steel plate, which correlated to the dark bottom band on the X-ray films.

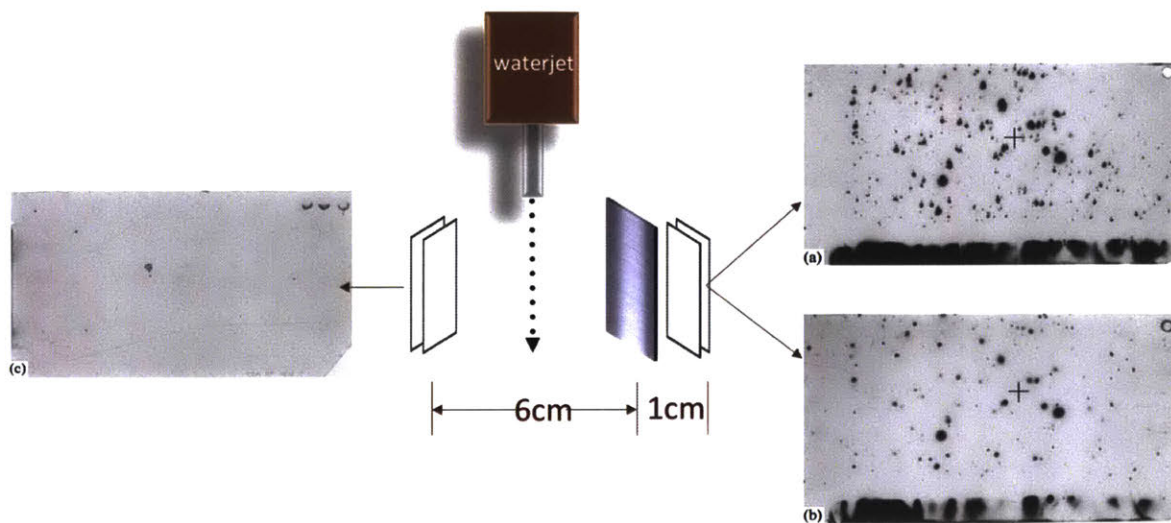


Figure 2.11: Images of X-ray films in the 2nd version of Kornilova experiment with X-ray films⁵

It was claimed that the energy of X-ray signals on the films corresponded to about 2 keV based on film absorption³. A separate analysis of X-ray transmission in the air for 1 cm and 6 cm is shown in Figure 2.12. The data is from the Center for X-ray Optics website.⁶ For the X-ray to reach 1 cm distance but not to reach 6 cm distance, the energy should be at least 1 keV but at most 2 keV. The claim of the X-ray energy detected in their experiment matches this analysis.

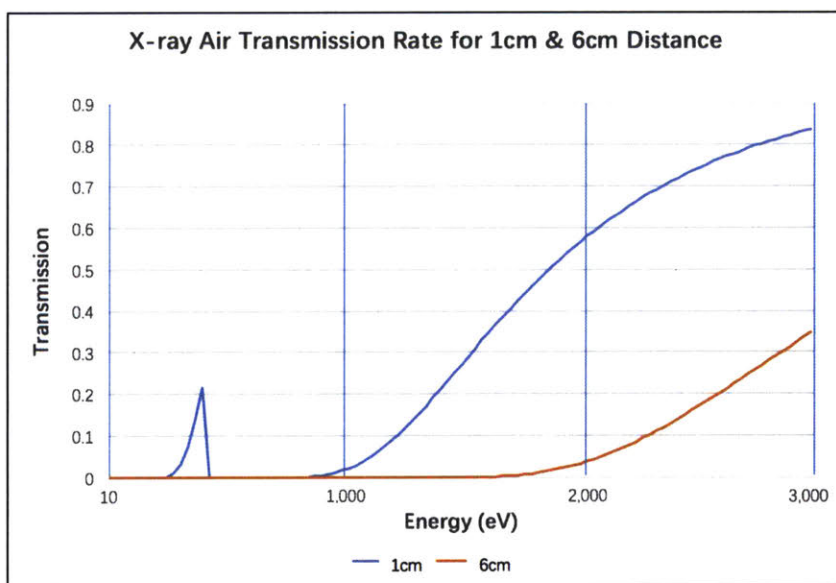


Figure 2.12: X-ray air transmission for 1 cm and 6 cm distance⁶

2.3 The Ivlev Experiment

Unexpected X-ray was also reported in the Ivlev experiment.⁷ Figure 2.13 shows the scheme of the Ivlev experiment. A piezoelectric bowl which can generate shock waves was attached on the bottom of a water tank full of water. The shock waves hit the lead foil sample positioned inside the water with the help of an XYZ positioner. X-ray film was put on top of the water tank. Figure 2.14 shows one of the X-ray film results in the Ivlev experiment. There were X-ray signals detected on the X-ray film.⁷

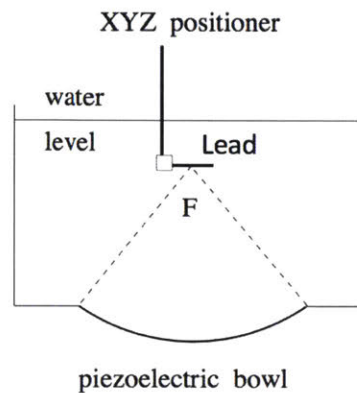


Figure 2.13: Scheme of the Ivlev experiment⁷

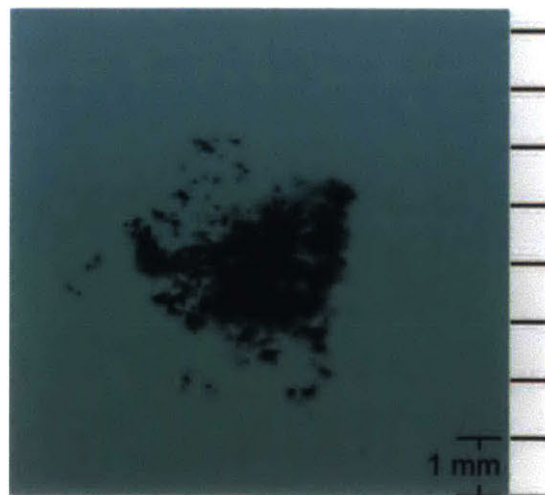


Figure 2.14: One of the X-ray film results in the Ivlev experiment⁷

X-ray emissions were reported in all the three above experiments without reasonable explanations with existing physical laws. Hagelstein is of the opinion that collimated X-ray emission in these experiments maybe due to up-conversion of phonons to produce nuclear excitation.⁸⁻¹² In each case the different groups have proposed alternate explanations. We were interested initially in the possibilities of seeing this effect at MIT (see Appendix D for our efforts to replicate a waterjet experiment).

References

- 1 Gorazdovskii, T. (1967). Hard Radiation from Solids Failing in Shear. *ZhETF Pis Ma Redaktsiiu*, 5, 78-82.
- 2 Karabut, A. (2002). EXCESS HEAT POWER, NUCLEAR PRODUCTS AND X-RAY EMISSION IN RELATION TO THE HIGH CURRENT GLOW DISCHARGE EXPERIMENTAL PARAMETERS. In *The 9th International Conference on Cold Fusion, Condensed Matter Nuclear Science*. Tsinghua Univ., Beijing, China: Tsinghua Univ. Press.
- 3 Karabut, A. (2002). X-RAY EMISSION IN THE HIGH-CURRENT GLOW DISCHARGE EXPERIMENTS. In *The 9th International Conference on Cold Fusion, Condensed Matter Nuclear Science*. Tsinghua Univ., Beijing, China: Tsinghua Univ. Press.
- 4 Karabut, A., Karabut, E., & Hagelstein, P. (2012). Spectral and Temporal Characteristics of X-ray Emission from Metal Electrodes in a High-current Glow Discharge. *Journal of Condensed Matter Nuclear Science*, 6, 217-240.
- 5 Kornilova, A. A., Vysotskii, V. I., Sysoev, N. N., Litvin, N. K., Tomak, V. I., & Barzov, A. A. (2010). Generation of intense x-rays during ejection of a fast water jet from a metal channel to atmosphere. *Journal of Surface Investigation. X-ray, Synchrotron and Neutron Techniques*, 4(6), 1008-1017. doi:10.1134/s1027451010060224
- 6 X-Ray Interactions With Matter. (n.d.). Retrieved from http://henke.lbl.gov/optical_constants/
- 7 Fernandez, F., Loske, A., & Ivlev, B. (2018). Observation of x-ray emission and matter collapse in lead. Manuscript submitted for publication.
- 8 Hagelstein, P. (2016). Quantum Composites: A Review, and New Results for Models for Condensed Matter Nuclear Science. *Journal of Condensed Matter Nuclear Science*, 20, 139-225.
- 9 Hagelstein, P., & Chaudhary, I. Possibility of observing a center of mass interaction in a Mossbauer experiment. Manuscript unpublished.
- 10 Hagelstein, P., & Chaudhary, I. (2011). Energy Exchange In The Lossy Spin-Boson Model. *Journal of Condensed Matter Nuclear Science*, 5, 52-71.

11 Hagelstein, P. (2015). Directional X-ray and gamma emission in experiments in condensed matter nuclear science. *Current Science*, 108(4), 601-607.

12 Hagelstein, P., & Chaudhary, I. (2015). Phonon models for anomalies in condensed matter nuclear science. *Current Science*, 108(4), 507-513.

3 Phonon-Nuclear Coupling Mechanism

After three decades of efforts, Hagelstein believes that the only plausible interpretation of the anomalies is that lattice vibrations are causing transitions inside nuclei. The question is how this can be true. We start our discussion of theory by looking at the coupling between vibrations and internal nuclear states. In early efforts at modeling it was thought that (indirect) electric or magnetic coupling between the lattice and internal nuclear transitions might provide a basis for the anomalies; however, both appear to be too weak to account quantitatively for the anomalies. A few years ago a relativistic coupling was identified by Professor Hagelstein which appears more promising.

Consider a many-particle Dirac model for the nucleus given by the following Hamiltonian, where for simplicity protons and neutrons are modeled with equal mass¹⁻³

$$\hat{H} = \sum_j \beta_j m c^2 + \sum_j \boldsymbol{\alpha}_j \cdot c \hat{\mathbf{p}}_j + \sum_{j < k} \hat{V}_{jk}(\mathbf{r}_j - \mathbf{r}_k) \quad (1)$$

Center of mass variables and relative variables can be defined by

$$\begin{aligned} \mathbf{R} &= \frac{1}{N} \sum_j \mathbf{r}_j & \hat{\mathbf{P}} &= \sum_j \hat{\mathbf{p}} \\ \boldsymbol{\xi}_j &= \mathbf{r}_j - \mathbf{R} & \hat{\boldsymbol{\pi}}_j &= \hat{\mathbf{p}}_j - \frac{\hat{\mathbf{P}}}{N} \end{aligned} \quad (2)$$

The many-particle Dirac model in the center of mass and relative variables is¹⁻³

$$\hat{H} = \sum_j \beta_j m c^2 + \sum_j \boldsymbol{\alpha}_j \cdot c \left[\frac{\hat{\mathbf{P}}}{N} + \hat{\boldsymbol{\pi}}_j \right] + \sum_{j < k} \hat{V}_{jk}(\boldsymbol{\xi}_j - \boldsymbol{\xi}_k) \quad (3)$$

It is possible to develop a model in which the nuclear motion is nonrelativistic, while the nucleon dynamics are treated relativistically. To accomplish this, we work with a partial Foldy-Wouthuysen rotation according to¹⁻³

$$\hat{H}' = e^{i\hat{S}} \hat{H} e^{-i\hat{S}} \quad (4)$$

based on

$$\hat{S} = -i \frac{1}{2Mc^2} \sum_j \beta_j \boldsymbol{\alpha}_j \cdot c\hat{\mathbf{P}} \quad (5)$$

The resulting transformed Hamiltonian can be written as¹⁻³

$$\begin{aligned} \hat{H}' = & \frac{|\hat{\mathbf{P}}|^2}{2M} \frac{1}{N} \sum_j \beta_j + \sum_j \beta_j mc^2 + \sum_j \boldsymbol{\alpha}_j \cdot c\hat{\boldsymbol{\pi}}_j + \sum_{j < k} \hat{V}_{jk} \\ & + \frac{1}{M} \sum_j \beta_j \hat{\mathbf{P}} \cdot \hat{\boldsymbol{\pi}}_j + \frac{1}{2Mc} \sum_{j < k} \left[(\beta_j \boldsymbol{\alpha}_j + \beta_k \boldsymbol{\alpha}_k) \cdot \hat{\mathbf{P}}, \hat{V}_{jk} \right] + \dots \end{aligned} \quad (6)$$

The first term is the kinetic energy term for the nucleus as a whole. The following three terms describe the relative Hamiltonian for the internal degrees of freedom of nuclear states. The last two terms explicitly couple the center of mass motion with the internal degrees of freedom. The rotation also generates a large number of higher order terms not written explicitly.

With this process, we can describe the nucleus as a quantum composite particle, which can be written as¹⁻³

$$\hat{H}' = \hat{H}_{CM} + \hat{H}_{rel} + \hat{H}_{int} + \hat{H}_{higher-order} \quad (7)$$

with

$$\begin{aligned}
\hat{H}_{CM} &= \frac{|\hat{\mathbf{P}}|^2}{2M} \\
\hat{H}_{rel} &= \sum_j \beta_j m c^2 + \sum_j \boldsymbol{\alpha}_j \cdot c \hat{\boldsymbol{\pi}}_j + \sum_{j < k} \hat{V}_{jk} \\
\hat{H}_{int} &= \left(\frac{1}{M} \sum_j \beta_j \hat{\boldsymbol{\pi}}_j + \frac{1}{2Mc} \sum_{j < k} \left[(\beta_j \boldsymbol{\alpha}_j + \beta_k \boldsymbol{\alpha}_k), \hat{V}_{jk} \right] \right) \cdot \hat{\mathbf{P}} \\
\hat{H}_{higher-order} &= \frac{|\hat{\mathbf{P}}|^2}{2M} \frac{1}{N} \sum_j \beta_j - \frac{|\hat{\mathbf{P}}|^2}{2M} + \dots
\end{aligned} \tag{8}$$

By treating the center of mass dynamics non-relativistically, we get coupling between the center of mass motion and the internal degrees of freedom which emerges naturally.¹⁻³ This coupling effect is similar to the effect that the motion of a whole atom can cause changes to the internal magnetic field due to electron spin. Nuclear forces work similarly to magnetic forces in this respect.

Hagelstein's relativistic quantum mechanics predicts a coupling between the center of mass motion and the internal nuclear states. He conjectures that this coupling is involved in the anomalies.¹⁻⁵

All the results reviewed in this chapter are directly from or based on Hagelstein's papers.

References

- 1 Hagelstein, P. (2016). Quantum Composites: A Review, and New Results for Models for Condensed Matter Nuclear Science. *Journal of Condensed Matter Nuclear Science*, 20, 139-225.
- 2 Hagelstein, P., & Chaudhary, I. Possibility of observing a center of mass interaction in a Mossbauer experiment. Manuscript unpublished.
- 3 Hagelstein, P., & Chaudhary, I. (2011). Energy Exchange In The Lossy Spin-Boson Model. *Journal of Condensed Matter Nuclear Science*, 5, 52-71.

4 Hagelstein, P. (2015). Directional X-ray and gamma emission in experiments in condensed matter nuclear science. *Current Science*, 108(4), 601-607.

5 Hagelstein, P., & Chaudhary, I. (2015). Phonon models for anomalies in condensed matter nuclear science. *Current Science*, 108(4), 507-513.

4 Resonant Phonon-Nuclear Excitation Transfer Mechanism

We discussed above a model that describes the coupling between phonon vibrations and internal nuclear degrees of freedom. Now we consider some examples, showing how this model can be used for applications. Phonon-nuclear interaction is algebraically very similar to photon-nuclear interaction. The photon-nuclear interaction can be expressed as

$$-\vec{j} \cdot \vec{A}$$

while the phonon-nuclear interaction can be expressed as

$$\vec{a} \cdot c\vec{P}$$

The terms \vec{j} and \vec{a} make internal nuclear transitions. The terms \vec{A} and \vec{P} create and destroy photons and phonons respectively

However, there are also differences between these two interactions. One excited nucleus can decay by emitting one single photon, but it cannot decay by emitting one single phonon. That is because the energy for a single phonon is much smaller than the nuclear transition energy except in the case of nuclear Zeeman splitting of degenerate states by a magnetic field.

This fact motivates us to look for the two-phonon process as the lowest order. It turns out that the most interesting of the two-phonon process is excitation transfer. Generally speaking, excitation transfer means the process that one nucleus originally in excited state transitions to ground state while a nearby nucleus originally in ground state transitions to excited state. Several examples of excitation transfer are introduced in the following paragraphs.¹⁻³

4.1 Example 1 (No phonon exchange or loss)

A simple model for excitation transfer with no phonon exchange or loss is shown in Figure 4.1. States 1-4 represent different states for a diatomic molecule with two identical nuclei. ΔE is the transition energy for the nucleus; the V terms describe direct coupling terms between different states.

- For state 0, both nuclei are in ground state.
- For state 1, the first nucleus is in excited state, while the second nucleus is in ground state.
- For state 2, the first nucleus is in ground state, while the second nucleus is in excited state.
- For state 3, both nuclei are in excited state.

Excitation transfer in this example means that occupation in state 1 is switched to state 2. We are interested in whether there is indirect coupling between state 1 and state 2. We would like to calculate the indirect coupling term V_{12} .

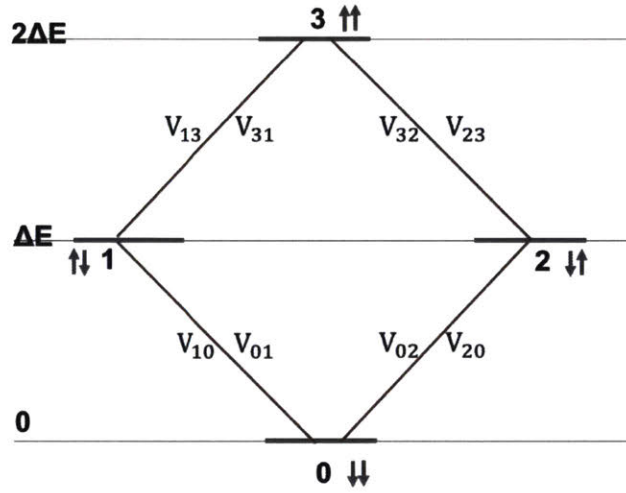


Figure 4.1: The 1st example for excitation transfer without phonon or loss

The wave function based on finite basis expansion can be written as¹⁻³

$$\Psi(t) = \sum_j c_j(t) \Phi_j = c_0(t) \Phi_0 + c_1(t) \Phi_1 + c_2(t) \Phi_2 + c_3(t) \Phi_3 \quad (9)$$

The finite basis equations for the coefficients can be written as¹⁻³

$$\begin{aligned} Ec_0 &= 0c_0 + V_{01}c_1 + V_{02}c_2 \\ Ec_1 &= \Delta Ec_1 + V_{10}c_0 + V_{13}c_3 \\ Ec_2 &= \Delta Ec_2 + V_{20}c_0 + V_{23}c_3 \\ Ec_3 &= 2\Delta Ec_3 + V_{31}c_1 + V_{32}c_2 \end{aligned} \quad (10)$$

As we are interested in the indirect coupling term between state 1 and state 2, we can eliminate c_0 and c_3 to get the following two-level system

$$E \begin{pmatrix} c_1 \\ c_2 \end{pmatrix} = \begin{pmatrix} H_{11} & V_{12} \\ V_{21} & H_{22} \end{pmatrix} \begin{pmatrix} c_1 \\ c_2 \end{pmatrix} \quad (11)$$

The indirect coupling term V_{12} is¹⁻³

$$V_{12} = V_{21}^* = \frac{1}{\Delta E} (V_{10}V_{02} - V_{13}V_{32}) = 0 \quad (12)$$

Due to the symmetry of the system, $V_{02} = V_{13}$ (the second nucleus is excited) and $V_{10} = V_{32}$ (the first nucleus transitions to the ground state). There is no net indirect coupling due to destructive interference. The two paths cancel with each other, and the indirect coupling term V_{12} is zero. There is no indirect coupling between state 1 and state 2, and hence no excitation transfer for this example.

4.2 Example 2 (Adding phonon exchange but no loss)

Figure 4.2 shows the second example for excitation transfer where phonon exchange is included, but there is still no loss. States 1-6 represent 6 different states for the same molecule with two identical nuclei inside. As before, ΔE is the transition energy for the nuclear transition. The V terms are the direct coupling terms between different states, and n is the number of phonons in different states.

- For state 1, the first nucleus is excited state while the second nucleus is in ground state; state 1 has n phonons.
- For state 2 and state 3, both nuclei are in ground state; state 2 has $n-1$ phonons, and state 3 has $n+1$ phonons.
- For state 4 and state 5, both nuclei are in excited state; state 4 has $n-1$ phonons, and state 5 has $n+1$ phonons.

- For state 6, the first nucleus is in ground state while the second nucleus is in excited state; state 6 has n phonons.
- For state 7, the first nucleus is in ground state while the second nucleus is in excited state; state 7 has $n+2$ phonons.
- For state 8, the first nucleus is in ground state while the second nucleus is in excited state; state 8 has $n-2$ phonons.

The excitation transfer we are interested in this example is the process that initial occupation of state 1 can be transferred to state 6. We call the excitation transfer between state 1 and state 6 resonant excitation transfer as they have the same number of phonons. There are also possibilities that initial occupation of state 1 can be transferred to state 7 or state 8. We call these process non-resonant excitation transfer as they have the different number of phonons.

For this example, we focus on resonant excitation transfer between state 1 and state 6. We are interested in whether there is coupling between state 1 and state 6; to investigate this, we calculate the indirect coupling term V_{16} .¹⁻³

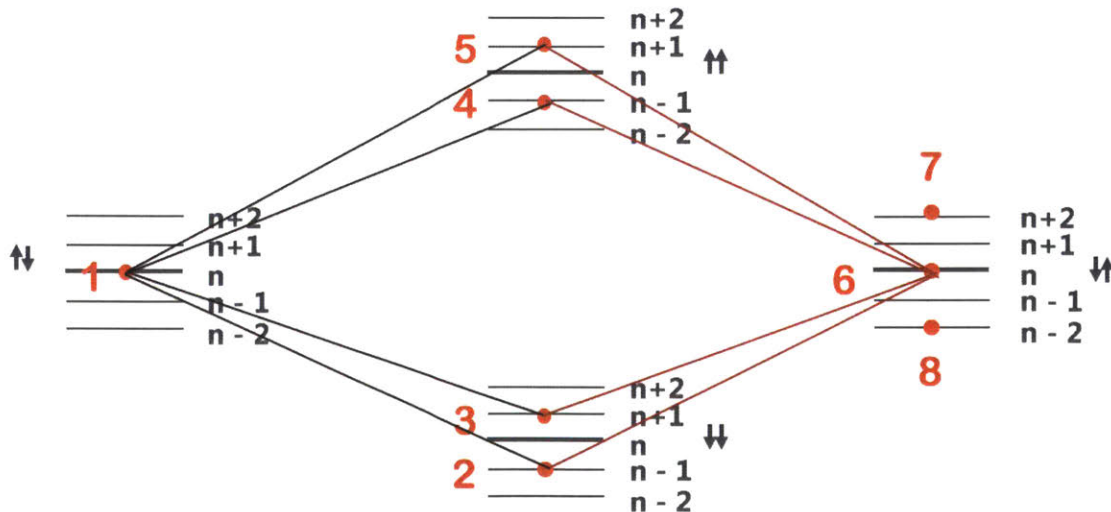


Figure 4.2: The 2nd example for excitation transfer with phonon but without loss

The approach is similar to that in the previous example. The wave function based on finite basis expansion can be written as¹⁻³

$$\Psi(t) = \sum_j c_j(t) \Phi_j = c_1(t) \Phi_1 + c_2(t) \Phi_2 + c_3(t) \Phi_3 + c_4(t) \Phi_4 + c_5(t) \Phi_5 + c_6(t) \Phi_6 \quad (13)$$

The finite basis equations for the coefficients can be written as¹⁻³

$$\begin{aligned} Ec_1 &= (\Delta E + (n + \frac{1}{2})\hbar\omega_0)c_1 + V_{12}c_2 + V_{13}c_3 + V_{14}c_4 + V_{15}c_5 \\ Ec_2 &= (n - 1 + \frac{1}{2})\hbar\omega_0c_2 + V_{21}c_1 + V_{26}c_6 \\ Ec_3 &= (n + 1 + \frac{1}{2})\hbar\omega_0c_3 + V_{31}c_1 + V_{36}c_6 \\ Ec_4 &= (2\Delta E + (n - 1 + \frac{1}{2})\hbar\omega_0)c_4 + V_{41}c_1 + V_{46}c_6 \\ Ec_5 &= (2\Delta E + (n + 1 + \frac{1}{2})\hbar\omega_0)c_5 + V_{51}c_1 + V_{56}c_6 \\ Ec_6 &= (\Delta E + (n + \frac{1}{2})\hbar\omega_0)c_6 + V_{62}c_2 + V_{63}c_3 + V_{64}c_4 + V_{65}c_5 \end{aligned} \quad (14)$$

As we are interested in the indirect coupling term between state 1 and state 6, we can eliminate c_2, c_3, c_4 and c_5 to get the following two-level system

$$E \begin{pmatrix} c_1 \\ c_6 \end{pmatrix} = \begin{pmatrix} H_{11} & V_{16} \\ V_{61} & H_{66} \end{pmatrix} \begin{pmatrix} c_1 \\ c_6 \end{pmatrix} \quad (15)$$

The expression for the indirect coupling term V_{16} is¹⁻³

$$V_{16} = V_{61}^* = \frac{V_{12}V_{26} - V_{15}V_{56}}{\Delta E + \hbar\omega_0} + \frac{V_{13}V_{36} - V_{14}V_{46}}{\Delta E - \hbar\omega_0} \quad (16)$$

To get V_{16} , we need to calculate the direct coupling terms in the above equation. We can get V_{12} from the following equation¹⁻³

$$\begin{aligned}
V_{12} &= \left\langle \uparrow \downarrow n \left| V_0 (a + a^\dagger) \left((|\phi_1\rangle\langle\phi_2| + |\phi_2\rangle\langle\phi_1|)_1 + (|\phi_1\rangle\langle\phi_2| + |\phi_2\rangle\langle\phi_1|)_2 \right) \right| \uparrow \uparrow n-1 \right\rangle \\
&= V_0 \left\langle n \left| a + a^\dagger \right| n-1 \right\rangle \left\langle \uparrow \downarrow \left| (|\phi_1\rangle\langle\phi_2| + |\phi_2\rangle\langle\phi_1|)_1 + (|\phi_1\rangle\langle\phi_2| + |\phi_2\rangle\langle\phi_1|)_2 \right| \uparrow \uparrow \right\rangle \\
&= V_0 \sqrt{n}
\end{aligned} \tag{17}$$

We can get other direct coupling terms from the similar approach

$$\begin{aligned}
V_{14} &= V_{26} = V_{46} = V_0 \sqrt{n} \\
V_{13} &= V_{15} = V_{36} = V_{56} = V_0 \sqrt{n+1}
\end{aligned} \tag{18}$$

Plugging back to the expression for V16, we have¹⁻³

$$\begin{aligned}
V_{16} &= \frac{V_0^2 (n - (n+1))}{\Delta E + \hbar\omega_0} + \frac{V_0^2 ((n+1) - n)}{\Delta E - \hbar\omega_0} \\
&= -\frac{V_0^2}{\Delta E + \hbar\omega_0} + \frac{V_0^2}{\Delta E - \hbar\omega_0} \\
&\approx -\frac{V_0^2}{\Delta E} \left(1 - \frac{\hbar\omega_0}{\Delta E}\right) + \frac{V_0^2}{\Delta E} \left(1 + \frac{\hbar\omega_0}{\Delta E}\right) = \frac{2V_0^2 \hbar\omega_0}{\Delta E^2}
\end{aligned} \tag{19}$$

$$V_{16} = V_{61} \approx \frac{2V_0^2 \hbar\omega_0}{\Delta E^2} \tag{20}$$

We see that the indirect coupling term is non-zero with phonon exchange, which means it is possible for excitation transfer to happen between state 1 and state 6. We also notice that the coupling term is stronger when the phonon energy is higher, and the transition energy is smaller.

Though the indirect coupling term is non-zero, it is a small value due to destructive interference. There is strong cancelation between the four paths which cancels the term n . The above analysis is for the E1 transition. Recent M1 transition analysis by Hagelstein shows much less destructive interference (no cancelations for n) for excitation transfer example 2 (adding phonon exchange but no loss).¹⁻³

There is another example for excitation transfer keeping phonon exchange and adding loss. The destructive interference for E1 transition can be reduced with the existence of loss. The details about this example are introduced in Appendix A.

Excitation transfer is the lowest order process that we have any chance of seeing in an experiment. From the above analysis, we know that to increase the chance of seeing excitation transfer effect, we would like low nuclear transition energy, high phonon energy and lots of energetic phonons.

All the materials reviewed in this chapter are directly from or based on Hagelstein's work.

References

- 1 Hagelstein, P. (2016). Quantum Composites: A Review, and New Results for Models for Condensed Matter Nuclear Science. *Journal of Condensed Matter Nuclear Science*, 20, 139-225.
- 2 Hagelstein, P., & Chaudhary, I. Possibility of observing a center of mass interaction in a Mossbauer experiment. Manuscript unpublished.
- 3 Hagelstein, P., & Chaudhary, I. (2011). Energy Exchange In The Lossy Spin-Boson Model. *Journal of Condensed Matter Nuclear Science*, 5, 52-71.

5 Observation of Unexpected Non-Exponential Decay from Co-57

Before May 20, 2017, we carried out several experiments in our lab. Some of them were to replicate previous experiments by other people at MIT. Some of them were newly designed experiments in order to test Hagelstein's theory. However, there were no significant results in all of these experiments.

On May 20, 2017, an experiment was done in our lab by my colleague Florian Metzler to look for excitation transfer with excited nucleus produced from the radioactive decay of Co-57.¹ We added strong MHz vibrations to Co-57 hoping to see excitation transfer effects. There was no prompt response from MHz vibrations. However, an unexpected non-exponential decay effect was seen.¹

Figure 5.1 shows the nuclear levels in Co-57. Co-57 decays to Fe-57 second excited state at 136 keV with a half-life of 271.74 days. It further decays to Fe-57 first excited state at 14.4 keV with a half-life of 8.7 ns. It finally decays to Fe-57 ground state with a half-life of 98.3 ns. The energy levels and half-life values are from the NUDAT2 website.²

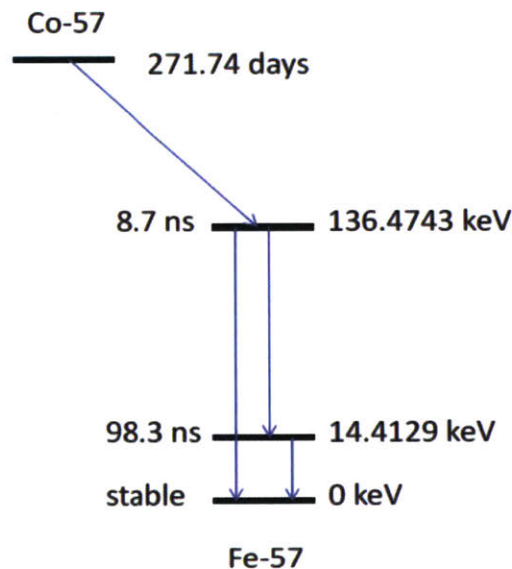


Figure 5.1: Nuclear levels of Co-57

Figure 5.2 shows the scheme of the May 20 experiment by my colleague Florian Metzler.¹ Co-57 was deposited onto the surface of a steel plate. The steel plate was tightened by wood blocks. A transducer was attached to the other surface of the steel plate to generate MHz vibrations. An Amptek X-123 detector was used to detect signals from Co-57. An aluminum mesh was put in the middle of the plate and detector to protect the detector.¹

Figure 5.3 shows the spectrum from the Amptek X-123 detector. We see the 14.4 keV gamma line from the Fe-57 first excited state. We see the Fe K-alpha (6.40 keV) and Fe K-beta (7.06 keV) lines from internal conversion. We see a weak Sn K-alpha line due to the photoionization of higher gammas. The Amptek X-123 detector is not sensitive to higher gammas of 122 keV and 136 keV.¹

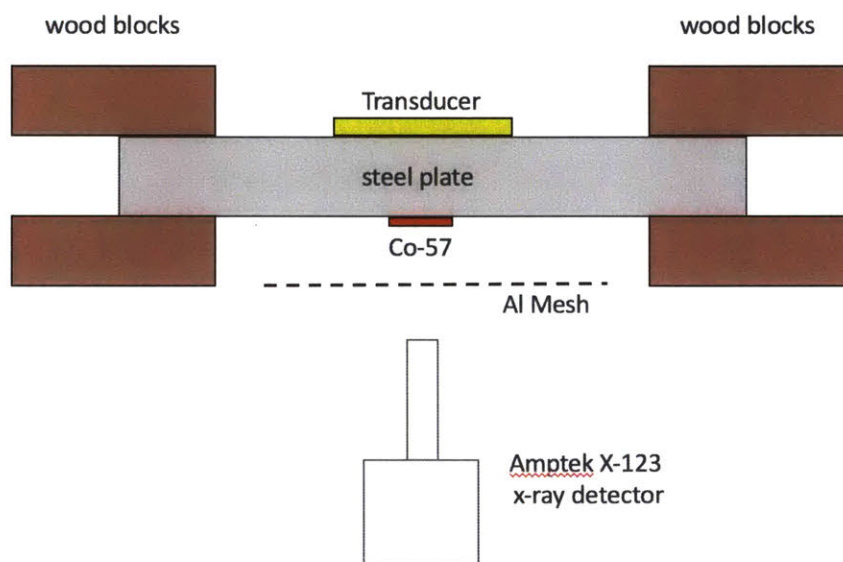


Figure 5.2: Scheme of the May 20 Experiment¹

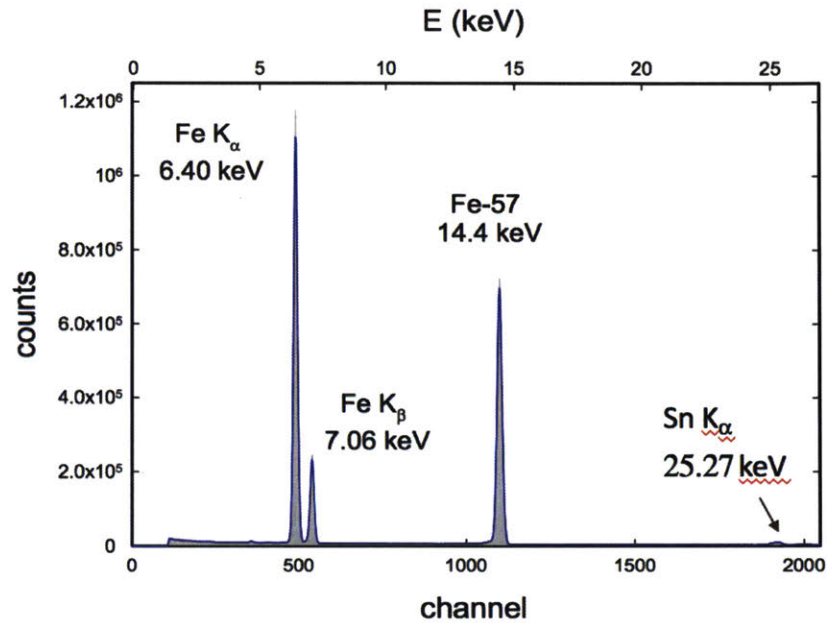


Figure 5.3: Spectrum from the Amptek X-123 detector¹

Figure 5.4 shows the time history of the Sn K-alpha line. The black line represents the expected 271-day half-life exponential decay. Each yellow or white shaded block represents 1-day of time. We see that the Sn K-alpha line follows the expected 271-day half-life exponential decay. As Sn K-alpha line is photoionized by higher gammas of 122 keV and 136 keV, that means Co-57 is decaying normally following the expected half-life.¹

If everything is normal, we should also expect both the 14.4 keV line and Fe K-alpha line follow the expected 271-day half-life exponential decay. However, that is not what we see. Figure 5.5 shows the time history of the 14.4 keV gamma. Figure 5.6 shows the time history of the Fe K-alpha line. We see that both the 14.4 keV line and Fe K-alpha line do not follow the expected half-life exponential decay. Instead, both lines show unexpected non-exponential decays for several days after the experiment starts. There are around 19% signal enhancements at the beginning of the experiments for the 14.4 keV gamma. There are around 17% signal enhancements at the beginning of the experiments for Fe K-alpha X-ray.¹

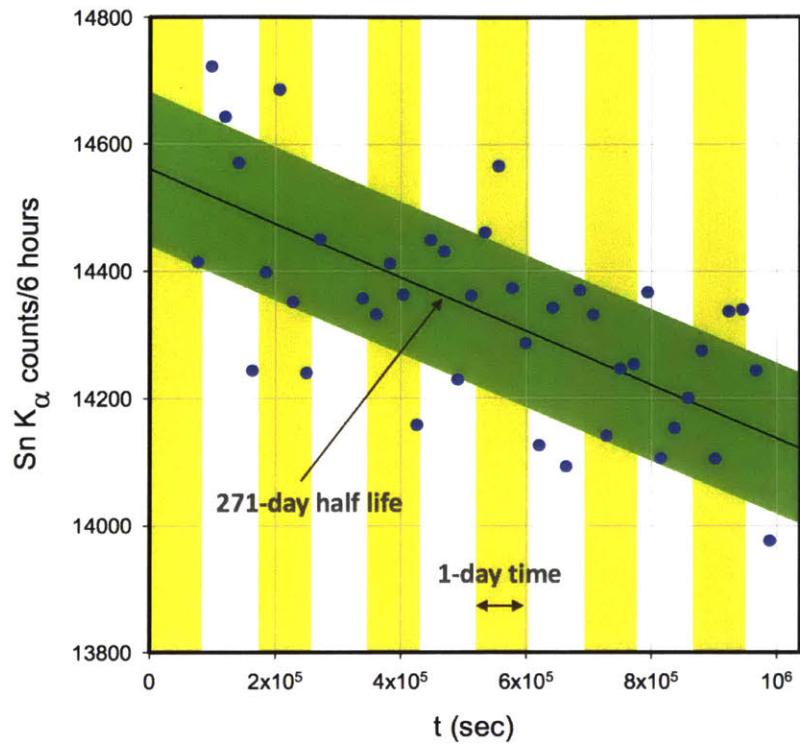


Figure 5.4: Time history of Sn K-alpha line in May 20 experiment¹

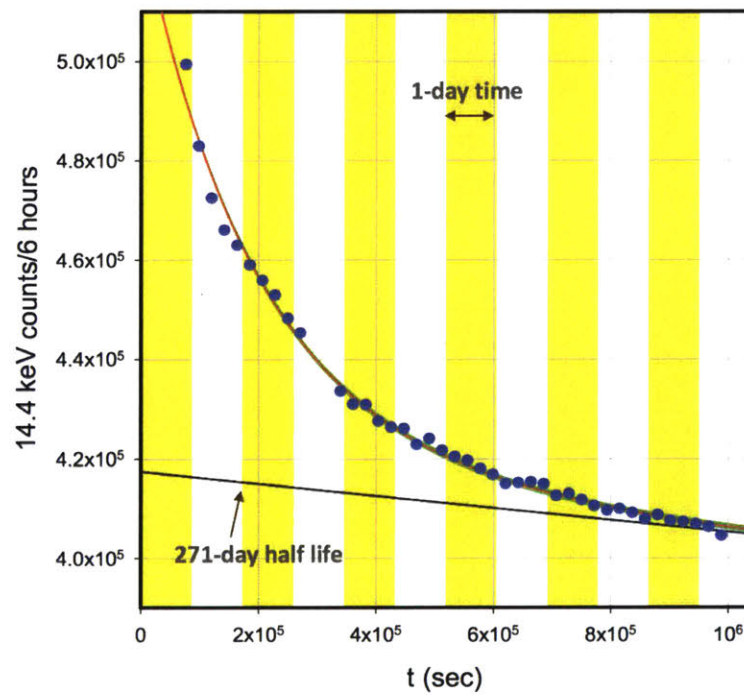


Figure 5.5: Time history of 14.4 keV line in May 20 experiment¹

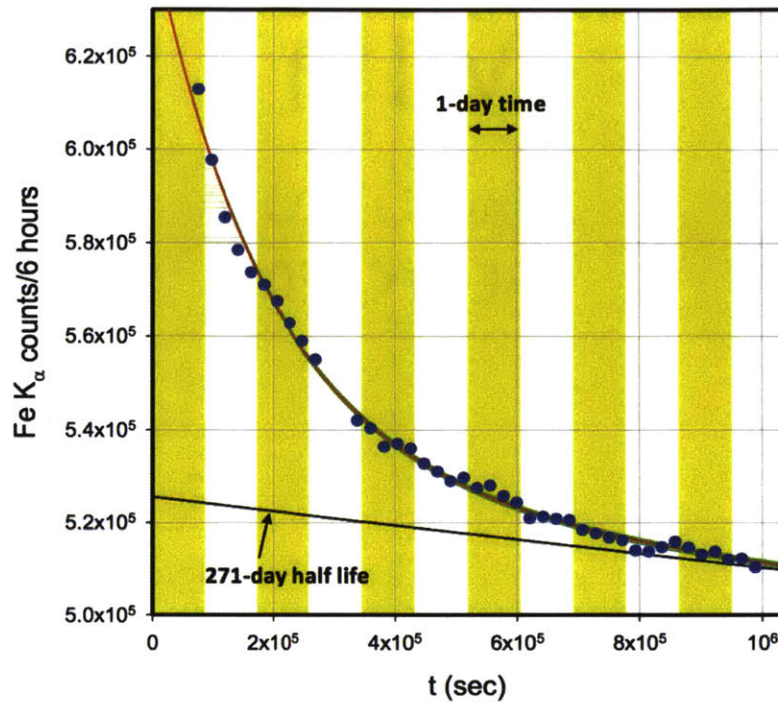


Figure 5.6: Time history of Fe K-alpha line in May 20 experiment¹

The original goal of the May 20 experiment was to detect excitation transfer effects caused by MHz vibrations induced by the transducer. However, there was no prompt response for the MHz vibrations. Instead, we saw unexpected non-exponential decays for both 14.4 keV gamma and Fe K-alpha X-ray. Exponential decay for Sn K-alpha (25.27 keV) by higher gammas (122 keV and 136 keV) indicates that Co-57 decays normally.¹

Figure 5.7 shows the time history of Fe K-alpha line with discrete MHz vibrations (red pulses) induced by the transducer. There is little or no impact of the MHz vibrations on the Fe K-alpha time history data, which indicates that the driven transducer is not contributing to the unexpected non-exponential decay anomaly.¹

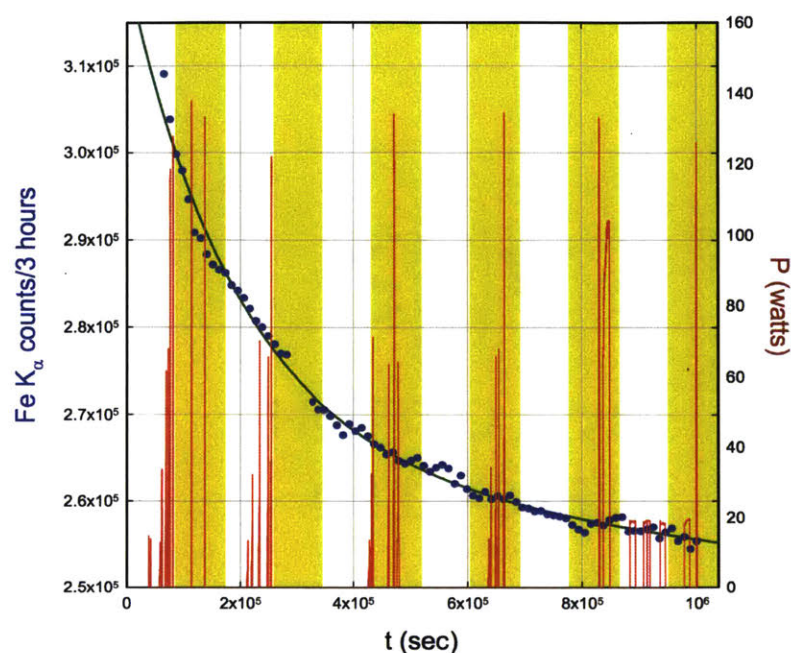


Figure 5.7: Time history of Fe K-alpha with MHz vibrations (red pulses) induced by the transducer¹

From subsequent experiments, we realize that initial clamping of the wood is ultimately responsible for the unexpected non-exponential decay.¹ We suspect that excitation transfer is involved for the 14.4 keV excited state of Co-57.¹ There is an important question here how excitation transfer result in a deviation from expected half-life exponential decay. We will consider this question in detail in a chapter 10.

The experiment introduced in this chapter is done by my colleague Florian Metzler. All data shown in this chapter is taken by Metzler and analyzed by Hagelstein. All materials reviewed in this chapter have been accepted for publication in the *Journal of Condensed Matter Nuclear Science* (JCMNS).¹

References

- 1 Metzler, F., Hagelstein, P., & Lu, S. (in press). Observation of Non-exponential Decay in X-ray and γ Emission Lines from Co-57. *Journal of Condensed Matter Nuclear Science*.
- 2 Nudat 2. (n.d.). Retrieved from <https://www.nndc.bnl.gov/nudat2/>

6 Heat Pulse Experiment

We did several subsequent runs after the May 20 experiment. The results are reproducible, but the effects are smaller. We would like a more reproducible experiment. On Aug 10, 2017, my colleague Florian Metzler did a heat pulse experiment using temperature increase to induce pressure increase by wood clamps. Figure 6.1 shows the scheme of this experiment. The set up is similar to the May 20 experiment except there is an extra heating pad on the surface of steel plate. When the heating pad heats everything, the wood blocks expand which leads to a pressure increase.

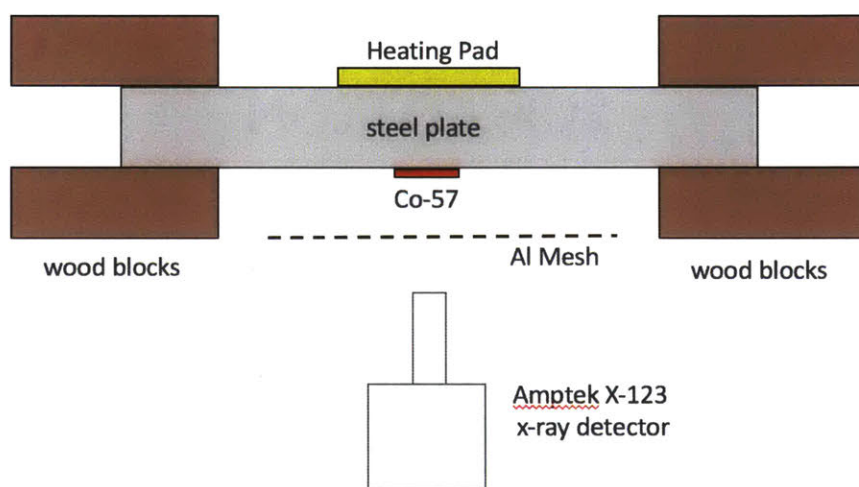


Figure 6.1: Scheme of the Aug 10 heat pulse Experiment

Figure 6.2 shows the time history of Sn K-alpha line. Again, the black line represents the expected 271-day half-life exponential decay. Each yellow or white shaded block represents 1-day of time. The red pulses represent the temperature history of the steel plate caused by the heating pad. We see that the Sn K-alpha line follows the expected half-life exponential decay. There is little or no impact of the temperature increase on the Sn K-alpha signals.

Figure 6.3 shows the time history of 14.4 keV line. Figure 6.4 shows the time history of Fe K-alpha line. Both lines do not follow the expected half-life exponential decay. There is a signal reduction instead of signal enhancement at the beginning of the experiment due to wood

clamping. Moreover, there are strong correlations between temperature pulses and signal counts for both 14.4 keV gamma and Fe K-alpha X-ray. Heat pulse triggers increments in the signal counts for both lines.

The Aug 10 heat pulse effects are reproducible. The heat pulse provides a powerful tool for us to enable other experiments. The critical question remains of how excitation could make unexpected non-exponential decay. We will start to address this question in the following section.

The experiment introduced in this chapter is done by my colleague Florian Metzler. All data shown in this chapter is taken by Metzler and analyzed by Hagelstein.

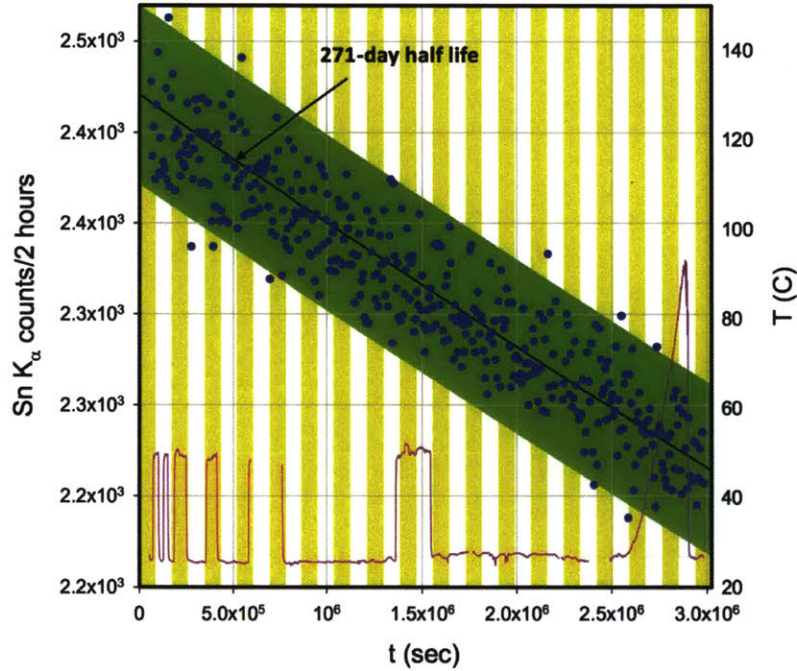


Figure 6.2: Time history of Sn K-alpha line in Aug 10 experiment

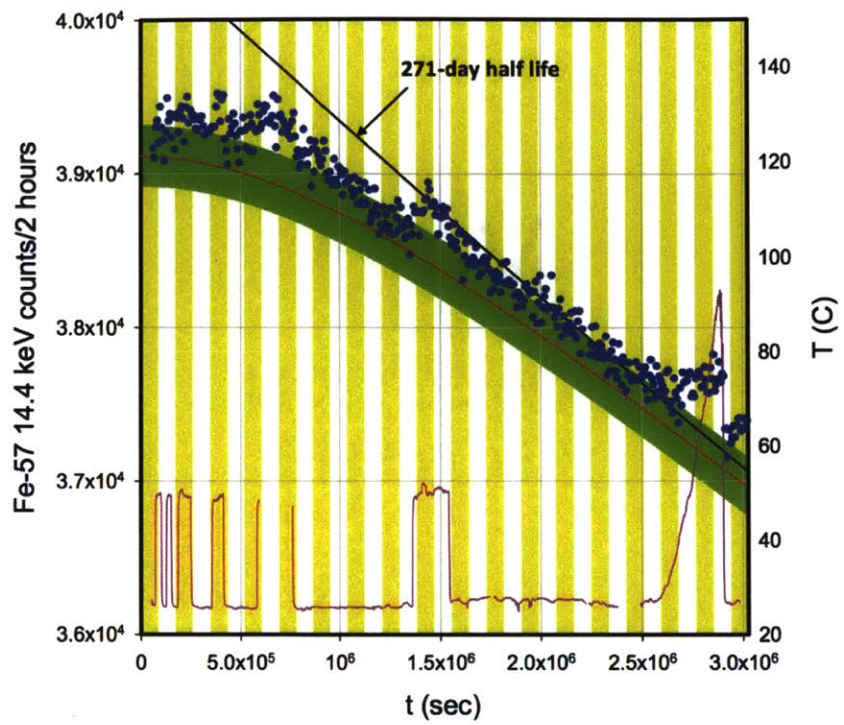


Figure 6.3: Time history of 14.4 keV line in Aug 10 experiment

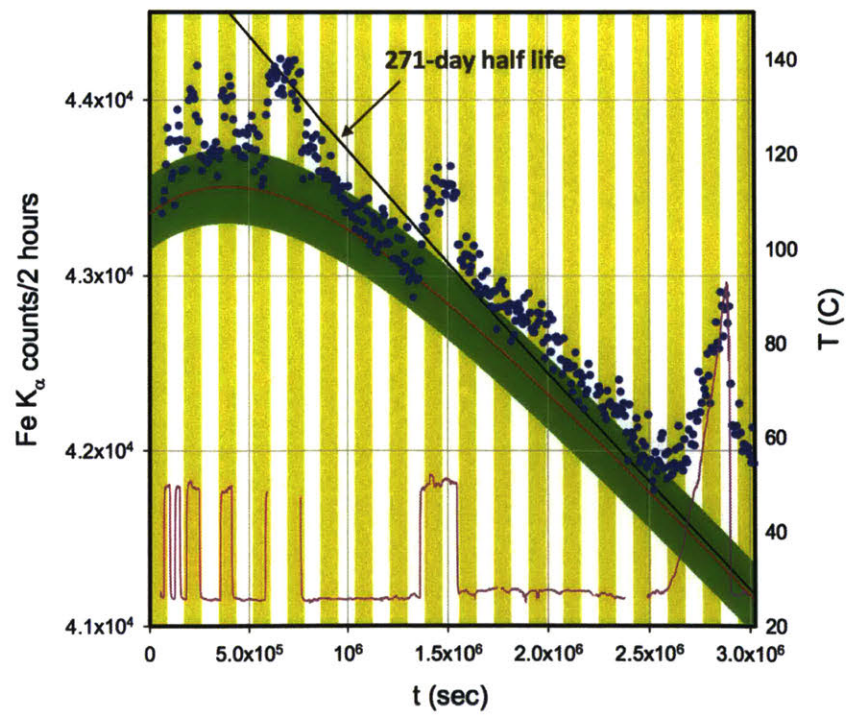


Figure 6.4: Time history of Fe K-alpha line in Aug 10 experiment

7 Theory: Angular Anisotropy

Resonant excitation transfer can produce phase coherence. Phase coherence can impact the angular distribution of emitted gammas. To observe phase coherence, experiments sensitive to angular anisotropy are needed.

Figure 7.1 shows the scheme of the incoherent radiation without excitation transfer. In this example, suppose there is one nucleus in the excited state (red color on the left side), and there are several nearby nuclei in ground state. When there is no excitation transfer, only one single dipole radiates. The emission pattern for this single dipole is shown on the right side of Figure 6.1. The overall emission will be isotropic by averaging over random single dipole polarizations.

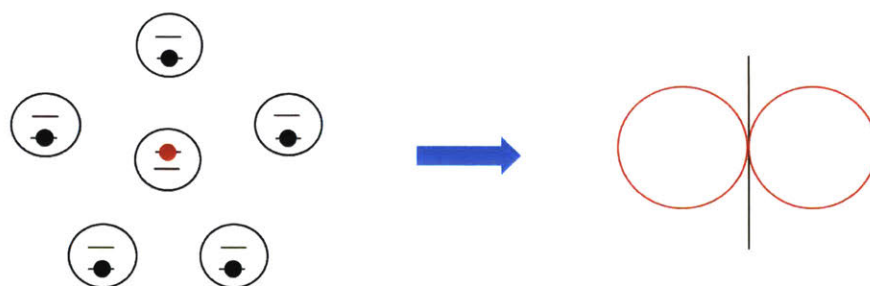


Figure 7.1: Scheme of incoherent radiation without excitation transfer

Figure 7.2 shows the scheme of the phase coherent radiation with resonant excitation transfer. When resonant excitation transfer occurs, the excited nucleus in Figure 7.1 can go to the ground state while one of the nearby nuclei originally in the ground state goes to the excited state. The plus signs in Figure 7.2 represent the quantum superposition in quantum mechanics. In this situation, the overall emission is from averaging over the multipole radiation pattern instead of the single dipole radiation pattern. Figure 7.3 shows an example of the multipole radiation pattern. With the local order, the overall emission pattern can be anisotropic. We would like to do experiments sensitive to angular anisotropy.

All the materials reviewed in this chapter are directly from or based on Hagelstein's theory.

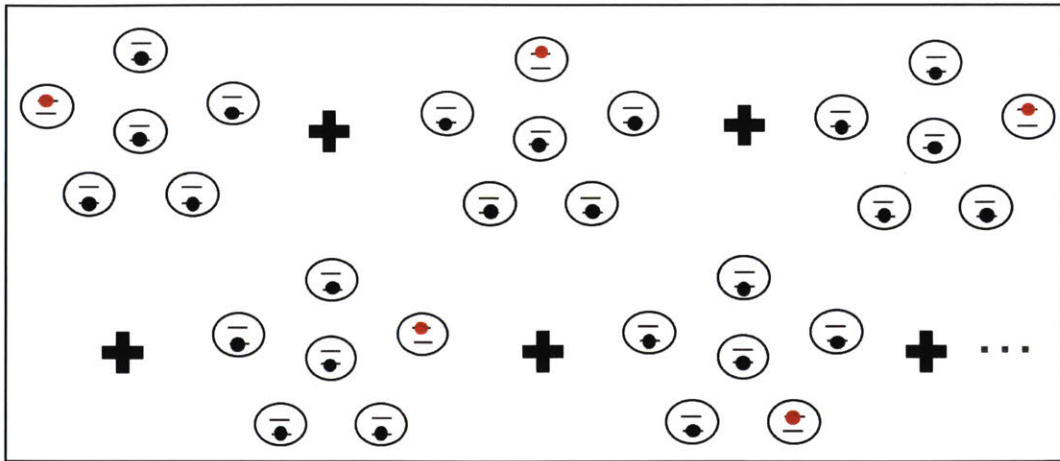


Figure 7.2: Scheme of phase coherent radiation with excitation transfer

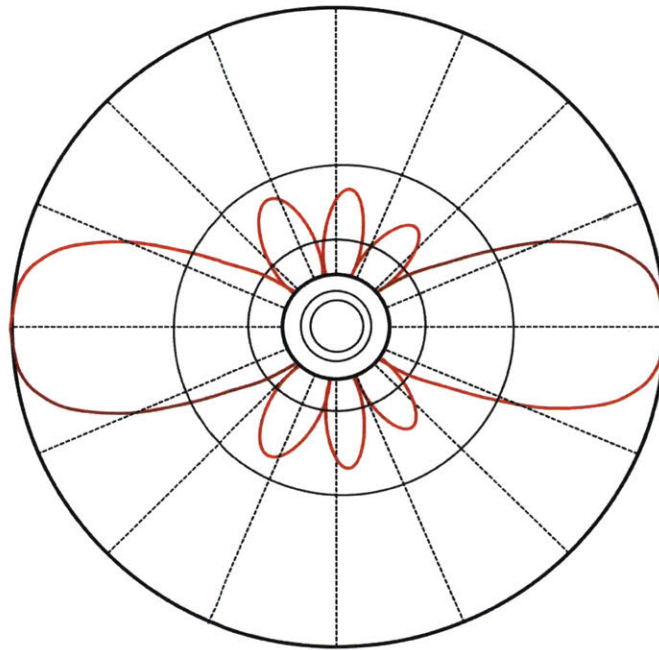


Figure 7.3: An example of multipole radiation pattern

8 Experiment: Angular Anisotropy

In the May 20 experiment, in addition to the Amptek X-123 detector on the front side of the plate, there was also a Geiger counter placed at a shallow angle on the back side of the plate. The back side Geiger saw an unexpected non-exponential decay. The Geiger counter responds only to harder gammas (122 keV and 136 keV). We interpret this effect as angular anisotropy of harder gammas. Last year we made 2 different samples for experiments. Sample 1 was used in the May 20 experiment. The angular anisotropy effects were reproduced in subsequent experiments with Sample 1. We would like to know whether Sample 2 was also active. We did experiments to look for angular anisotropy in Sample 2.

Figure 8.1 shows the scheme of the angular anisotropy experiment with Sample 2. Co-57 was deposited on the surface of a steel plate. The steel plate was tightened by wood blocks and was put in front of the Ortec high purity Germanium X-ray detector at a shallow angle. Figure 8.2 shows a picture of the experimental setup. The steel plate with Co-57 tightened by wood blocks was standing in front of the Ortec detector at a shallow angle. The Ortec detector was surrounded by lead bricks to reduce noise. Figure 8.3 shows the spectrum from the Ortec detector. We see all the relevant lines from Co-57 including Fe K-alpha, Fe K-beta, 14.4 keV, 122 keV and 136 keV. We also see the Pb K-alpha lines due to the lead bricks.

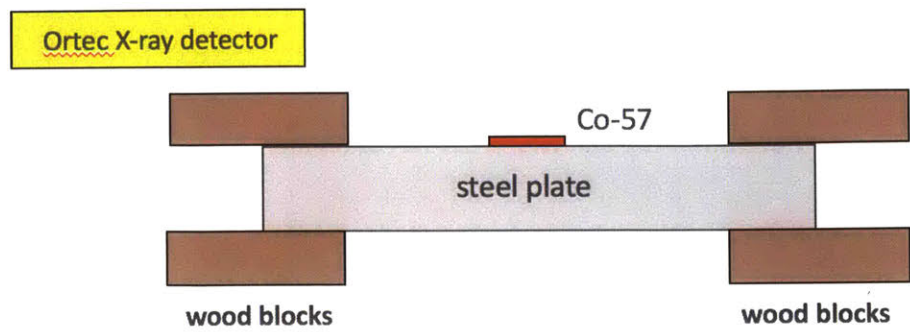


Figure 8.1: Scheme of the angular anisotropy experiment with Sample 2



Figure 8.2: Picture of the angular anisotropy experiment setup with Sample 2

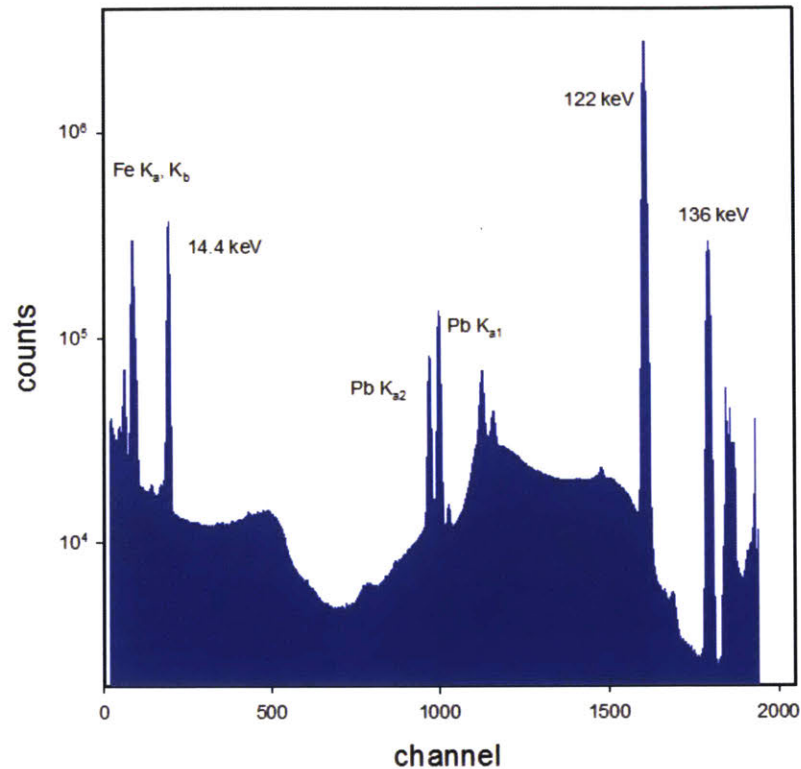


Figure 8.3: Spectrum from the Ortec detector

Figure 8.4 shows the time history of 122 keV line in an angular anisotropy control test. In this control test, the plate had been tightened by wood blocks for a long time, and Sample 2 had been in equilibrium status. Before the starting of the experiment, a lead plate with a quarter inch thickness was held in air between the sample and the detector to block the harder gammas. At the starting of the experiment, the lead plate was moved away so that the detector started acquiring signals. We see from Figure 8.4 that the 122 keV line follows the expected 271-day half-life line (the black line) in the control test.

Figure 8.5 shows the time history of 122 keV line in the angular anisotropy wide angle test with the wood blocks just having been tightened. In this test, the plate was put in front of the Ortec detector at a wide angle immediately after the wood blocks were tightened. Before tightening the wood blocks, the plate had rested for a long time, and Sample 2 had been in

equilibrium. We see fast transients in Figure 8.5 during the first 2 hours of the experiment. There is around 7% signal reduction at the beginning of the experiment. There are two different decay curves for the fast transients. The faster decay has a 7-minute time constant, and the slower decay has a 76-minute decay time.

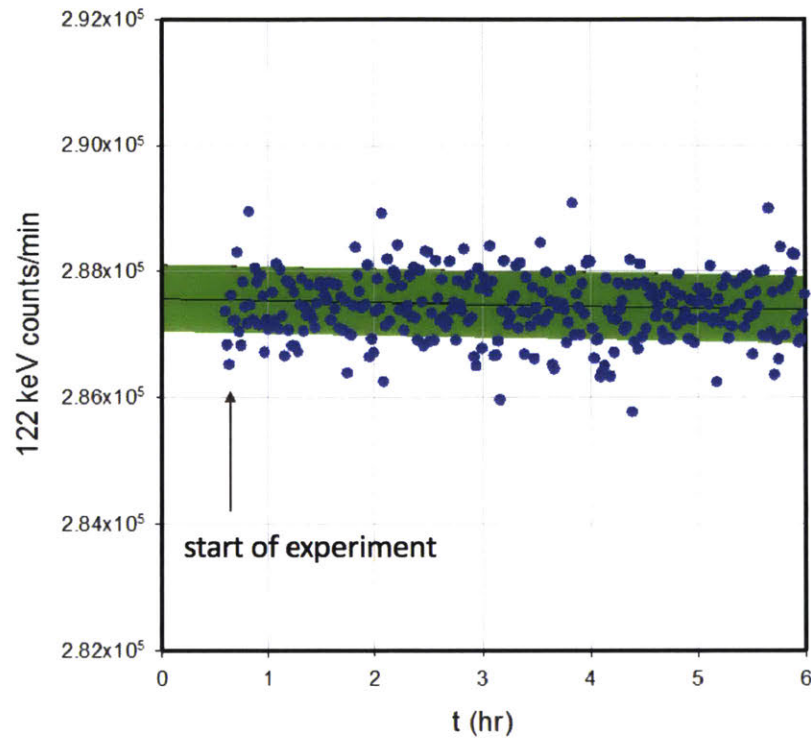


Figure 8.4: Time history of 122 keV line in the angular anisotropy control test

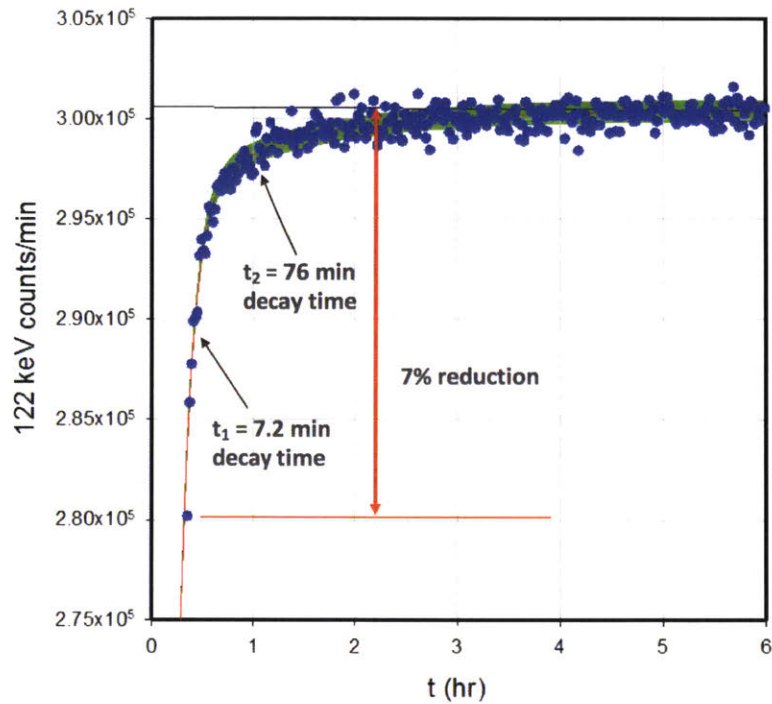


Figure 8.5: Time history of 122 keV line in the wide angle test with wood blocks just being tightened.

Figure 8.6 shows the scheme of the angular anisotropy wide angle test with the wood blocks just being loosened. In this test, the plate was put in front of the Ortec detector at a wide angle immediately after the wood blocks being loosened. Before loosening the wood blocks, the plate had been tightened by wood blocks for 24 hours, and Sample 2 had been in an equilibrium status. Figure 8.7 shows the time history of 122 keV line in this test. We see similar fast transients in this wide angle loosening test as we see in the wide angle tightening test (Figure 8.5). There is around 5% signal reduction at the beginning of the wide angle loosening test.

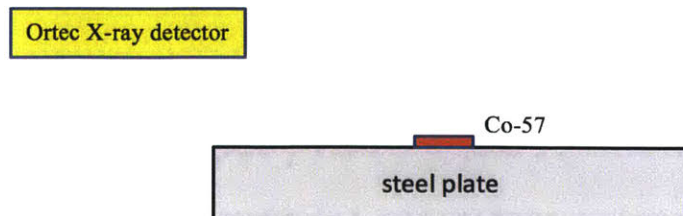


Figure 8.6: Scheme of the wide angle test with wood blocks just being loosened

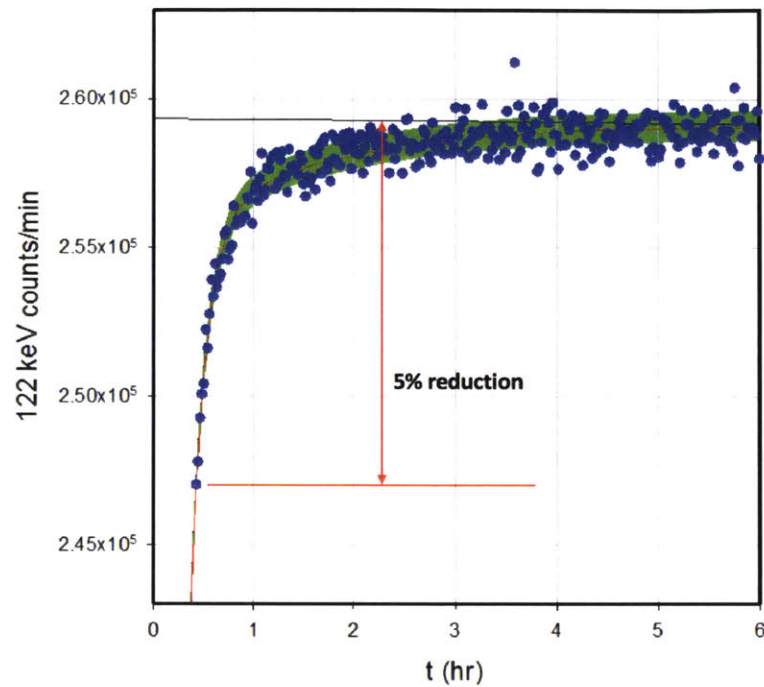


Figure 8.7: Time history of 122 keV line in the wide angle test with wood blocks just being loosened

Figure 8.8 shows the scheme of the angular anisotropy normal angle test with the wood blocks just being tightened. In this test, the plate was put in front of the Ortec detector at the normal angle immediately after the wood blocks being tightened. Before tightening the wood blocks, the plate had been rested for a long time, and Sample 2 had been in equilibrium status. Figure 8.9 shows the time history of 122 keV line in this test. The early transients in the normal angle test are much smaller than those in the wide angle tests. There is around 1% signal increase at the beginning of the normal angle test.

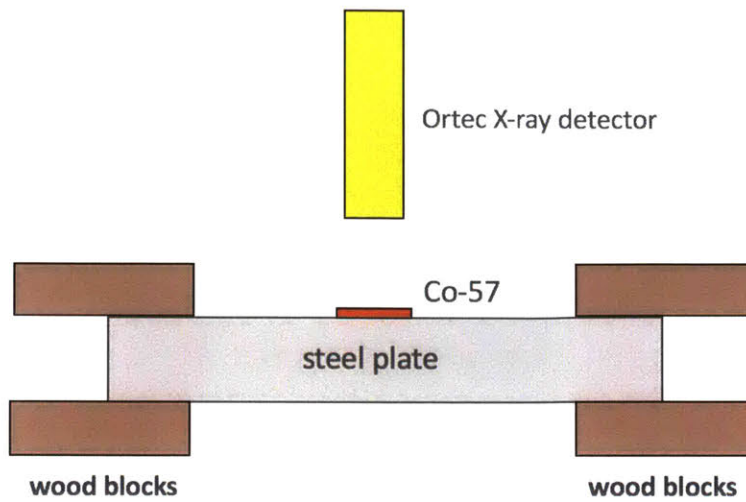


Figure 8.8: Scheme of the normal angle test with wood blocks just being tightened

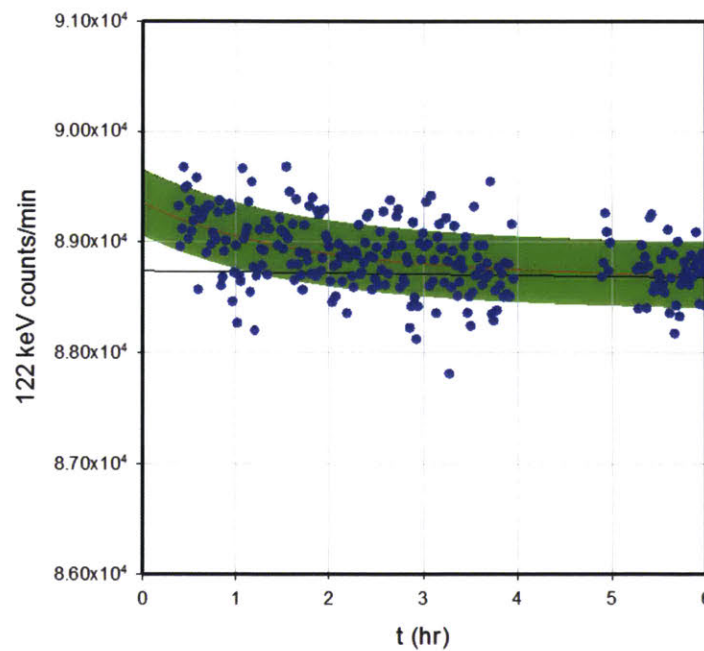


Figure 8.9: Time history of 122 keV line in normal angle test with wood blocks just being tightened

The result shown in Figure 8.5 is our first observation of fast early transients for harder gammas, which is also a confirmation that Sample 2 is active. This effect is observed with reasonable reproducibility. There are big differences in the amplitude change seen at the

beginning of the experiment, with the largest reduction near 7% and the smallest a few tenths of a percent.

Figure 8.10 shows an interpretation of angular anisotropy experimental results. If nothing happens to the steel plate and the sample has been in equilibrium status for a long time, the emission patterns for harder gammas of Co-57 will be isotropic (blue color). When the sample just gets tightened by the wood blocks, there will be THz vibrations around Co-57 which will cause resonant excitation transfer for Co-57 136 keV state, leading to phase coherent radiations for harder gammas (122 keV and 136 keV). In this situation, the emission patterns for harder gammas of Co-57 will first become anisotropic (red color), and then slightly change back to isotropic (blue color) when time passes by and sample relaxes. This is why in the wide angle tests we see fast transients and signal reductions for 122 keV line at the beginning of the experiments, and then the 122 keV line slowly changes back to expected half-life exponential decay after several hours when the sample gets fully relaxed.

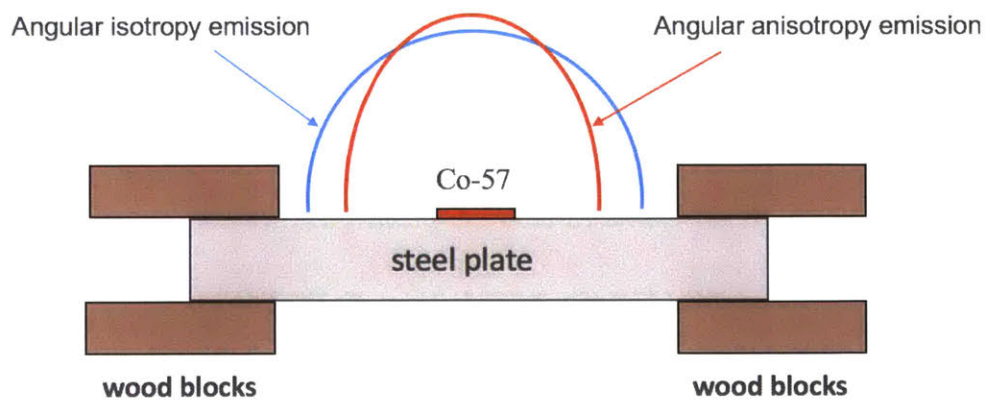


Figure 8.10: Interpretation of angular anisotropy experimental results

In the above experiments, the harder gammas of Co-57 (122 keV and 136 keV) respond to initial clamping of wood blocks, which is similar to the effect seen in the May 20 experiment (unexpected non-exponential decay of 14.4 keV gamma). The harder gamma effects are

interpreted as due to angular anisotropy. The angular anisotropy experimental results support our conjecture that excitation transfer occurs for Co-57 136 keV excited state. There is no clear evidence for strong angular anisotropy for 14.4 keV gamma in the experimental results. We will consider the reason for the absence of significant angular anisotropy for the 14.4 keV gamma in the following chapters. In subsequent angular anisotropy experiments we noticed that the harder gammas not only responded to wood clamping but also to some other stimulation. These experiments are talked about in Appendix J.

The experiment introduced in this chapter is done by me. All data shown in this chapter is taken by me and analyzed by Hagelstein.

9 Theory: Delocalization

Angular anisotropy implies phase coherence which implies excitation transfer for 136 keV state. Hagelstein's theory suggests that there should be a faster excitation transfer effect for the 14.4 keV excited state than for the 136 keV excited state due to a much smaller nuclear transition energy. We would like to observe this faster excitation transfer effect, but there is no strong angular anisotropy effect for 14.4 keV in the experimental results. We interpret the faster excitation transfer effect for 14.4 keV excited state to be due to the delocalization of excitation.

Figure 9.1- 9.3 show the schemes of the delocalization effect. Similar as the angular anisotropy effect discussed in chapter 7, the initial excited nucleus (Figure 9.1 red color) can go to the ground state while one of the nearby nucleus originally in ground state goes to the excited state (Figure 9.2). However, instead of stopping after 1 step for angular anisotropy effect (Figure 7.2), the fast excitation transfer can go further and further, leading to the delocalization effect.

The ideas reviewed in this chapter are directly from or based on Hagelstein's theory.

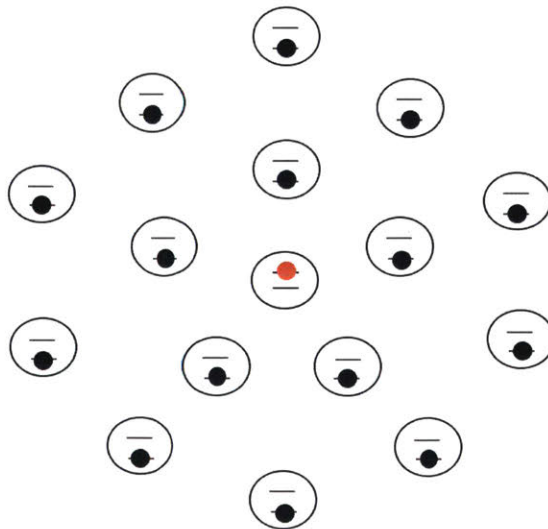


Figure 9.1: Schematic 1 of the delocalization effect

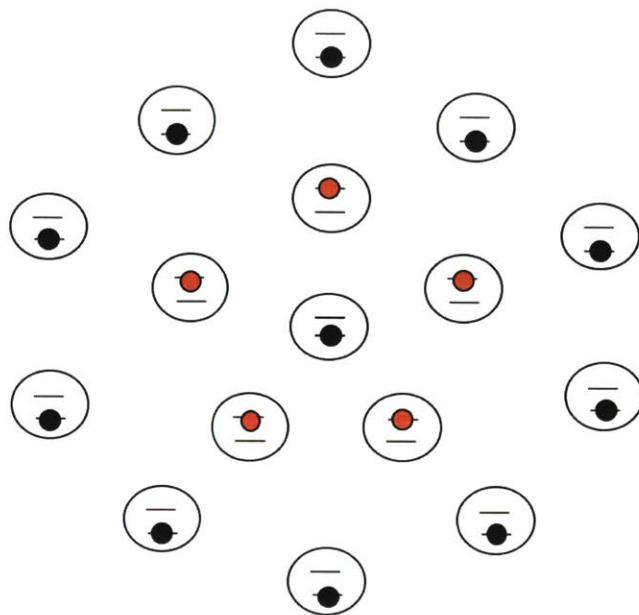


Figure 9.2: Schematic 2 of the delocalization effect

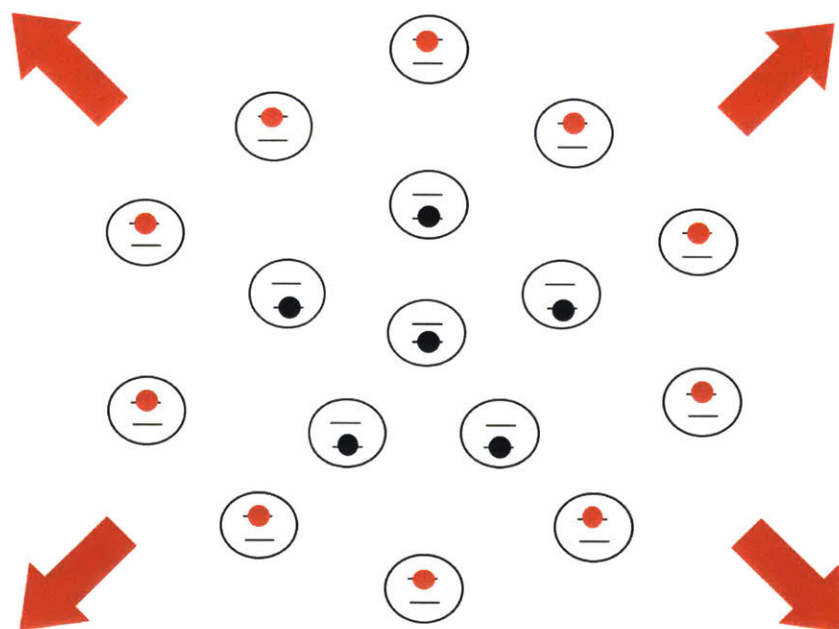


Figure 9.3: Schematic 3 of the delocalization effect

10 Experiment: Pinhole/Film

To interpret experiments looking for delocalization, we first need to know where the signals start at the beginning. Figure 10.1 shows a picture of Sample 1 used in the May 20 experiment. There was around 200 μCi Co-57 on the surface of the steel plate at the beginning of the May 20 experiment. The Co-57 is a circular source with about 10 mm diameter. There is a ring area on the edge of the circle.

In order to know the distribution of Co-57 low energy emissions (14.4 keV, Fe K-alpha and Fe K-beta), we did the pinhole/film X-ray imaging experiment. Figure 10.2 shows the scheme of this experiment. A 0.5 mm pinhole is 6 mm away from the Co-57 source. A photographic film (Ilford ISO 3200 B&W Film) is 6 mm away from the pinhole. The photographic film is sensitive to Co-57 low energy radiations (14.4 keV, Fe K-alpha and Fe K-beta).^{1,2} We can get a 1 to 1 image for the distribution of Co-57 low energy emissions since the distance of the pinhole to source is matched to the distance from pinhole to film.

Figure 10.3 shows a high-resolution optical picture of the Co-57 ring taken with a Canon digital single-lens reflex camera. Figure 10.4 shows the pinhole/film image of Co-57 with 23-hour exposure. We see that the two pictures match with each other quite well. Moreover, with the help of the pinhole/film image, it is the first time that we understood the Co-57 radioactive materials are predominantly on the edge of the circle area. Most of the Co-57 radiations come from the ring area on the edge of the circle. We also learn that there is a “hot spot” on the up-right corner of the ring with lots of radiation.

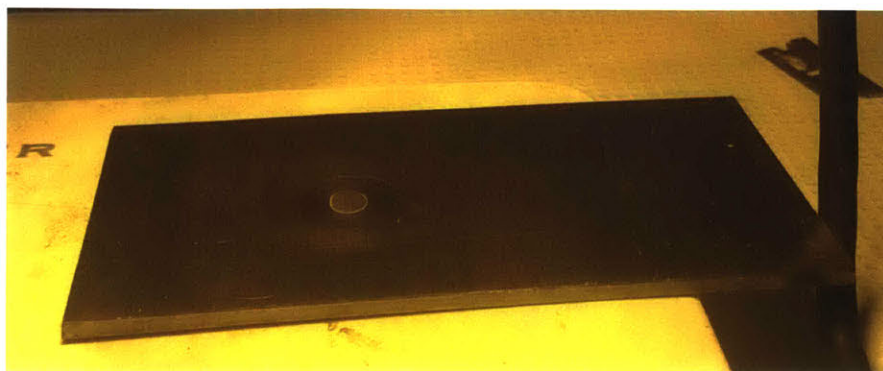


Figure 10.1: Picture of Sample 1 used in the May 20 experiment

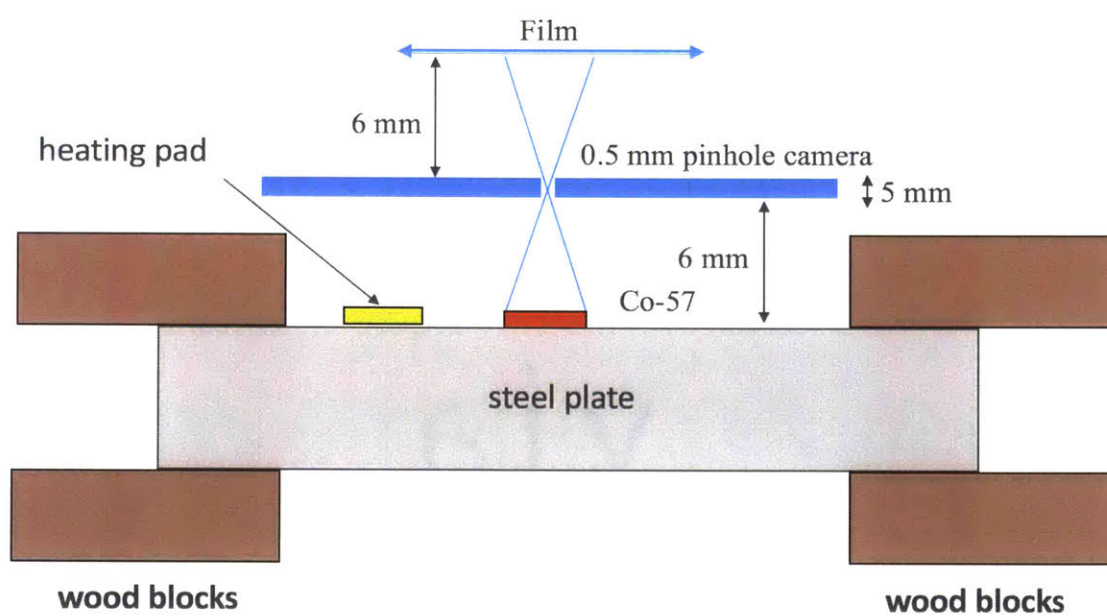


Figure 10.2: Scheme of the pinhole/film X-ray imaging experiment

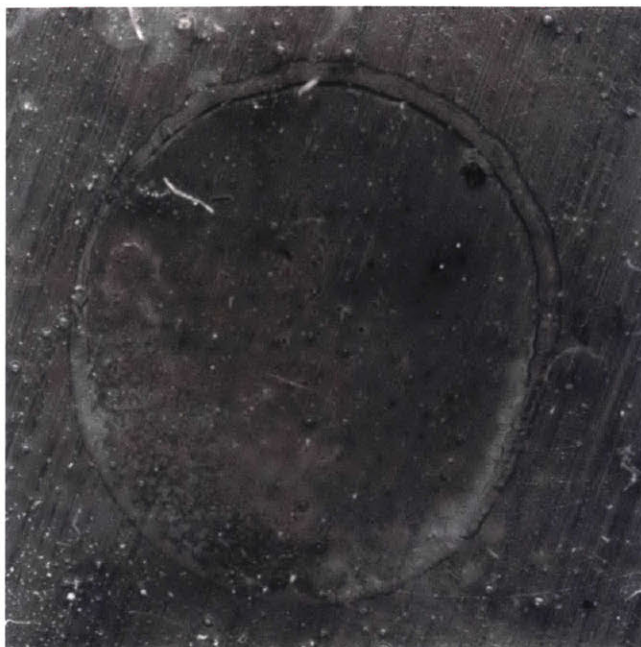


Figure 10.3: High-resolution optical picture of Co-57 by DSLR



Figure 10.4: Pinhole/film picture of Co-57 with a 23-hour exposure time

Delocalization could account for the unexpected 14.4 keV non-exponential decay in the May 20 experiment. Figure 10.5 helps explain how this could work. In the May 20 experiment, there was an aluminum mesh between the Co-57 source and the Amptek X-123 detector. The original

purpose of the aluminum mesh is to protect the detector. We understood much later that the aluminum mesh plays an important role in the unexpected non-exponential decay for the 14.4 keV line. As shown in Figure 10.5, some areas of the Co-57 ring are blocked by aluminum mesh. If everything is normal, the radiation coming from these areas should not go to the detector. However, the delocalization effect could make some of the 14.4 keV excitation move from areas blocked by mesh to areas not blocked by mesh, resulting in the signal increase for 14.4 keV in the detector at the beginning of the experiment.

We did not control where we put the aluminum mesh when we did the May 20 experiment. It should be possible that if we slightly changed the position of the mesh, delocalization effect could make some of the 14.4 keV excitation move from areas not blocked by mesh to areas blocked by mesh. In this situation, we would see signal decrease instead of signal increase at the beginning of the experiment. In the Aug 10 heat pulse experiment, we did see a signal decrease for 14.4 keV and Fe K-alpha (Figure 6.3 and Figure 6.4) at the beginning of the experiment.

We also did an experiment without the aluminum mesh expecting to see expected half-life exponential decay for the 14.4 keV signals. In this experiment, we saw a tiny signal decrease (less than 0.5%) at the beginning of the experiment for Sample 2, which was probably because a small fraction of delocalization moved from Co-57 to the steel plate.

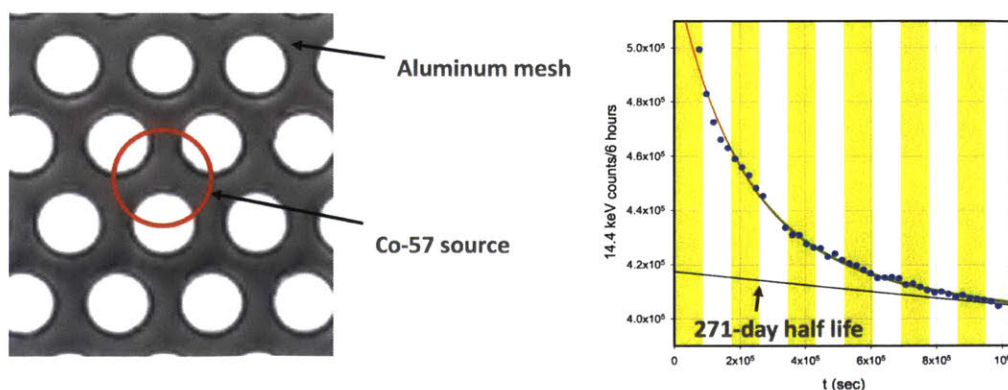


Figure 10.5: Scheme of how delocalization could account for the May 20 experiment anomaly

Except for observing the distribution of Co-57 source, another purpose of the pinhole/film experiment is to attempt to see the delocalization effect with a heat pulse. As shown in Figure 10.2, there is a heating pad on the surface of steel plate which can heat the sample. We did several experiments with the same kind of film (Ilford ISO 3200 B&W Film) and the same exposure time (23-hour) but with different plate temperatures. We used insulators and thermoelectric cooling to make sure the temperature around the film was always the same. We expected to see differences among films in different experiments with different plate temperatures.

Figure 10.6 shows two film images in two different experiments. For the left image, the plate is at room temperature. For the right image, the plate is at a temperature higher than 100C. Comparing these two images with eyeballs, we can already see some differences. Figure 10.7 shows the x channel density scan for the two images. There are differences between the hot image scan (red color) and the cold image scan (blue color). However, the differences are too subtle to prove delocalization. We need a more sensitive method.

The experiment introduced in this chapter is done by me. All data shown in this chapter is taken by me and analyzed by Hagelstein.

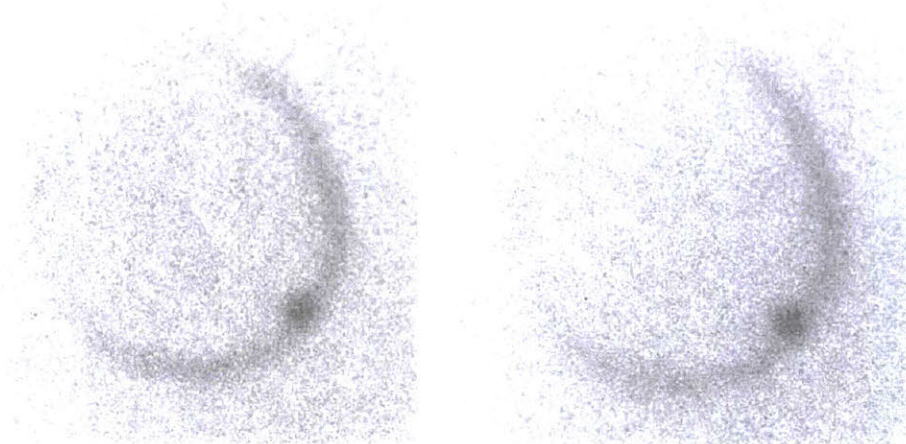


Figure 10.6: Film images in two experiments (Left: $T=25^{\circ}\text{C}$ for plate, Right: $T>100^{\circ}\text{C}$ for plate)

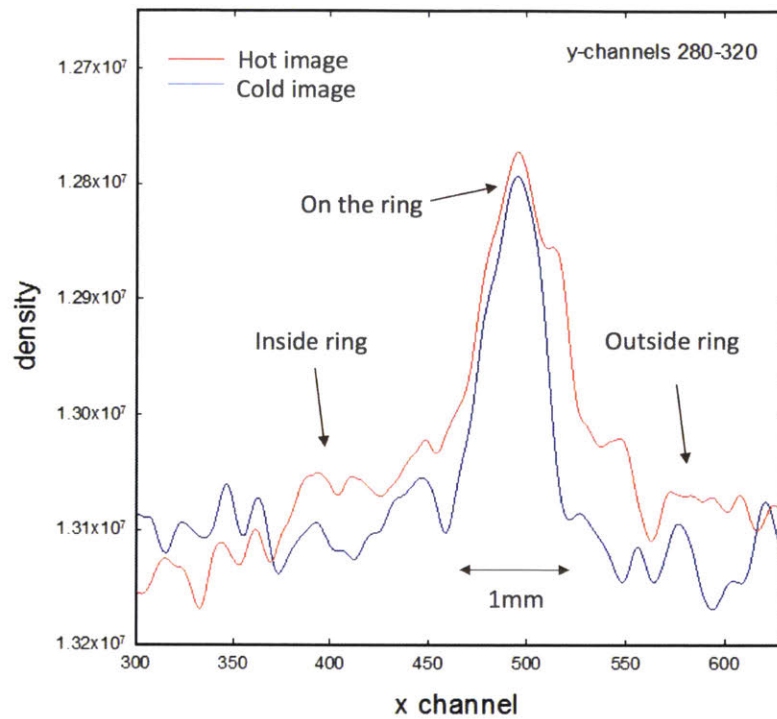


Figure 10.7: X-channel density scan for two film images

References

- 1 Chandler, K. M., Pikuz, S. A., Shelkovenko, T. A., Mitchell, M. D., Hammer, D. A., & Knauer, J. P. (2005). Cross calibration of new x-ray films against direct exposure film from 1 to 8 keV using the X-pinch x-ray source. *Review of Scientific Instruments*, 76(113111), 1-8. doi:10.1063/1.2135276
- 2 Henke, B., Fujiwara, F., Tester, M., Dittmore, C., & Palmer, M. (1984). Low-energy x-ray response of photographic films. II. Experimental characterization. *Journal of the Optical Society of America B*, 1(6), 828-849.

11 Experiment: Pinhole/SDD

The differences seen in pinhole/film experiment are at a level less than 10%. A subtle effect on the film is not impressive. We need a better way to clarify the delocalization. We need a more sensitive tool to analyze every point on the Co-57 source. The idea behind the pinhole/SDD experiment is that we can look at the time history from a localized region with the sensitive SDD (silicon drift detector) for X-rays.

Figure 11.1 shows the scheme of the pinhole/SDD experiment. The 1 mm pinhole is touching the Co-57 source. The silicon drift detector is about 10 cm away from the pinhole. In this experiment, the pinhole is no longer used as a pinhole camera. It is simply used as a hole to select a particular region. Figure 11.2 shows an example selecting the “hot spot” area. In this case, only radiation from near the “hot spot” not covered by pinhole can go the SDD.

Figure 11.3 shows the first experiment we did with the pinhole/SDD method. We looked at an area near the “hot spot.” We aligned the pinhole with the red laser point to analyze that area. Figure 11.4 shows the time history of 14.4 keV for this area. This result is important as it is our first demonstration of localized time history with the pinhole/SDD method. We see that the emissions from the local spot respond to the heat pulse. The 14.4 keV signals increase when the temperature increases. We also see a transient due to mechanical stress at the beginning of the experiment.

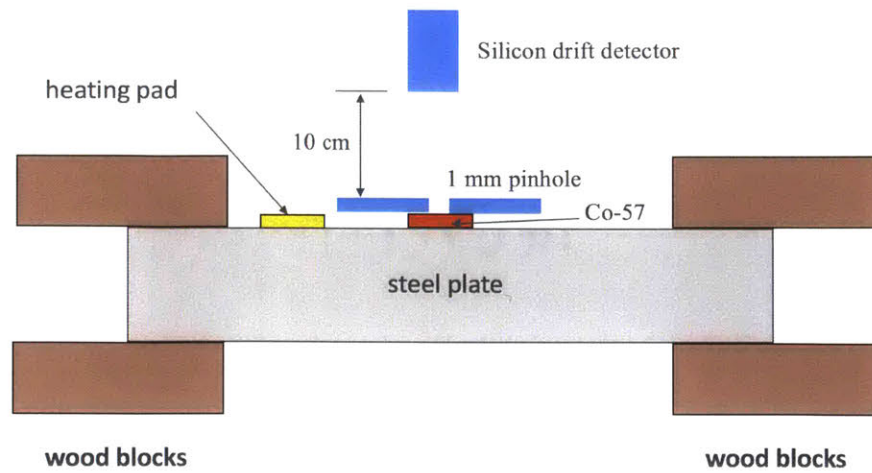


Figure 11.1: Scheme of the pinhole/SDD experiment

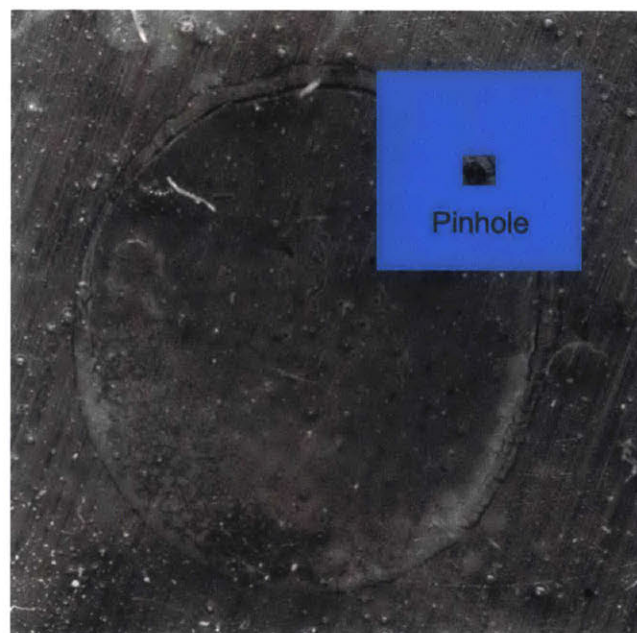


Figure 11.2: An example of looking at the "hot spot" area

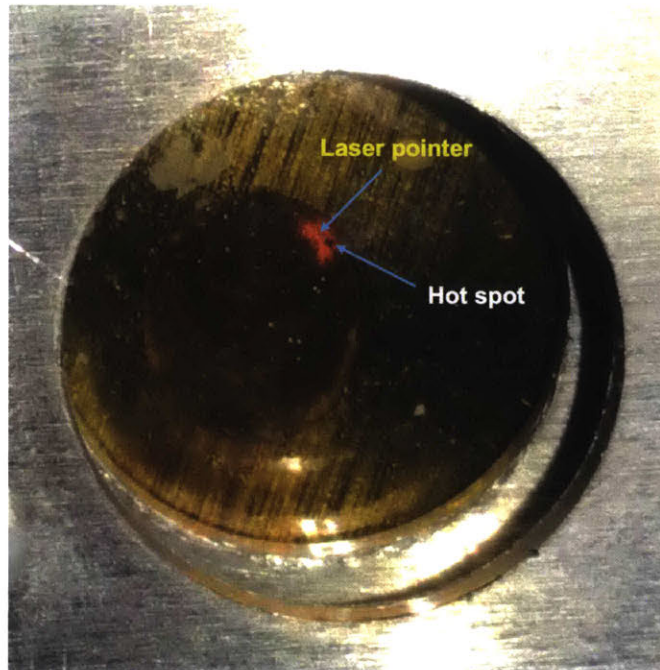


Figure 11.3: First pinhole/SDD experiment

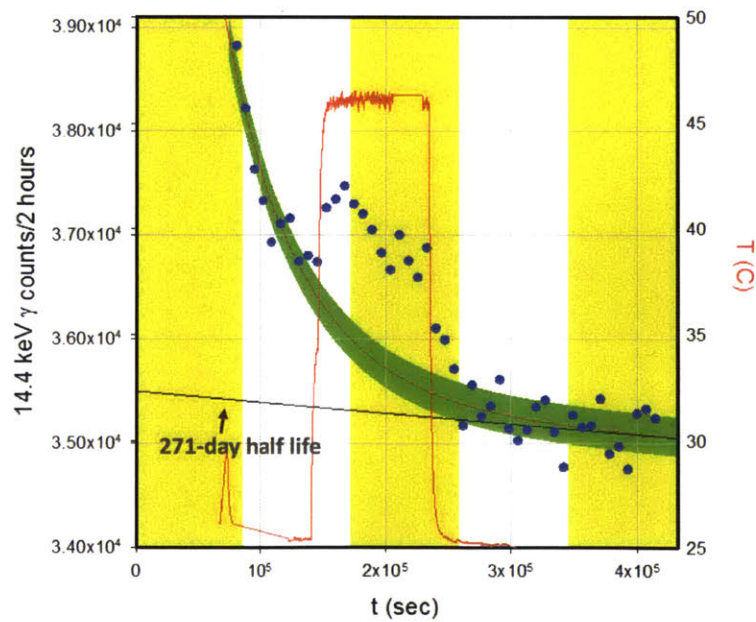


Figure 11.4: Time history of 14.4 keV for the first pinhole/SDD experiment

Figure 11.5 shows another pinhole/SDD experiment looking at an area on the ring away from the “hot spot.” We aligned the pinhole with the red laser point to analyze that area. Figure 11.6

shows the time history of 14.4 keV for this area. The signals slightly decrease when the temperature increases. Again there is a transient due to stress at the beginning of the experiment.

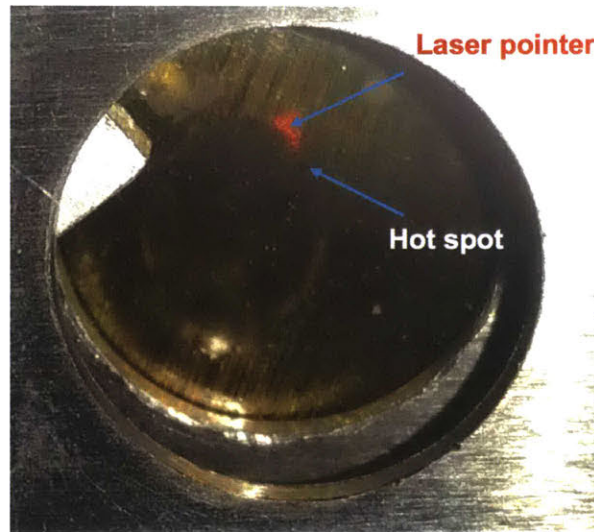


Figure 11.5: Pinhole/SDD experiment looking at an area on the ring sway from “hot spot”

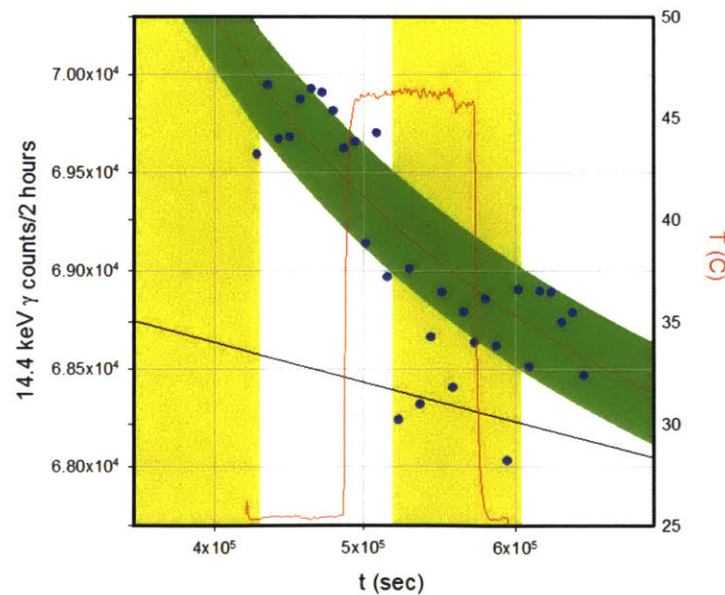


Figure 11.6: Time history of 14.4 keV for an area on the ring far from “hot spot”

At this point, we realized that only relying on laser point for alignment was not accurate. In the following experiments, we used laser pointer for rough alignment. For fine alignment, we

scanned the pinhole to get localized maximum signal counts in the SDD to make sure we were hitting at the target point. With this new method, we experimented again looking at the same area in Figure 11.5. Figure 11.7 shows the time history of Fe K-alpha and 14.4 keV for this experiment. Both signals increase when the temperature increases. There is a weaker transient due to stress at the beginning of the experiment for both lines.

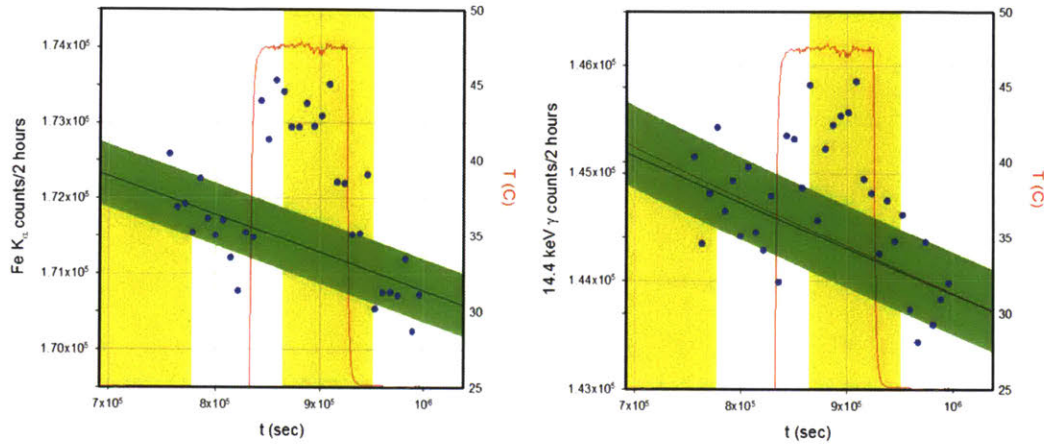


Figure 11.7: Time history of Fe K-alpha and 14.4 keV for ring area in Figure 11.5 with fine alignment

Figure 11.8 shows another pinhole/SDD experiment with fine alignment looking at another ring area away from the “hot spot” in the opposite direction. Figure 11.9 shows the time history of Fe K-alpha and 14.4 keV for this experiment. There is a minor increase in the intensity in response to the thermal pulse, but with weak statistical significance.

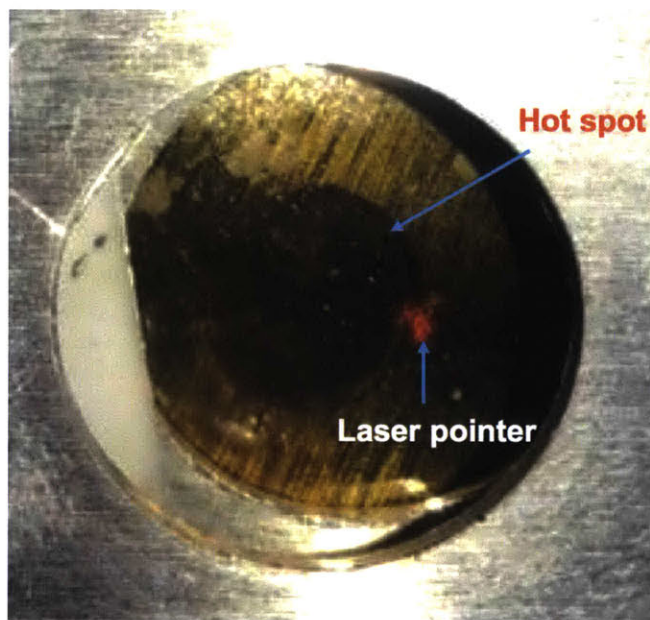


Figure 11.8: Pinhole/SDD experiment looking at another ring area away from “hot spot”

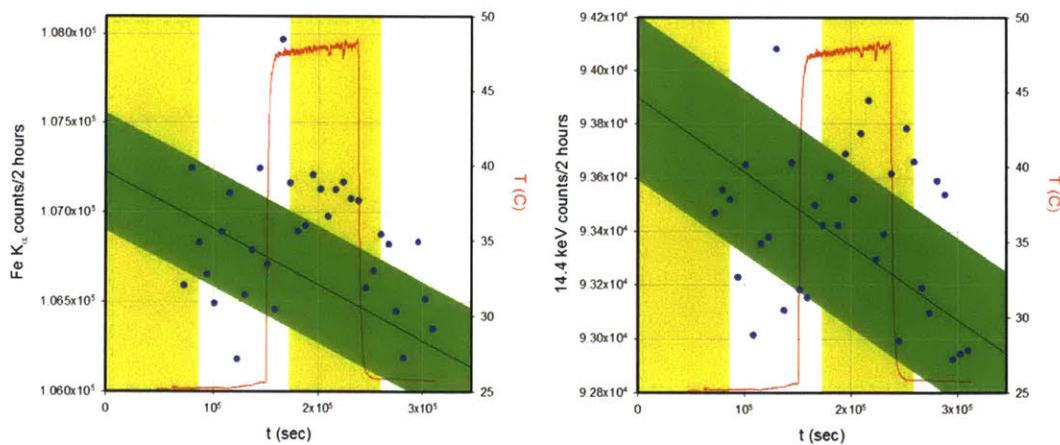


Figure 11.9: Time history of Fe K-alpha and 14.4 keV for ring area in figure 11.8

From above experiments, we see that the Pinhole/SDD experiment enables us to analyze the time history for all locations on the Co-57 source. With the new alignment method, we located the “hot spot” by signal optimization and looked at the “hot spot” again.

Figure 11.10 shows the time history of Fe K-alpha and 14.4 keV in an experiment on the “hot spot” when the temperature reached around 78 C. Both lines increase about 1-2% when the temperature increases. Figure 11.11 shows the time history of 122 keV and Sn K-alpha in this

experiment. There is no or little response to the heat pulse for both 122 keV and Sn K-alpha. The results of this experiment are consistent with the conjecture that delocalization occurs at Co-57 14.4 keV excited state but does not occur at Co-57 136 excited state. We will talk more about this conjecture in the following chapter.

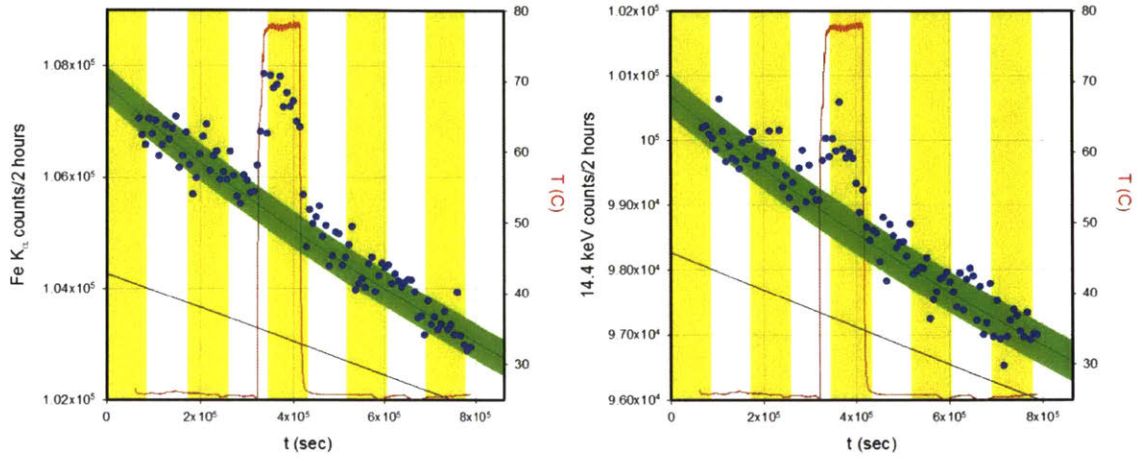


Figure 11.10: Time history of Fe K-alpha and 14.4 keV for "hot spot" with heat pulse reaching 78C

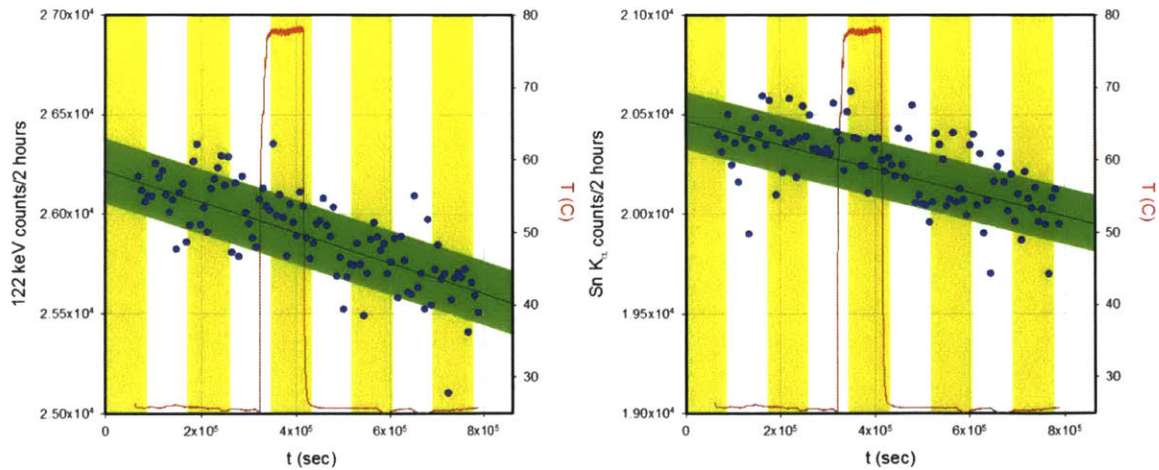


Figure 11.11: Time history of Fe 122 keV and Sn K-alpha for "hot spot" with heat pulse reaching 78C

To make sure the "hot spot" result is reproducible, we did more than one pinhole/SDD experiment on the "hot spot." Figure 11.12 shows the time history of Fe K-alpha and 14.4 keV in another experiment on the "hot spot" when the temperature reached around 44 C. In this

experiment we turned on the heat pulse for two times. We lost temperature data during the first heat pulse period. In Figure 11.12, we use the temperature data during the second heat pulse period to represent the temperature data for the first heat pulse. There is a significant signal increase in response to heat pulse for both the Fe K-alpha and 14.4 keV line in this experiment, which is the biggest unit response per unit temperature so far (3-4% signal increase with 20 C temperature increase). The decay rate after the second heat pulse is slower than that after the first heat pulse. The second heat pulse was turned on before the sample fully relaxed after the first heat pulse.

As discussed before, the signal increase is around 3-4% with temperature increased to 44 C in this experiment. While in the previous run the signal increase is around 1-2% with temperature increased to 78 C. We did not get the same unit per temperature result in these two runs. This was in part because we were not looking at the same locations on the “hot spot.” We tried to maximize the SDD signal by scanning the pinhole before we started both the experiments. However, the signal counts for the 78 C run was 12% less than the signal counts for the 44 C run.

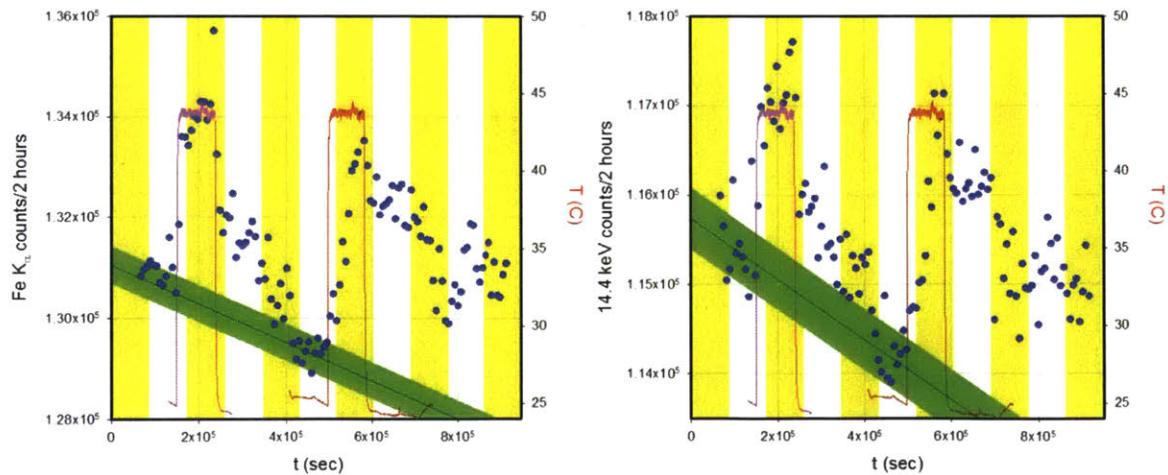


Figure 11.12: Time history of Fe K-alpha and 14.4 keV for “hot spot” with heat pulse reaching 44C

We also did a SDD experiment looking at the whole Co-57 source without any pinhole. For Sample 2 we saw a reduction in the emission for this kind of test, which suggested excitation

transfer into the steel; we are interested in what we might see for sample Sample 1. We know that Sample 1 and Sample 2 behave differently, perhaps due to the hot spot, perhaps for other reasons.

Figure 11.13 shows the time history of Fe K-alpha and 14.4 keV in this experiment without any pinhole when the temperature reached around 44 C. There is around 1% increase in the Fe K-alpha line and a smaller 0.3% increase in the 14.4 keV line. This experiment gives a result different than for Sample 2 and not easy to understand. Increases seen in the 14.4 keV gamma and in the Fe K-alpha look bigger than what would be expected due to changes in air absorption. Occupation of off-resonant states could increase the Fe K-alpha, but would expect a decrease in the 14.4 keV emission. The best interpretation so far is that the increase in Fe K-alpha is due to off-resonant state occupation, and the increase in 14.4 keV might be the first time we see a weak angular anisotropy effect for the 14.4 keV gamma.

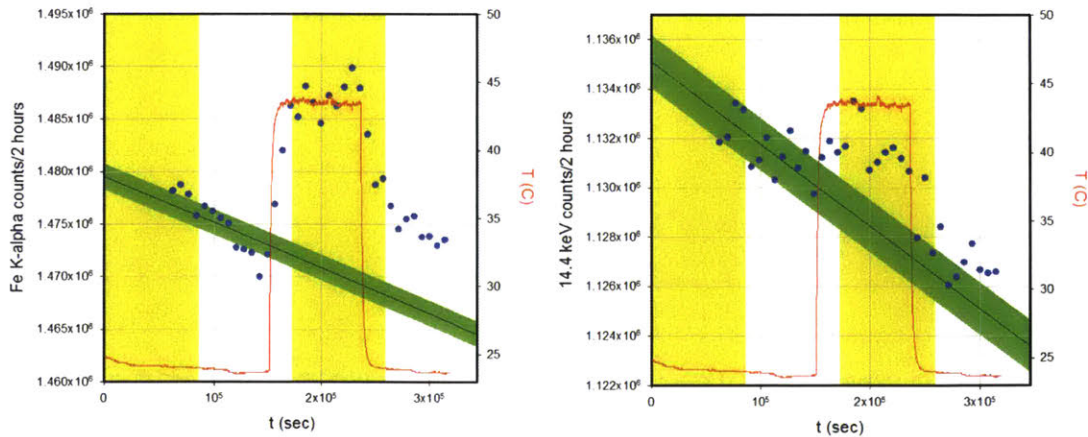


Figure 11.12: Time history of Fe K-alpha and 14.4 keV without any pinhole

The pinhole/SDD experiment provides us a powerful tool to systematically explore local emission. It gives us a way to analyze what is really going on. We see signal increase at some locations and decrease at others in response to heat pulse. The “hot spot” result is with good

reproducibility. We always see signal increase in response to heat pulse at “hot spot.” The observations in the pinhole/SDD experiments support our delocalization conjecture.

The experiment introduced in this chapter is done by me. All data shown in this chapter is taken by me and analyzed by Hagelstein.

12 Interpretations

An important question for the delocalization scenario is where the excitation transfer moves from and where it moves to. The above experimental results offer us some answers. As shown in Figure 12.1, excitation transfer can move from Co-57 residue to steel plate. The residue contains $^{57}\text{CoCl}_2$ and Fe-57. There is around 2.1% Fe-57 in stainless steel. One evidence supporting this picture is that in the May 20 experiment we saw a slight signal decrease when we removed the aluminum mesh for Sample 2. Excitation moving into the steel can happen both for the angular anisotropy effect and for the delocalization effect, however, probably only a small part of the excitation goes into the steel.

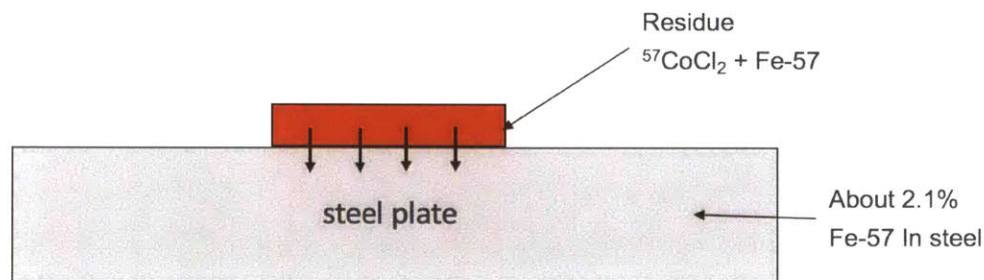


Figure 12.1: Excitation transfer goes from residue into the steel

The more dominant process is shown in Figure 12.2. Excitation transfer moves inside residue. Strong evidence is that in the pinhole/SDD experiments we see signal increase at some locations and decrease at others in response to heat pulse.

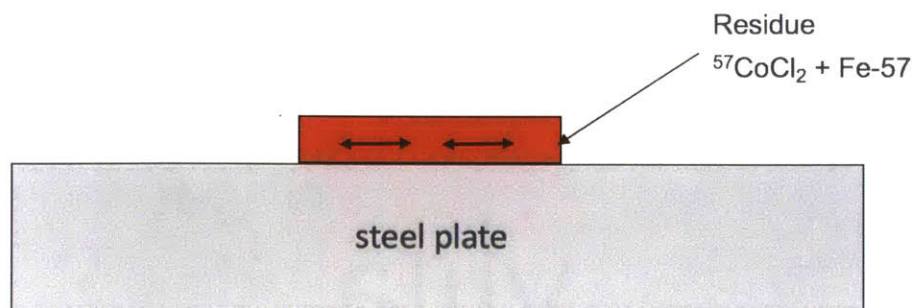


Figure 12.2: Excitation transfer moves inside residue

The pinhole/film experiment tells us that the Co-57 residue is not uniform. There are some parts of the residue with lots of Fe-57 such as the “hot spot.” There are some other parts of the residue with less Fe-57. In the pinhole/SDD experiments on the “hot spot,” we always see signal increase in response to heat pulse. This indicates that delocalization moves from locations with less Fe-57 to locations with more Fe-57. Figure 12.3 shows this process. Excitation transfer wants to go where there is more Fe-57. Figure 12.4 shows where delocalization travels in the pinhole/SDD experiment on the “hot spot.” Delocalization moves from surrounding ring areas with less Fe-57 to the “hot spot” with more Fe-57.

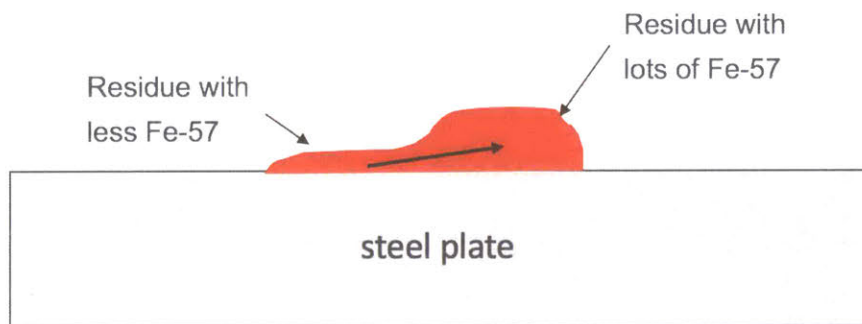


Figure 12.3: Excitation transfer wants to go where there is more Fe-57

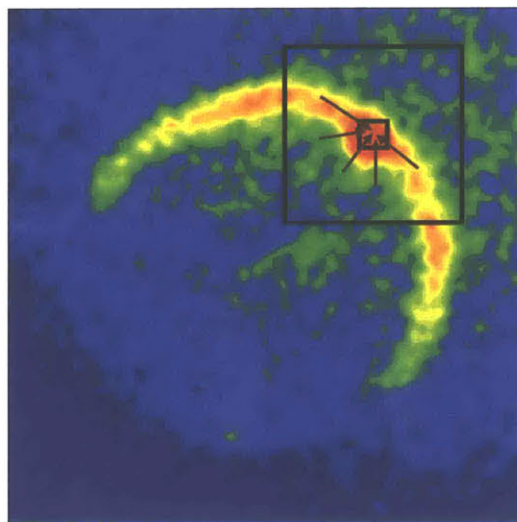


Figure 12.4: Delocalization moves from surrounding ring areas to the “hot spot”

There are important issues concerning how THz phonons are created in our experiments. This has been discussed previously in the JCMNS paper on May 20 experiment,¹ and here we review briefly the basic picture and related notions. We would expect substantial compressional stress in the steel plate between the wood blocks, and also within the wood, due to the tightening of the steel bolts. Under stress creep occurs in wood²⁻⁴ and in steel,⁵⁻⁷ and we would expect local generation of THz vibrations near the wood clamps (see Figure 12.5). However, THz vibrations are very lossy, and we would not expect vibrations with frequencies above about 10 MHz to be able to transport from the vicinity of the clamps to where the Co-57 residue is.⁸⁻¹⁰

Consequently, the question arises as to how THz phonons can be generated in the vicinity of the residue. Two possible mechanisms are worth consideration (see Figure 12.6). One concerns THz generation in the steel itself in the vicinity of the residue. We would expect shear stress in the steel over a range of a few times the plate thickness (about 4 mm), and we know that shear stress leads to a force on linear dislocations,¹¹ that cause them to move. When linear dislocations move they can radiate THz phonons, and also scatter them.¹²⁻¹⁵ This provides a mechanism for producing a non-thermal distribution of THz phonons in the steel at the location of the residue. The other mechanism is friction between the residue, and the steel underneath, as well as the epoxy above, caused by strain in the steel and epoxy in the vicinity of the residue.

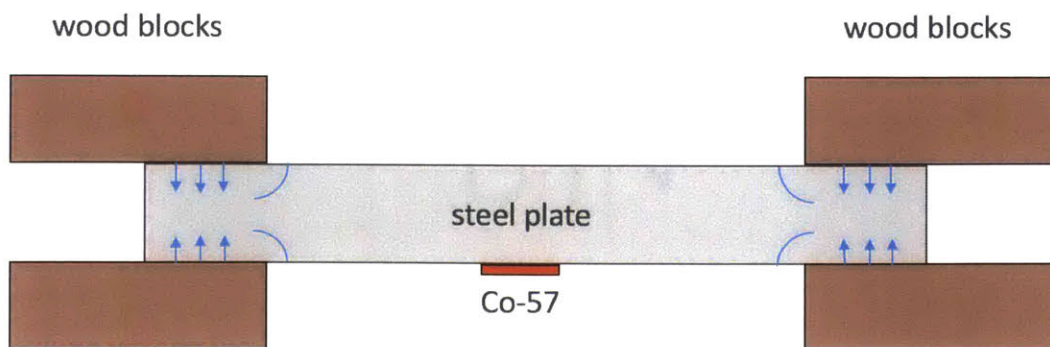


Figure 12.5: Wood clamping and stress

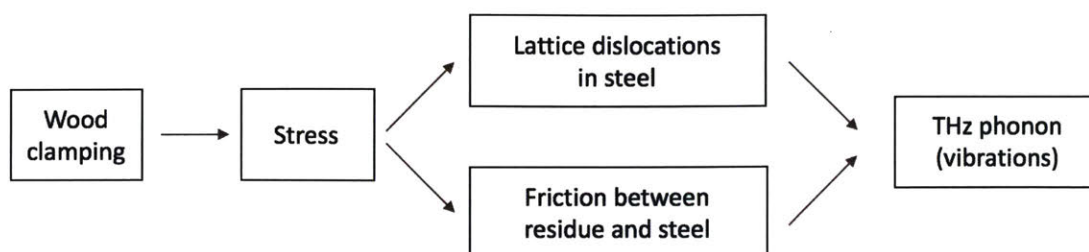


Figure 12.6: Connection between wood clamping and THz phonon vibrations around Co-57

Figure 12.7 summarizes the connection between THz phonon vibrations and effects seen in our experiments. As shown in the upper path, THz phonons can cause slow excitation transfer for Co-57 136 keV excited state. This process is dominated by resonant excitation transfer which can cause phase coherence. This process finally leads to the angular anisotropy effect.

As shown in the lower path, THz phonon can cause fast excitation transfer for Co-57 14.4 keV excited state. This process is dominated by non-resonant excitation transfer which cannot cause phase coherence. This process finally leads to the delocalization effect.

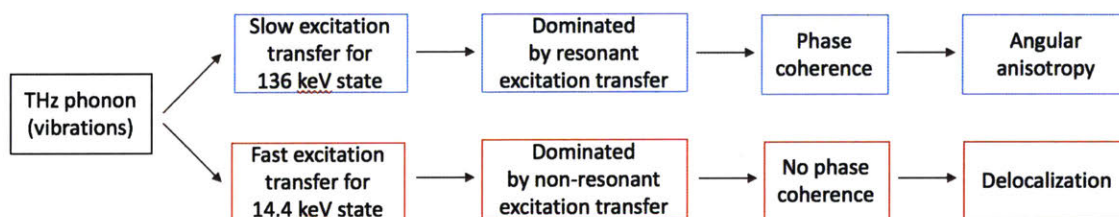


Figure 12.7: Connection between THz phonon vibrations and effects seen in experiments

The interpretations covered in this chapter are based on our experimental results and Professor Hagelstein's theory. Much input to this chapter was provided by Hagelstein.

References

1 Metzler, F., Hagelstein, P., & Lu, S. (in press). Observation of Non-exponential Decay in X-ray and γ Emission Lines from Co-57. *Journal of Condensed Matter Nuclear Science*.

2. Gressel, P. (1972). Untersuchungen ber das Zeitstandbiegeverhalten von Holzwerkstoffen in Abhngigkeit von Klima und Belastung. *European Journal of Wood and Wood Products*, 30, 347-355.
3. Smulski, S. (1989). Creep functions for wood composite materials. *Wood and Fiber Science*, 21, 45.
4. Lyon, D., & Schniewind, A. (2007). Prediction of creep in plywood Part I. Prediction models for creep in plywood. *Wood and Fiber Science*, 10, 28-38.
5. Cuddy, L. J. (1970). Internal stresses and structures developed during creep. *Metallurgical and Materials Transactions B*, 1(2), 395-401. doi:10.1007/bf02811548
6. Krempl, E. (1979). An experimental study of room-temperature rate-sensitivity, creep and relaxation of AISI type 304 stainless steel. *Journal of the Mechanics and Physics of Solids*, 27(5-6), 363-375.
doi:10.1016/0022-5096(79)90020-6
7. Deibler, L. A. (2014). Room temperature creep in metals and alloys. *Sandia National Lab Report*, No.SAND2014-17935. doi:10.2172/1323556
8. Roderick, R. L., & Truell, R. (1952). The Measurement of Ultrasonic Attenuation in Solids by the Pulse Technique and Some Results in Steel. *Journal of Applied Physics*, 23(2), 267-279. doi:10.1063/1.1702187
9. Kamigaki, K. (1957). Ultrasonic attenuation in steel and cast iron. *Science Reports of the Research Institutes, Tohoku University. Ser. A, Physics, Chemistry and Metallurgy*, 9, 48-77.
10. Aussel, J., & Monchalain, J. (1989). Measurement of ultrasound attenuation by laser ultrasonics. *Journal of Applied Physics*, 65, 2918-2922.
11. Peach, M., & Koehler, J. S. (1950). The Forces Exerted on Dislocations and the Stress Fields Produced by Them. *Physical Review*, 80(3), 436-439. doi:10.1103/physrev.80.436
12. Marian, J., & Caro, A. (2006). Moving dislocations in disordered alloys: Connecting continuum and discrete models with atomistic simulations. *Physical Review B*, 74(2), 024113.
doi:10.1103/physrevb.74.024113

13. Lothe, J. (1962). Theory of Dislocation Mobility in Pure Slip. *Journal of Applied Physics*, 33(6), 2116-2125. doi:10.1063/1.1728907
14. Eshelby, J. (1962). The interaction of kinks and elastic waves. *Proc. Royal Soc. (London). Series A, Mathematical and Physical Sciences*, A266, 222-246.
15. Hikata, A., Johnson, R. A., & Elbaum, C. (1970). Interaction of Dislocations with Electrons and with Phonons. *Physical Review Letters*, 24(5), 215-218. doi:10.1103/physrevlett.24.215

13 Summaries, Conclusions, and Future Work

The research reported in this thesis was motivated in part by the many anomalies that have been reported as discussed in the Introduction, and specific examples involving collimated x-ray emission reviewed in Chapter 2, and in part by the phonon-nuclear coupling approach pioneered by Hagelstein, and by Hagelstein and Chaudhary. The theoretical approach provides a framework through which most of the anomalies might be accounted for systematically, and has the potential to move the field of Condensed Matter Nuclear Science closer to acceptance by the mainstream scientific community. As discussed in the Introduction, what has been needed is feedback from experiment -- specifically from focused experiments that permit an unambiguous interpretation. There have certainly been experiments reported earlier for which anomalies of one sort or another have been claimed, and for which interpretations are possible in terms of the theory under consideration. However, in most cases the experiments are sufficiently complicated that a unique interpretation is at present elusive.

In the early days of my research, the immediate goal was to develop a well controlled experiment in which samples were vibrated and collimated x-rays produced. The successful demonstration of such an effect, had we been successful, would have constituted a substantial step forward in connecting theory to experiment. Documentation of some of this effort has been included in the Appendixes; including the discussion of the waterjet experiments, resonator experiments, and mercury deposition. Unfortunately, we did not achieve this goal. While unfortunate, this is a feature of an emerging field where a clarification of the underlying science has not yet been achieved. In the field of Condensed Matter Nuclear Science, there have been a great many research efforts that have not succeeded, including earlier experimental efforts at MIT in the 1990s. Research in an emerging field carries risks, and one of the risks is that things may not work in the lab as hoped.

It cannot be overemphasized how important the May 2017 excitation transfer experiment has been to our research effort. This experiment is important in that it worked, the effect/anomaly was reproducible, and that it worked within an experimental configuration intended to test for excitation transfer. As a result, it was plausible that what we were seeing could be understood in terms of excitation transfer as a result of phonon-nuclear coupling. What was needed was a clarification of how and why we were seeing a non-exponential decay effect.

In the weeks and months following the experiment a variety of hypothesis were contemplated, including the possibility that we might be seeing a subdivision effect (in which a highly-excited state made a transition to the ground state, resulting in several other nuclei being promoted from the ground state to the lowest excited state), or perhaps up-conversion. In time we evolved to a scenario involving more basic mechanisms, including (weak) resonant excitation transfer to establish phase coherence leading to angular anisotropy, and including (strong) excitation transfer leading to a macroscopic delocalization of the excitation. This evolution was driven in part by the accumulation of data from many experiments, and through a process of discarding ideas which were not in agreement with the data or else could be dispensed with based on theoretical arguments.

Although much research was done in connection with this thesis research, it may be that the most significant results came late in the effort, in part due to encouragement by the committee to make sure to come away with some unambiguous positive experimental results. These are worth considering specifically here.

My study of the angular anisotropy effect seen for the harder gammas was the first attempt at a systematic study of the effect. Prior to this research we were not certain that Sample 2 was active (Sample 1 had shown dynamics on the harder gammas which are interpreted currently as due to angular anisotropy), and from my experiments we have some confidence that it is active. Sample 2 was developed in part to achieve a faster relaxation time, which was important in late

2017 as the experiments of that time took weeks to complete. In my experiments a fast response (one the order of 10 minutes) was found, which was the first time such a fast response was seen for a plate (Metzler has observed earlier a fast response by accident in an experiment with a calibration source that had been inadvertently stressed). This fast response could be reproduced, as can be seen in the data reported in this thesis. Initially we thought that simply by tightening the bolts on the wood clamps that a non-exponential decay could be observed. I found that more subtle stimulations could be important, that a fast response could be obtained when the sample was moved to the detector after resting in a different configuration (see Appendix J). This is a preliminary observation, as we were not able to determine from the experiments precisely what stress was responsible for producing the effect -- this remains for future studies.

The connection between theory and experiment in this case is worth some consideration. Had the excitation transfer experiment responded to the MHz transducer, we would have been pretty sure that we were seeing a phonon-induced excitation transfer effect. However, the effects which we see instead arise from stressing the sample, which permits the interpretation of phonon-induced excitation transfer due to high frequency THz vibrations. A weakness of the approach is that we have no direct measurement of any THz vibrations in these experiments, and we do not have a controllable source to provide for THz vibrational stimulation on demand. We see non-exponential decay effects in the harder gammas in response to stress stimulation, which based on theoretical arguments can only be due to angular anisotropy. However, in the experiments done so far there is not a systematic study of the dynamical strength of the emission at different angles (however, in the May 20 experiment the back side Geiger counter shows an early enhancement, and the scintillator/PMT shows an early reduction, which is consistent with angular anisotropy). The pinhole/film data taken with the 0.2 mm pinhole shows a broad enhancement, which may be due to angular anisotropy (less likely is the possibility of increased film sensitivity at elevated temperature).¹⁻³ These preliminary observations will need to be followed up in the future to provide clarification. In general, the angular anisotropy experiments

are particularly important as they have the potential to provide unambiguous evidence for phase coherence and phonon-nuclear coupling.

The first pinhole and film experiments provided some clarification of where the emission was coming from. Previously we had contact images with poor spatial resolution which seemed to indicate that x-ray emission was uniform within the circular evaporation region. In the first pinhole/film experiments we saw that the emission was strongest from the ring around the circle (which in retrospect should have been obvious from experience with rings formed in coffee stains). The first sample has a pronounced "hot spot" near the ring where the emission is stronger than elsewhere, with a corresponding "dark spot" apparent in the optical image. The second sample has weaker "hot spots".

I was the lead experimentalist for the live run with the pinhole and film experiment. We first tried an experiment with the 0.5 mm pinhole, which traded off spatial resolution for better signal to noise ratio. We see subtle differences between the hot image and the prior cold image, which might be due to a delocalization of the nuclear excitation, or might be due to noise or thermal effects. This experiment is important since we previously did not know whether there was a strong or a weak delocalization effect. To account for the large effect seen in the May 20 experiment, models based on circle or ring emission would require mm-scale delocalization to produce a nearly 20% effect through the coarse mesh. However, it was clear from the pinhole/film experiment that we were not seeing a spreading of the ring on the mm-scale, or a filling in of the circle (which were leading pictures prior to the experiment). A second experiment was run with the 0.2 mm pinhole and film. In this case technical constraints placed limitations on the temperature increase (we could only go up 25 C), and we faced much bigger signal to noise issues. In this experiment there was no evidence for a spreading of the emission in the vicinity of the ring or "hot spot", now with higher spatial resolution (on the order of 0.2 mm).

These results, combined with some observations of a visitor Malcolm Fowler (retired from Los Alamos, who is an expert on radiation measurements and radioactive sources), have led to a new picture for what is going on in the vicinity of the Co-57. Originally the thought was to work with steel because there was Fe-57 present (at the 2.11% level assuming natural isotopic abundances), and we thought that the excitation transfer would go from near the Co-57 in the residue into the steel. In this scenario it would be reasonable for the excitation to be transferred away from the ring and "hot spot". This scenario was inconsistent with the pinhole/film measurements, and in its place a new scenario emerged. According to the revised scenario, the evaporated residue was probably nearly pure Fe-57, so that the excitation transfer would take place preferentially within the residue. In this scenario, theory would suggest that the excitation transfer would want to go to where there was the most Fe-57. This would favor excitation transfer going to the "hot spot", which is hot because it has the most Co-57 but comes with the most Fe-57 (produced from the decay of the Co-57).

The pinhole/SDD experiment and results are perhaps deserving of special consideration in connection with this discussion. While the pinhole/film x-ray images shed much light on where the emission was coming from, and was encouraging in suggesting a subtle difference between the cold and hot images, what was needed were more sensitive measurements capable of determining at the percent level or better changes in the local emission in response to thermal or stress triggers. The basic idea was to make use of the Amptek SDD to monitor emission from a local region, ideally with a specially designed pinhole optimized to pass low energy x-rays to the closely positioned detector. Keeping the detector cool in the presence of a heat pulse was a primarily technical issue, which was solved with the help of Metzler who fielded thermoelectric coolers on an aluminum bar with a hole for transmission. Even so, the detector had to be a few cm away for safety reasons, so much of the transmitted signal was lost. We made use of the SDD over the X-123 detector due to the larger detector area and hence higher efficiency of the SDD. It

was fortuitous that we were able to get good results from the very first of these experiments, discussed above in Chapter 11.

The demonstration of the ability to measure time histories accurate to better than 1% for a localized (1 mm diameter) region is a major research result (there were no guarantees that this was possible). In the modest number of experiments of this type that were done it has become clear that we can see substantial non-exponential dynamics, with some reproducibility, from localized regions that we chose to inspect. From the results obtained so far we have evidence that emission from the "hot spot" is increased with the application of a thermal pulse, and we have seen the largest enhancement of the signal per unit temperature from the "hot spot". A weak reduction of emission from one region was seen as well, suggesting that excitation may be going from one part of the residue to another. The results so far are supportive of the delocalization scenario, in which excitation transfer moves nuclear excitation within the residue following the Fe-57. More certainty would be possible were we able to measure how much Fe-57 is in the residue, and if we could monitor the levels of THz vibrations.

Members of the committee were interested in the question of whether the experiments so far have succeeded in proving, or in disproving, the phonon theory under consideration. Things would have been simpler and clearer had the MHz version of the excitation transfer experiment given a clear positive signal. With non-exponential dynamics showing up in the x-ray and gamma ray lines in response to stress, the situation becomes complicated. The good news is that we are able to study the anomalies now with improved experiments, and with better associated scenarios. The hoped for unambiguous experimental demonstration of a phonon-nuclear coupling effect will probably require a new kind of experiment in which THz phonons are produced in a controlled way, measured, and their effects on the nuclear system observed at the same time. Based on the experiments done so far it seems likely that anomalies can be produced with a high degree of confidence using the approaches pioneered in our group over the past year, and we need to find a way to make use of this experience to develop new and stronger

experiments. It should be noted that the presentations of research from our group at the recent international ICCF21 conference were well received, and there is much interest in our work generally, and interest specifically on the part of several groups to replicate and to extend our results.

Much input to this chapter was provided by Hagelstein.

References

- 1 Evans, C. H. (1942). The Effect of Temperature upon the Spectral Sensitivity of Photographic Emulsions. *Journal of the Optical Society of America*, 32(4), 214. doi:10.1364/josa.32.000214
- 2 Webb, J. H. (1935). The Effect of Temperature upon Reciprocity Law Failure in Photographic Exposure. *Journal of the Optical Society of America*, 25(1), 4. doi:10.1364/josa.25.000004
- 3 Berg, W. F., & Mendelssohn, K. (1938). Photographic Sensitivity and the Reciprocity Law at Low Temperatures. *Proceedings of the Royal Society A: Mathematical, Physical and Engineering Sciences*, 168(933), 168-175. doi:10.1098/rspa.1938.0167

Appendix A: Sample Model for Excitation Transfer with Loss

In Chapter 4, we have seen that in first two excitation transfer examples destructive interference limits indirect coupling, and that if a way could be found to unbalance the system, it might be possible to accelerate excitation transfer. Figure A.1 illustrates a third excitation transfer example, where phonon exchange and loss are both included. The system in this case is similar to example 2, except that a loss term is now included for all states. Phonon-electron coupling is contributing to the loss, and nuclear decays are also possible.¹⁻³

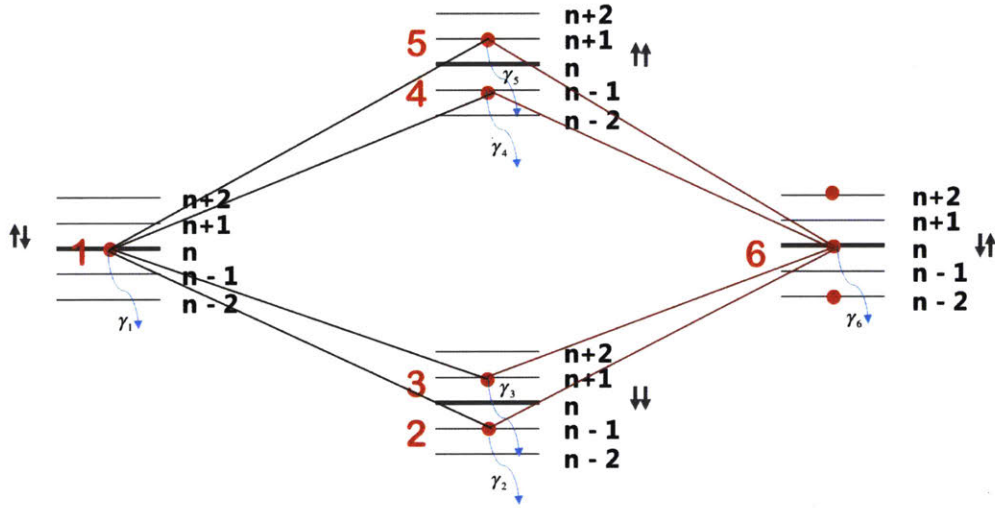


Figure A.1: The 3rd example for excitation transfer with phonon and loss

The wave function is the same as that in example 2. The finite basis equations for the coefficients can be written as¹⁻³

$$\begin{aligned}
 Ec_1 &= (\Delta E - \frac{i\hbar\gamma_1}{2} + (n + \frac{1}{2})\hbar\omega_0)c_1 + V_{12}c_2 + V_{13}c_3 + V_{14}c_4 + V_{15}c_5 \\
 Ec_2 &= (-\frac{i\hbar\gamma_2}{2} + (n - 1 + \frac{1}{2})\hbar\omega_0)c_2 + V_{21}c_1 + V_{26}c_6 \\
 Ec_3 &= (-\frac{i\hbar\gamma_3}{2} + (n + 1 + \frac{1}{2})\hbar\omega_0)c_3 + V_{31}c_1 + V_{36}c_6 \\
 Ec_4 &= (2\Delta E - \frac{i\hbar\gamma_4}{2} + (n - 1 + \frac{1}{2})\hbar\omega_0)c_4 + V_{41}c_1 + V_{46}c_6 \\
 Ec_5 &= (2\Delta E - \frac{i\hbar\gamma_5}{2} + (n + 1 + \frac{1}{2})\hbar\omega_0)c_5 + V_{51}c_1 + V_{56}c_6 \\
 Ec_6 &= (\Delta E - \frac{i\hbar\gamma_6}{2} + (n + \frac{1}{2})\hbar\omega_0)c_6 + V_{62}c_2 + V_{63}c_3 + V_{64}c_4 + V_{65}c_5
 \end{aligned} \tag{21}$$

Using the same approach as before we get the expression for V_{16} as

$$V_{16} = \frac{V_{12}V_{26}}{\Delta E + \hbar\omega_0 + i\hbar\frac{(\gamma_2 - \gamma_1)}{2}} + \frac{V_{13}V_{36}}{\Delta E - \hbar\omega_0 + i\hbar\frac{(\gamma_3 - \gamma_1)}{2}} - \frac{V_{14}V_{46}}{\Delta E - \hbar\omega_0 - i\hbar\frac{(\gamma_4 - \gamma_1)}{2}} - \frac{V_{15}V_{56}}{\Delta E + \hbar\omega_0 - i\hbar\frac{(\gamma_5 - \gamma_1)}{2}} \quad (22)$$

In writing this, we assume that $\gamma_1 = \gamma_6$. The indirect coupling term V_{16} simplifies to¹⁻³

$$V_{16} = V_0^2 \left(\frac{n}{\Delta E + \hbar\omega_0 + i\hbar\frac{(\gamma_2 - \gamma_1)}{2}} + \frac{n+1}{\Delta E - \hbar\omega_0 + i\hbar\frac{(\gamma_3 - \gamma_1)}{2}} - \frac{n}{\Delta E - \hbar\omega_0 - i\hbar\frac{(\gamma_4 - \gamma_1)}{2}} - \frac{n+1}{\Delta E + \hbar\omega_0 - i\hbar\frac{(\gamma_5 - \gamma_1)}{2}} \right) \quad (23)$$

We can see in this that the destructive interference can be reduced if the loss terms are important and if the off-resonant loss is different from the loss on resonance. For example, the situation is qualitatively similar in the lattice case where n can be very large, where the coupling can be very strong, and where states very far off of resonance contribute. In this case, the loss for basis states with energies greater than E can be much less than the loss for basis states with energies less than E .¹⁻³

Returning to the case of the molecule, we can use a first order Taylor series expansion to obtain

$$V_{16} \approx \frac{V_0^2}{\Delta E^2} \left(-i\hbar \left(n + \frac{1}{2} \right) \frac{(\gamma_2 + \gamma_3 + \gamma_4 + \gamma_5)}{2} + 2\hbar\omega_0 \right) \quad (24)$$

For the molecular problem the loss terms are small; however, in the closely related lattice version of the problem n can be very large so the loss can be much more important.¹⁻³

The notion that dephasing or loss can impact the rate for excitation transfer has recently been considered in biophysics,⁴⁻⁵ making use of a density matrix approach.

All the materials reviewed in this appendix are directly from or based on Hagelstein's theory.

References

- 1 Hagelstein, P. (2016). Quantum Composites: A Review, and New Results for Models for Condensed Matter Nuclear Science. *Journal of Condensed Matter Nuclear Science*, 20, 139-225.
- 2 Hagelstein, P., & Chaudhary, I. Possibility of observing a center of mass interaction in a Mossbauer experiment. Manuscript unpublished.

3 Hagelstein, P., & Chaudhary, I. (2011). Energy Exchange In The Lossy Spin-Boson Model. *Journal of Condensed Matter Nuclear Science*, 5, 52-71.

4 Mohseni, M., Rebentrost, P., Lloyd, S., & Aspuru-Guzik, A. (2008). Environment-assisted quantum walks in photosynthetic energy transfer. *The Journal of Chemical Physics*, 129(17), 174106.
doi:10.1063/1.3002335

5 Plenio, M. B., & Huelga, S. F. (2008). Dephasing-assisted transport: Quantum networks and biomolecules. *New Journal of Physics*, 10(11), 113019. doi:10.1088/1367-2630/10/11/113019

Appendix B: Conjecture to Explain the Karabut and Kornilova Experiment

Up-conversion is proposed to account for the anomaly in the Karabut experiment¹ and the Kornilova experiment.² The concept is illustrated in the case of a low-energy nuclear transition in Fe-57 in Figure B.1, in which a great many low energy vibrational quanta are up-converted to promote population from the ground state to the first excited state.³⁻⁷

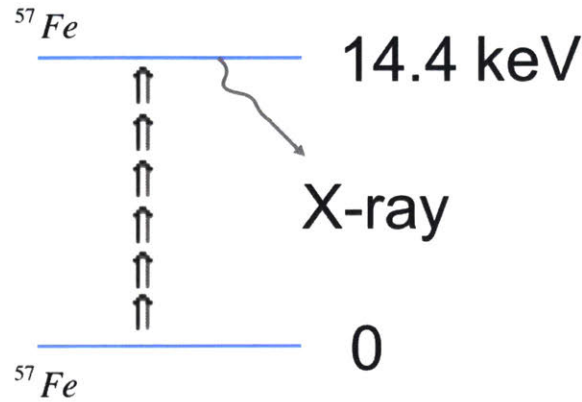


Figure B.1: Up-conversion process for ^{57}Fe ³⁻⁷

The discharge in the Karabut experiment generates high frequency vibrations in steel in the vacuum chamber. High pressure water flow in the Kornilova experiment generates ultrasound in the air which results in vibrations in the steel. We might expect Fe-57 nuclei in steel to be excited through up-conversion resulting in x-ray emission near 14.4 keV, in the absence of other effects. However, in both Karabut and Kornilova experiment, emissions are observed instead near 1.7 keV, and not at 14.4 keV.^{1,2} While the 14.4 keV transition is one of the lower energy nuclear transitions, the lowest excited nuclear state of all stable nuclei occurs in ^{201}Hg at 1565 eV. Some theoretical notions will be discussed in the following section. According to models in which two different sets of two-level systems are coupled to a common highly-excited oscillator, the up-conversion requires many nuclei containing a low-energy nuclear transition; however, excitation transfer from incomplete excitation to a small number of impurity nuclei with a lower energy transition is predicted. This is illustrated in Figure B.2. We propose that ^{201}Hg is contaminated in both Karabut

and Kornilova experiment. Up-conversion is initiated at Fe-57 but does not go up all the way to 14.4 keV. Instead, up-conversion is transferred to ^{201}Hg .³⁻⁷

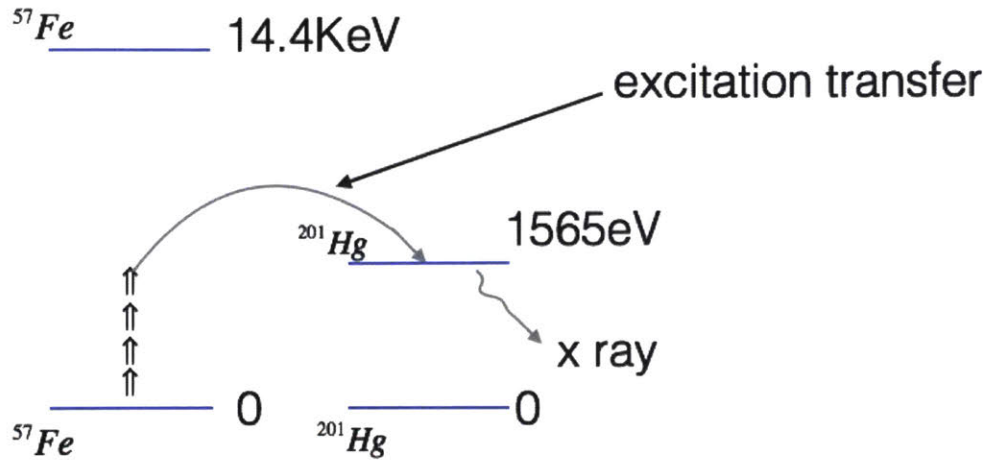


Figure B.2: Our up-conversion conjecture for Karabut and Kornilova experiment³⁻⁷

We have seen that loss has the potential to reduce the destructive interference for excitation transfer. The two-nucleus example selected here is useful because it allows us to examine the impact of loss simply. In the lattice version of the problem, more nuclei are involved and the coupling is much stronger; however, in this case, destructive interference limits the indirect coupling with the absence of loss, and the impact of loss becomes much greater.³⁻⁷

All the materials reviewed in this appendix are directly from or based on Hagelstein's theory and conjecture.

References

- 1 Karabut, A., Karabut, E., & Hagelstein, P. (2012). Spectral and Temporal Characteristics of X-ray Emission from Metal Electrodes in a High-current Glow Discharge. *Journal of Condensed Matter Nuclear Science*, 6, 217-240.
- 2 Kornilova, A. A., Vysotskii, V. I., Sysoev, N. N., Litvin, N. K., Tomak, V. I., & Barzov, A. A. (2010). Generation of intense x-rays during ejection of a fast water jet from a metal channel to

atmosphere. *Journal of Surface Investigation. X-ray, Synchrotron and Neutron Techniques*, 4(6), 1008-1017. doi:10.1134/s1027451010060224

3 Hagelstein, P. (2016). Quantum Composites: A Review, and New Results for Models for Condensed Matter Nuclear Science. *Journal of Condensed Matter Nuclear Science*, 20, 139-225.

4 Hagelstein, P., & Chaudhary, I. Possibility of observing a center of mass interaction in a Mossbauer experiment. Manuscript unpublished.

5 Hagelstein, P., & Chaudhary, I. (2011). Energy Exchange In The Lossy Spin-Boson Model. *Journal of Condensed Matter Nuclear Science*, 5, 52-71.

6 Hagelstein, P. (2015). Directional X-ray and gamma emission in experiments in condensed matter nuclear science. *Current Science*, 108(4), 601-607.

7 Hagelstein, P., & Chaudhary, I. (2015). Phonon models for anomalies in condensed matter nuclear science. *Current Science*, 108(4), 507-513.

Appendix C: Up-conversion and Down-conversion

In this section we discuss Hagelstein's theory of up-conversion and down-conversion. We recall that the Hamiltonian for nuclei in a lattice including the relativistic interaction between center of mass motion and internal nuclear degrees of freedom is¹⁻³

$$\hat{H} = \sum_j \frac{|\hat{\mathbf{p}}_j|^2}{2M_j} + \sum_{j < k} V(\mathbf{R}_j - \mathbf{R}_k) + \sum_j \mathbf{M}_j c^2 + \sum_j \mathbf{a}_j \cdot c \hat{\mathbf{p}}_j \quad (25)$$

We can quantize the vibrations and make two-level system approximations according to¹⁻³

$$\sum_j \frac{|\hat{\mathbf{p}}_j|^2}{2M_j} + \sum_{j < k} V(\bar{\mathbf{R}}_j - \bar{\mathbf{R}}_k) \rightarrow \hbar \omega_0 \hat{a}^+ \hat{a} \quad (26)$$

$$\sum_j \mathbf{M}_j c^2 \rightarrow \frac{\Delta E}{\hbar} \hat{S}_z \quad (27)$$

$$\sum_j \mathbf{a}_j \cdot c \hat{\mathbf{p}}_j \rightarrow V_0 (\hat{a}^+ + \hat{a}) \frac{2\hat{S}_x}{\hbar} \quad (28)$$

In this case the more complicated nuclei and lattice problem reduces to the simpler (and well known) spin-boson model¹⁻³

$$\hat{H} = \frac{\Delta E}{\hbar} \hat{S}_z + \hbar \omega_0 \hat{a}^+ \hat{a} + V_0 (\hat{a}^+ + \hat{a}) \frac{2\hat{S}_x}{\hbar} \quad (29)$$

C.1 Multi-phonon exchange with no loss

In Figure C.1 the states associated with the lowest order three quantum exchange are shown. In this example, there is phonon exchange but no loss. State 1-6 represent six different states for a lattice with many identical nuclei inside; these are the basis states involved at lowest order in perturbation theory for indirect coupling with the exchange of three oscillator quanta. ΔE is again the transition energy for the nucleus, and the V terms are for direct coupling between the different states. As before n is the number of phonons, and m keeps track the number of excited state nuclei.¹⁻³

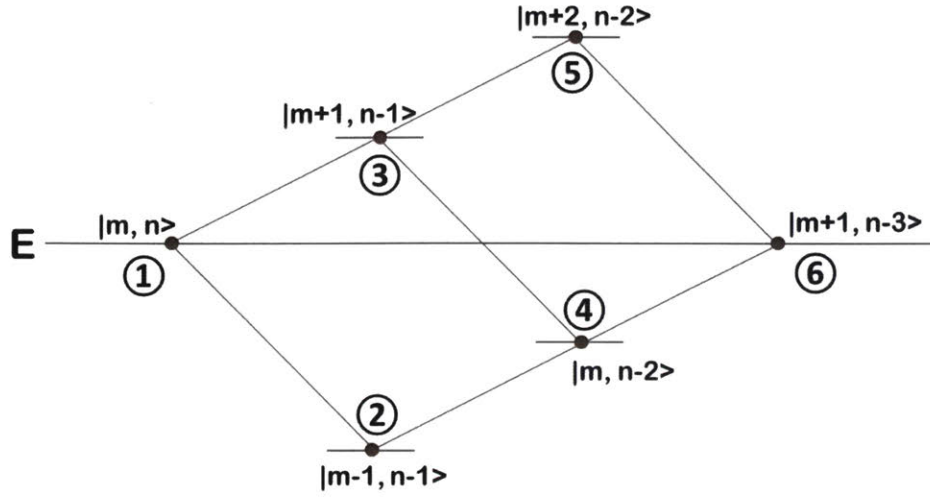


Figure C.1: An example for up-conversion with the exchange of three oscillator quanta

- For state 1, the energy of the nuclei is $m \Delta E$, and state 1 has n phonons.
- For state 2, the energy of the nuclei is $(m-1) \Delta E$, and state 2 has $n-1$ phonons.
- For state 3, the energy of the nuclei is $(m+1) \Delta E$, and state 3 has $n-1$ phonons.
- For state 4, the energy of the nuclei is $m \Delta E$, and state 4 has $n-2$ phonons.
- For state 5, the energy of the nuclei is $(m+2) \Delta E$, and state 5 has $n-2$ phonons.
- For state 6, the energy of the nuclei is $(m+1) \Delta E$, and state 6 has $n-3$ phonons.

In this example, we assume the transition energy equals the energy of three oscillator quanta.

$$\Delta E = 3\hbar\omega_0 \quad (30)$$

The total energy for state 1 equals the total energy for state 6.

$$E = m\Delta E + n\hbar\omega_0 \quad (31)$$

Up-conversion in this example means state 1 could exchange three oscillator quanta and gain one unit of excitation to couple to state 6. We are interested in whether there is coupling between state 1 and state 6, which can be understood through the indirect coupling term V_{16} .

A finite basis approximation can be developed as¹⁻³

$$\begin{aligned}
\Psi &= \sum_j c_j \phi_j \\
&= c_1 |S, m\rangle |n\rangle + c_2 |S, m-1\rangle |n-1\rangle + c_3 |S, m+1\rangle |n-1\rangle \\
&\quad + c_4 |S, m\rangle |n-2\rangle + c_5 |S, m+2\rangle |n-2\rangle + c_6 |S, m+1\rangle |n-3\rangle
\end{aligned} \tag{32}$$

The finite basis equations for the coefficients can be written as v^{1-3}

$$\begin{aligned}
Ec_1 &= (m\Delta E + n\hbar\omega_0)c_1 + V_{12}c_2 + V_{13}c_3 \\
Ec_2 &= ((m-1)\Delta E + (n-1)\hbar\omega_0)c_2 + V_{21}c_1 + V_{24}c_4 \\
Ec_3 &= ((m+1)\Delta E + (n-1)\hbar\omega_0)c_3 + V_{31}c_1 + V_{34}c_4 + V_{35}c_5 \\
Ec_4 &= (m\Delta E + (n-2)\hbar\omega_0)c_4 + V_{42}c_2 + V_{43}c_3 + V_{46}c_6 \\
Ec_5 &= ((m+2)\Delta E + (n-2)\hbar\omega_0)c_5 + V_{53}c_3 + V_{56}c_6 \\
Ec_6 &= ((m+1)\Delta E + (n-3)\hbar\omega_0)c_6 + V_{64}c_4 + V_{65}c_5
\end{aligned} \tag{33}$$

The direct coupling terms in the above equation are v^{1-3}

$$\begin{aligned}
V_{12} = V_{21} &= \langle n | \langle S, m | \hat{H} | S, m-1 \rangle | n-1 \rangle = V_0 \sqrt{n} \sqrt{(S+m)(S-m+1)} \\
V_{13} = V_{31} &= \langle n | \langle S, m | \hat{H} | S, m+1 \rangle | n-1 \rangle = V_0 \sqrt{n} \sqrt{(S-m)(S+m+1)} \\
V_{24} = V_{42} &= \langle n-1 | \langle S, m-1 | \hat{H} | S, m \rangle | n-2 \rangle = V_0 \sqrt{n-1} \sqrt{(S+m)(S-m+1)} \\
V_{34} = V_{43} &= \langle n-1 | \langle S, m+1 | \hat{H} | S, m \rangle | n-2 \rangle = V_0 \sqrt{n-1} \sqrt{(S-m)(S+m+1)} \\
V_{35} = V_{53} &= \langle n-1 | \langle S, m+1 | \hat{H} | S, m+2 \rangle | n-2 \rangle = V_0 \sqrt{n-1} \sqrt{(S-m-1)(S+m+2)} \\
V_{46} = V_{64} &= \langle n-2 | \langle S, m | \hat{H} | S, m+1 \rangle | n-3 \rangle = V_0 \sqrt{n-2} \sqrt{(S-m)(S+m+1)} \\
V_{56} = V_{65} &= \langle n-2 | \langle S, m+2 | \hat{H} | S, m+1 \rangle | n-3 \rangle = V_0 \sqrt{n-2} \sqrt{(S-m-1)(S+m+2)}
\end{aligned} \tag{34}$$

As we are interested in the indirect coupling term between state 1 and state 6, we can eliminate c_2, c_3, c_4 and c_5 to get the two level system v^{1-3}

$$E \begin{pmatrix} c_1 \\ c_6 \end{pmatrix} = \begin{pmatrix} H_{11} & V_{16} \\ V_{61} & H_{66} \end{pmatrix} \begin{pmatrix} c_1 \\ c_6 \end{pmatrix} \tag{35}$$

The indirect coupling term V_{16} is v^{1-3}

$$V_{16} = V_{61} = \frac{V_0^3 \sqrt{n(n-1)(n-2)} \sqrt{(S-m)(S+m+1)} (-16(\hbar\omega_0)^2 - V_0^2(n-1)(S+m)(S-m+1))}{64(\hbar\omega_0)^4 + V_0^4(n-1)^2(S+m)(S-m+1)(S-m-1)(S+m+2) + 16V_0^2(n-1)(\hbar\omega_0)^2} \tag{36}$$

In this example, we assume the direct coupling terms are weak so that we could use perturbation theory.¹⁻³

$$V_0 \sqrt{n} \sqrt{(S+m)(S-m)} \ll \hbar \omega_0 \quad (37)$$

We can approximate the result for V_{16} as¹⁻³

$$\begin{aligned} V_{16} = V_{61} &\approx \frac{V_0^3 \sqrt{n(n-1)(n-2)} \sqrt{(S-m)(S+m+1)} (-16(\hbar \omega_0)^2)}{64(\hbar \omega_0)^4} \\ &= -\frac{9}{4} \frac{V_0^3 \sqrt{n(n-1)(n-2)} \sqrt{(S-m)(S+m+1)}}{\Delta E^2} \end{aligned} \quad (38)$$

C.2 Summing over the different paths

The lowest-order contribution to the indirect coupling coefficient V_{16} can also be obtained by summing over the three different paths¹⁻³

$$V_{16} \approx \frac{V_{12} V_{24} V_{46}}{(E-H_2)(E-H_4)} + \frac{V_{13} V_{34} V_{46}}{(E-H_3)(E-H_4)} + \frac{V_{13} V_{35} V_{56}}{(E-H_3)(E-H_5)} \quad (39)$$

The value for the 1st path 1-2-4-6 is

$$\frac{V_{12} V_{24} V_{46}}{(E-H_2)(E-H_4)} = -\frac{9}{4} \frac{V_0^3 \sqrt{n(n-1)(n-2)} \sqrt{(S-m)(S+m+1)}}{\Delta E^2} \left(-\frac{(S-m+1)(S+m)}{2} \right) \quad (40)$$

The value for the 2nd path 1-3-4-6 is

$$\frac{V_{13} V_{34} V_{46}}{(E-H_3)(E-H_4)} = -\frac{9}{4} \frac{V_0^3 \sqrt{n(n-1)(n-2)} \sqrt{(S-m)(S+m+1)}}{\Delta E^2} (S-m)(S+m+1) \quad (41)$$

The value for the 3rd path 1-3-5-6 is

$$\frac{V_{13} V_{35} V_{56}}{(E-H_3)(E-H_5)} = -\frac{9}{4} \frac{V_0^3 \sqrt{n(n-1)(n-2)} \sqrt{(S-m)(S+m+1)}}{\Delta E^2} \left(-\frac{(S-m-1)(S+m+2)}{2} \right) \quad (42)$$

Summing over the three different paths, we get the result for V_{16} as¹⁻³

$$V_{16} \approx -\frac{9}{4} \frac{V_0^3 \sqrt{n(n-1)(n-2)} \sqrt{(S-m)(S+m+1)}}{\Delta E^2} \quad (43)$$

This is the exact same result as we have got from the elimination of the intermediate expansion coefficients above. We notice that the indirect coupling term V_{16} is small; however, the values for the three individual paths are big. As we have discussed above in connection with excitation transfer, there is strong cancelation between the three paths, and the indirect coupling term is small due to destructive interference.¹⁻³

C.3 Multi-phonon exchange with loss

We expect that the addition of loss to the model would significantly reduce the destructive interference. It could be argued that we should have included the loss at the outset. The spin-boson model could be augmented with loss according to¹⁻³

$$\hat{H} = \frac{\Delta E}{\hbar} \hat{S}_z + \hbar \omega_0 \hat{a}^\dagger \hat{a} + V_0 (\hat{a}^\dagger + \hat{a}) \frac{2\hat{S}_x}{\hbar} - i \frac{\hbar \hat{\Gamma}(E)}{2} \quad (44)$$

The last term in the above equation is a loss operator. We note that more sophisticated models have been studied in which loss is model through coupling to a bath of two-level systems, which show a reduction of the destructive interference and acceleration of the rate for multi-phonon exchange.¹⁻³

From the above discussion, we see that up-conversion and down-conversion are included in the spin-boson model. Many-phonon exchange happens in this model through sequential single phonon exchanges. The spin-boson model does up-conversion and down-conversion exactly as we would like, but the effect is not strong enough (it only works up to about 30 phonons, as the destructive interference makes it impossible to do better).¹⁻³

Loss can reduce the destructive interference, which results in indirect coupling coefficients orders of magnitude greater; this leads to very much accelerated up-conversion and down-conversion effects. Loss is present in the physical system, and should be included in the models. More complicated problems in which much large numbers of phonons are exchanged have been analyzed, and approximate results for the indirect coupling matrix element have been obtained

in the strong coupling limit. These models show a gentle (algebraic) scaling in the limit where the number of exchanged quanta is very large.¹⁻³ There is currently work being done on M1 excitation transfer. Early work indicates that M1 excitation transfer behaves similarly to E1 excitation transfer does.

All the materials reviewed in this appendix are directly from or based on Hagelstein's theory.

References

- 1 Hagelstein, P. (2016). Quantum Composites: A Review, and New Results for Models for Condensed Matter Nuclear Science. *Journal of Condensed Matter Nuclear Science*, 20, 139-225.
- 2 Hagelstein, P., & Chaudhary, I. Possibility of observing a center of mass interaction in a Mossbauer experiment. Manuscript unpublished.
- 3 Hagelstein, P., & Chaudhary, I. (2011). Energy Exchange In The Lossy Spin-Boson Model. *Journal of Condensed Matter Nuclear Science*, 5, 52-71.

Appendix D: Water Jet Experiment at MIT

D.1 Brief Review of the Kornilova Water Jet Experiment

As discussed in Chapter 2, collimated X-ray emission was reported in the Kornilova water jet experiment.¹ In the first version of Kornilova experiment, X-ray energy around 1.7 keV was detected near the water jet nozzle with both X-ray detector and X-ray films.¹ In the second version of the Kornilova experiment, X-ray signals were detected on X-ray films behind the steel plate near water flow.¹ According to the analysis of the film absorption rate and X-ray transmission rate in air, the energy of the X-ray signals should be between 1 keV and 2 keV.¹ We tried to replicate the second version of the Kornilova water jet experiment at MIT.

D.2 Brief Review of Water Jet Experimental Effort at MIT

An effort was made to look for x-ray emission in local versions of the Kornilova experiment. Figure D.1 shows the scheme of our water jet experiment at MIT. Similar to the Kornilova experiment, high pressure water flow was generated from a water jet. A steel plate was placed near the nozzle and water flow. Photographic film inside a light protective envelop with aluminum or graphite cover was placed behind the steel plate to detect potential X-ray signals. A sliding steel plate was placed under the nozzle in order to protect the envelope from water and maximize the ultrasound around the area.

Figure D.2 shows the real picture of the water jet experiment at MIT. The pressure of the water flow coming out of the nozzle was around 3200 atm. The water jet was usually running around 4 minutes in our experiments. The photographic film was then developed by a professional lab technician.

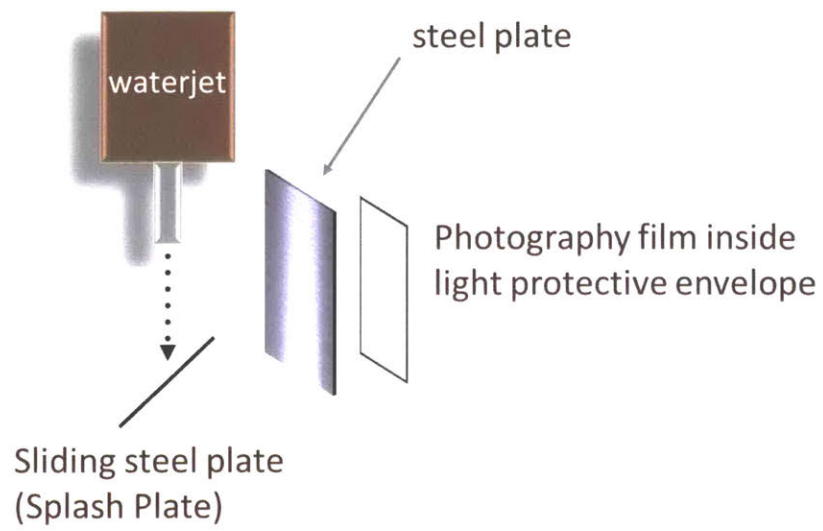


Figure D.1: Scheme of the water jet experiment at MIT

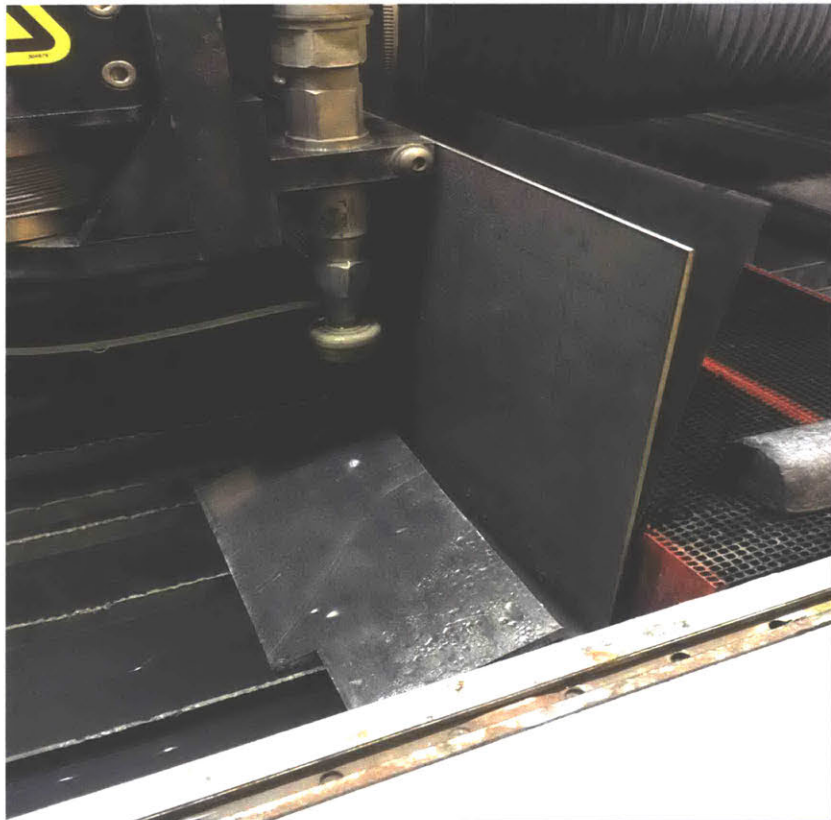


Figure D.2: Water jet experiment at MIT

D.3 Issues with Aluminum and Graphite Foil

In order to detect potential X-ray signals, we put photographic films inside a light protective envelope.^{2,3} We opened a small window on the envelope and covered the window with aluminum or graphite foil. The aluminum or graphite foil could block visible light and allow X-ray to pass through. Both the aluminum and graphite foils used in our experiment were very thin (around 20 micrometers). Some film exposures were obtained in our experiments; however, these were tracked down and found to be attributable to pinholes in the aluminum and graphite film cover. Figure D.3 shows an example of exposure due to pinholes.



Figure D.3: Signals due to pinholes on aluminum and graphite foil

D.4 Issues with Film Developing and Film Sensitivity

We also saw qualitatively different kinds of images on our film in our water jet experiments which later were found to be due to rough handling of the film during the developing process. Figure D.4 shows this result. The semi-curve was from the bending of the film by a professional

lab technician during development. In order to figure out the reason for the semi-curve, we took a brand new film out of the box and strongly bent the film in a dark room. The film was never exposed to any visible light or X-ray source. With developers and fixtures, we developed the film by ourselves in the dark room and saw similar semi-curves around the areas we bent the film. The origin of the vertical line in this photograph is still unknown.

Later we realized another issue with the sensitivity of the photographic films we used in our water jet experiment. We put a Fe-51 X-ray source on the film in a dark room for 10 minutes. We developed the film in the dark room but could see nothing on the film. We could only barely see the signal when the waiting time is around 1 hour. The sensitivity of the film we used for our water jet experiment was so low that we might still see nothing on the film even if there were X-ray signals behind the steel plate. We made some efforts finding the most sensitive film in the market and it would be worth to repeat similar water jet experiments with this film

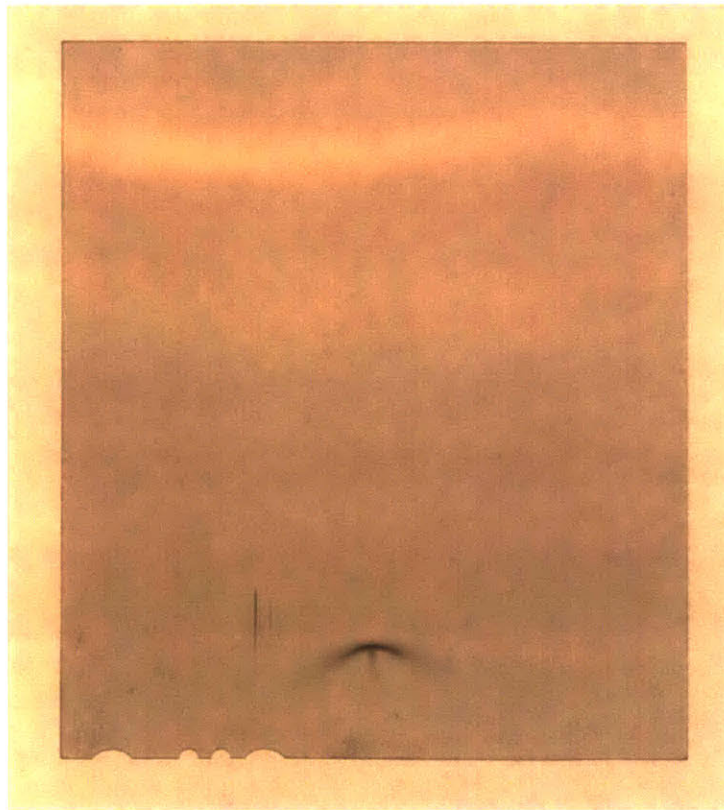


Figure D.4: Signals due to rough handling of the film

D.5 Discussion and Plans

Up to now, our attempt to look for x-ray emission in local versions of the Kornilova experiment has not been successful. We considered a second campaign where we replicate as much as possible their experiment. For instance, it would be good to find the same model water jet as the one in their experiment (or go to Russia to work with theirs). For our current water jet at MIT, the diameter of the nozzle is around 0.02 mm which is much smaller than their nozzle diameter of 0.3-1 mm.¹ The pressure of the water flow from our water jet is around 3200 atm which is much larger than their water pressure of 600 atm.¹

We would like to use X-ray film or more sensitive photography film to detect signals. A mesh test will be necessary for the future runs to confirm that the signals are not artifacts. It would be also worth to carry out similar experiments with tantalum plate and cobalt plate. We expect to see the same effect with tantalum as it has a low transition energy of around 6.2 keV. A cobalt plate can be used as a control experiment, as cobalt has a very high transition energy in the MeV range.

Another thought is that the vibration source in the Kornilova experiment might be not from the ultrasound around the high pressure water flow. We noticed that in the Kornilova experiment the steel plate was jammed into a wood holder. It is possible that the vibration was from the fact that the steel plate was tightly clamped by wood. It would be worth to do some experiments regarding this hypothesis.

Our experiments at MIT raise a question as to whether Kornilova's results might be due also to pinholes. Kornilova presents results from control experiments which are free of the signals; however, there are questions as to the details of their protocol. We considered traveling to Moscow in order to work with her on tests at her installation. We would like to ask her for help to do the mesh test with their equipment to confirm the results. We also would like to repeat the experiment with tantalum and cobalt plate at their facility.

The experiment introduced in this appendix is done by me. All data shown in this section is taken and analyzed by me.

References

- 1 Kornilova, A. A., Vysotskii, V. I., Sysoev, N. N., Litvin, N. K., Tomak, V. I., & Barzov, A. A. (2010). Generation of intense x-rays during ejection of a fast water jet from a metal channel to atmosphere. *Journal of Surface Investigation. X-ray, Synchrotron and Neutron Techniques*, 4(6), 1008-1017. doi:10.1134/s1027451010060224
- 2 Chandler, K. M., Pikuz, S. A., Shelkovenko, T. A., Mitchell, M. D., Hammer, D. A., & Knauer, J. P. (2005). Cross calibration of new x-ray films against direct exposure film from 1 to 8 keV using the X-pinch x-ray source. *Review of Scientific Instruments*, 76(113111), 1-8. doi:10.1063/1.2135276
- 3 Henke, B., Fujiwara, F., Tester, M., Dittmore, C., & Palmer, M. (1984). Low-energy x-ray response of photographic films. II. Experimental characterization. *Journal of the Optical Society of America B*, 1(6), 828-849.

Appendix E: Amplitude Modulation Studies

The theoretical ideas and experimental results from other labs discussed in Chapter 2 motivated us to focus on experiments in which samples are vibrated strongly in the MHz range under controlled conditions in our lab. These experiments involve generating controlled vibrations on samples and detecting potential X-ray signals around samples. The samples we used include steel plate, tantalum plate, and ConFlat resonator. Signal generators, amplifiers, and transducers are used to generate MHz vibrations on the samples. Lasers, photodiodes, and oscilloscopes are used to monitor sample vibrations.

E.1 Introduction to Use of Lasers to Monitor Surface Motion

Taking advantage of amplitude modulation, we were able to monitor the surface vibrations on the sample plate or resonator. The instruments we used include laser, photodiode, and oscilloscope. The laser used for our experiment is the stabilized red He-Ne laser from Thorlabs (part number: HRS015B). The photodiode used in our experiment is the biased Si detector with a range from 200 - 1100 nm from Thorlabs (part number: DET10A). The oscilloscope used in our experiment is the PicoScope from Pico Technology (part number: 5444B).

E.1.1 Brief Explanation of Amplitude Modulation

Figure E.1 shows the scheme of our optical setup measuring the plate vibration via amplitude modulation method. A beam of collimated red laser reflected at the surface of the steel plate and was directed to a photodiode connected with an oscilloscope. The vibration in the steel plate caused amplitude change on the surface of the plate, resulting in the corresponding change at the laser which was recorded at the frequency domain in the oscilloscope. We could get the vibration frequency and intensity from the frequency domain data in the oscilloscope.

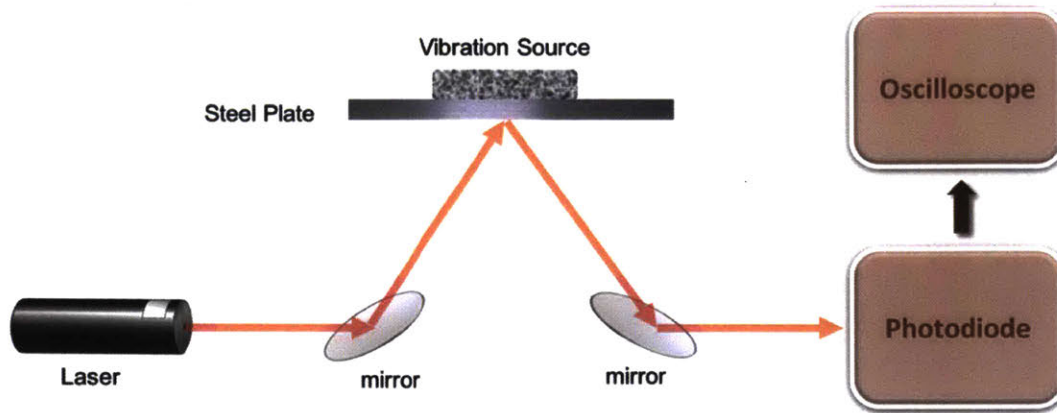


Figure E.1: Scheme of the amplitude modulation method

E.1.2 Brief Explanation of Doppler Frequency Modulation

Figure E.2 shows the scheme of our optical setup measuring the plate vibration via Doppler frequency modulation method. A beam of collimated red laser was divided into two identical beams by the first beam splitter. One beam reflected at the surface of the steel plate. The other beam was directed to the second beam splitter without hitting the steel plate. Both beams were combined into one single beam by the second beam splitter. The combined beam was directed to a photodiode connected with an oscilloscope. The vibration in the steel plate causes a Doppler shift for the beam hitting the moving surface, and we hoped to observe a beating with the reference beam in the scope. Unfortunately, the surface motion in our experiments was too small to produce much of a Doppler shift, so we were not able to see the associated FM modulation in the experiments discussed in this Appendix. All of the laser signals reported here were taken with amplitude modulation.

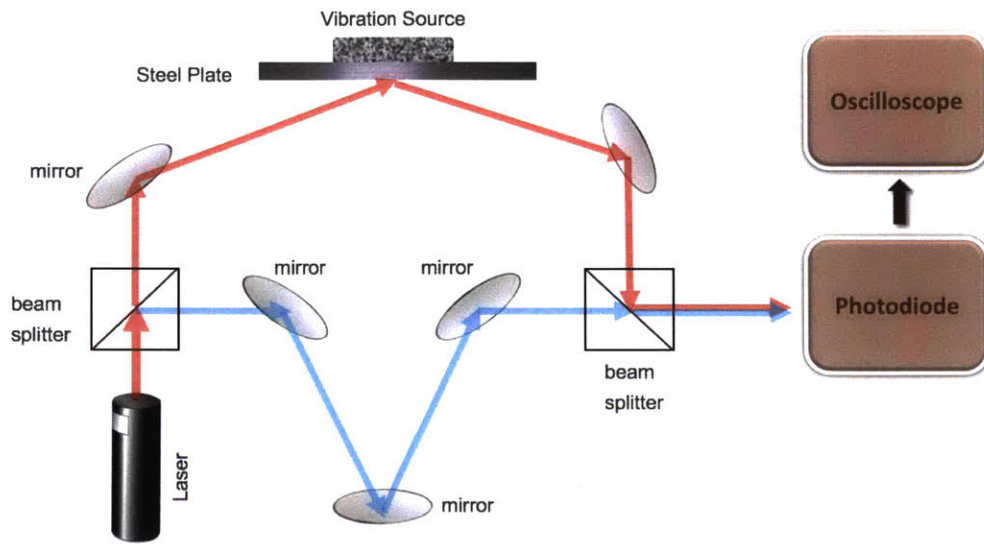


Figure E.2: Scheme of the Doppler frequency modulation method

E.2 Early Amplitude Modulation Experiments

At the beginning of the experiment, we used the SoundCare plus clinical ultrasound device as our vibration source. Figure E.3 shows the instrument. The ultrasound device generated ultrasound vibrations at the sound head surface with 1 MHz frequency and 1 W/cm^2 power. With the amplitude modulation setup, the laser reflected at the sound head surface and was directed to the photodiode. Figure E.4 shows the frequency domain data in the oscilloscope. It shows a clear peak at 1.02 MHz matching the ultrasound device data. From this experiment, we were able to confirm that our amplitude modulation optical setup could accurately measure the frequency and intensity of surface vibrations.

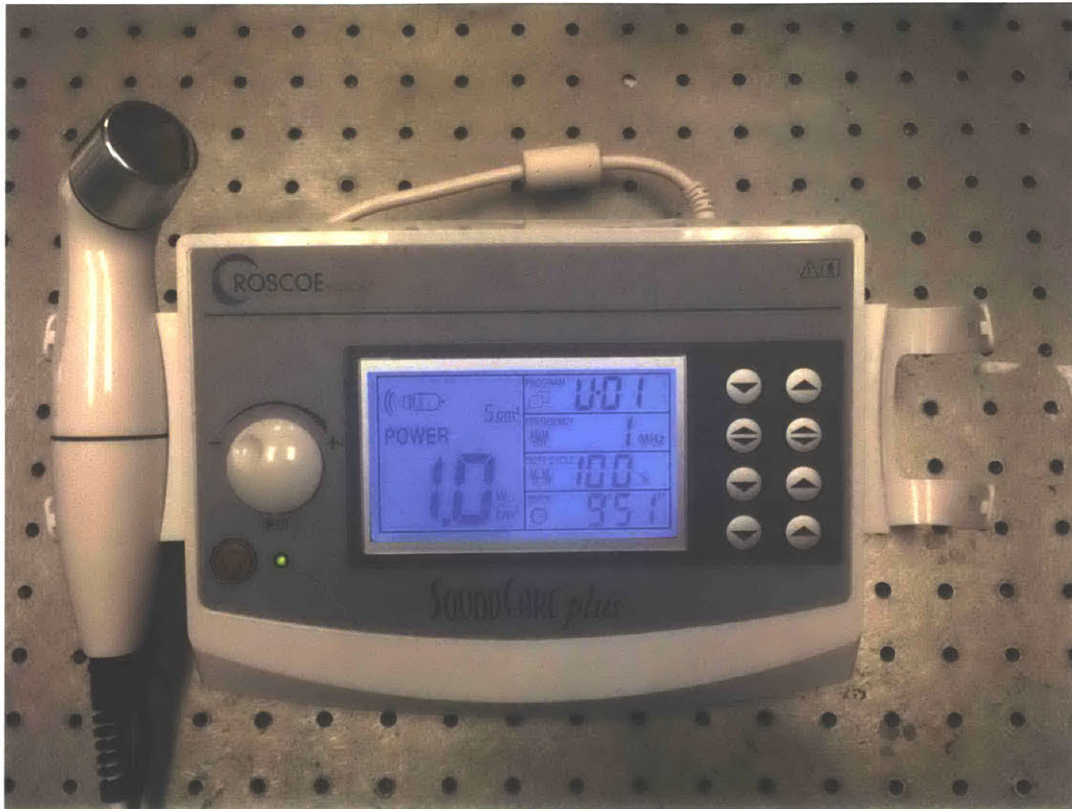


Figure E.3: SoundCare plus clinical ultrasound device

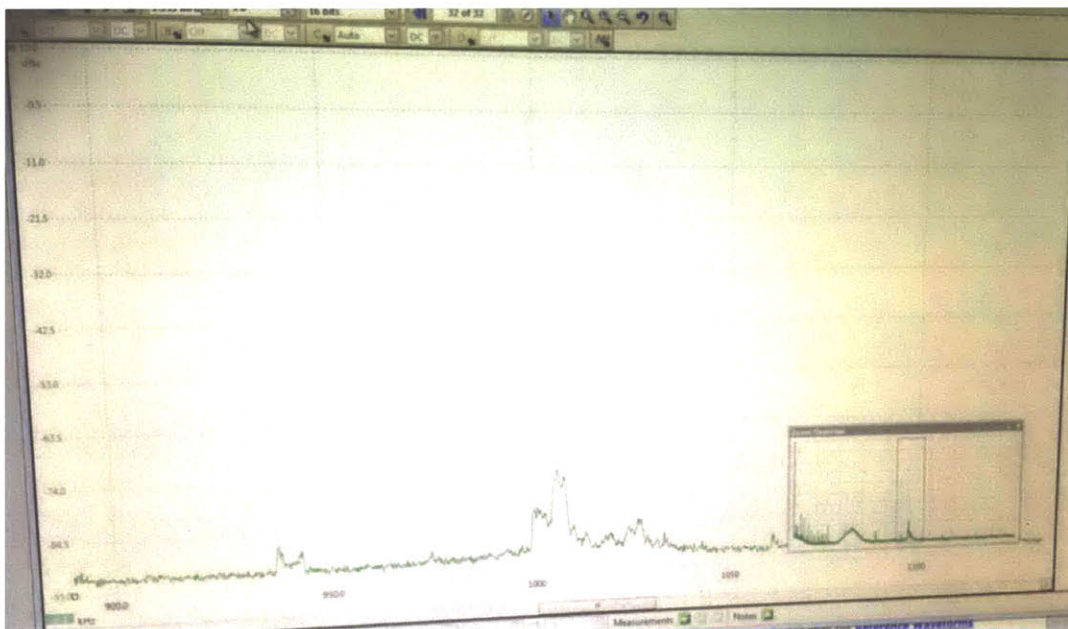


Figure E.4: Frequency domain data for the ultrasound device surface vibrations

E.3 Experiments with Plates

In the lab we have built an experimental setup with which we can drive metal plates on their fundamental resonances in the MHz regime and detect the vibrational response, hoping to detect X-ray emission from nuclear excitation near the plate. The sample plates used in our experiments include a steel plate and a tantalum plate. Fe-57 has a low energy nuclear transition at 14.4 keV and Ta has a low energy nuclear transition at 6230 eV.

Figure E.5 is the flow chart of our lab vibration experimental setup with the steel plate. AC signals are generated from the signal generator and amplified by the amplifier. The high power transducer sitting on the steel plate transforms the AC signals to ultrasound, resulting in the plate vibration. The impedance and power of the transducer are determined based on bi-directional coupler measurements of forward and reflected voltages. We controlled the frequency of vibration by adjusting the frequency of the signal generator. We were able to drive the plate very strongly when the frequency of vibration matched the fundamental resonance of the plate.

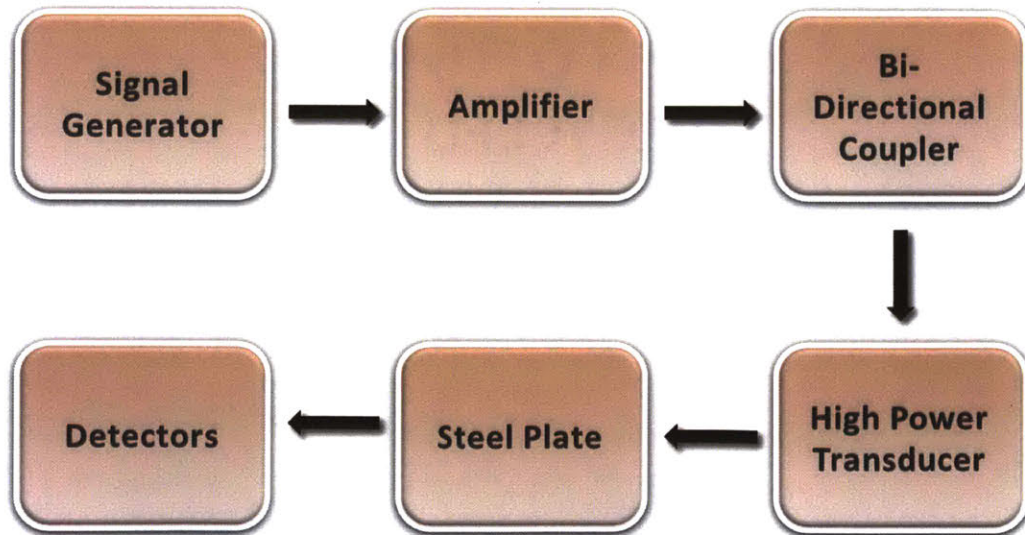


Figure E.5: Flow chart of our lab vibration experiment system with steel plate

We have two powerful transducers with a small working range around 2.23 MHz. It only works well within 2.23 MHz \pm 0.02 MHz.

The resonance frequency of the steel plate is

$$f = \frac{nv}{2d} \quad (45)$$

where n is the fundamental number, v is the sound of speed in steel, d is the thickness of the steel plate. In order to match the working frequency of the transducer with the steel plate resonance frequency, we need to choose the thickness of the plate carefully. With $f = 2.23$ MHz, $n = 3$ and longitudinal sound speed in steel $v = 5790$ m/s, we get the thickness at 3.90 mm.

The power of the transducer was measured by the bi-directional coupler. The frequency and intensity of the steel plate vibration were measured through amplitude modification by the optical setup shown in Figure E.1.

Figure E.6 shows the transducer power and the plate vibration intensity in our experiment. There was a good match between the working range of the transducer and the resonance frequency of the steel plate. The plate was driven very strongly near the resonance frequency.

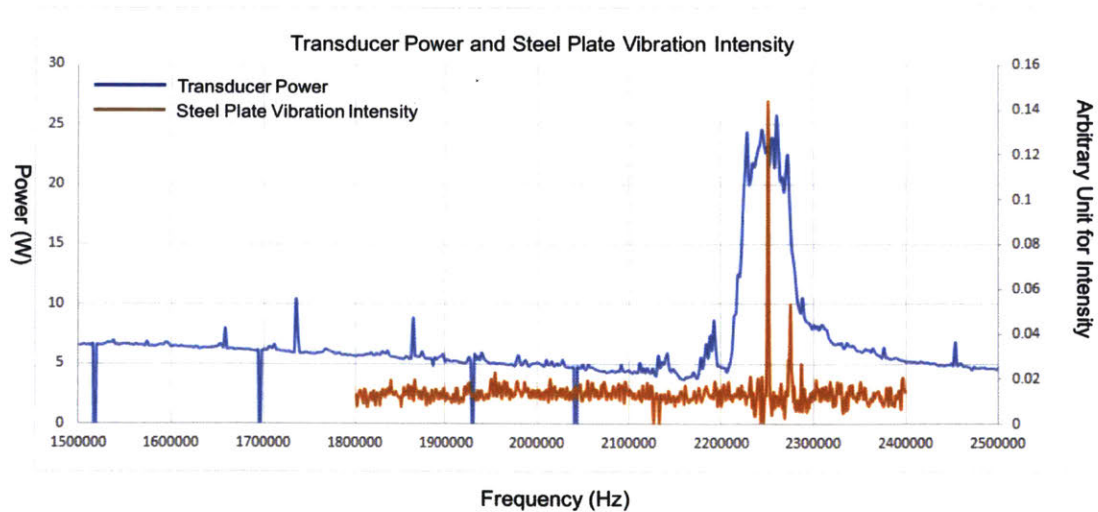


Figure E.6: Transducer power and steel plate vibration

A few attempts were made to detect X-ray signals from the vibrated steel plate using film, but these did not give positive results. Subsequently, a test was done by Metzler using more sensitive

diagnostics (see the diagnostics described in reference 1) and no signal above background was detected. Shortly after these tests we saw unexpected non-exponential decay in the experiment of May 20, 2017, which redirected the focus of our research effort.

E.4 Experiments with a Resonator

According to theory higher frequency vibrations (such as THz vibrations) should be most effective for up-conversion. However, in the Karabut experiment and in the Kornilova experiment one would expect lower frequency vibrations to be present. We decided on an exploratory effort to see whether x-ray emission could be seen driving lower frequency modes in the 10-25 kHz range. An advantage of working in this frequency range is that it becomes very easy to put in substantial power with low-frequency ultrasound transducers. The focus of our experiments was on bending modes in the steel plate (not described in this Appendix), and on longitudinal and drumhead modes in a resonator (discussed below). The motivation for considering the resonator is that in the Karabut experiment a large steel vacuum chamber is present, which we would expect to act as a resonator for vibrations in the frequency range of interest. Note that the big result of the May 20, 2017 experiment occurred while this work was ongoing, and that this caused a refocusing of our research effort.

We consider now ultrasound experiments with a steel conflat resonator, making use of the scheme shown in Figure E.7. The length of the steel conflat resonator was chosen to get 20 kHz longitudinal resonance frequency. Copper sheets were attached to the top and bottom of the resonator. The thickness of the copper sheets was chosen to get 20 kHz drumhead mode resonance frequency. The purpose of this experiment is to simulate the Karabut experiment in our lab. We once proposed that the phonon vibrations in the Karabut experiment were due to the drumhead mode in the cathode matching longitudinal mode in the steel chamber.

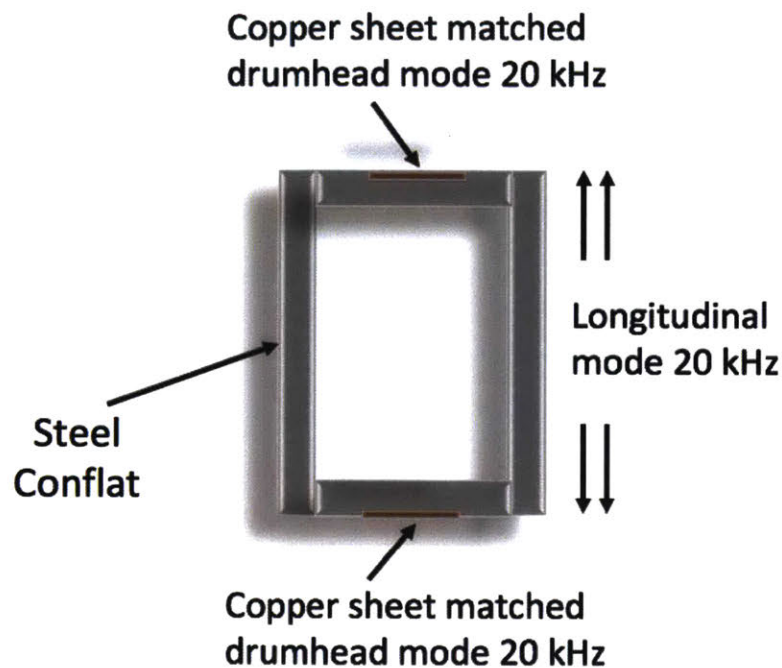


Figure E.7: Scheme of the steel conflat resonator

The flow chart of the vibration experiment with the resonator is the same as the one shown in Figure E.5 except that the sample changes from steel plate to the resonator. Figure E.8 shows the real picture of the conflat resonator. The resonator is Conflat 6" full nipple with length 10.62" from Kurt J. Lesker company (part number: FN-0600). The copper plates are 0.003" thick multipurpose copper sheets from McMaster (part number: 9053K322). The extension steel plates attached on the bottom of the resonator are for adjusting the length and longitudinal resonance frequency of the whole system. The extension steel plates are 0.188" thick 304 stainless steel sheet from McMaster (part number: 8983K119). The vibration source is a 20 kHz transducer sitting on top of the resonator tightened by three pieces of plexiglass. We put gel between the transducer and the copper plate to make impedance match so that the power of the transducer could go into the resonator effectively.

The red laser reflected at the bottom surface of the resonator and was directed to the photodiode connected with the oscilloscope to monitor the resonator vibrations. The vibrations frequency and intensity could also be obtained from the power data in the bi-directional coupler. Figure E.9 – E.12 show the power data and optical data of the resonator vibrations with or without tightening the plexiglass. We can see clear peaks in both the power spectrum and optical spectrum. We notice that tightening the plexiglass (adding force to the transducer) caused splitting of peaks. It appears that the lower frequency peak could be associated with the resonator resonance and the higher frequency peak with the transducer resonance. We might get a cleaner look at the resonator resonance if we could use a transducer with a resonance farther from the expected resonator resonance.

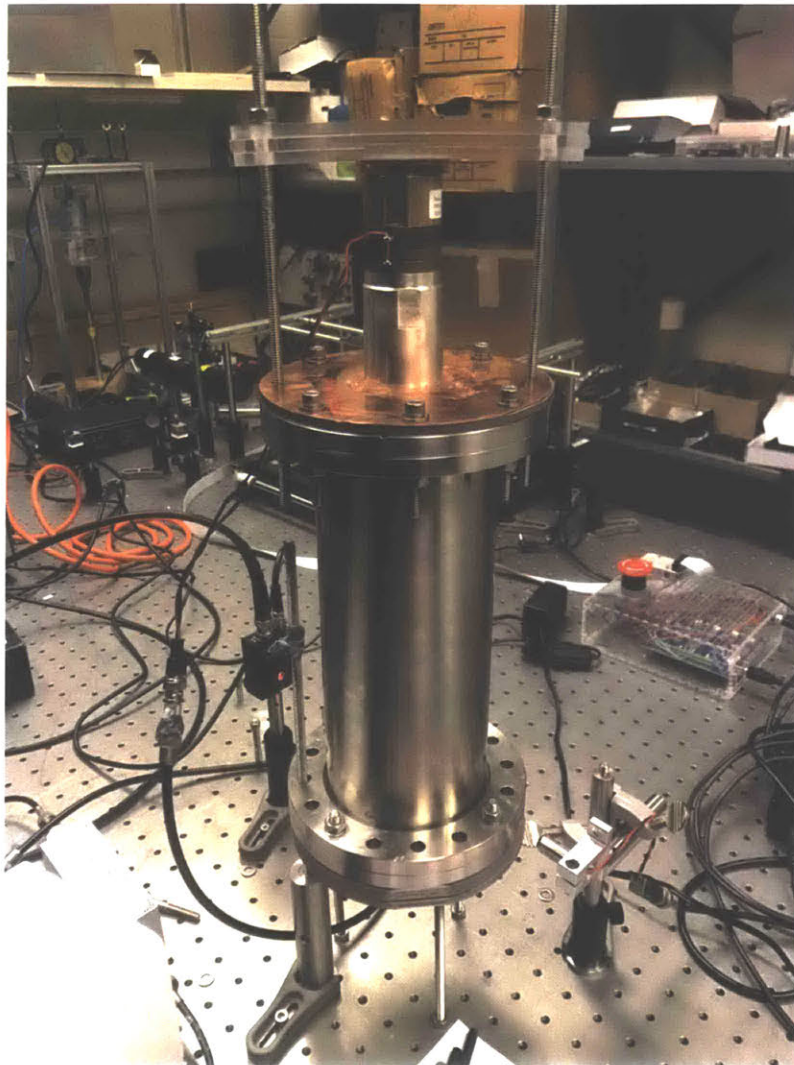


Figure E.8: Steel conflat resonator vibrated by 20 kHz transducer

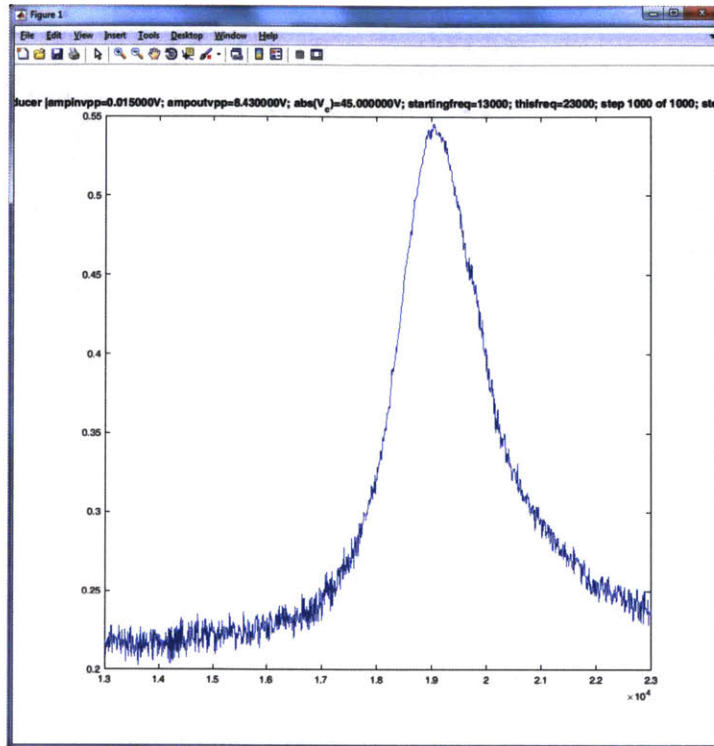


Figure E.9: Power data from 13-23 kHz without tightening the plexiglass

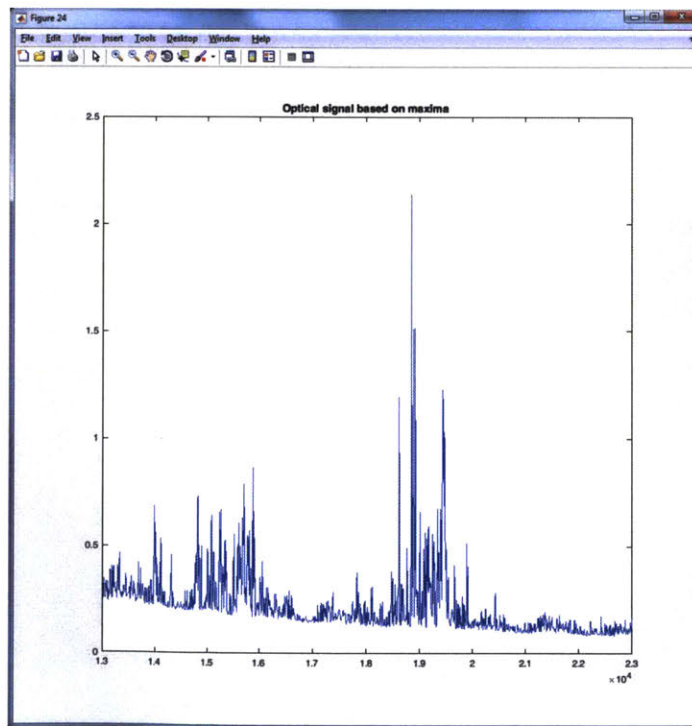


Figure E.10: Optical data from 13-23 kHz without tightening the plexiglass

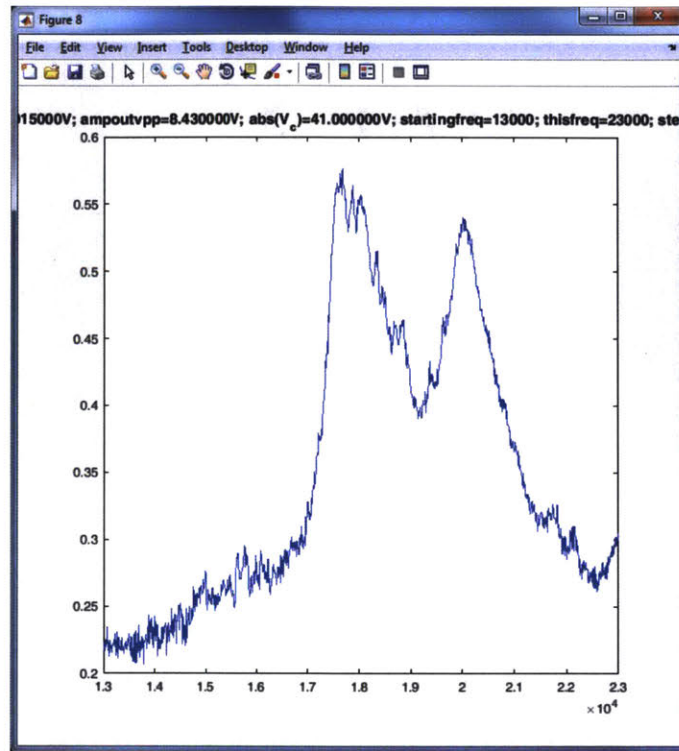


Figure E.11: Power data from 13-23 kHz with tightening the plexiglass

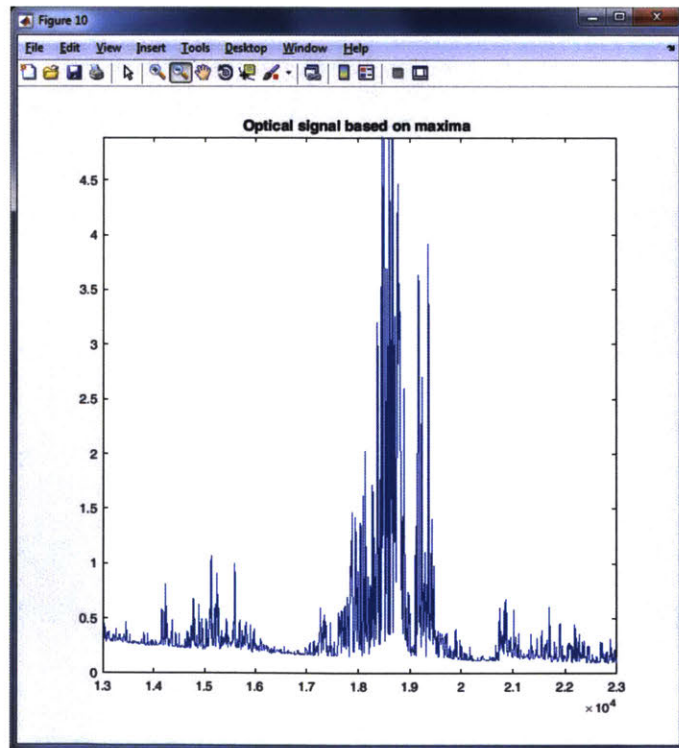


Figure E.12: Optical data from 13-23 kHz with tightening the plexiglass

In order to confirm whether the peaks in the above figures belonged to the longitudinal resonator resonance, we did another test by adding an extra extension steel ring.

Every steel ring is $0.188'' = 4.78\text{mm}$ thick. The length of the resonator with 3 steel rings is 285.09mm and with 4 steel rings it is 289.87mm .

The corresponding expected $n = 2$ resonances are:

$$f_{3\text{rings}} = (2 * 5790) / (2 * 285.09) \text{ Hz} = 20.309 \text{ KHz}$$

$$f_{4\text{rings}} = (2 * 5790) / (2 * 289.87) \text{ Hz} = 19.975 \text{ KHz}$$

So increasing from 3 to 4 rings should shift the resonance frequency downward by:

$$f_{\text{delta}} = 0.336 \text{ KHz}$$

Figure E.13 shows the power data with 3 steel rings. Figure E.14 shows the power data with 4 steel rings. The observed shift in this test roughly matched the above value from the calculation, which increased our confidence that we did observe the longitudinal resonator resonance in the power spectrum.

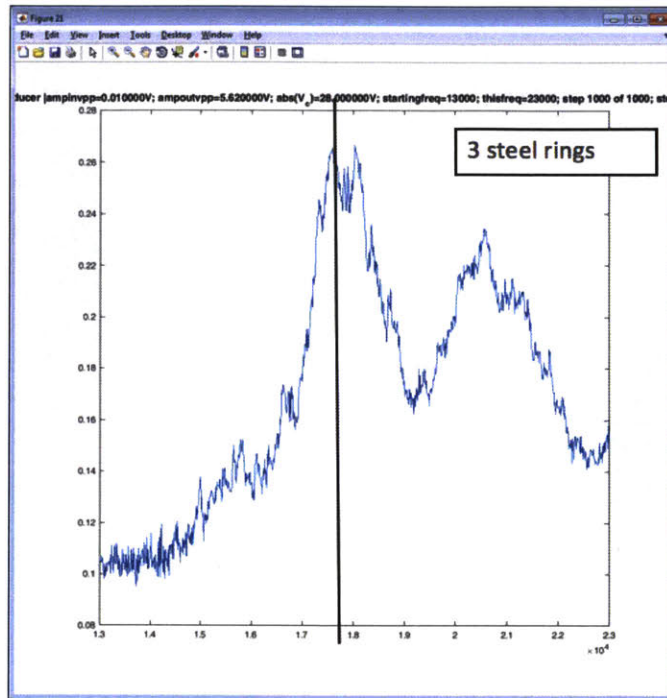


Figure E.13: Power data from 13-23 kHz with 3 steel rings

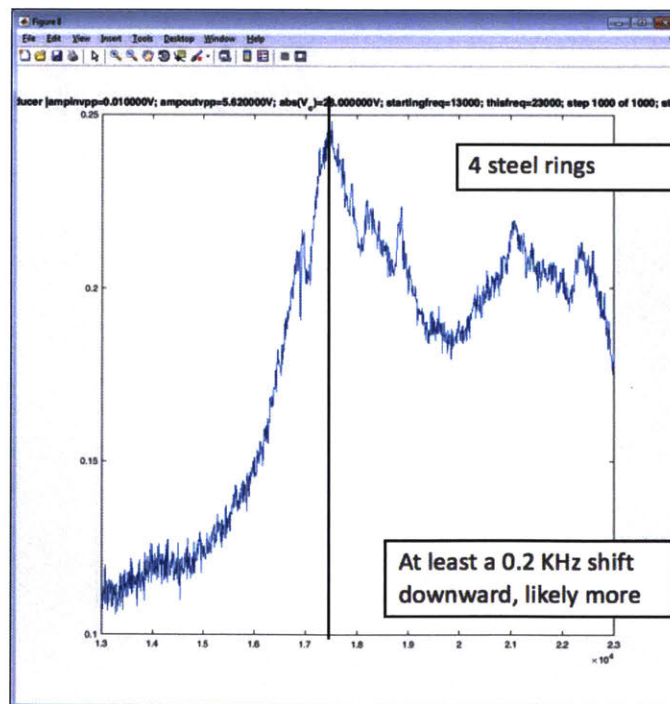


Figure E.14: Power data from 13-23 kHz with 4 steel rings

E.5 Comparison with Microphone

In addition to using a laser to measure the vibrations of the resonator, we also used a microphone to help us analyze the resonator vibrations. Figure E.15 shows where we placed the microphone and laser. The microphone was placed close to the bottom of the resonator. The vibrations of the resonator caused sound signals through the air. The microphone could detect the frequency and intensity of the sound signals and therefore monitor the local resonator vibrations. Figure E.16 shows both the microphone signals and laser signals from 12 - 25 kHz. The two signals approximately match each other. Figure E.17 shows the microphone signals from a long scan between 5 - 25 kHz. There are several potential resonance peaks according to the following calculation. We are interested in further analysis of the peak around 5.7 kHz (n=1 shear mode).

The resonance frequency $f = nv/2d$. The length of the resonator $d = 270\text{mm}$.

For shear mode $v=3100\text{m/s}$

$f=5.7\text{ kHz}$ for $n=1$, $f=11.5\text{ kHz}$ for $n=2$, $f=17.2\text{ kHz}$ for $n=3$, $f=23.0\text{ kHz}$ for $n=4$

For longitudinal mode $v=5790\text{m/s}$

$f=10.7\text{ kHz}$ for $n=1$, $f=21.4\text{ kHz}$ for $n=2$

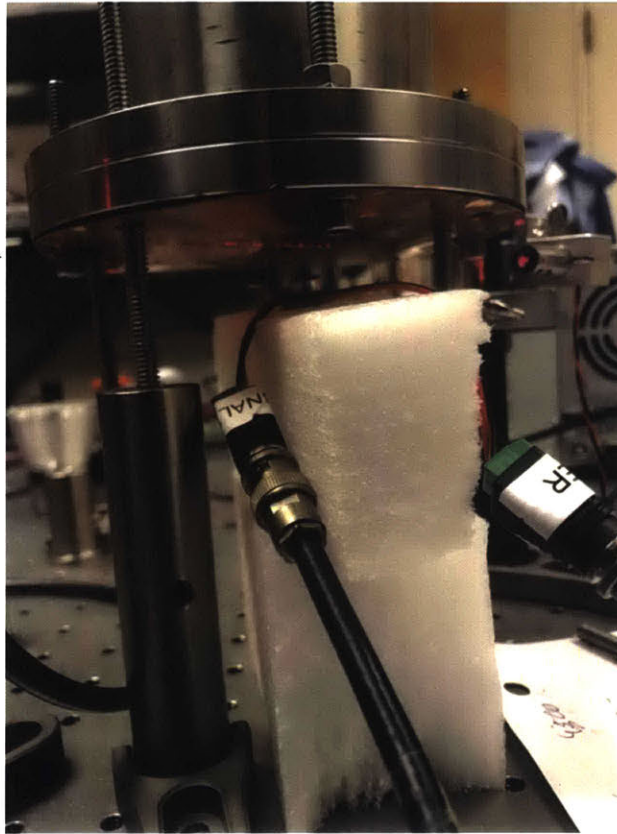


Figure E.15: Using both laser and microphone to measure resonator vibrations

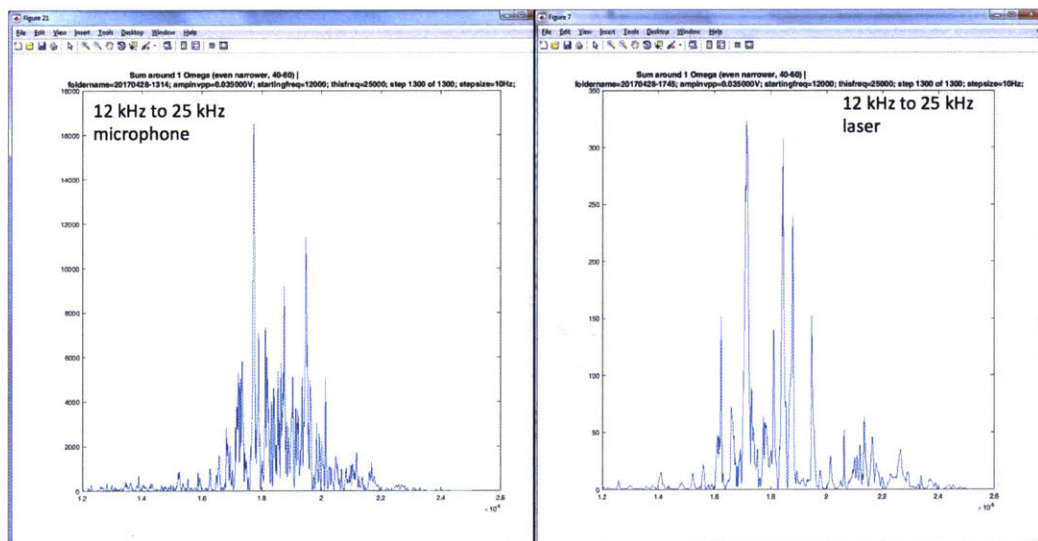


Figure E.16: Comparison between microphone signals and laser signals from 12-25 kHz

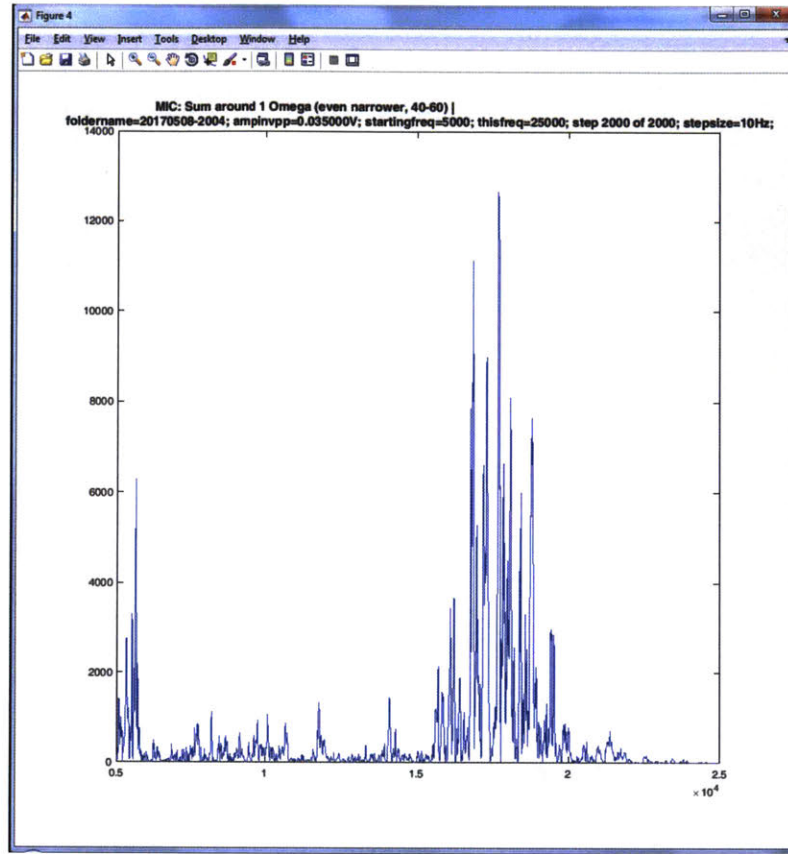


Figure E.17: Microphone signal from 5 kHz to 25 kHz

E.5.1 Further Analysis of the $n=1$ Shear Mode Peak near 5.7 kHz

Figure E.19 shows the microphone signals for a finer scan at the bottom of the resonator between 4 kHz and 6 kHz with step size 10 Hz. The peak near 5.5 kHz is a candidate for the fundamental shear mode resonance. In order to confirm this, we did several scans with the microphone at 5 different positions along the resonator. Figure E.20, E.21 and E.22 show the 5 different positions named position '0', position '1/4', position '1/2', position '3/4' and position '1'. If the 5.5 kHz peak does belong to the fundamental shear mode, we should expect to see the distribution shown in Figure E.18 for the intensity of the peaks at the 5 different positions. The peak signals at position '0' and '1' should be much stronger than the peak signals at other locations.

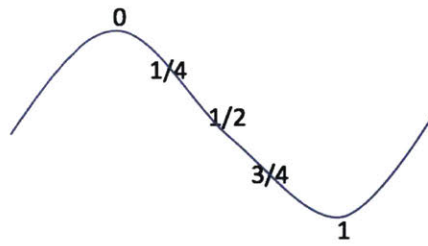


Figure E.18: Expected intensity distribution of the 5.5 kHz peaks at 5 different locations

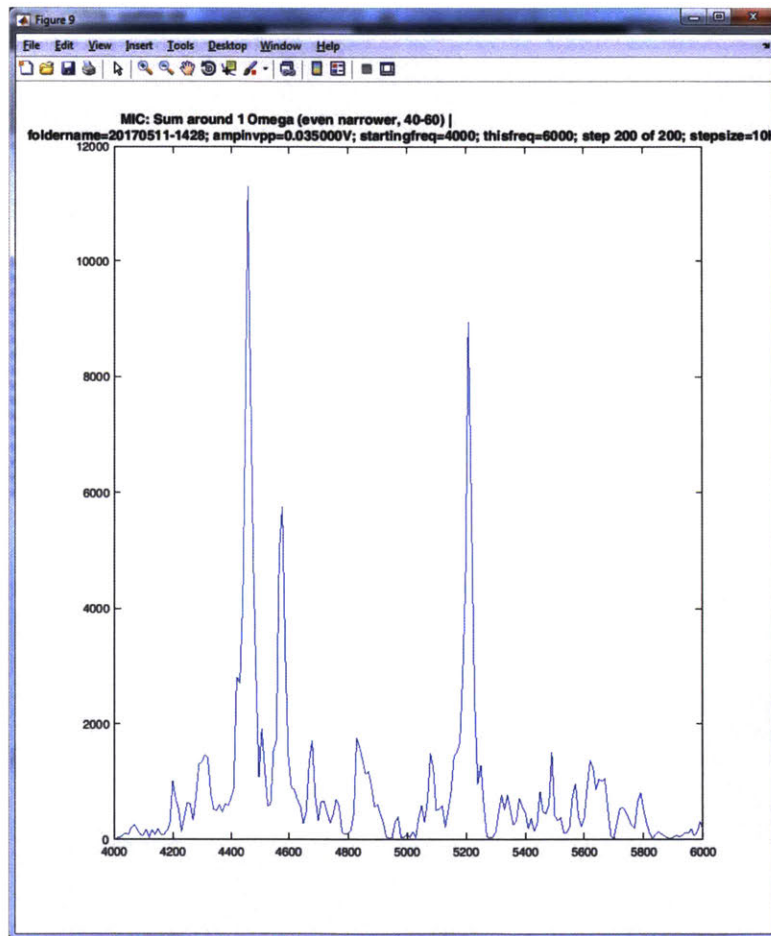


Figure E.19: Microphone signal from 4 kHz to 6 kHz with 10 Hz step size

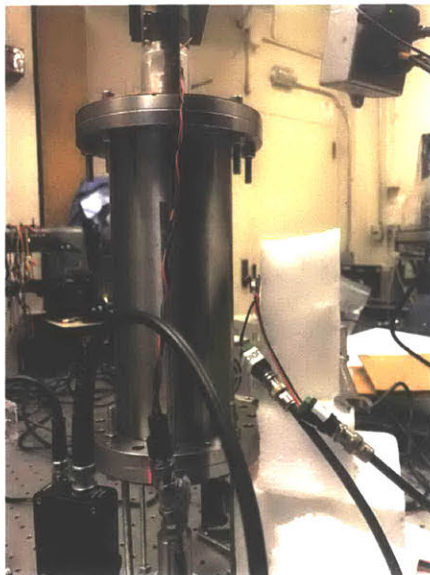


Position 0



Position 1/4

Figure E.20: Microphone test at position '0' and position '1/4'



Position 1/2



Position 3/4

Figure E.21: Microphone test at position '1/2' and position '3/4'



Figure E.22: Microphone test at position '1'

Figure E.23, E.24 and E.25 show the microphone signals for the 5 different positions. Most of the 5.5 kHz peak signals match the expected intensity distribution in Figure E.18 except for position '1/2'. It is likely that the 5.5 kHz peak belongs to the fundamental shear mode.

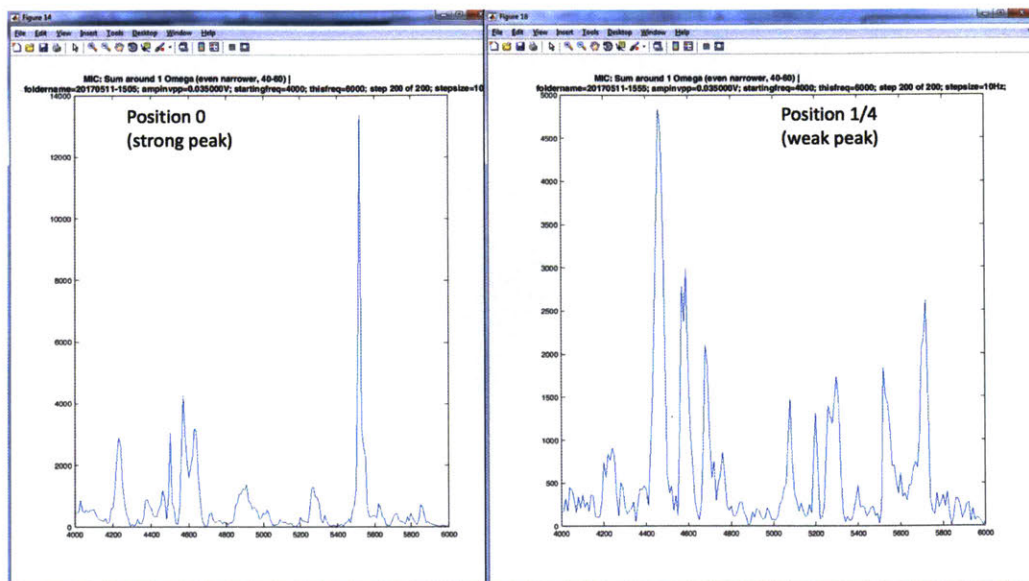


Figure E.23: Microphone signals from 4-6 kHz at position '0' and position '1/4'

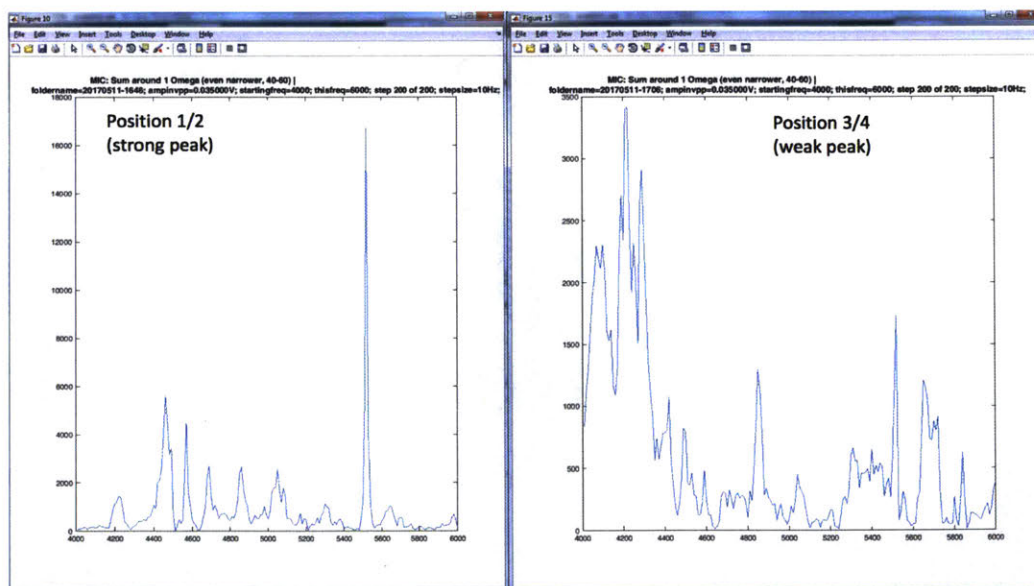


Figure E.24: Microphone signals from 4-6 kHz at position '1/2' and position '3/4'

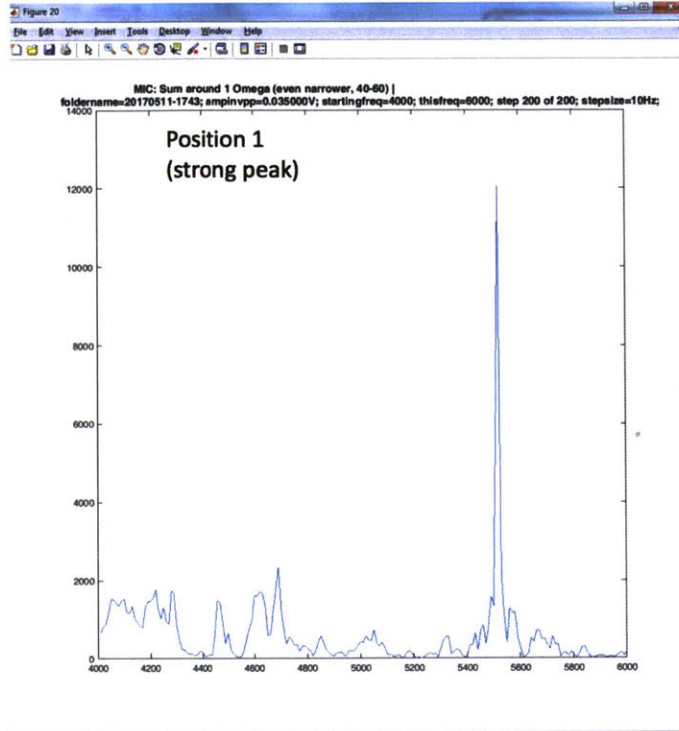


Figure E.25: Microphone signals from 4-6 kHz at position '1'

E.5.2 Asymmetric Resonator Analysis

In order to figure out why the peak signals for position '1/2' did not match the expected distribution, we did several scans around the resonator at 4 different '1/2' positions. Figure E.26 and E.27 show the 4 different positions named position 'a' - 'd'. Figure E.28 and E.29 show the microphone signals for the 4 positions. We notice that the 5.7 kHz peak signals for different '1/2' positions around the resonator are quite different from each other. Position 'a' and position 'b' both have weak signals. Position 'c' has the highest peak. Position 'd' has medium peak signals. From this experiment, we can learn that the resonator is asymmetric with angular momentum, which makes the vibration modes of the resonator very complicated. In order to decrease or avoid the angular momentum, we would like to redesign the resonator.

We redesigned the bolts and screws to make a more symmetric configuration hoping that we could get simpler spectrum and also get rid of the angular momentum. Figure E.30 shows the redesigned resonator. We added more evenly distributed bolts and screws at the top and bottom

of the resonator. Figure E.31 and E.32 show the microphone and laser signals at the bottom of the redesigned resonator. The laser spectrum from 5-15 kHz looks simpler and cleaner. According to the following calculation, we could find candidates for $n=1$ shear mode, $n=2$ shear mode and $n=1$ longitudinal mode in that spectrum.

The resonance frequency $f = nv/2d$. The length of the resonator $d = 270\text{mm}$.

For shear mode $v=3100\text{m/s}$. $f=5.7\text{ kHz}$ for $n=1$, $f=11.5\text{ kHz}$ for $n=2$

For longitudinal mode $v=5790\text{m/s}$. $f=10.7\text{ kHz}$ for $n=1$

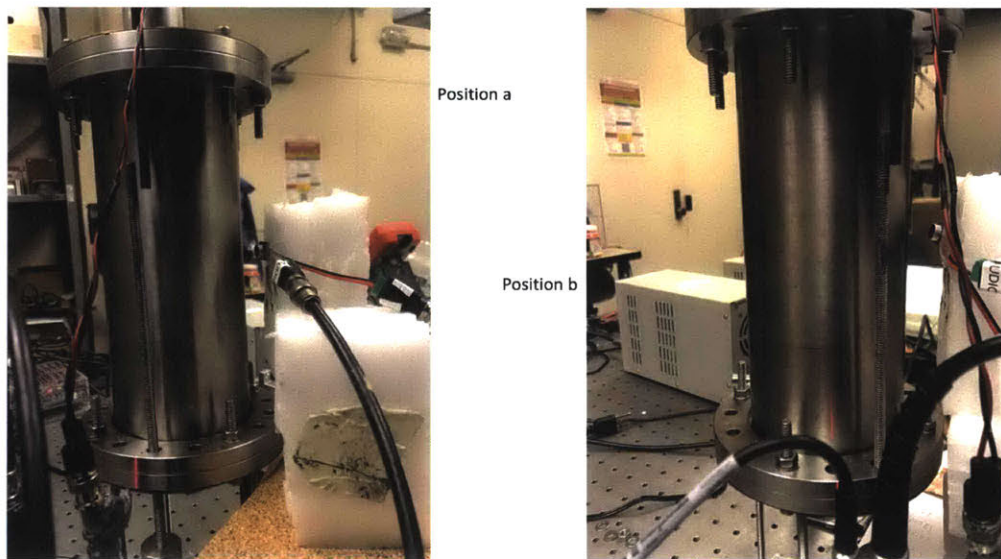


Figure E.26: Microphone test at position 'a' and position 'b'

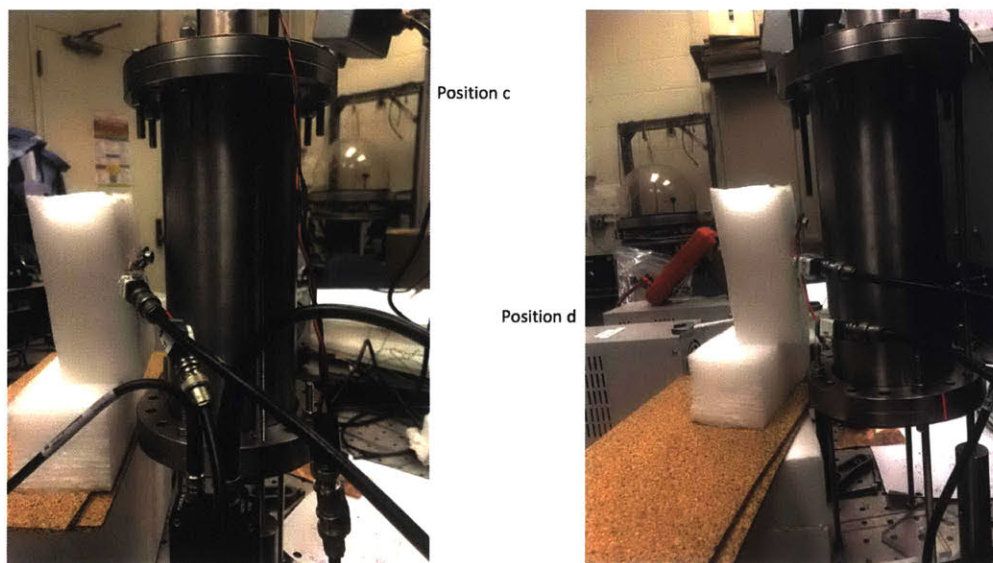


Figure E.27: Microphone test at position 'c' and position 'd'

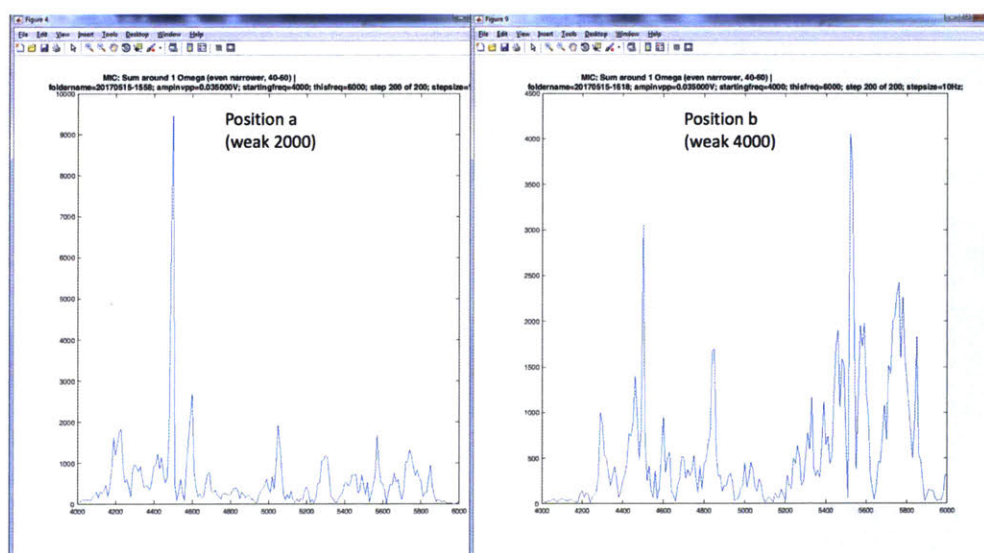


Figure E.28: Microphone signals from 4-6 kHz at position 'a' and position 'b'

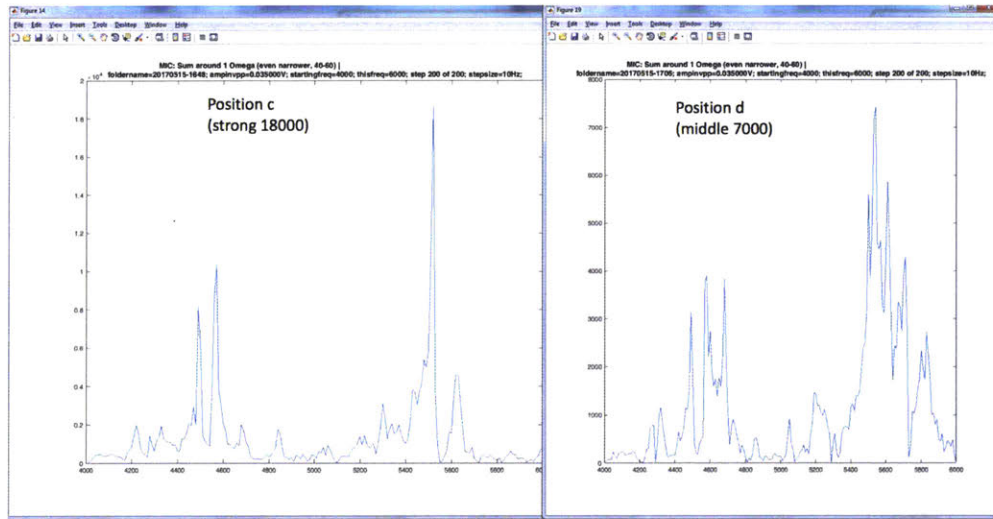


Figure E.29: Microphone signals from 4-6 kHz at position 'c' and position 'd'

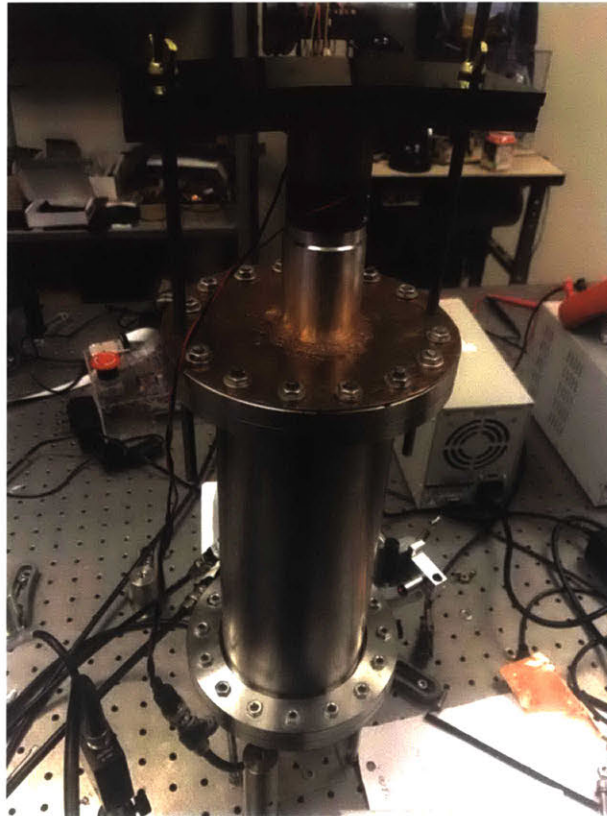


Figure E.30: Resonator with more evenly distributed bolts and screws

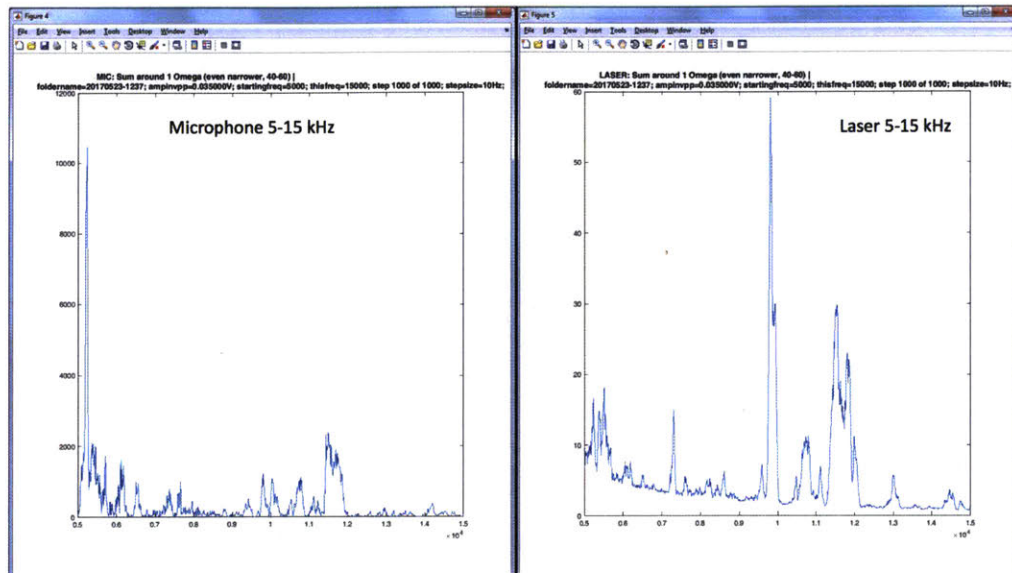


Figure E.31: Microphone and laser signals at the bottom of the new resonator (5 -15 kHz)

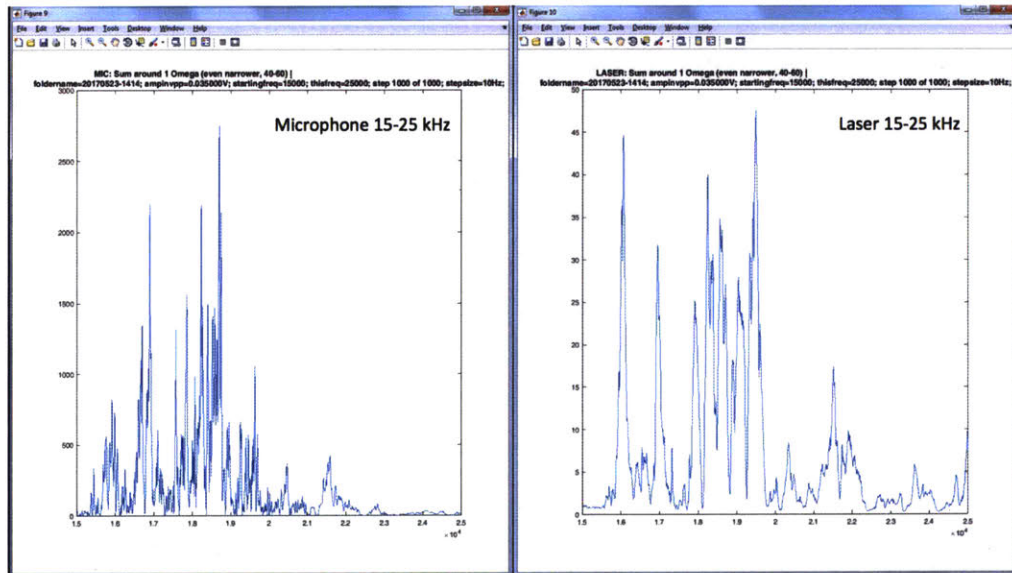


Figure E.32: Microphone and laser signals at the bottom of the new resonator (15 -25 kHz)

E.5.3 Further Analysis of the $n=1$ Longitudinal Mode Peak near 10.7 kHz

Figure E.33 shows the microphone and laser signals for a finer scan at the bottom of the redesigned resonator between 9 kHz and 12 kHz with step size 10 Hz. The peak near 9.8 kHz is a candidate for the fundamental longitudinal mode resonance, which is 10.7 kHz according to the

calculation. In order to confirm this, we did several scans with the microphone at 4 different '0' positions around the resonator. Figure E.34 and E.35 show the 4 different positions named position 'a' - 'd'. If the 9.8 kHz peak does belong to the fundamental longitudinal mode, we should expect to see the peak signals at the 4 different '0' positions much weaker than the peak signals at the bottom. That is because for longitudinal modes much more energy should be detected at the bottom of the resonator compared with the surrounding areas.

Figure E.36 and E.37 show the microphone signals for the 4 different '0' positions. Most of the 9.8 kHz peak signals at these positions are much weaker than those at the bottom. Position 'c' is the only exception with strong 9.8 kHz peak signals. We are confident that the 9.8 kHz peak should belong to the fundamental longitudinal resonance. From this run we also learn that the angular momentum for the redesigned resonator still exists but it is much less than that in the original resonator.

After all of the efforts studying the resonator vibration modes, we understand that the modes of the resonator system are complicated. We would like to attach mercury amalgam at the bottom of the resonator and simulate the Karabut experiment in our lab. The details about making mercury amalgam are discussed in Appendix F.

The experiment introduced in this appendix is done by me and my colleague Florian Metzler. All data shown in this section is taken and analyzed by me and Metzler.

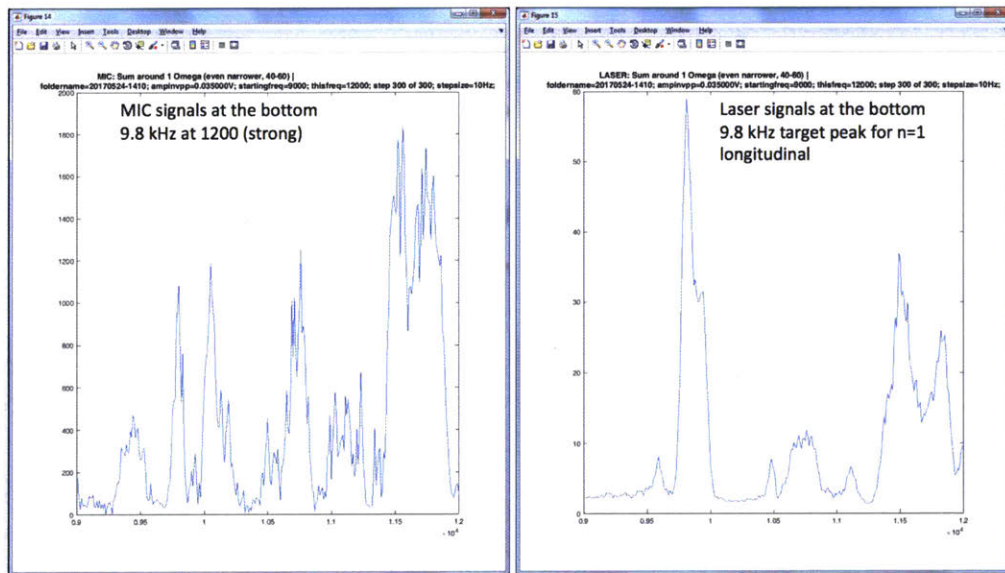


Figure E.33: Finer scan at the bottom of the new resonator from 9-12 kHz with 10 Hz step size

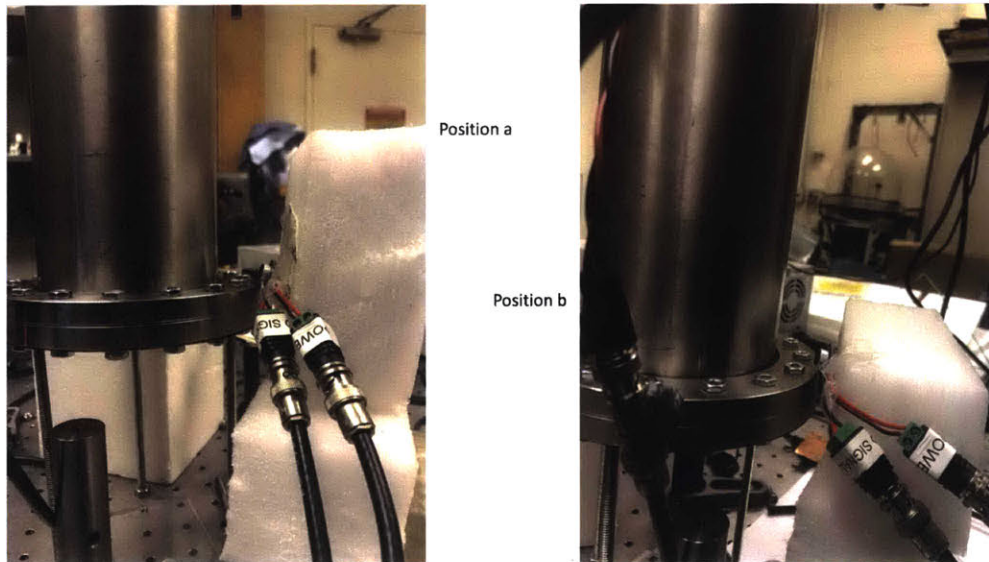


Figure E.34: Microphone test for new resonator at position 'a' and position 'b'

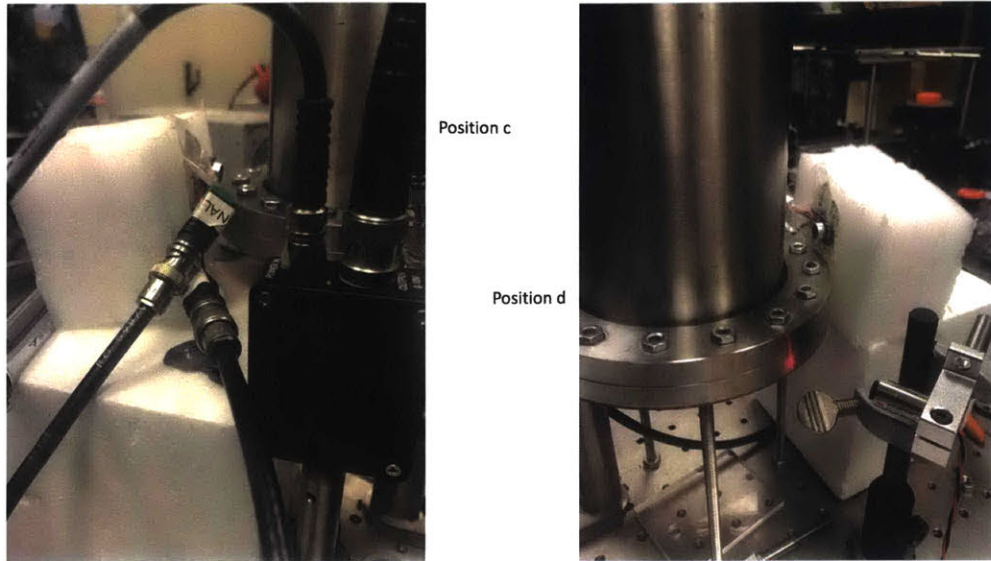


Figure E.35: Microphone test for new resonator at position 'c' and position 'd'

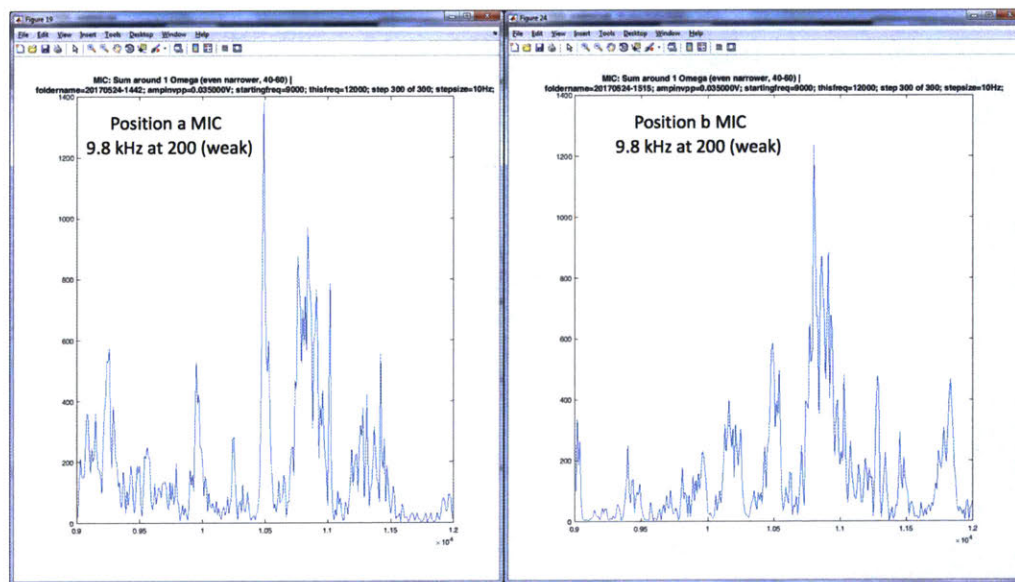


Figure E.36: Microphone signals for new resonator at position 'a' and position 'b' (9.8-10.2 kHz)

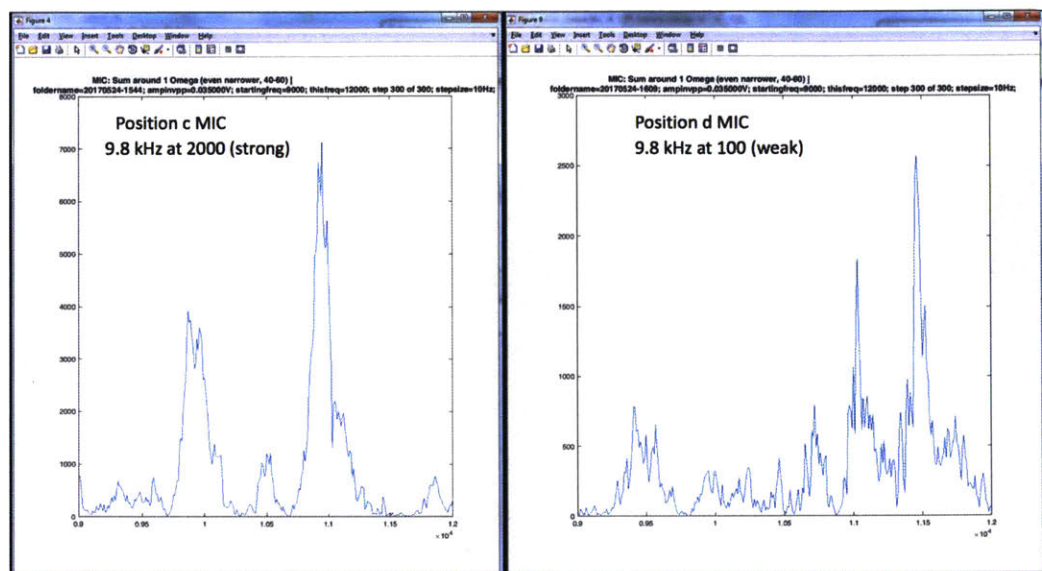


Figure E.37: Microphone signals for new resonator at position 'c' and position 'd' (9.8-10.2 kHz)

References

- 1 Metzler, F., Hagelstein, P., & Lu, S. (2017). Developing Phonon–Nuclear Coupling Experiments with Vibrating Plates and Radiation Detectors. *Journal of Condensed Matter Nuclear Science*, 24, 98-113.

Appendix F: Mercury Co-Deposition

F.1 Introduction to Role of Mercury in Phonon-Nuclear Studies

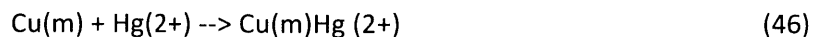
According to Hagelstein's up-conversion model, the lower the nuclear transition energy is, the more likely up-conversion can happen. The lowest excited nuclear state of all stable nuclei occurs in ^{201}Hg at 1565 eV, which makes mercury the best candidate to test the up-conversion hypothesis. In addition, both Karabut and Kornilova claimed that they detected collimated X-ray around 1.5 keV in their experiments.^{1,2} We proposed that there was mercury contamination in both experiments and the reported 1.5 keV X-ray was due to the up-conversion of contaminated mercury. In order to test the hypothesis, a lab vibration experiment with mercury co-deposition was necessary.

F.2 Introduction to Health Issues Working with Mercury

It is well known that mercury can be toxic. Mercury is the only metal that is liquid at room temperature. Not only touching the mercury can cause health issues, but also the inhalation of mercury vapor can be harmful and even fatal. There are usually very strict standards for scientific research with metal mercury. On the other hand, mercury in an amalgam is much safer. Mercury amalgam is widely used as a filling material in dental clinics. In our experiment, in order to get a sample with a small amount of mercury for tests involving vibrations, we introduced less than 1 microgram mercury in a copper sample to form a small amount of amalgam near the surface.

F.3 Electroless Mercury Deposition Procedure

We prepared the mercury amalgam sample following input from Francis Tanzella at SRI according to the following reaction³



This reaction is well known in the literature. It is used as a standard test to determine whether there is mercury contamination in water. Copper is the best candidate for this approach as it is

well known to bind with mercury strongly. Mercury binds to copper to form an amalgam and there is no volatile mercury in the bound copper.³

An atomically clean copper metal surface forms an oxide in air rapidly. In order to make the mercury amalgam sample, we need to remove the oxide layer of copper before exposure to mercury. Acid is known to be effective to remove the oxide layer. For instance, oxide removal with H_2SO_4 is reported in the literature. When a copper foil is placed in sulfuric acid, the oxide layer is removed; if mercury is dissolved in the sulfuric acid then it plates out on the copper foil. The mercury is tightly bonded to the copper in this case.

We used 0.003'' copper foil from McMaster and prepared several square copper pieces with an area around 2'' x 2''. We obtained a 0.1 M H_2SO_4 solution (pH = 0.7) and Hg_2SO_4 salt from Sigma-Aldrich. We prepared saturated Hg_2SO_2 / H_2SO_4 solution by mixing 0.1 g Hg_2SO_4 salt in 100 mL H_2SO_4 at room temperature. The solubility of Hg_2SO_4 salt in 0.1 M H_2SO_4 at room temperature is 0.04 g/100 mL. After cleaning the copper foil with acetone and de-ionized water, we applied a small amount (less than 1 mL) of Hg_2SO_2 / H_2SO_4 solution to the center of copper foil surface with a micropipette. The solution helps remove the oxide layer and form mercury amalgam at the center of copper foil surface. The micropipette helps control the volume of the solution at a very accurate small amount. We were able to calculate how much mercury we deposited to the copper surface from the volume of Hg_2SO_2 / H_2SO_4 solution we applied with the micropipette and the solubility of the saturated solution. After applying the solution, we waited until all mercury went into copper and wiped the remaining drops with tissue.

F.4 Experimental Results with Mercury Deposition

The MIT EHS (Environment, Health, and Safety) department approved our sample preparation procedure before we started making samples. We ran the above process at MIT EHS. At the end of the experiment, we disposed of all used materials and chemicals in their satellite trash can. We repeated the process several times to obtain multiple mercury amalgam samples.

F.4.1 First Mercury Deposition Experiment

The following Figure F.1 and F.2 show the process and results of the first mercury deposition experiment. As shown in Figure F.1, we added several different volume drops of $\text{Hg}_2\text{SO}_4 / \text{H}_2\text{SO}_4$ solution to several pieces of copper foils. All the drops fully evaporated after 4 hours and the results are shown in Figure F.2. In this experiment we could get the exact amount of Hg deposited to Cu as all the drops were fully evaporated; therefore all the Hg should be bounded to Cu.

Another goal for our mercury deposition experiment was to get a quantitative correlation between the silveriness of the sample and the density of Hg deposited on Cu per area. The color of the sample turns silver after Hg is deposited on the Cu surface. The extent of the silveriness should be proportional to the amount of Hg deposited on Cu per area. However, as shown in Figure F.2, except for the silveriness, there is also some yellow color residue left on the sample covering the silveriness area. This yellow color residue would influence the appearance of silveriness which would make us unable to get an accurate correlation between the extent of silveriness and the density of Hg.

We cleaned the sample with de-ionized water but the residue could not be washed away. We put two samples in de-ionized water overnight, resulting in random black and purple spots which may belong to CuO and Cu_2O . To verify where the residue comes from, we put only H_2SO_4 on Cu foils without Hg_2SO_4 and we still got the same residue. From this result, we learned that the residue was from H_2SO_4 acid. However, we were not sure what exactly the residue was.

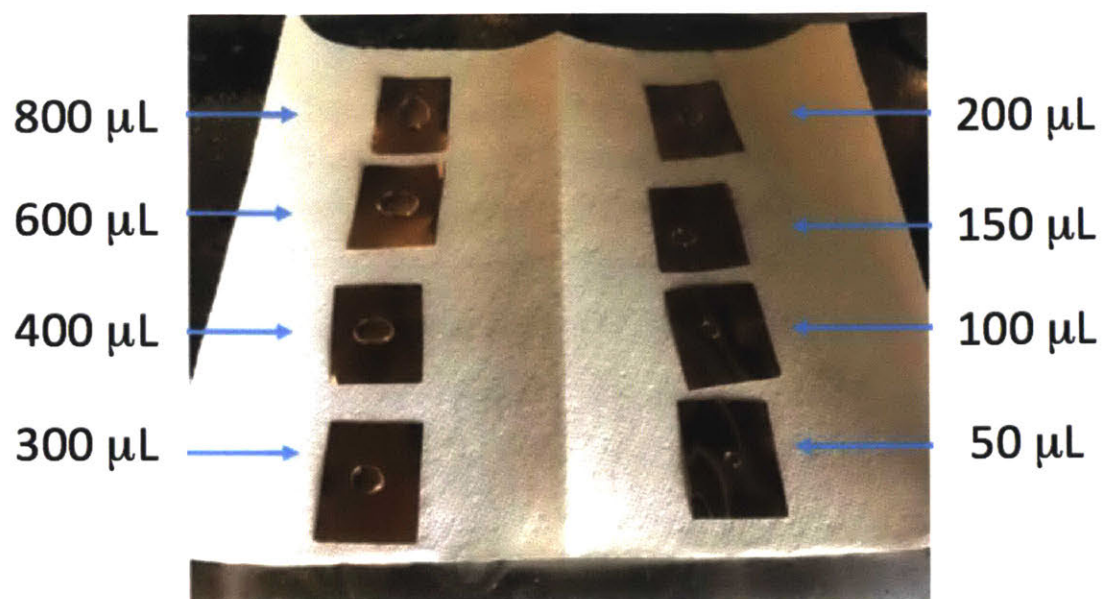


Figure F.1: Process of 1st mercury deposition experiment

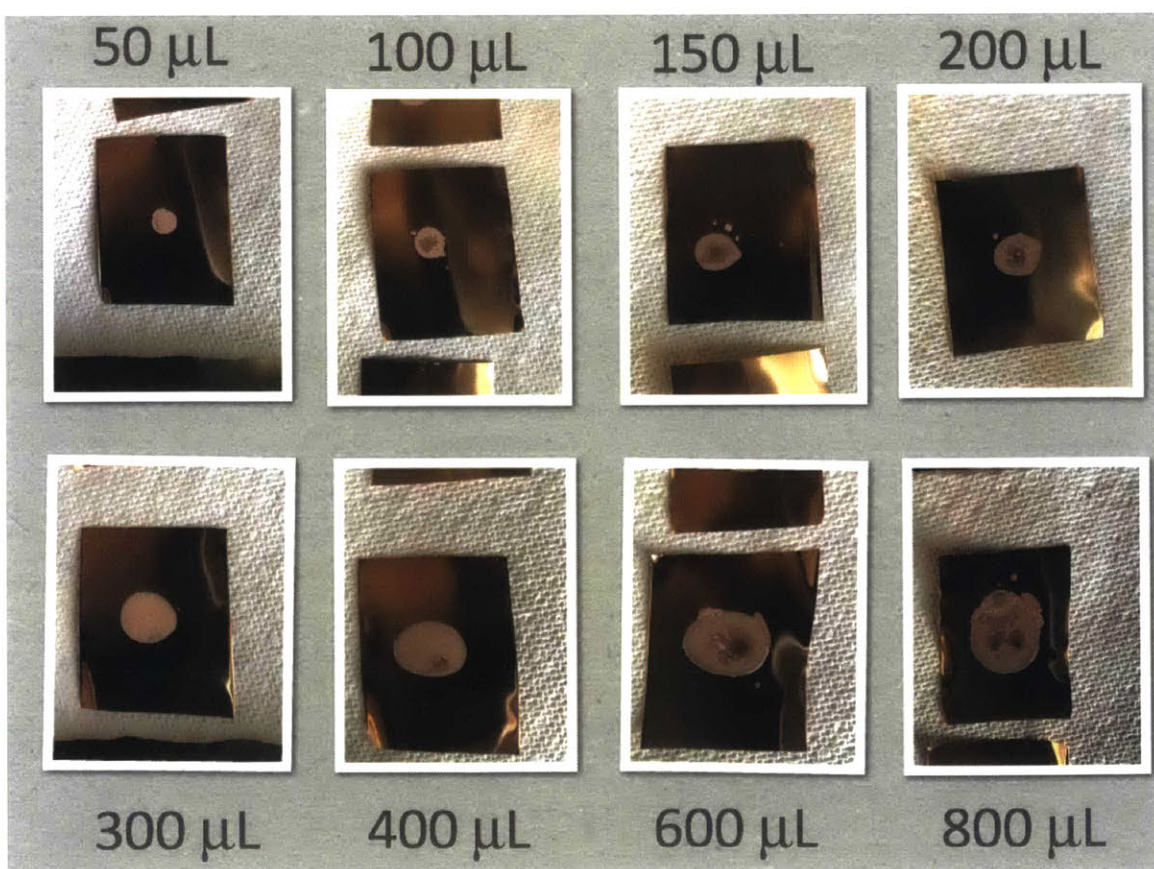


Figure F.2: Results of 1st mercury deposition experiment

F.4.2 Second Mercury Deposition Experiment

The second experiment was similar to the first one except that we wiped the drops right before they fully evaporated. By doing this we hope all Hg would go into Cu after a while so that we could still know the exact amount of Hg. Moreover, we were hoping we could get rid of the residue but keep the silveriness so that we can get a good correlation between the silveriness and amount of Hg per area.

Figure F.3 shows the results of the 2nd experiment with different volume drops and corresponding evaporating times before wiping the drops. The residue looks better but still exists. We still cannot get good correlation due to the residue.

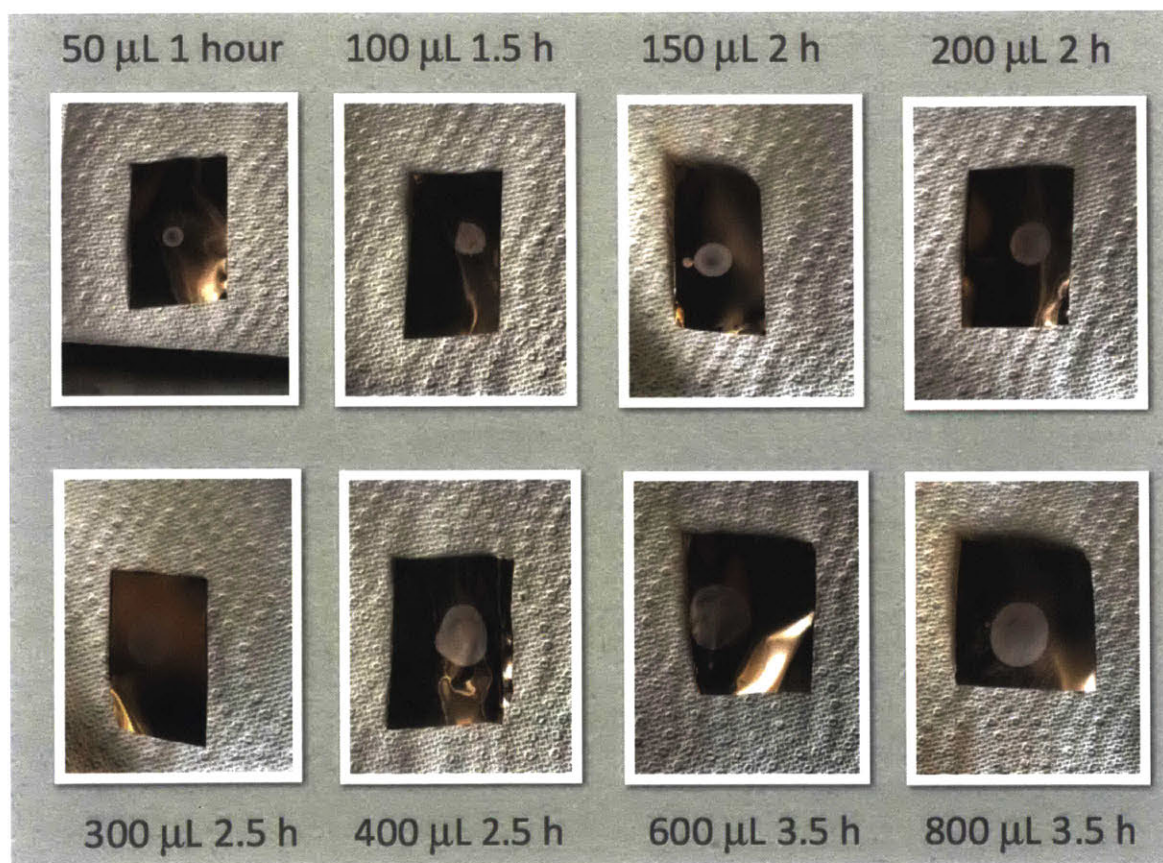


Figure F.3: Results of 2nd mercury deposition experiment

F.4.3 Third Mercury Deposition Experiment

The main purpose of this experiment is to make different samples with the same amalgam areas but different amounts of Hg. In previous experiments, we had different amounts of Hg in different samples, but we also had different areas in different samples. We might get the same amount of Hg per area in different samples, which would not work for our calibration purpose as the silveriness should be correlated to the density of Hg per area. Figure F.4 shows the results of the 3rd experiment. All drops were 100 μL so that areas are all the same. We used solutions with different concentrations so that amounts of Hg are different. The numbers next to each drop indicate the percentage of drop concentration compared with the solubility (0.04 g/100 mL). We wiped all the drops after 1.5 hours right before they fully evaporated.

We can see that the silveriness is clearly different in different samples. We probably can calculate the exact amount of Hg as we wait for 1.5 hours. We still cannot get good correlation due to the residue.

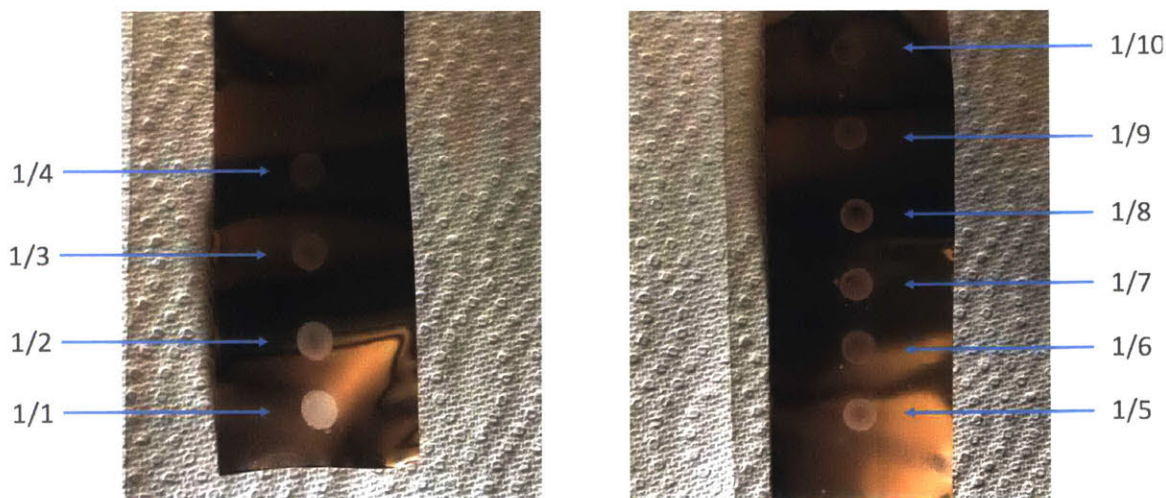


Figure F.4: Results of 3rd mercury deposition experiment

F.4.4 Fourth Mercury Deposition Experiment

We noticed that the residue would be less if the drop evaporation time were shorter. The purpose of this experiment is to find the shortest time that silveriness does not increase which

means most Hg has gone into Cu. By doing this, we could minimize the residue while knowing the exact amount of Hg deposited into Cu.

Figure F.5 and F.6 show the results of the 4th experiment. All drops are saturated Hg_2SO_4 / H_2SO_4 solution with different evaporation times. All the evaporation times for this experiment are much shorter than those in previous experiments. Initially we thought that Hg should go into Cu very fast. However, the '45 mins' picture still shows much more silveriness than the '30 mins' picture does. This indicates that the process of Hg going into Cu is not as fast as we were hoping. Regarding the residue, there is no residue before 12 minutes but the residue gets very clear after 20 minutes. From this experiment, we learn that we probably can not avoid residue if we want all Hg to go into Cu.

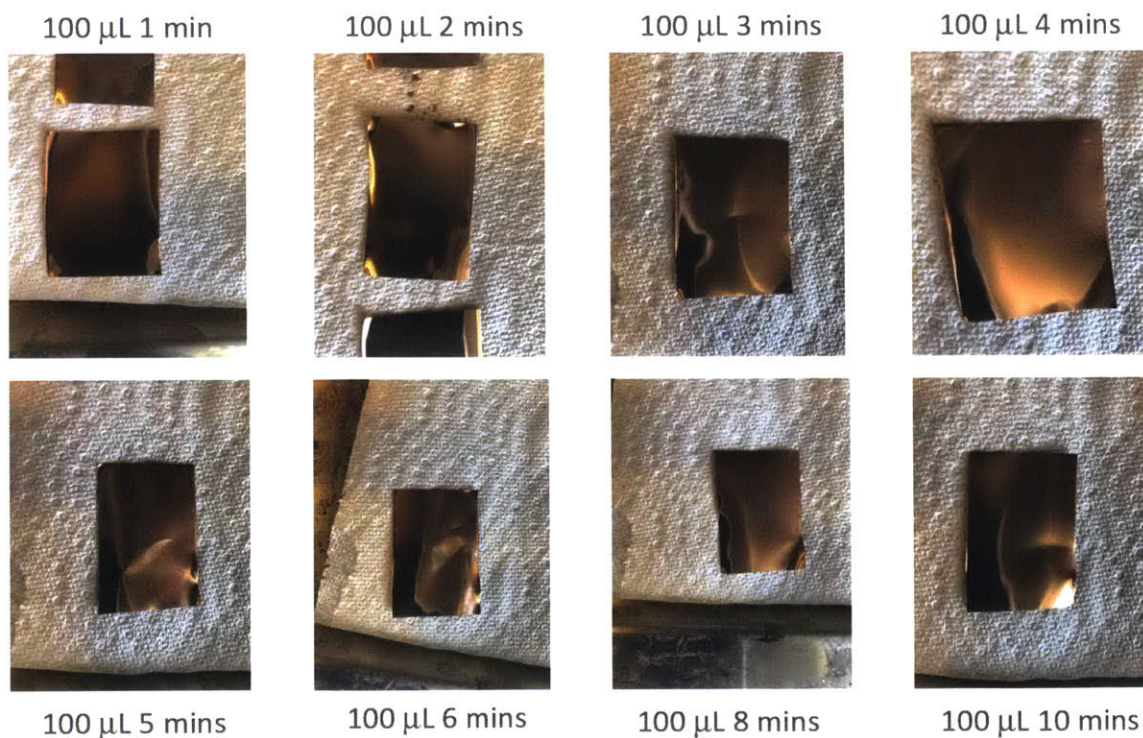


Figure F.5: Results of 4th mercury deposition experiment

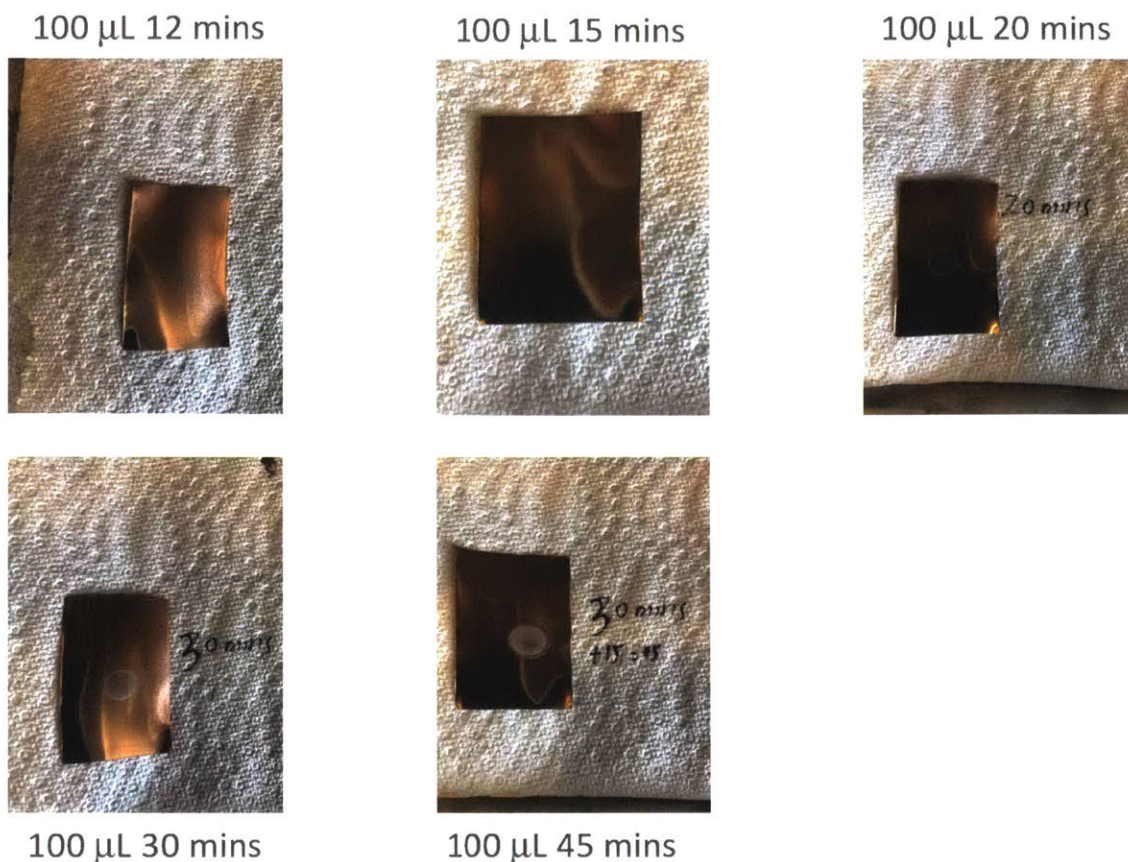


Figure F.6: Results of 4th mercury deposition experiment continued

F.4.5 Fifth Mercury Deposition Experiment

In this experiment we made a sample with a larger amount of Hg than previous samples. We would like to use this sample for the X-ray fluorescence test to make sure there is Hg in the sample. We added 800 μL saturated solution drop to the copper foil and wiped the drop after 15 minutes of evaporating. We immediately added another 800 μL drop and wiped it after 15 minutes. Then we repeated the same process for the third time

Figure F.7 shows the results of the 5th experiment. Later we realized from the 4th experiment results that 15 minutes evaporating time might be not enough. So we did another similar experiment as the 5th experiment with longer evaporation time.

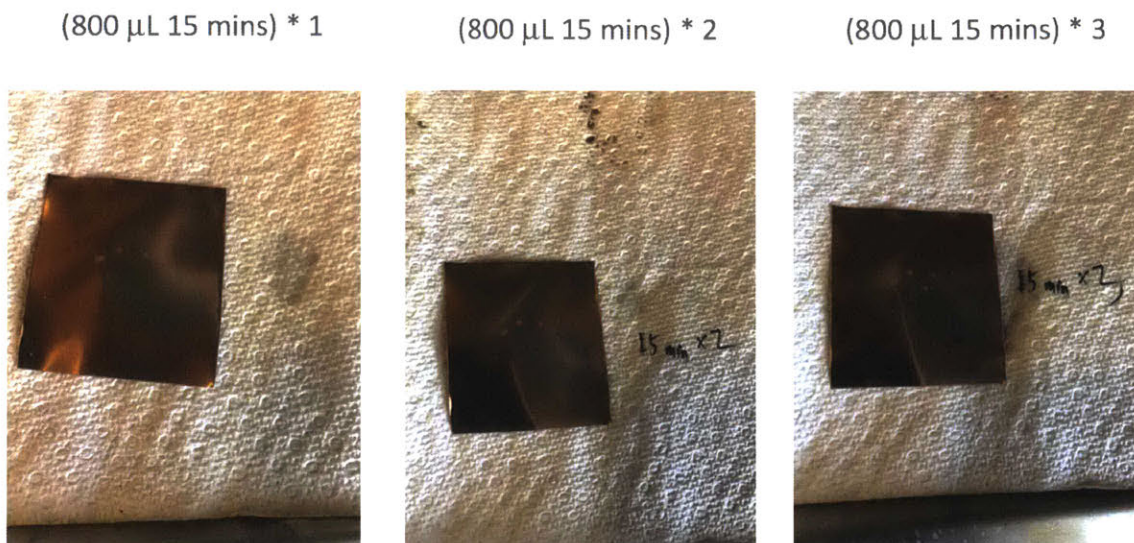


Figure F.7: Results of 5th mercury deposition experiment

F.4.6 Sixth Mercury Deposition Experiment

This experiment was similar to the fifth one except that the evaporation time for each drop changed to 28 minutes and there was a 24 hour waiting period between each drop which allowed Hg more time to go inside Cu.

Figure F.8 shows the results of the 6th experiment. This sample should have the largest amount of Hg compared with all samples. We handled this sample with extreme caution and always put it in a sealed plastic bag. This sample would also be used for X-ray fluorescence test.

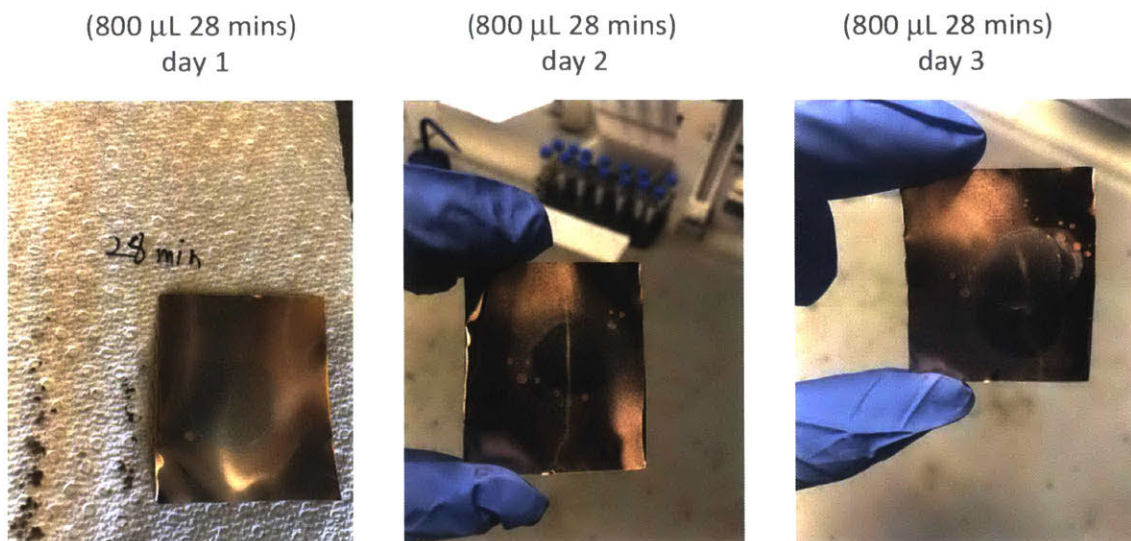


Figure F.8: Results of 6th mercury deposition experiment

F.4.7 X-ray Fluorescence Test

An X-ray fluorescence test was done at the MIT X-ray Diffraction Shared Experimental Facility for the sample we got in the sixth mercury deposition experiment. In order to confirm that mercury did exist on the sample, we ran X-ray fluorescence tests at two different spots on the sample surface. The first spot is within the solution drop area while the second spot is far outside that area. Figure F.9 shows the result of the X-ray fluorescence test. The green spectrum representing the first spot shows a clear peak for Hg while the red spectrum representing the second spot shows no Hg peak. From this result, we can confirm that Hg is successfully deposited into our sample.

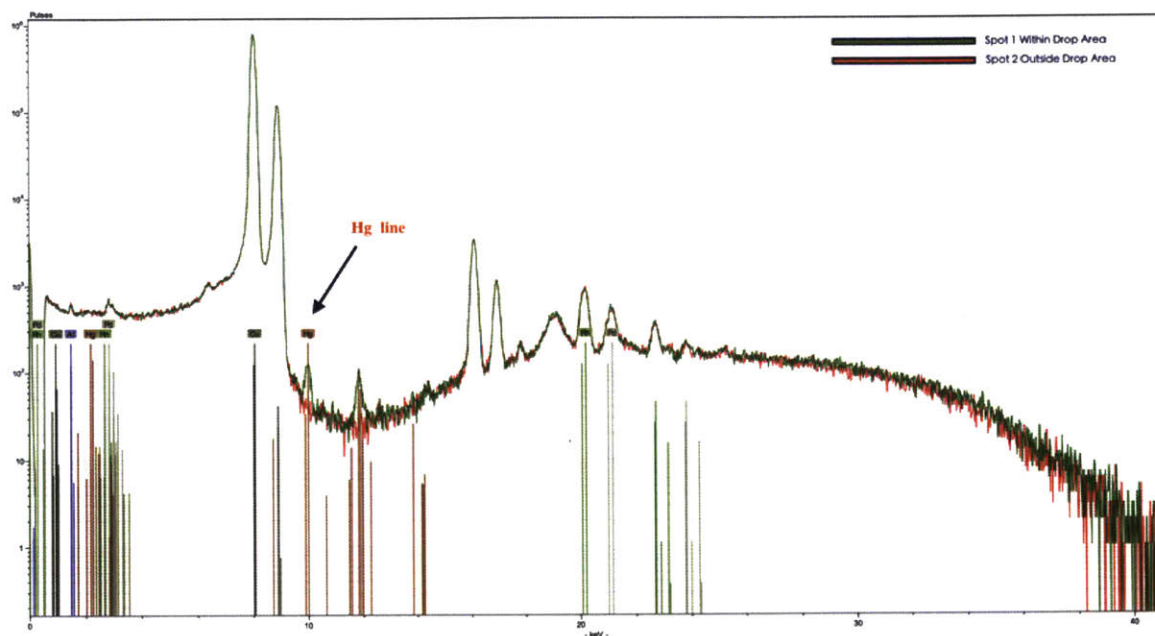


Figure F.9: X-ray fluorescence test of the sample in the 6th deposition experiment

F.4.8 Discussion of the Results

According to all the above results, we would have no problem if we only wanted to make a sample for our vibration experiment. We can control the amount of Hg deposited to Cu and the area of Hg. This should be good enough for our vibration experiment as we do not need to worry about residue for the vibration experiment. However, if we would like to get an accurate quantitative correlation between the silveriness and the amount of Hg per area, the residue would remain a problem as it would influence the calibration of the silveriness. In order to solve this problem, we analyzed the results of the 4th mercury deposition experiment. We found that there would be no residue before 12 minutes of evaporation. We assumed that Hg would go into Cu at a constant rate so that we could calculate the amount of Hg deposited into Cu based on the evaporation time. We would set 12 minutes as our standard evaporation time so that we could get rid of the residue and get a good quantitative correlation between the silveriness and the amount of Hg per area.

F.5 Future Plans

F.5.1 Experiment with Mercury and Resonator

We introduced the Karabut experiment in section 1.1. Our conjecture to explain the Karabut experiment is up-conversion theory and we proposed that there was mercury contamination in that experiment. We once thought that the phonon vibrations in the Karabut experiment were drumhead modes instead of longitudinal or transverse modes. In order to prove or disprove our conjecture, we would like to attach the mercury amalgam sample to the resonator in appendix E.4 which is designed to generate drumhead mode vibrations. We would like to see whether we could detect potential X-ray signals around the mercury amalgam sample due to up-conversion initiated by the resonator drumhead mode vibrations.

F.5.2 Experiment with Steel-Cu-Hg

According to Hagelstein's up-conversion theory, Fe-57 should play an important role in the Karabut and Kornilova experiments in terms of initiating the up-conversion. So instead of only doing experiments with Cu-Hg foils, we also would like to do experiments with Steel-Cu-Hg plate. The plan is to e-beam a thin layer of Cu on a steel substrate and apply Hg on the Cu layer. By doing this, we would have enough Fe-57 for up-conversion experiments and a safe mercury amalgam on the Cu layer at the same time.

The experiment introduced in this appendix is done by me. All data shown in this section is taken and analyzed by me.

References

1 Karabut, A., Karabut, E., & Hagelstein, P. (2012). Spectral and Temporal Characteristics of X-ray Emission from Metal Electrodes in a High-current Glow Discharge. *Journal of Condensed Matter Nuclear Science*, 6, 217-240.

2 Kornilova, A. A., Vysotskii, V. I., Sysoev, N. N., Litvin, N. K., Tomak, V. I., & Barzov, A. A. (2010).

Generation of intense x-rays during ejection of a fast water jet from a metal channel to atmosphere. *Journal of Surface Investigation. X-ray, Synchrotron and Neutron Techniques*, 4(6), 1008-1017. doi:10.1134/s1027451010060224

3 Amalgam_(chemistry), (2018, August 3). In *Wikipedia*. Retrieved August 3, 2018, from [https://en.wikipedia.org/wiki/Amalgam_\(chemistry\)](https://en.wikipedia.org/wiki/Amalgam_(chemistry))

Appendix G: Film Calibration

In the pinhole/film experiment, there is a difference between the cold image and the hot image. It is possible that the anomaly might be due to a nonlinear film response. A series of calibration exposures was done. The basic idea was to use the Co-57 Mossbauer source to expose the film for different time durations. Figure G.1 shows the images of several calibration exposures with different time.

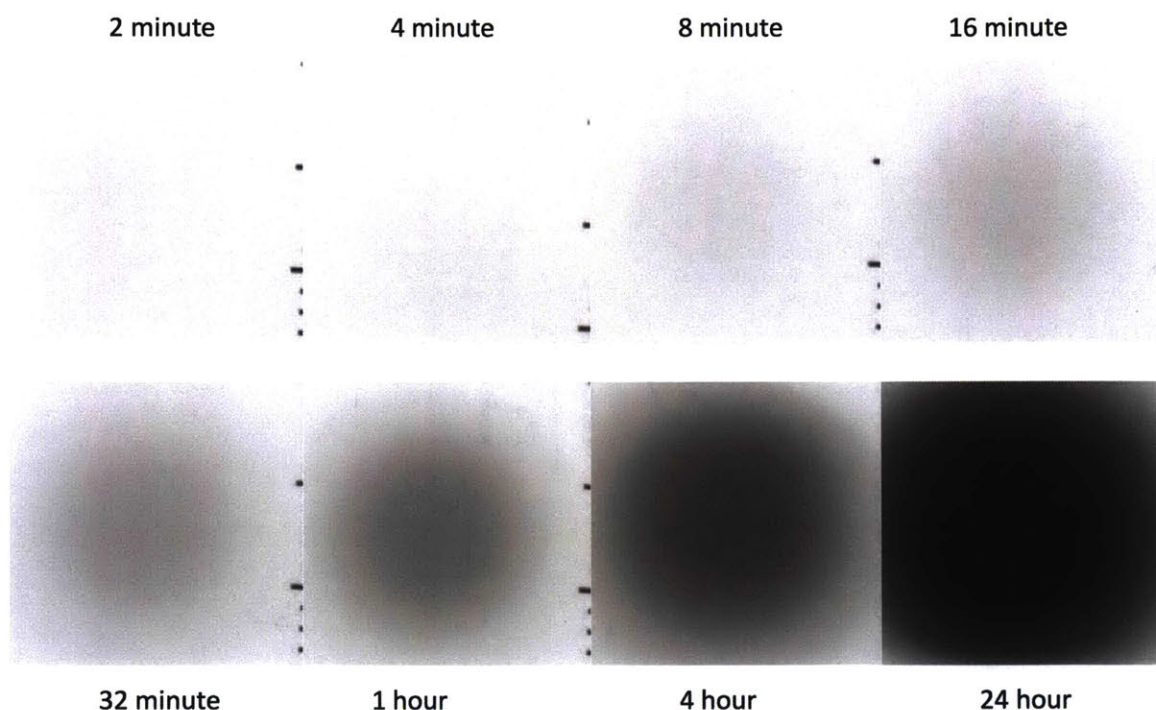


Figure G.1: A series of calibration exposures with different time durations

Knowing the duration and estimating the resulting peak exposure allows the construction of a calibration curve. In the live experiment, we have less low energy content and more high energy content. But the low energy content is favored in the calibration run. We determine the strongest exposure level for each image, make a histogram of counts per film density, and then choose lowest density corresponding to onset. Figure G.2 shows the calibration curve. With the calibration curve, we can have better analysis for the films in the pinhole/film experiment, and

we can determine whether the difference between cold and hot images is due to a nonlinear film response or not.

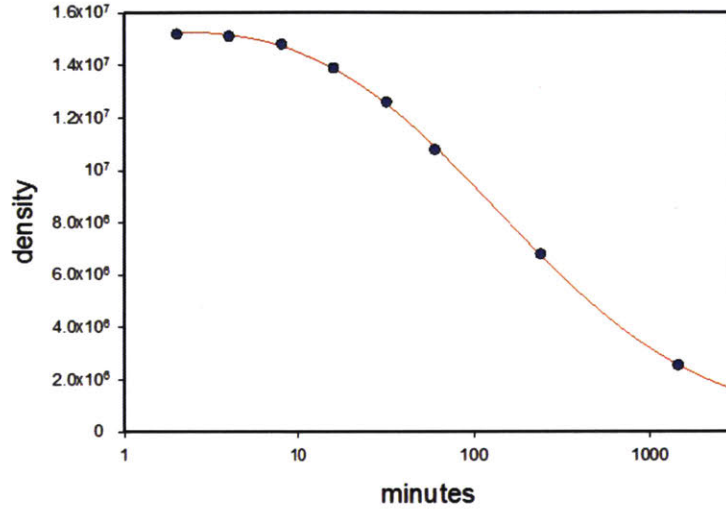


Figure G.2: Calibration curve

The fitting equation is shown as the following:

$$\text{density}(t) = A \frac{1 + a_1 \ln t + a_2 (\ln t)^2}{1 + b_1 \ln t + b_2 (\ln t)^2} \quad (47)$$

$$A = 1.5167 \times 10^7$$

$$a_1 = -0.194126 \quad a_2 = 0.00993522$$

$$b_1 = -0.212085 \quad b_2 = 0.0229389$$

The experiment introduced in this appendix is done by me. All data shown in this section is taken by me and analyzed by Hagelstein.

Appendix H: Pinhole/Film Experiment with 0.2 mm Pinhole

The results from the 0.5 mm images are very interesting and may provide evidence for delocalization. Experiments were done with the 0.2 mm pinhole in the hope of getting a higher resolution result, where it might be easier to see a delocalization effect. Figure H.1 shows the film images of the 0.2 mm pinhole/film experiment. The left image is the first cold image at room temperature. The middle image is the second cold image in room temperature. The right image is the hot image with the temperature increased to around 50C. Figure H.2 shows the heat map of film images.

A headache is that the light through the pinhole is reduced by a factor of $2.5^2=6.25$, but the harder gammas are not correspondingly reduced. It is hard to see features of interest in the analysis since background due to the harder gammas is so strong. Another headache is that there is a gradient of density across the image, which makes analysis a headache. It is not clear why there is such a gradient present. Also, weaker effect is expected since the heat pulse was much weaker than for the 0.5 mm images.

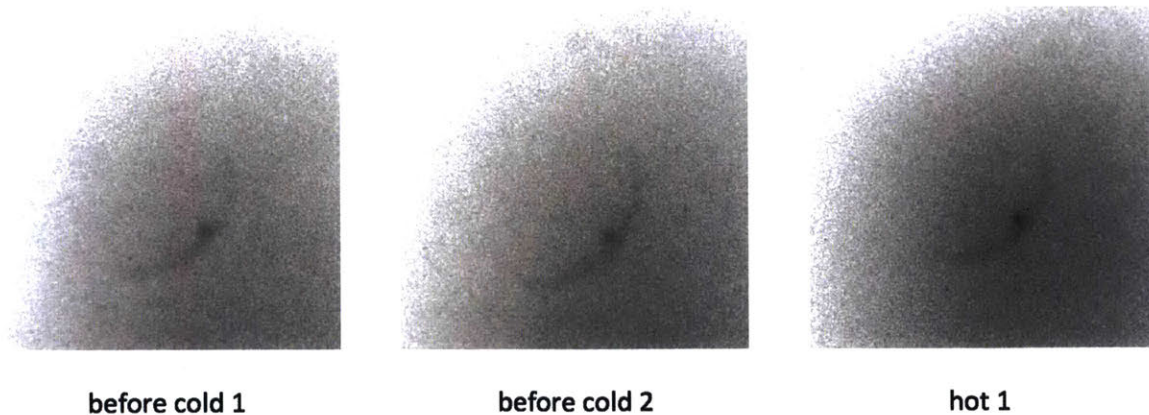


Figure H.1: Film images of the 0.2 mm pinhole/film experiment

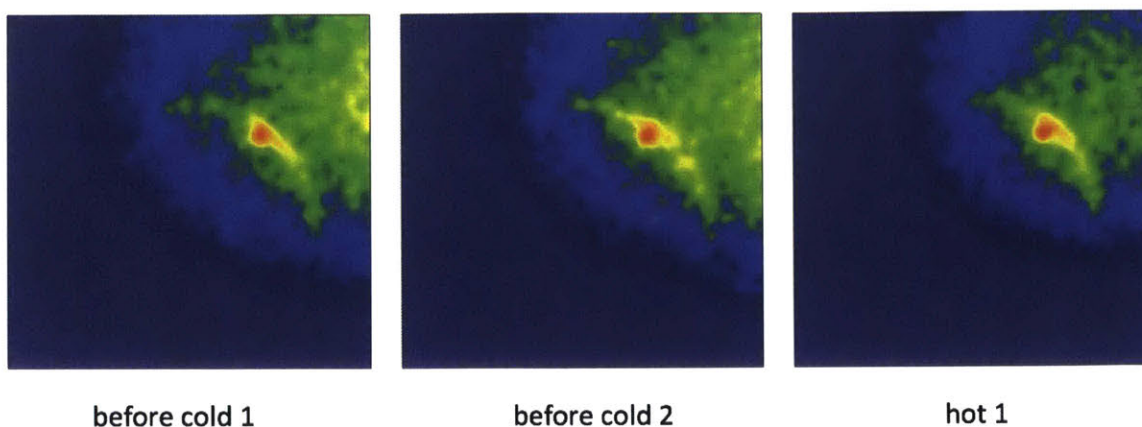


Figure H.2: Heat map of film images of the 0.2 mm pinhole/film experiment

The region around the ring is very similar in the three images. There does not seem to be a compelling difference between the two cold images before, and the hot image after. However, there is a major difference in the background density, which may be due to the harder gammas, or possibly the elevated temperature. We can see this in the diagonal scans shown in Figure H.3 and H.4 in the vicinity of the hot spot.

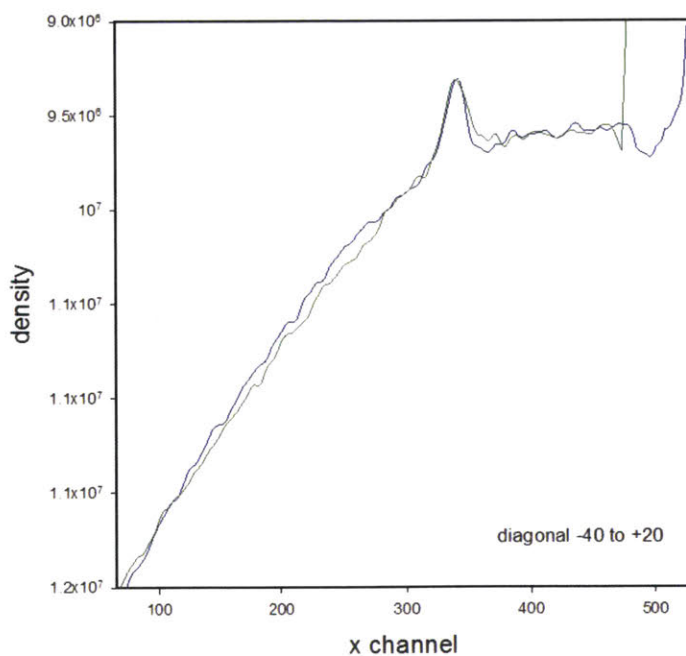


Figure H.3: Diagonal scan of the two cold images

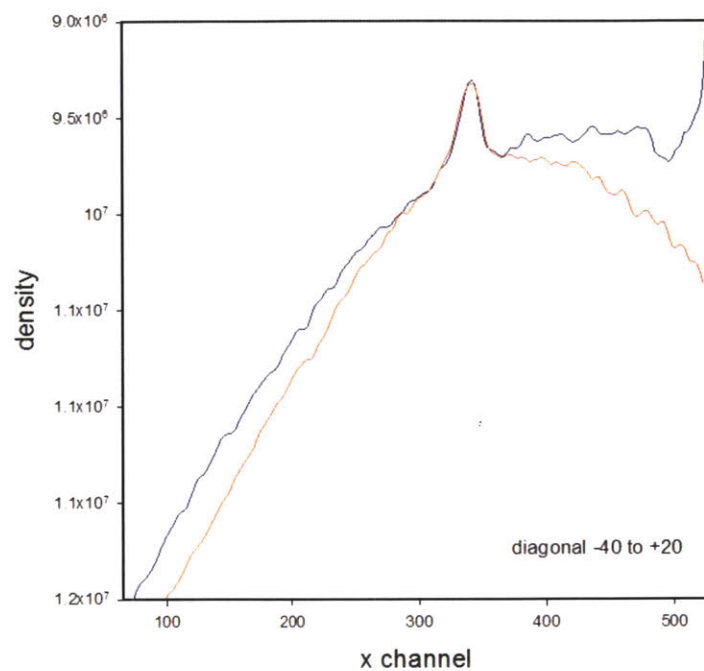


Figure H.4: Diagonal scan of the first cold image and the hot image

Figure H.5 shows the subtraction heat map of film images. The left one shows the heat map that the first cold image minus the second cold image. There is no apparent difference between the two cold images. The right one shows the heat map that the hot image minus the first cold image. There is a big difference in the background between the first cold image and the hot image.

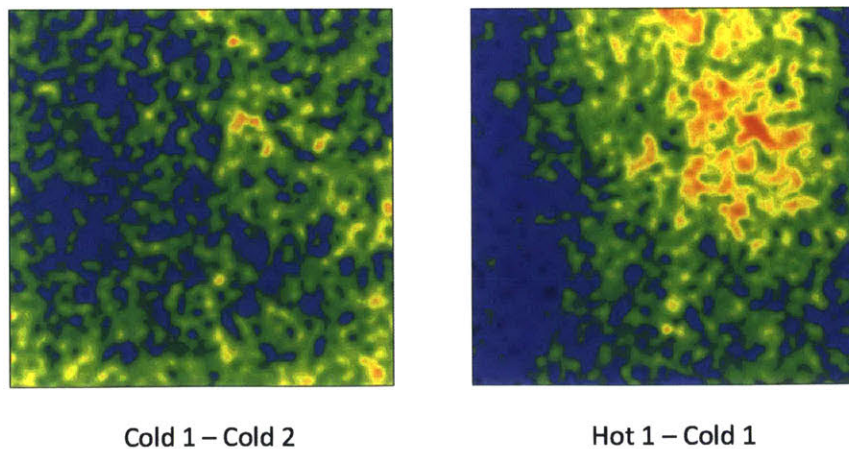


Figure H.5: Subtraction heat map of different film images

A lower temperature heat pulse was used for the 0.2 mm experiment (around 45 C) than for the 0.5 mm experiment (higher than 100 C), so it is not expected to see as much change. Harder gammas dominate film exposure with 0.2 mm pinhole, and the low energy lines give a minor increment. The ring contributes only a minor increment to the density. It is hard to say much quantitative for the lower gammas due to the weak signal.

We see a substantial change in the background between cold images and hot image. If this effect is real, it would suggest a substantial change in the harder gammas. Film temperature effect is also a possibility,¹⁻³ but we would have expected a change in the relative density at the “hot spot.” It is not sure whether we have seen an angular anisotropy effect in the harder gammas or just a thermal effect in the 0.2 mm pinhole/film experiment. We would like to clarify in future experiments if possible.

The experiment introduced in this appendix is done by me. All data shown in this section is taken by me and analyzed by Hagelstein.

References

- 1 Evans, C. H. (1942). The Effect of Temperature upon the Spectral Sensitivity of Photographic Emulsions. *Journal of the Optical Society of America*, 32(4), 214. doi:10.1364/josa.32.000214
- 2 Webb, J. H. (1935). The Effect of Temperature upon Reciprocity Law Failure in Photographic Exposure. *Journal of the Optical Society of America*, 25(1), 4. doi:10.1364/josa.25.000004
- 3 Berg, W. F., & Mendelssohn, K. (1938). Photographic Sensitivity and the Reciprocity Law at Low Temperatures. *Proceedings of the Royal Society A: Mathematical, Physical and Engineering Sciences*, 168(933), 168-175. doi:10.1098/rspa.1938.0167

Appendix I: Pinhole/Film Experimental Results for Sample 2

We made 2 samples for our experiments. We evaporated more Co-57 on Sample 2 than on Sample 1, in part to test to see whether having more Co-57 would give us a stronger version of the anomalies. Based on our experience with Sample 2 so far, there is no indication that more Co-57 gives any enhancement.

We also made the evaporation spot closer to the edge in Sample 2, in the hope of getting a faster response. Figure I.1 shows the picture of Sample 2 tightened by wood blocks. We can see that the Co-57 spot is close to the steel plate edge.

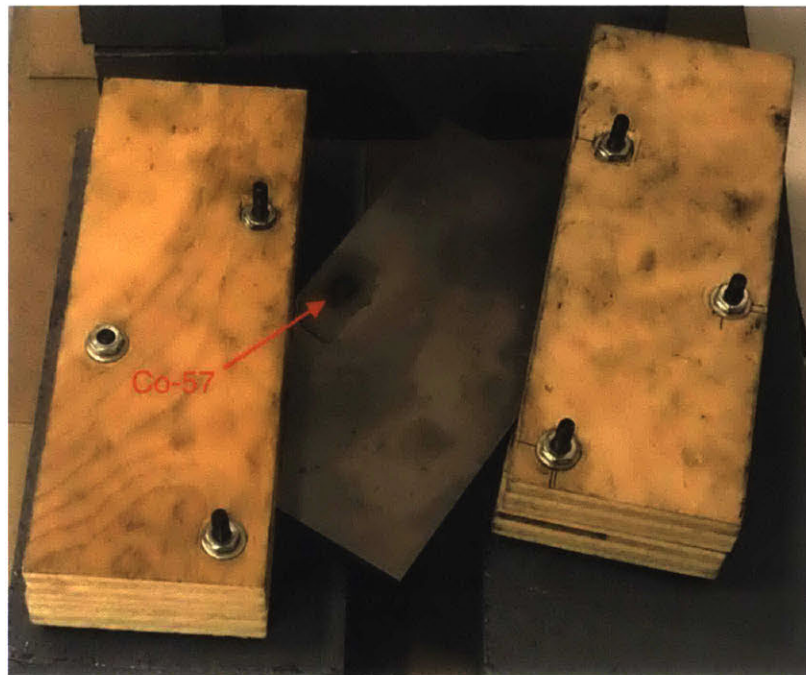


Figure I.1: Picture of Sample 2 tightened by wood blocks

To learn the distribution of radiation, a pinhole/film experiment was done for Sample 2 with a 1 mm pinhole camera. Figure I.2 shows the high-resolution picture of Co-57 in Sample 2 taken by Canon digital single-lens reflex camera. Figure I.3 shows the pinhole/film image of Co-57 in Sample 2 with 1 mm pinhole camera and 23-hour exposure time. We see that the two pictures match with each other quite well.

The experiment introduced in this appendix is done by me. All data shown in this section is taken and analyzed by me. The high resolution DSLR picture is taken by Metzler.

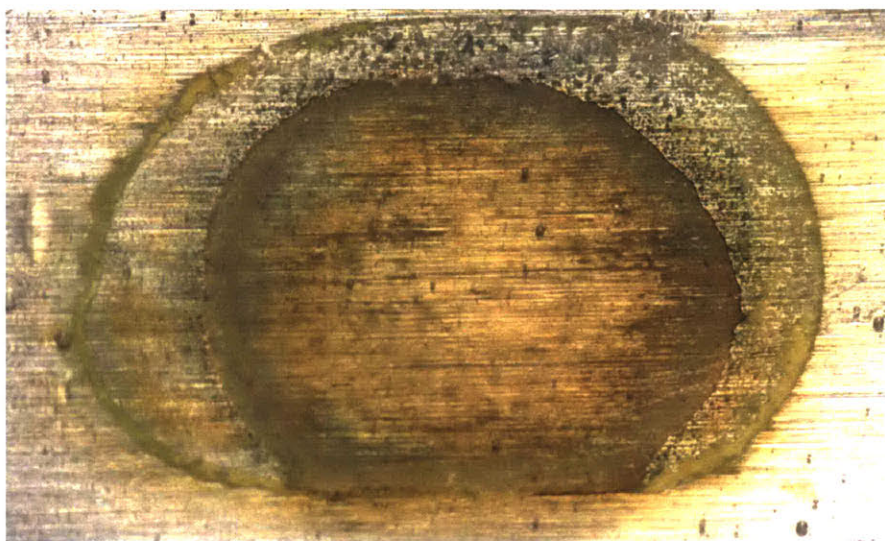


Figure I.2: High-resolution picture of Co-57 in Sample 2 taken by DSLR

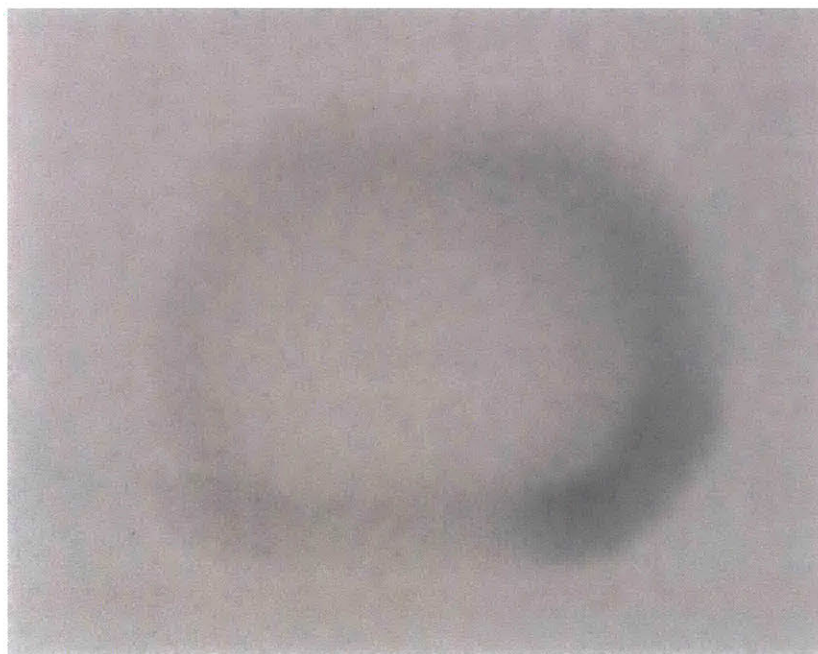


Figure I.3: Pinhole/film picture of Co-57 in Sample 2 with 1mm pinhole and 23-hour exposure time

Appendix J: More Angular Anisotropy Experimental Data

In the angular anisotropy experiments, the harder gammas of Co-57 (122 keV and 136 keV) responded not only to wood clamping but also to some other stimulation. This was first noticed in an experiment originally intended as a control test. The idea was to leave the wood clamps on for a long time, and then move the plate from a position far from the detector to a position in front of the detector. Figure J.1 shows the time history of 122 keV in this experiment. There are clear fast transients at the beginning of the experiment, which indicates that the sample responds to moving.

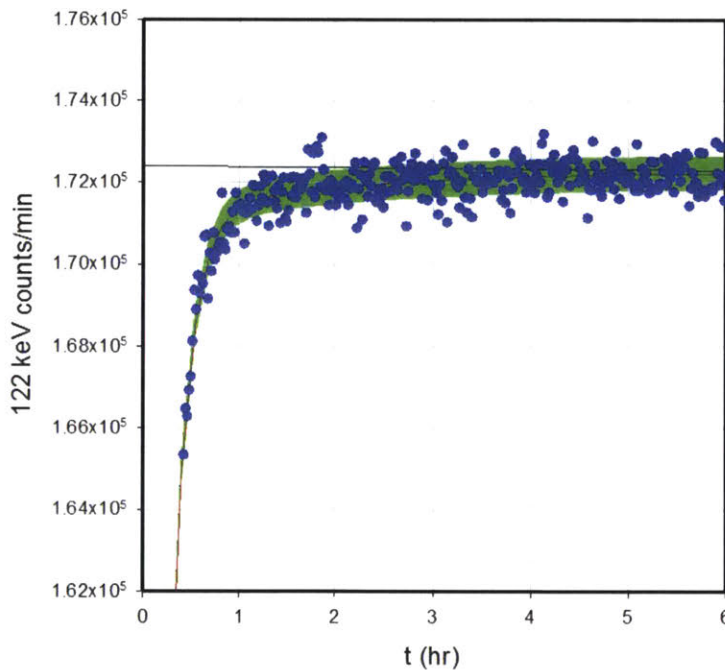


Figure J.1: Time history of 122 keV in the angular anisotropy moving test

The possibility that the early fast transients were artifacts due to the detector was ruled out with the help of the lead plate control test introduced in Chapter 8. In order to figure out what exactly the sample was responding to, several subsequent tests were done. In an experiment, the sample was pushed twice by fingers. The idea was to see whether introducing a shear stress could induce an anomaly. The first push was not too hard lasting 30 seconds. The second push was much

harder lasting 60 seconds. There were no early transients nor other anomalies in both of the two finger push tests.

In another experiment, the plate was taken away from the detector, twisted by hand, and then put back in front of the detector. Figure J.2 shows the time history of 122 keV in the first couple of hours. There is no early fast transient. Figure J.3 shows the time history of 122 keV in a longer time. There seems to be a longer-term response. It is a small effect, but noticeable because our statistics are pretty good.

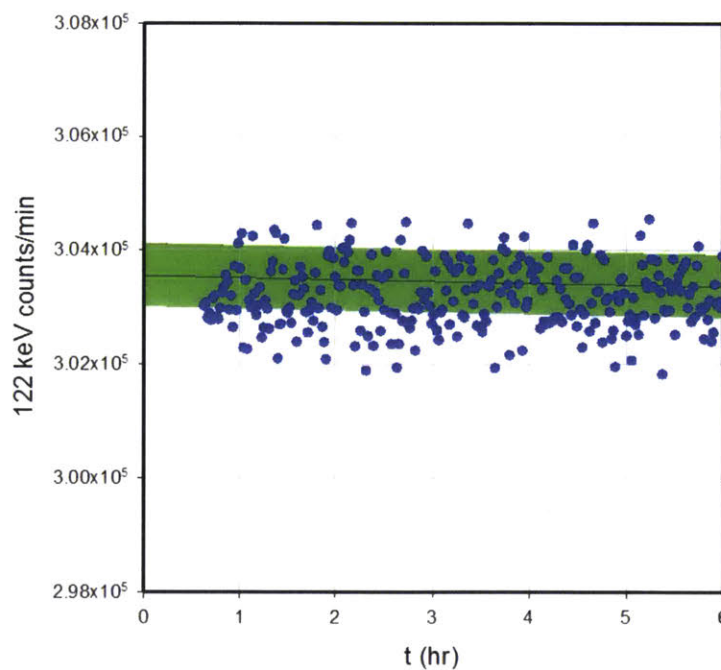


Figure J.2: Shorter time history of 122 keV in the angular anisotropy twisting test

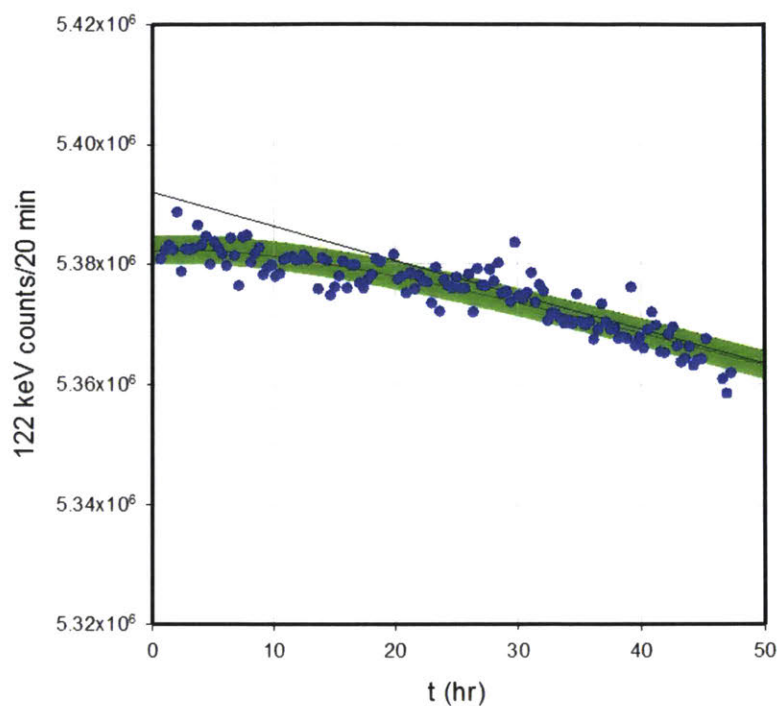


Figure J.3: Longer time history of 122 keV in the angular anisotropy twisting test

In another test, the plate had been lying horizontally before the experiment and was moved to the vertical position at the beginning of the experiment. The idea here was to go between lying and standing upright, to see if that could make a difference. Figure J.4 shows the time history of 122 keV in the first couple of hours. This relative gentle and mild movement perhaps gives us a version of the fast transient.

In a similar experiment, the plate was standing up prior to the run and was laid horizontally at the beginning of the test. Figure J.5 shows the time history of 122 keV in the first couple of hours. There is no fast transient this time. Figure J.6 shows the time history of 122 keV in longer time. There is a slower transient that looks like a real effect with longer accumulation.

Up to now, we have not confirmed yet what exactly the plate responds to in the angular anisotropy experiment. We would like to figure it out in future experiments if possible.

The experiment introduced in this appendix is done by me. All data shown in this section is taken by me and analyzed by Hagelstein.

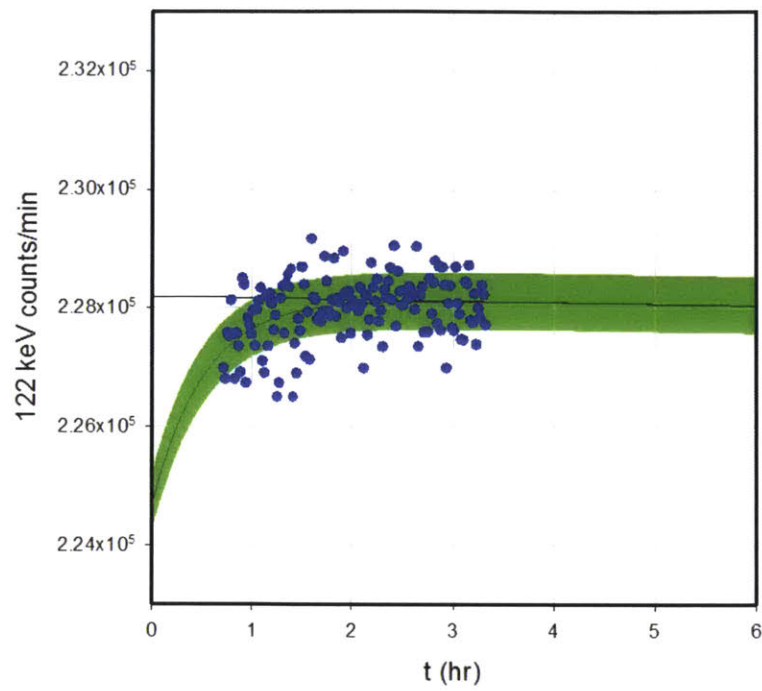


Figure J.4: Time history of 122 keV in the angular anisotropy lying to standing test

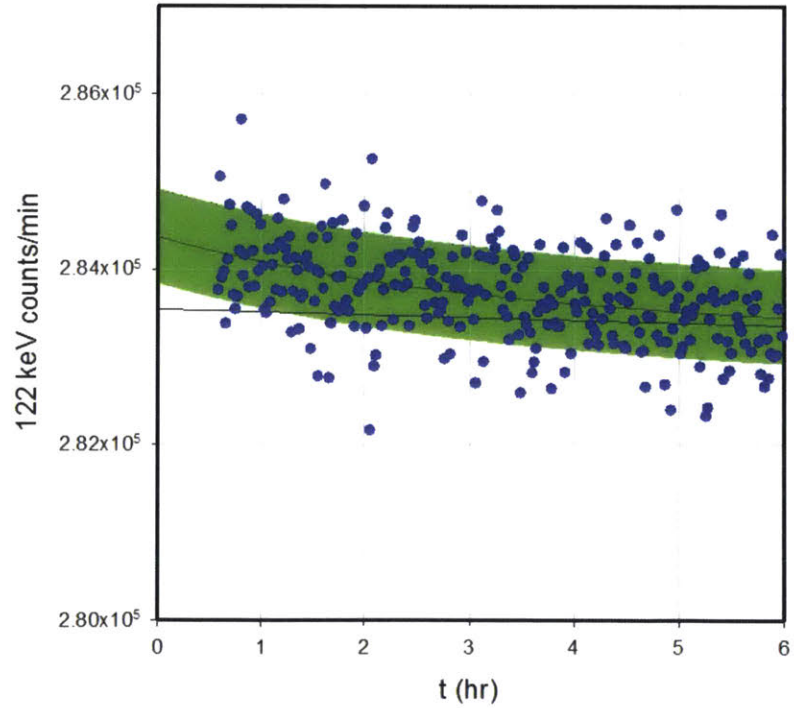


Figure J.5: Shorter time history of 122 keV in the angular anisotropy standing to lying test

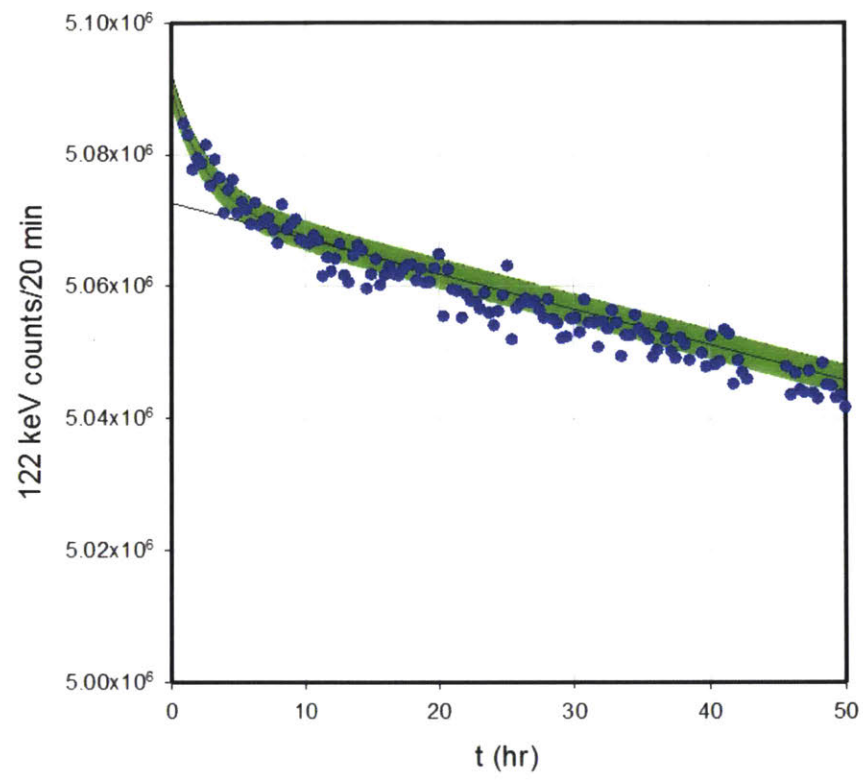


Figure J.6: Longer time history of 122 keV in the angular anisotropy standing to lying test

Appendix K: Bent Crystal Spectrometer

When excitation transfer happens, there can be energy exchange between Co-57 14.4 keV excited state and phonon energy. The energy exchange can lead to line broadening for the 14.4 keV spectrum. The line broadening should be very small in the eV range. The resolution for the Amptek detector at 14.4 keV is around 200 eV, which is not enough to detect the line broadening due to energy exchange.

Except for the 14.4 keV, we are also interested in detecting several other lines such as Hg line (1565 eV), Ta line (6238 eV) and Fe K-alpha line (6.4 keV) with very high resolution. Similarly, the resolution for the Amptek detector at these lines cannot satisfy our requirements. We need to build a high-resolution X-ray spectrometer. We started by building a bent crystal spectrometer for the Fe K-alpha line at 6.4 keV.

The wavelengths for X-rays are in the nm range. For example, the wavelength for Fe K-alpha (6.4 keV) is 0.194 nm. It is difficult to make a regular grating with constant in the nm range. Lattice constants for crystals are in the nm range. Crystals can be used to disperse various X-ray components.¹ Figure K.1 shows how a crystal selects X-rays with particular wavelengths. For a given incident angle, the crystal only reflects X-rays with wavelengths matching the Bragg equation.¹

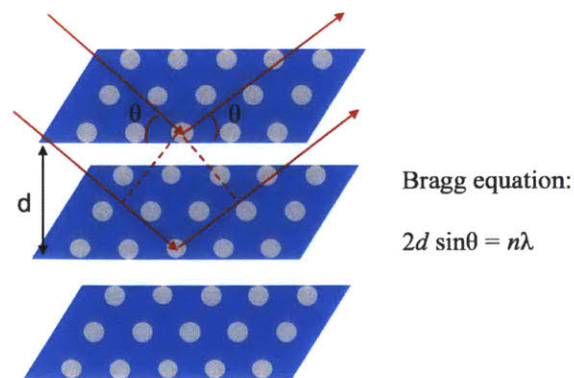


Figure K.1: A crystal only reflects X-rays with wavelengths matching the Bragg equation¹

If our target is Fe K-alpha line with 0.194 nm wavelength, we want a crystal with lattice constant $2d$ slightly larger than 0.194 nm. Applying the wavelength to the Bragg equation¹

$$2d\sin\theta = n\lambda \quad (48)$$

Choosing order $n=1$ allows getting more intensity. The Bragg angle can be written as

$$\theta_B = \arcsin\left(\frac{\lambda}{2d}\right) \quad (49)$$

The resolving power is²

$$\frac{E}{\Delta E} = \frac{\lambda}{\Delta\lambda} = \frac{\tan\theta_B}{\Delta\theta_C} \quad (50)$$

$\Delta\theta_C$ can be approximately estimated as 1 arcmin.²

The resolution ΔE is better when the Bragg angle θ_B is larger.

$2d$ has to be larger than $\lambda = 0.194\text{nm}$, but we want $2d$ to be as close to λ as possible.

There are many different crystals with different lattice constants.³ Table K.1 shows the top 3 options for Fe K-alpha. The cost is for a spherically bent crystal with curvature radius 1000 mm, wafer diameter 100 mm, and thickness 0.3 mm. We got the price and leading time information from two suppliers in December 2017. Company S is a French multinational company named Saint-Gobain.³ Company X is a New Jersey company named XRStech.⁴ We chose to purchase the best option Ge(440) from XRStech to build the bent crystal spectrometer for Fe K-alpha.

Table K.1: Top 3 crystal options for Fe K-alpha

Material	Ge(440)	Si(333)	Ge(333)
$2d$ (nm)	0.200	0.209	0.218
θ_B (degree)	75.43	67.87	62.79
$\lambda/\Delta\lambda$	13293	8453	6686
ΔE (eV)	0.48	0.76	0.96
Cost (\$)	Company S: 12470 Company X: 11000	Company S: 8240 Company X: 6000	Company S: 12470 Company X: 11000
Leading time (weeks)	Company S: 8 Company X: 8	Company S: 8 Company X: 1	Company S: 8 Company X: 1

Professor Seidler's group at the University of Washington offered us great help with our bent crystal spectrometer design. It was very kind of Professor Seidler answering our questions by phone calls and email exchanges. Figure K.2 shows the scheme of our bent crystal spectrometer design at MIT with the help of several publications from Seidler's group.⁵⁻⁷ The crystal used is a Johann spherical bent³ Ge(440) crystal with 1000 mm curvature, 100 mm diameter and 0.3 mm thickness. Sample 2 (Co-57 on steel plate) is used as the Fe K-alpha source. An adjustable slit is put in front of the Co-57 area. The source and the slit are stabilized on a one-dimension translation stage. The detector used is the Ortec X-ray detector. The crystal, the source, and the detector are aligned on a 1000 mm Rowland circle⁵⁻⁷ according to the 75.43 degrees Bragg angle.

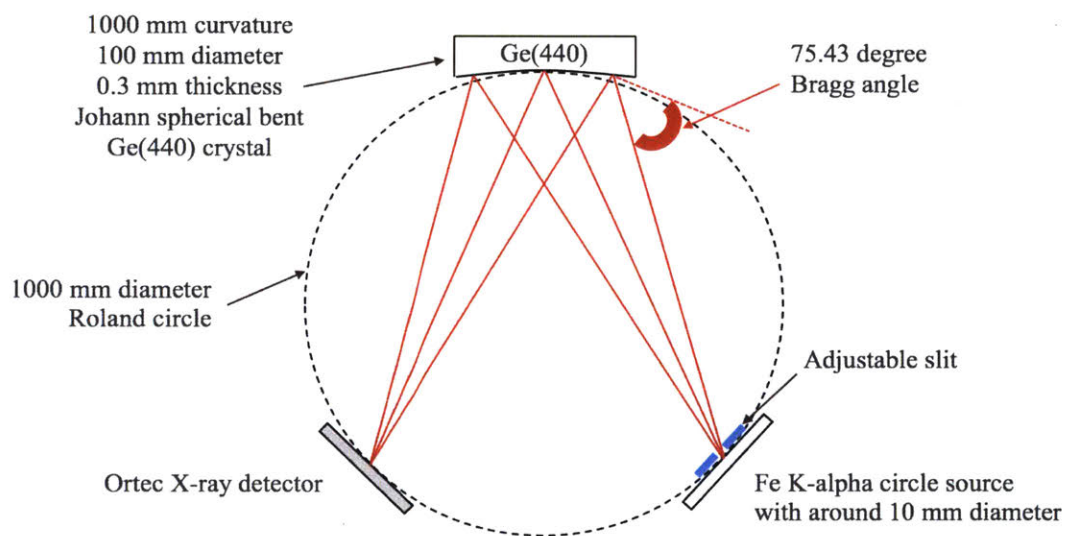


Figure K.2: Scheme of our bent crystal spectrometer for Fe K-alpha⁵⁻⁷

Figure K.3 and K.4 show two pictures of the Ge(440) spherically bent crystal we got from XRStexh. As shown in Figure K.5, the crystal is mounted on a mirror mount (Model Number KS4) from Thorlabs. As shown in Figure K.6, the mirror mount is mounted on a high-precision rotation stage (Model Number PR01) from Thorlabs which provides 5 arcmin resolution. Figure K.7 shows the picture of the Ge(440) bent crystal spectrometer alignment poster that we designed. We used

the poster for rough alignment and used the high-precision rotation stage for fine alignment. As X-ray is invisible, we also used a multi-direction laser (Model Number: GPL5) from Bosch to improve our alignment. The laser is shown in Figure K.8.

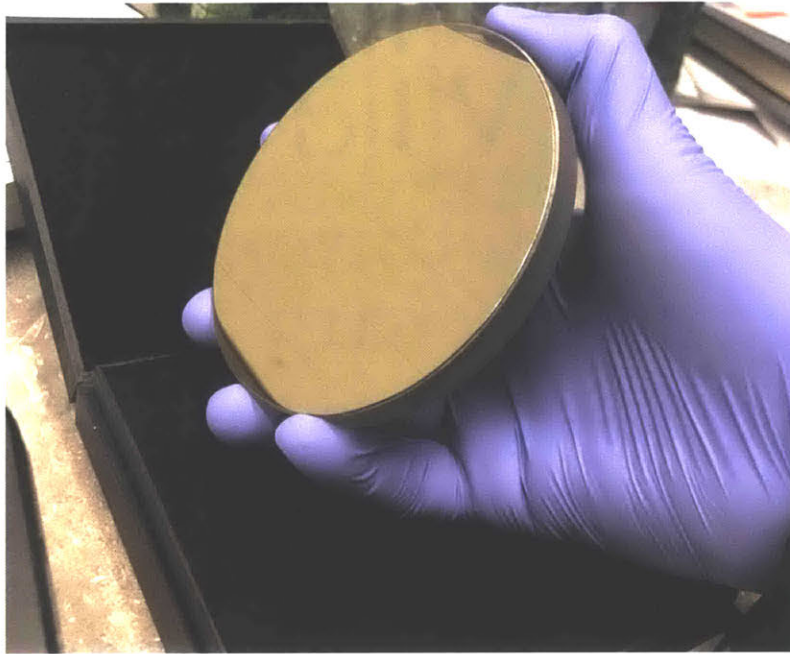


Figure K.3: Picture of the Ge(440) spherically bent crystal from XRStech

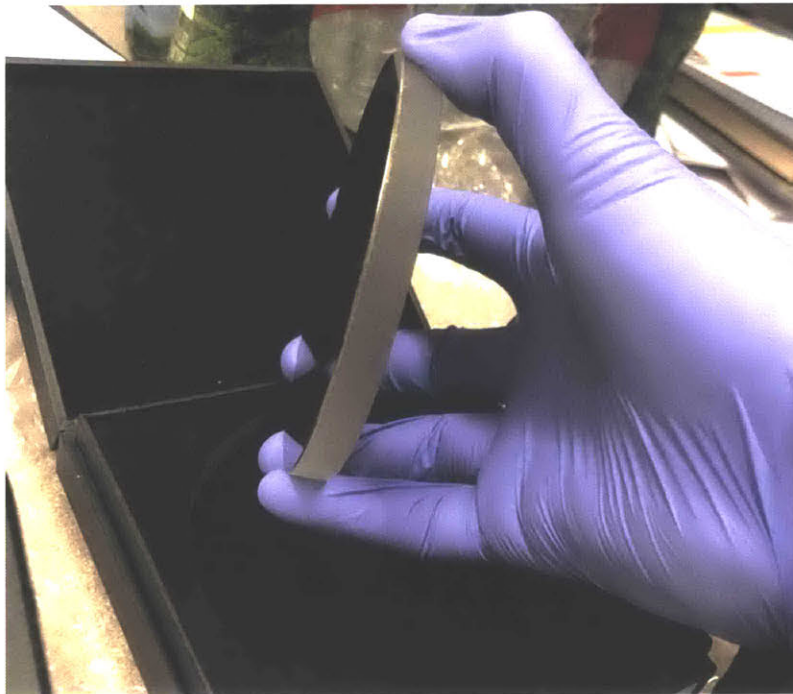


Figure K.4: Side picture of the Ge(440) spherically bent crystal from XRStech



Figure K.5: Crystal mounted on a mirror mount from Thorlabs



Figure K.6: Mirror mount mounted on a high-precision rotation stage from Thorlabs

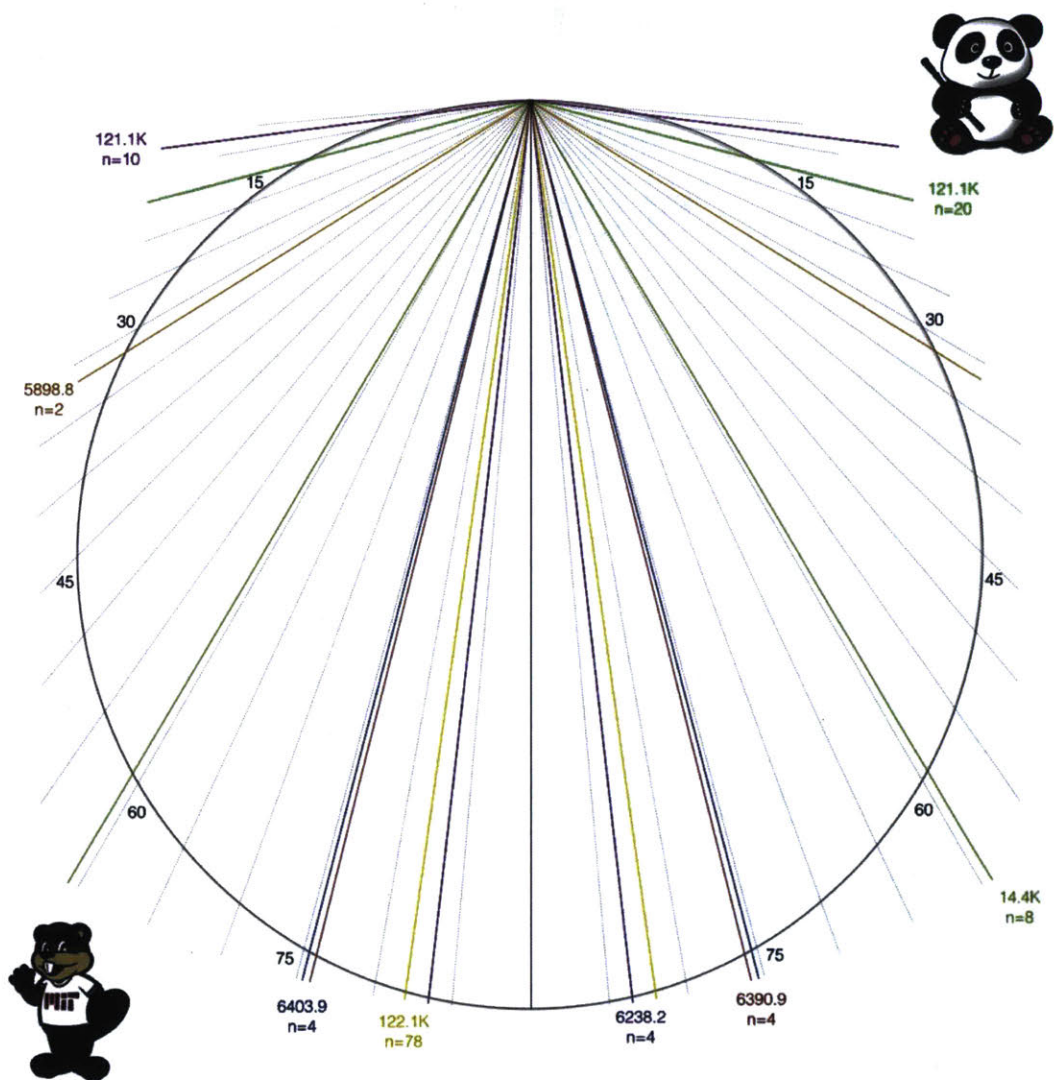


Figure K.7: Ge(440) bent crystal spectrometer alignment poster

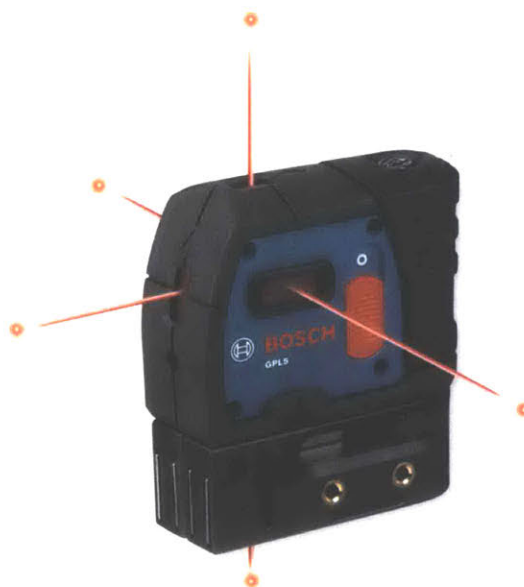


Figure K.8: Multi-direction alignment laser from Bosch

Figure K.9 shows the adjustable slit (Model number: VA100) from Thorlabs. The slit range is from 0 to 0.24 inch. The micrometer graduation is 0.001 inch. Figure K.10 and K.11 show how we fixed the adjustable slit in front of the Co-57 source. The slit was fixed in front of a single source point. The slit and the plate source moved together. Figure K.12 and K.13 show how we mounted the plate source. The plate was first mounted on breadboards (Model Number: MB6) from Thorlabs. Then the breadboards were mounted on a linear translation stage (Model Number: Parker 404100XRMP Linear Actuator). Figure K.14 shows the whole picture of the bent crystal spectrometer experiment. The plate source, the Ortec detector and the Ge(440) bent crystal were all aligned to right positions according to the correct Bragg angle (75.43 degrees) for Fe K-alpha. According to the Center for X-ray Optics website,⁸ the transmission rate for Fe K-alpha after traveling in the air for around 2 meters is less than 1%. To solve this problem, a V shape mylar helium bag was put along the X-ray path. The Fe K-alpha signals reaching the detector was increased by a factor of about 40. Lead bricks were put between the source and the detector to reduce noise.



Figure K.9: Adjustable slit from Thorlabs

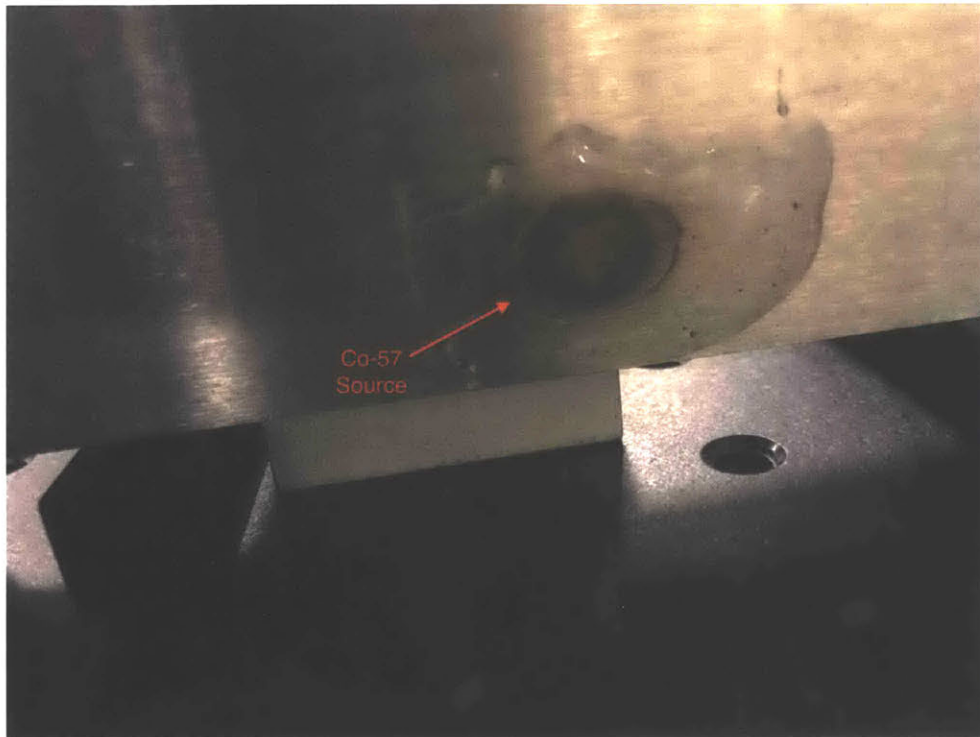


Figure K.10: Co-57 source on the steel plate

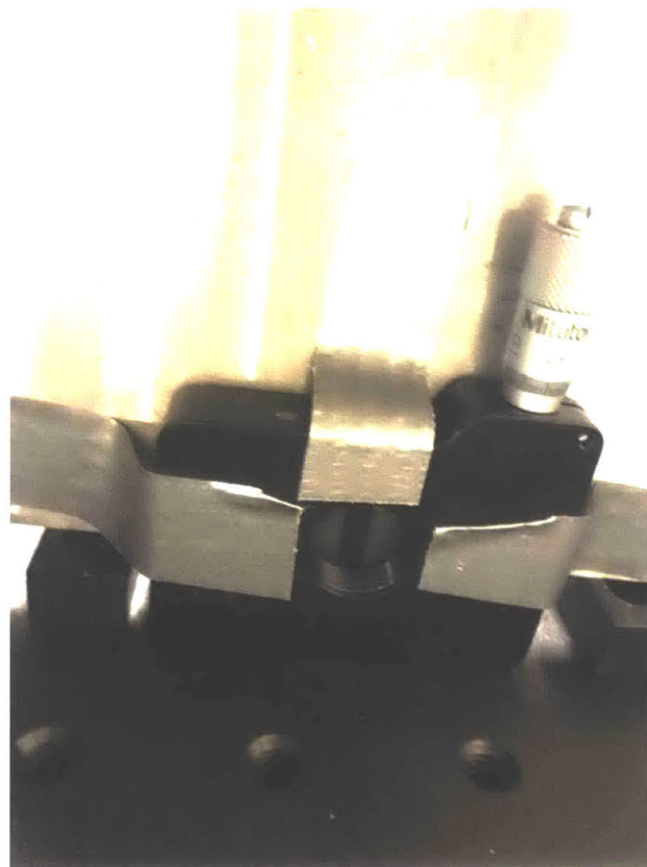


Figure K.11: Adjustable slit fixed in front of the Co-57 source

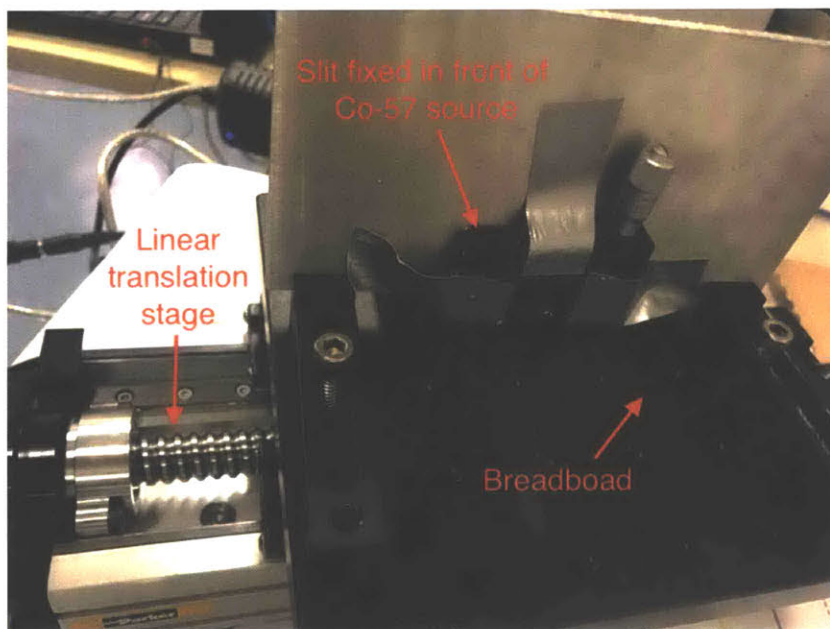


Figure K.12: Plate source mounted on the breadboard and translation stage

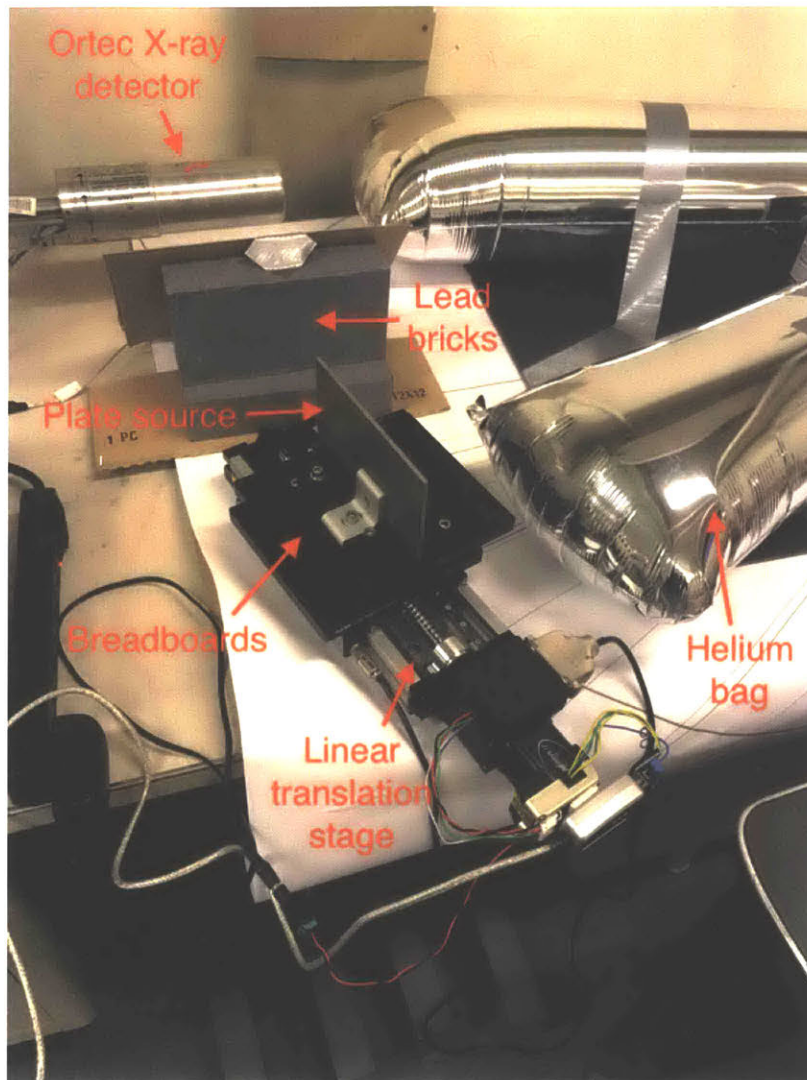


Figure K.13: Another picture of the plate mounted on the breadboard and translation stage

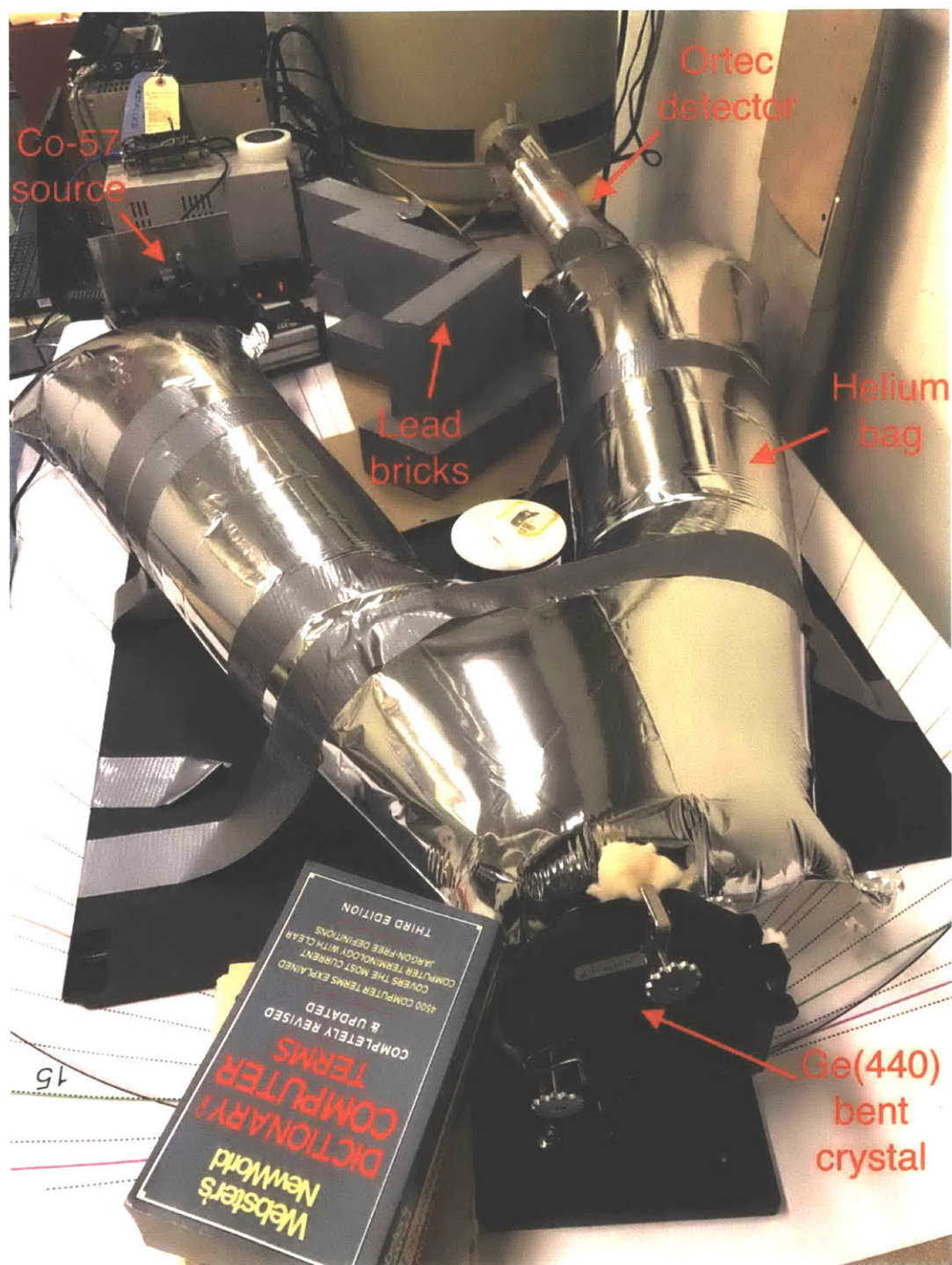


Figure K.14: Whole picture of the bent crystal spectrometer experiment

For Fe K-alpha, there is Fe K-alpha 1 at 6403 eV and Fe K-alpha 2 at 6391 eV.⁹ With the Amptek detector, it is impossible to distinguish these two lines. Figure K.15 shows the high-resolution spectrum from our bent crystal spectrometer when the slit width is set to be 1.5 mm. The resolution is around 3eV. The Fe K-alpha 1 line and the Fe K-alpha 2 line are distinguished.

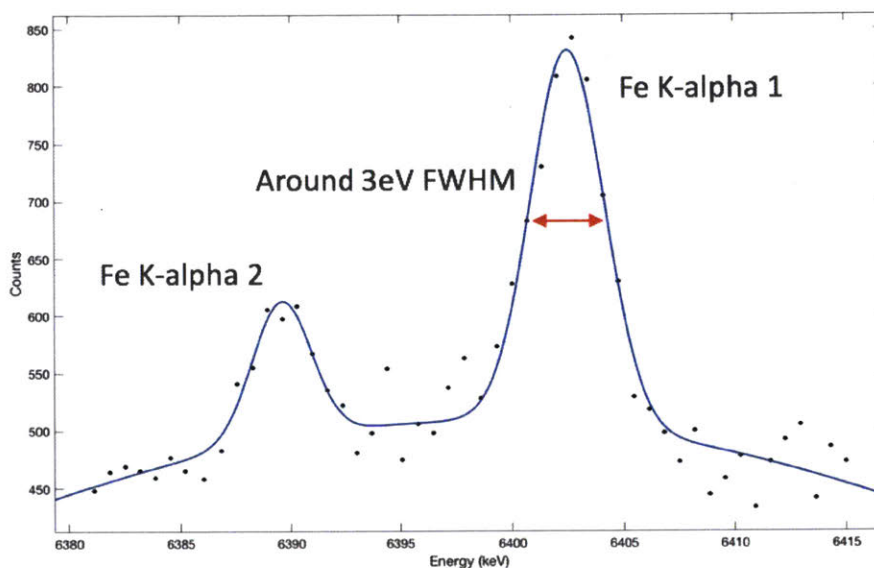


Figure K.15: High-resolution spectrum for Fe K-alpha from the bent crystal spectrometer

Though the Ge(440) crystal is not designed for the 14.4 keV line, we still did some experiments trying to measure the 14.4 keV gamma with the Ge(440) crystal. We first tried order $n=8$ with Bragg angle at 59.32 degrees. We hardly saw any 14.4 keV signal. Later we tried order $n=6$ with Bragg angle at 40.17 degrees. We got some signals as shown in Figure K.16. We first did a test with the correct angle 40.17 degrees. Then we immediately repeated the test at a wrong angle for the same amount of time. By comparing the two spectrums, we roughly got 40 counts per hour signal for the 14.4 keV gamma.

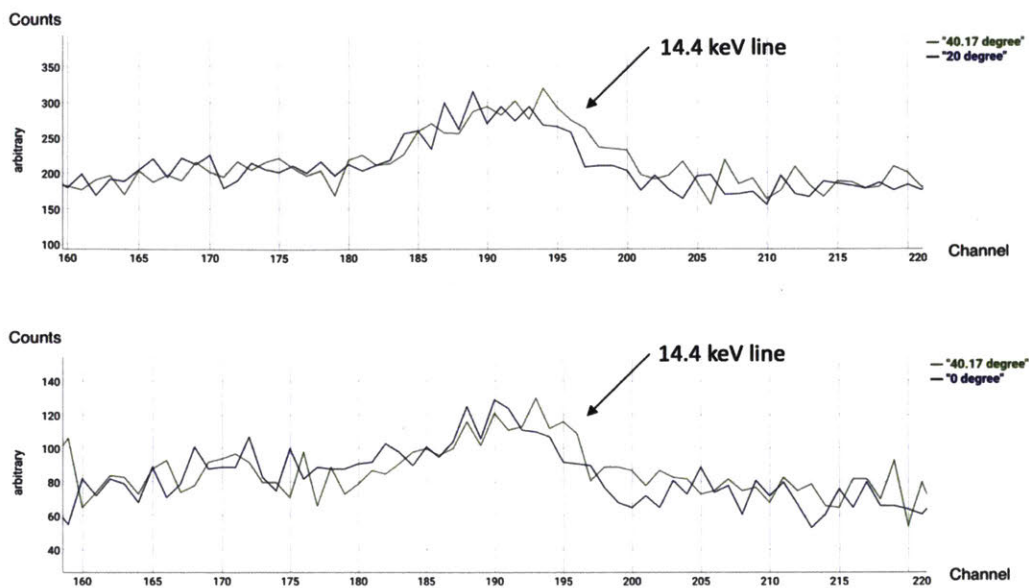


Figure K.16: 14.4 keV signals using Ge(440) crystal

In order to build a bent crystal spectrometer for 14.4 keV line, we need another crystal designed for 14.4 keV. We got some quotations from XRStech in March 2018. The best option is Ge(993) with Bragg angle at 84.37 degrees. The theoretical resolution can be as good as 0.41 eV. The cost was around \$12K. The leading time was about 4 months. The second best option is Si (975) with Bragg angle at 80.7 degrees. The theoretical resolution is around 0.69 eV. The cost was around \$6-7k. The leading time was about 4 months.

If we can have a position sensitive detector to replace the Ortec detector in Figure K.2, we no longer need to put a slit in front of the source. For example, an X-ray camera is a position sensitive detector. Figure K.17 shows the scheme of our bent crystal spectrometer design with an X-ray camera with the help of several publications from Seidler's group.⁵⁻⁷ The position of the X-ray signal on the X-ray camera corresponds to the energy of the X-ray. With the position information and signal counts from the X-ray camera, we can get the high-resolution spectrum. This configuration works best if the source is isotropic.

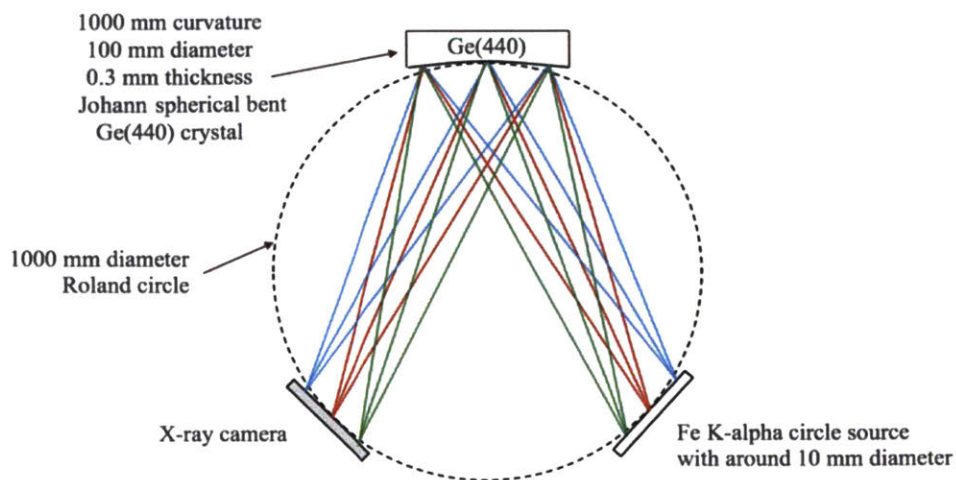


Figure K.17: Scheme of our bent crystal spectrometer for Fe K-alpha with an X-ray camera⁵⁻⁷

It is straightforward to get a good position sensitive detector if the budget is more than \$30K. For instance, the Pilatus area detector is around \$100K, the Princeton Instrument X-ray camera is around \$60K, and the Andor X-ray camera is around \$30K. All of these options are high-quality position sensitive detectors with good cooling and low noise. We spent lots of efforts looking for high-quality alternatives with the price around \$10K.

One supplier we were initially interested in working with is Hamamatsu from Japan. Hamamatsu offers several different models of linear CCD image sensors with the cost less than \$1K. However, the dark current noise is not good. Moreover, there are no drivers for some of the linear image sensors. Hamamatsu also offers several different models of area CCD image sensors with cost around \$10K. The dark current noise is much better for area image sensors than that for linear image sensors. However, it requires extra work to build a vacuum container for the sensor to avoid condensation on the sensor chip with cooling. Also, the lead time is long (around 4 months).

We ended up working with another supplier from the UK named Photonics Science. Photonics Sciences offers a built-in X-ray camera with cooling as low as -20C and dark current as low as

0.0018 e⁻/s/p. This camera can be configured for different energy X-rays by installing different scintillators. It can be used directly after delivery. When we got the quotation in January 2018. The cost was around \$15K. The lead time was around 6 weeks.

Table K.2 shows the detailed information of several position sensitive detectors from Hamamatsu and Photonics Science. The product in the last row is from Photonics Science. Products from all the other rows are from Hamamatsu.

The experiment introduced in this chapter is done by me. All data shown in this section is taken analyzed by me.

Table K.2: Information of several position sensitive detectors from Hamamatsu and Photonics Science

Product	Linear one-stage cooled 14 by 500 μm	Linear one-stage cooled 14 by 1000 μm	Linear non cooled 14 by 500 μm	Linear non cooled 14 by 1000 μm	Area one-stage cooled 24 by 24 μm	Area two-stage cooled 24 by 24 μm	Area non cooled 24 by 24 μm	Photonics Science -20 C 11.35 by 11.35 μm
Dark C per pixel	1500 e ⁻ /s/p	2000 e ⁻ /s/p	10000 e ⁻ /s/p	15000 e ⁻ /s/p	2.5 e ⁻ /s/p	0.2 e ⁻ /s/p	150 e ⁻ /s/p	0.0018 e ⁻ /s/p
Dark C per area	0.214 e ⁻ /s/ μm^2	0.143 e ⁻ /s/ μm^2	1.428 e ⁻ /s/ μm^2	1.071 e ⁻ /s/ μm^2	4.34*10 ⁻³ e ⁻ /s/ μm^2	3.47*10 ⁻⁴ e ⁻ /s/ μm^2	0.26 e ⁻ /s/ μm^2	1.40*10 ⁻⁵ e ⁻ /s/ μm^2
Driver	No	No	Yes	Yes	Yes	Yes	Yes	Yes
Price	898 only sensor	980 only sensor	Unknown	Unknown	10540	11830	Unknown	14150
Lead time	Unknown	Unknown	Unknown	Unknown	4 month	Unknown	Unknown	4-6 weeks

References

- 1 Bragg, W. H., & Bragg, W. L. (1913). The Reflection of X-rays by Crystals. *Proceedings of the Royal Society A: Mathematical, Physical and Engineering Sciences*, 88(605), 428-438. doi:10.1098/rspa.1913.0040
- 2 Hölzer, G., Wehrhan, O., Heinisch, J., Förster, E., Pikuz, T. A., Faenov, A. Y., . . . Shelkovenko, T. A. (1998). Flat and Spherically Bent Muscovite (Mica) Crystals for X-ray Spectroscopy. *Physica Scripta*, 57(2), 301-309. doi:10.1088/0031-8949/57/2/029

3 Crystals for X-Ray Spectrometry. (n.d.). Retrieved August 3, 2018, from <https://www.crystals.saint-gobain.com/sites/imdf.crystals.com/files/documents/crystals-for-xray-spectroscopy.pdf>

4 XRS TECH LLC. (n.d.). Retrieved August 3, 2018, from <http://xrstech.com/>

5 Holden, W. M., Hoidn, O. R., Ditter, A. S., Seidler, G. T., Kas, J., Stein, J. L., . . . Fakra, S. (2017). A compact dispersive refocusing Rowland circle X-ray emission spectrometer for laboratory, synchrotron, and XFEL applications. *Review of Scientific Instruments*, 88(7), 073904. doi:10.1063/1.4994739

6 Mortensen, D. R., & Seidler, G. T. (2017). Robust optic alignment in a tilt-free implementation of the Rowland circle spectrometer. *Journal of Electron Spectroscopy and Related Phenomena*, 215, 8-15. doi:10.1016/j.elspec.2016.11.006

7 Seidler, G. T., Mortensen, D. R., Remesnik, A. J., Pacold, J. I., Ball, N. A., Barry, N., . . . Hoidn, O. R. (2014). A laboratory-based hard x-ray monochromator for high-resolution x-ray emission spectroscopy and x-ray absorption near edge structure measurements. *Review of Scientific Instruments*, 85(11), 113906. doi:10.1063/1.4901599

8 X-Ray Interactions With Matter. (n.d.). Retrieved from http://henke.lbl.gov/optical_constants/

9 X-Ray Transition Energies Database. (2017, June 30). Retrieved from <https://www.nist.gov/pml/x-ray-transition-energies-database>